

SYNTHESIS AND EVALUATION OF TELLUROPHENE-APPENDED BODIPYS

by

Jacob W. Campbell

Submitted in partial fulfilment of the requirements
for the degree of Doctor of Philosophy

at

Dalhousie University
Halifax, Nova Scotia
July 2024

Dalhousie University is located in Mi'kma'ki, the
ancestral and unceded territory of the Mi'kmaq.
We are all Treaty people.

© Copyright by Jacob W. Campbell, 2024

To Abby

Table of Contents

List of Tables	x
List of Figures.....	xi
List of Schemes.....	xxiii
Abstract.....	xxv
List of Abbreviations and Symbols Used.....	xxvi
Acknowledgements	xxix
Chapter 1. Introduction	1
1.1. Pyrroles: Structure and Synthesis.....	1
1.2. Dipyrrins.....	4
1.3. BODIPYs	7
1.4. Multimodal (Hybrid) Cellular Imaging.....	9
1.5. A Possible Theragnostic Approach Using Photodynamic Therapy	11
1.6. Mass Cytometry (MC).....	14
1.7. Late-Stage Functionalisation of <i>F</i> -BODIPYs.....	16
1.7.1. <i>Meso</i> -Position.....	16
1.7.2. Pre-functionalisation.....	16
1.7.3. Palladium-Mediated Cross-Coupling of <i>F</i> -BODIPY.....	18
1.7.4. Substitution at Boron.....	19
1.8. Previous Work by Thompson-Group Members	20
1.9. Thesis Overview	26

Chapter 2. Palladium-Catalysed Cross-Coupling Towards Late-Stage Functionalisation of <i>F</i>-BODIPYs	28
2.1. Preface.....	28
2.2. Introducing the Tellurophene-Appended BODIPY: PDT Agent With Mass Cytometry Tracking Capabilities.....	30
2.2.1. Abstract.....	30
2.2.2. Introduction.....	31
2.2.3. Results and Discussion.....	35
2.2.4. Conclusions.....	42
2.2.5. Experimental	43
2.3. Optimisation Studies.....	43
2.3.1. Experimental	46
2.4. Chapter Conclusions and Future Perspectives	46
Chapter 3. Nucleophilic Substitution of <i>F</i>-BODIPYs At Boron Towards the Synthesis of Chalcogenophene-BODIPYs	49
3.1. Preface.....	49
3.2. BODIPYs with Chalcogenophenes at Boron: Synthesis and Properties	50
3.2.1. Abstract.....	50
3.2.2. Introduction.....	51
3.2.3. Results and Discussion.....	52
3.2.4. Conclusions.....	62
3.2.5. Experimental	63
3.3. Chapter Conclusions and Future Perspectives	63
Chapter 4. Synthesis of a Series of <i>[Te]</i>-BODIPYs	65
4.1. Preface.....	65

4.2. A Series of Potent BODIPY Photosensitisers Featuring Tellurophene Motifs at Boron	66
4.2.1. Abstract	66
4.2.2. Introduction	67
4.2.3. Results and Discussion	70
4.2.4. Conclusions	79
4.2.5. Experimental	80
4.3. Chapter Conclusions and Future Perspectives	80
Chapter 5. Synthesis of Estradiol [Te]-BODIPYs	82
5.1. Introduction	82
5.2. Design Principles and Targets	85
5.3. Discussion	88
5.4. Experimental	97
5.5. Chapter Conclusions and Future Perspectives	98
Chapter 6. Overall Conclusions	102
References	105
Appendix A. Chapter 2, Section 2.2 Supporting Information	133
A.1. Experimental Procedures	133
A.1.1. General Remarks	133
A.1.2. Synthesis of tellurophene, b1	134
A.1.3. Synthesis of 2-(pinacolatoboron)tellurophene, b2	136
A.1.4. Synthesis of 8-(4-bromophenyl)BODIPY, b3	137
A.1.5. Synthesis of 8-(4-(tellurophenyl)phenyl)BODIPY, b4	138
A.2. Photophysical Characterisation	139

A.3. Nuclear Magnetic Resonance Spectra	141
A.4. Crystallographic Information	148
A.5. Singlet Oxygen Detection Experiments	157
A.5.1. Spectra General Considerations	157
A.5.2. UV-Vis Absorbance Spectra	157
A.5.3. Determination of Molar Extinction Coefficients (ϵ) in DMSO Using Quantitative NMR	158
A.5.4. Singlet Oxygen Quantum Yield Experiments	159
A.5.5. Photostability of BODIPY compounds	162
A.5.6. Singlet Oxygen Determination of Compound b3	162
A.6. Cell Assays and Viability	163
A.6.1. Cell Culture General Notes	163
A.6.2. Cell viability Assays	164
A.6.3. Determining Reactive Oxygen Species Generation Within Cells	166
A.6.4. Mechanism of Cell Death	167
A.6.5. Cell Spheroid	168
A.7. Mass Cytometry	169
Appendix B. Chapter 2, Section 2.3 Supporting Information	172
B.1. General Remarks	172
B.2. Experimental	173
B.2.1. General Procedure for the Synthesis of 8-(4-bromophenyl)BODIPYs, GP1	173
B.2.2. Synthesis of 8-(4-bromo-2,6-difluorophenyl)BODIPY, b5	174
B.2.3. Synthesis of 8-(4-bromo-2-methylphenyl)BODIPY, b6	175

B.2.4. Synthesis of 8-(2,6-difluoro-4-(tellurophenyl)phenyl)BODIPY, b10.....	176
B.3. Nuclear Magnetic Resonance Spectra	178
Appendix C. Chapter 3 Supporting Information	185
C.1. Experimental Procedures	185
C.1.1. General Remarks	185
C.1.2. General Procedure for the Synthesis of <i>/E/</i> -BODIPYs, GP	188
C.1.3. Synthesis of 2,6-diethyl-1,3,5,7-tetramethyl-4,4-ditellurophenylBODIPY, c2.....	189
C.1.4. Synthesis of 2,6-diethyl-1,3,5,7-tetramethyl-4,4-diselenophenylBODIPY, c3.....	189
C.1.5. Synthesis of 2,6-diethyl-1,3,5,7-tetramethyl-4,4-dithiophenylBODIPY, c4	191
C.1.6. Synthesis of 2,6-diethyl-4,4-difuryl-1,3,5,7-tetramethylBODIPY, c5....	191
C.2. Photophysical Spectra.....	194
C.3. Cell Assays and Viability.....	197
C.3.1. Fluorescent Images	197
C.3.2. Cell viability assays	198
C.4. Nuclear Magnetic Resonance Spectra.....	200
C.5. Crystallographic Information.....	207
Appendix D. Chapter 4 Supporting Information	244
D.1. Experimental Procedures	244
D.1.1. General Remarks	244
D.2. Procedures	248
D.2.1. Synthesis of d3d.....	248
D.2.2. Synthesis of d3f.....	249

D.2.3. Synthesis of d3i.....	251
D.2.4. Synthesis of d3l.....	252
D.2.5. General procedure for the synthesis of <i>[Te]</i> -BODIPYs (GP).....	253
D.2.6. Synthesis of d4a	254
D.2.7. Synthesis of d4b.....	254
D.2.8. Synthesis of d4c	255
D.2.9. Synthesis of d4d.....	256
D.2.10. Synthesis of d4e	256
D.2.11. Synthesis of d4f.....	257
D.2.12. Synthesis of d4g	258
D.2.13. Synthesis of d4h.....	258
D.2.14. Synthesis of d4i.....	259
D.3. Photophysical Spectra.....	260
D.4. Cell Assays and Viability.....	268
D.5. NMR Spectra	270
Appendix E. Chapter 5 Supporting Information.....	289
E.1. Experimental Procedures	289
E.1.1. General Remarks.....	289
E.2. Procedures.....	291
E.2.1. General procedure for the synthesis of estradiol-appended <i>[Te]</i> -BODIPYs, GP	291
E.2.2. Synthesis of e1.....	292
E.2.3. Synthesis of e2a.....	293
E.2.4. Synthesis of e2b.....	294

E.3. Photophysical Spectra.....	295
E.4. Nuclear Magnetic Resonance Spectra	297
Appendix F. Copywrite Permission Letters	302
Appendix G. Contribution to Manuscript Form	304

List of Tables

Table 1. Summary of preliminary study of tellurophene-appended <i>F</i> -BODIPYS as photosensitisers.	26
Table 2. Photophysical data for c1-c5 in CH ₂ Cl ₂ solution.	58
Table 3. Absolute IC ₅₀ values of BODIPYS c1-c5	61
Table 4. Synthetic scope of nucleophilic substitution of tellurophene at boron of various BODIPYS.	72
Table 5. Challenging substrates for incorporation of tellurophene at boron of BODIPYS.	74
Table 6. <i>In vitro</i> and <i>in cellulo</i> data for [<i>Te</i>]-BODIPYS.	76
Table 7. Photophysical data for estradiol-appended [<i>Te</i>]-BODIPYS in CH ₂ Cl ₂ solution.	97
Table 8. Crystal data and structure refinement details.	151
Table 9. LED specifications used for singlet oxygen experiments.	160
Table 10. Lamp specifications used for cell experiments.	165
Table 11. IC ₅₀ of compound b4	165
Table 12. Crystal data and structural refinement details.	224
Table 13. Selected structural properties of [<i>E</i>]-BODIPYS.	229
Table 14. Photophysical characteristics of [<i>Te</i>]-BODIPYS in CH ₂ Cl ₂ and PBS.	260

List of Figures

- Figure 1.** The numbering and common nomenclature of pyrrole (left). Chemical structure of heme (centre) and chlorophyll (right)..... 2
- Figure 2.** The numbering and common nomenclature of dipyrin, **a4**..... 5
- Figure 3.** Dipyrinato, **a5**, resonance contributors. BODIPY, **a6**. Bis(dipyrinato)metal(II) complex, **a7**. Tris(dipyrinato)metal(II) complex, **a8**..... 7
- Figure 4.** The numbering and common nomenclature of *X*-BODIPY, **a9**. The numbering of *s*-indacene, **a10**..... 8
- Figure 5.** Chemical structure of Gd-DOTA-fluorescein: gadolinium-gadoteric acid complex, thiourea linker, and fluorescein..... 10
- Figure 6.** Representative photophysical pathways of photodynamic therapy. Modified from Kulbacka *et al.*⁷⁶..... 12
- Figure 7.** Palladium-catalysed functionalisation of *F*-BODIPYs with aryl coupling partners..... 17
- Figure 8.** Regiochemical considerations of published palladium-mediated cross-coupling of halogenated *F*-BODIPYs..... 19
- Figure 9.** Tellurophene-appended *F*-BODIPYs previously synthesised by Roberto Diaz-Rodriguez *via* Suzuki-Miyaura cross-coupling of 2-bromotellurophene and borylated *F*-BODIPYs.¹⁴⁶..... 23
- Figure 10.** Borylated tellurophene analogue, **a15**, tellurophene-2-pincolborate. α -tellurophene-appended *F*-BODIPY, **a16**, previously synthesised by Roberto Diaz-Rodriguez *via* Suzuki-Miyaura cross-coupling of tellurophene-2-BPin and the corresponding dibrominated *F*-BODIPY.¹⁴⁶..... 24
- Figure 11.** Side-on view of **b2** highlighting planarity of [Te]. 35
- Figure 12.** Side-on view of compound **b4**. Disorder removed for clarity..... 36
- Figure 13.** Cell Viability with **b4**. HeLa cells were incubated with 0–7.9 μ M **b4** for 3 h and left either in the dark or irradiated for the given duration with a 525 nm green

lamp (23.60 mW/cm²) IC₅₀ for dark condition = 1.35 μM, 1 min irradiation = 0.094 μM (1.42 J/cm²), 3 min irradiation = 0.053 μM (4.25 J/cm²), 5 min irradiation = 0.017 μM (7.08 J/cm²). Experiments were conducted in triplicate. 38

Figure 14. ROS Generation in HeLa Cells using DCFDA. HeLa cells were incubated with **b4** (25 μM) and DCFDA (10 μM) and fluorescence was monitored before and after 5-min irradiations with a 525 nm green lamp (23.60 mW/cm²). Green fluorescence indicates the production of ROS in cells. 20x magnification, scale bar = 50 μm..... 39

Figure 15. Mechanism of Cell Death. HeLa cells with no **b4** (top) or after incubation with **b4** (1.25 μM) and irradiated with 525 nm green lamp (bottom, 23.60 mW/cm²) were stained with Annexin V-FITC and PI four h post-treatment. Green fluorescence was only observed after treatment, showcasing cell death occurring through apoptotic pathways. 10x magnification, scale bar = 100 μm..... 40

Figure 16. Cell Viability of HeLa Cell Spheroids. HeLa spheroids treated with/without 100 nM **b4** under 5 min-irradiations (525 nm, 23.60 mW/cm²) or dark conditions. (top row) brightfield images of HeLa spheroids; (middle row) nuclear staining of all cells; (bottom row) cell death monitored by green fluorescence. Only spheroids treated with 100 nM of **b4** and irradiated exhibited significant cell death (10x magnification, scale bars = 100 μm). 41

Figure 17. Mass cytometry of **b4** within HeLa cells. Overlaid histogram of ¹³⁰Te signals with increasing concentrations of **b4** (25 nM (red), 250 nM (blue), 1000 nM (orange) and 4000 nM (green)). Cells were incubated with different concentrations of **b4** for 3 h before preparing cells for MC..... 42

Figure 18. Tellurophene-appended *F*-BODIPY featuring bulky ortho groups on the *meso*-aryl substituent. 43

Figure 19. *F*-BODIPYs, featuring steric bulk at the ortho-position on the *meso*-aryl substituents. Chemical structures in grey represent ongoing studies..... 44

Figure 20. Fluorine NMR spectrum of **b6**, highlighting the doublet of quartets for each fluorine atom. 45

Figure 21. The minor (left, matching **c5**) and major (right) components of the model used to refine the structure of a crystal grown from a reaction mixture obtained after attempts to synthesise **c5**. Disorder of the furan rings has been removed. Thermal ellipsoids are drawn at the 50% probability level and only selected atoms have been labelled..... 55

Figure 22. Structures of **c7** (one of the major components featuring three furan rings), **c4**, **c3** and **c2** (left to right), highlighting heterocyclic ring orientations at boron (top) and

dipyrrin planarity (bottom). Disorder (where present) has been removed for clarity with only the major component shown. Thermal ellipsoids are drawn at the 50% probability level and only selected atoms have been labelled.	56
Figure 23. Singlet oxygen generation of BODIPYs detected by DPBF in 2% DMSO/MeOH under 530 nm irradiation (2.15 mW/cm ²). EosY was chosen as the standard and DPBF alone was irradiated as a control. Experiments were conducted in triplicate.	59
Figure 24. Photostability of [<i>E</i>]-BODIPYs and parent <i>F</i> -BODIPY in 2% DMSO/MeOH. Absorbance was monitored at the λ_{max} during irradiation with a 530 nm LED (2.15 mW/cm ²).	59
Figure 25. Fluorescent images of HeLa cells incubated with [<i>E</i>]-BODIPY (1 μ M) for 3 h, obtained using an EGFP filter set (Ex 450-490 nm, Em 500-550 nm), 20x magnification, scale bar = 50 μ m.	60
Figure 26. Cell viability with [<i>E</i>]-BODIPYs. HeLa cells were incubated with varying concentrations of compounds for three h and left either in the dark or irradiated with a 525-nm green lamp (5 min, 15.60 mW/cm ² , 4.68 J/cm ²). Experiments were conducted in triplicate.	62
Figure 27. Proposed [<i>N</i>]-BODIPYs featuring various substituents on the nitrogen atom.	64
Figure 28. Tellurophene-appended BODIPY <i>via</i> Suzuki coupling.	69
Figure 29. Tellurophene-appended BODIPY <i>via</i> nucleophilic substitution at boron.	69
Figure 30. Photophysical characterisations of d4b . (a) Normalised absorbance of d4b in solutions of 1% DMSO in MeOH and 1% DMSO in PBS. (b) Singlet oxygen generation of d4b detected by DPBF in 1% DMSO in MeOH with 530 nm irradiation (2.15 mW/cm ²), n = 3. (c) Cell viability of HeLa cells incubated with varying concentrations of d4b under dark or light (525 nm, 4.68 J/cm ²) conditions, n = 9. .	77
Figure 31. Bioconjugate cartoon highlighting all components.	84
Figure 32. Examples of bioconjugation strategies.	84
Figure 33. 17 β -Estradiol highlighting numbering.	86
Figure 34. Estradiol-appended [<i>Te</i>]-BODIPY targets.	88
Figure 35. Target alkyne-functionalised estradiol.	90

Figure 36. Protecting group strategies for C3 and C17 alcohol protection of estradiol. .	93
Figure 37. Chemical structure of folic acid.....	99
Figure 38. Potential target folic acid appended photosensitiser <i>via</i> amide bond forming reactions.	100
Figure 39. Potential target folic acid appended photosensitiser <i>via</i> CuAAC bond forming reactions.	101
Figure 40. Normalised absorption and emission spectra of compound b4 in dichloromethane.....	140
Figure 41. ^1H NMR spectrum of compound b1 in CDCl_3	141
Figure 42. $^{125}\text{Te}\{^1\text{H}\}$ NMR spectrum of compound b1 in CDCl_3	142
Figure 43. ^1H NMR spectrum of compound b2 in CDCl_3	142
Figure 44. $^{13}\text{C}\{^1\text{H}\}$ NMR spectrum of compound b2 in CD_2Cl_2	143
Figure 45. ^{11}B NMR spectrum of compound b2 in CD_2Cl_2	143
Figure 46. ^1H NMR spectrum of compound b3 in CDCl_3	144
Figure 47. ^1H NMR spectrum of compound b4 in CD_2Cl_2	144
Figure 48. $^{13}\text{C}\{^1\text{H}\}$ NMR spectrum of compound b4 in CD_2Cl_2	145
Figure 49. ^{11}B NMR spectrum of compound b4 in CD_2Cl_2	145
Figure 50. ^{19}F NMR spectrum of compound b4 in CD_2Cl_2	146
Figure 51. HSQC NMR (126 MHz, 500 MHz) spectrum of compound b4 in CD_2Cl_2	146
Figure 52. $^{125}\text{Te}\{^1\text{H}\}$ NMR spectrum of compound b4 in CD_2Cl_2	147
Figure 53. Structure of compound b2 . Thermal ellipsoids have been drawn at the 50% probability level. Hydrogen atoms have not been labelled.	153
Figure 54. Side-on view of compound b2	153
Figure 55. Packing diagram for compound b2 viewed down the Y-axis.	154
Figure 56. Intermolecular interactions to the sum of the van der Waals radii of the Te atom in compound b2 . Only the atoms involved in the interactions have been labelled.	154

Figure 57. Structure of compound b4 . The two-part disorder of compound b4 (left) has been modelled by two ordered parts, part A 89.94(5) % and part B 10.06 % (centre and right, respectively). Thermal ellipsoids have been drawn at the 50% probability level. Hydrogen atoms have not been labelled.	155
Figure 58. Side-on view of compound b4	155
Figure 59. Packing diagram for compound b4 viewed down the X-axis.	156
Figure 60. Intermolecular interactions to the sum of the van der Waals radii of the Te atoms in one central molecule of compound b4 . Only the atoms involved in the interactions have been labelled.	156
Figure 61. Absorbance of compound b4 in MeOH and PBS with 2% DMSO. λ_{\max} values were 499 nm in MeOH and 532 nm in PBS, respectively.	157
Figure 62. Determination of molar extinction coefficient of compound b4 in DMSO .	159
Figure 63. Singlet oxygen generation of compound b4 (1 μ M) was compared to Eosin Y in MeOH with irradiation at 490 nm (17.0 mW/cm ²) at room temperature. Experiments were conducted n = 6 times.	161
Figure 64. Quenching of ¹ O ₂ production of compound b4 with NaN ₃ in MeOH at room temperature (1 μ M) under irradiation at 490 nm (17.0 mW/cm ²). Experiments were conducted in triplicate.	161
Figure 65. Photostability of compound b4 (1 μ M) under irradiation at 490 nm (17.0 mW/cm ²) in MeOH at room temperature. Experiments were conducted in triplicate.	162
Figure 66. Singlet oxygen generation of compound b3 (2 μ M) was compared to Eosin Y in MeOH with irradiation at 490 nm (28.0 mW/cm ²) at room temperature. Minimal ¹ O ₂ was detected, and experiments were conducted in triplicate.....	163
Figure 67. Cell viability of HeLa cells under 5-min irradiations and in the dark. No phototoxicity was observed under irradiation conditions with the 525 nm lamp (23.60 mW/cm ²). Experiments were done in triplicate.	165
Figure 68. Controls for intracellular ROS detection. (a) Cell incubated with 10 μ M DCFDA before and after 5-minute irradiation with 525 nm lamp (23.60 mW/cm ²) (b) Cells incubated with 25 nM b4 without DCFDA before and after 5-minute irradiation with 525 nm lamp (23.60 mW/cm ²).	167
Figure 69. A plot of ¹³⁰ Te intensities versus concentration of b4 . 75 thousand events were taken per concentration.	171

Figure 70. ^1H NMR (500 MHz) spectrum of compound b5 in CDCl_3	178
Figure 71. $^{13}\text{C}\{^1\text{H}\}$ NMR (126 MHz) spectrum of compound b5 in CDCl_3	178
Figure 72. ^{11}B NMR (160 MHz) spectrum of compound b5 in CDCl_3	179
Figure 73. ^{19}F NMR (470 MHz) spectrum of compound b5 in CDCl_3	179
Figure 74. ^1H NMR (500 MHz) spectrum of compound b6 in CDCl_3	180
Figure 75. $^{13}\text{C}\{^1\text{H}\}$ NMR (126 MHz) spectrum of compound b6 in CDCl_3	180
Figure 76. ^{11}B NMR (160 MHz) spectrum of compound b6 in CDCl_3	181
Figure 77. ^{19}F NMR (470 MHz) spectrum of compound b6 in CDCl_3	181
Figure 78. ^1H NMR (500 MHz) spectrum of compound b10 in CDCl_3	182
Figure 79. $^{13}\text{C}\{^1\text{H}\}$ NMR (126 MHz) spectrum of compound b10 in CDCl_3	182
Figure 80. ^{11}B NMR (160 MHz) spectrum of compound b10 in CDCl_3	183
Figure 81. ^{19}F NMR (470 MHz) spectrum of compound b10 in CDCl_3	183
Figure 82. $^{125}\text{Te}\{^1\text{H}\}$ NMR (95 MHz) spectrum of compound b10 in CDCl_3	184
Figure 83. Normalised absorbance spectra for solutions of c2-c5 in CH_2Cl_2 highlighting a slight bathochromic shift corresponding with the heavy-atom effect of the heteroatom.	194
Figure 84. Normalised absorption and emission spectra of compound c1 in dichloromethane.....	194
Figure 85. Normalised absorption and emission spectra of compound c2 in dichloromethane.....	195
Figure 86. Normalised absorption and emission spectra of compound c3 in dichloromethane.....	195
Figure 87. Normalised absorption and emission spectra of compound c4 in dichloromethane.....	196
Figure 88. Normalised absorption and emission spectra of compound c5 in dichloromethane.....	196

Figure 89. Fluorescent images of compounds c2 and c3 with longer exposure times compared to the background. 20x magnification, scale bar = 50 μm	198
Figure 90. ^1H NMR (500 MHz) spectrum of compound c2 in CDCl_3	200
Figure 91. $^{13}\text{C}\{^1\text{H}\}$ NMR (126 MHz) spectrum of compound c2 in CDCl_3	201
Figure 92. ^{11}B NMR (160 MHz) spectrum of compound c2 in CDCl_3	201
Figure 93. ^1H NMR (500 MHz) spectrum of compound c3 in CDCl_3	202
Figure 94. $^{13}\text{C}\{^1\text{H}\}$ NMR (126 MHz) spectrum of compound c3 in CDCl_3	202
Figure 95. ^{11}B NMR (160 MHz) spectrum of compound c3 in CDCl_3	203
Figure 96. ^1H NMR (500 MHz) spectrum of compound c4 in CDCl_3	203
Figure 97. $^{13}\text{C}\{^1\text{H}\}$ NMR (126 MHz) spectrum of compound c4 in CDCl_3	204
Figure 98. ^{11}B NMR (160 MHz) spectrum of compound c4 in CDCl_3	204
Figure 99. ^1H NMR (500 MHz) spectrum of compound c5 in CDCl_3	205
Figure 100. $^{13}\text{C}\{^1\text{H}\}$ NMR (126 MHz) spectrum of compound c5 in CDCl_3	205
Figure 101. ^{11}B NMR (160 MHz) spectrum of compound c5 in CDCl_3	206
Figure 102. ^{11}B NMR spectra of the <i>[E]</i> -BODIPYs series.....	206
Figure 103. Calculated electrostatic potential maps of the gas phase heterocycles.....	219
Figure 104. Calculated HOMO and LUMO diagrams of gas phase heterocycles.	219
Figure 105. Structures of c7 (one of the major components featuring three furan rings), c4 , c3 and c2 (left to right), highlighting heterocyclic ring orientations at boron (top) and planarity (bottom). Disorder (where present) has been removed for clarity. Thermal ellipsoids are drawn at the 50% probability level and only selected atoms have been labelled.....	220
Figure 106. Structure of c2 . Thermal ellipsoids have been drawn at the 50% probability level. Hydrogen atoms have not been labelled.	230
Figure 107. Packing diagram for c2 viewed down the Z-axis.	230

- Figure 108.** Intermolecular interactions involving Te (below the sum of the Van der Waals radii) in the solid-state structure of **c2**. Only those atoms directly involved in the contacts have been labelled..... 231
- Figure 109.** Structure of **c3** showing only the major component of the four total components refined for each of the independent molecules in the asymmetric unit. Thermal ellipsoids have been drawn at the 50% probability level. Hydrogen atoms have not been labelled..... 232
- Figure 110.** Structure of **c3** showing all four disordered components refined for each of the independent molecules in the asymmetric unit. Thermal ellipsoids have been drawn at the 50% probability level. Only selected atoms have been labelled for clarity. 232
- Figure 111.** Composite diagram of molecule 1 in the structure of **c3** showing how the four disordered components are arranged relative to each other in the crystal. Top – all four components together. Middle – the two different orientations of the BODIPY framework separated. Bottom – the four different orientations of the selenophene ring separated. Thermal ellipsoids have been drawn at the 50% probability level. Only selected atoms have been labelled for clarity. 233
- Figure 112.** Packing diagram for **c3** viewed down the Y-axis. The disorder has not been removed..... 234
- Figure 113.** Structure of **c4** showing only the major component of the two total components refined for each of the independent molecules in the asymmetric unit. Thermal ellipsoids have been drawn at the 50% probability level. Hydrogen atoms have not been labelled. 234
- Figure 114.** Structure of **c4** showing both disordered components refined for each of the independent molecules in the asymmetric unit. Thermal ellipsoids have been drawn at the 50% probability level. Only selected atoms have been labelled for clarity. . 235
- Figure 115.** Molecule 1 in the structure of **c4** showing separately the two disordered components making up the refined model. Thermal ellipsoids have been drawn at the 50% probability level. Only selected atoms have been labelled for clarity..... 235
- Figure 116.** Packing diagram for **c4** viewed down the Y-axis. The disorder has not been removed..... 236
- Figure 117.** Structure of **c6** showing both disordered components refined. Thermal ellipsoids have been drawn at the 50% probability level. Hydrogen atoms have not been labelled. 237

Figure 118. Structure of c6 showing only the major component of the disordered model. Thermal ellipsoids have been drawn at the 50% probability level. Hydrogen atoms have not been labelled.....	238
Figure 119. Structure of c6 showing only the minor component of the disordered model (actually containing one intact furan ring). Thermal ellipsoids have been drawn at the 50% probability level. Hydrogen atoms have not been labelled.	238
Figure 120. Packing diagram for c6 viewed down the X-axis. The disorder has not been removed.....	239
Figure 121. Structure of c7 showing only the major component of the four total components refined in the disordered model. Thermal ellipsoids have been drawn at the 50% probability level. Hydrogen atoms have not been labelled.....	240
Figure 122. Structure of c7 showing only the third component of the four total components refined in the disordered model. It is shown separately here as it is analogous to the other compounds being reported in this work. Thermal ellipsoids have been drawn at the 50% probability level. Hydrogen atoms have not been labelled.....	240
Figure 123. Structure of c7 showing all four disordered components refined for the model chosen. Thermal ellipsoids have been drawn at the 50% probability level. Only selected atoms have been labelled for clarity.	241
Figure 124. Composite diagram of c7 rings showing how the four disordered components are arranged relative to each other in the crystal. Top – all four components together. Middle – the two different substituents on the BODIPY framework (furan ring or hydrogen atom) separated. Bottom – the different orientations of the furan ring separated. Thermal ellipsoids have been drawn at the 50% probability level. Only selected atoms have been labelled for clarity.	242
Figure 125. Packing diagram for compound c7 viewed down the X-axis. The disorder has not been removed.....	243
Figure 126. Normalised absorption and emission spectra of compound d4a in CH ₂ Cl ₂	261
Figure 127. Normalised absorption and emission spectra of compound d4b in CH ₂ Cl ₂	261
Figure 128. Normalised absorption spectrum of compound d4c in CH ₂ Cl ₂	262
Figure 129. Normalised absorption and emission spectra of compound d4d in CH ₂ Cl ₂	262

Figure 130. Normalised absorption and emission spectra of compound d4e in CH ₂ Cl ₂	263
Figure 131. Normalised absorption and emission spectra of compound d4f in CH ₂ Cl ₂	263
Figure 132. Normalised absorption spectrum of compound d4g in CH ₂ Cl ₂	264
Figure 133. Normalised absorption and emission spectra of compound d4h in CH ₂ Cl ₂	264
Figure 134. Normalised absorption spectrum of compound d4i in CH ₂ Cl ₂	265
Figure 135. Normalised absorbance spectra of [<i>Te</i>]-BODIPYs in MeOH and PBS (containing 1% DMSO).	266
Figure 136. Singlet oxygen generation of [<i>Te</i>]-BODIPYs detected by DPBF in 1% DMSO in MeOH.	267
Figure 137. Photostability of [<i>Te</i>]-BODIPYs under irradiation.	267
Figure 138. Cell viability of HeLa cells incubated with varying concentrations of [<i>Te</i>]- BODIPYs in dark or light conditions.....	269
Figure 139. ¹ H NMR (400 MHz) spectrum of compound d3d in CDCl ₃	270
Figure 140. ¹³ C{ ¹ H} NMR (101 MHz) spectrum of compound d3d in CDCl ₃	271
Figure 141. ¹¹ B NMR (128 MHz) spectrum of compound d3d in CDCl ₃	271
Figure 142. ¹⁹ F NMR (377 MHz) spectrum of compound d3d in CDCl ₃	272
Figure 143. ¹ H NMR (500 MHz) spectrum of compound d3f in CDCl ₃	272
Figure 144. ¹³ C{ ¹ H} NMR (126 MHz) spectrum of compound d3f in CDCl ₃	273
Figure 145. ¹¹ B NMR (160 MHz) spectrum of compound d3f in CDCl ₃	273
Figure 146. ¹⁹ F NMR (470 MHz) spectrum of compound d3f in CDCl ₃	274
Figure 147. ¹ H NMR (500 MHz) spectrum of compound d3i in CDCl ₃	274
Figure 148. ¹ H NMR (500 MHz) spectrum of compound d3l in CDCl ₃	275
Figure 149. ¹ H NMR (500 MHz) spectrum of compound d4a in CDCl ₃	275

Figure 150. $^{13}\text{C}\{^1\text{H}\}$ NMR (126 MHz) spectrum of compound d4a in CDCl_3	276
Figure 151. ^{11}B NMR (160 MHz) spectrum of compound d4a in CDCl_3	276
Figure 152. ^1H NMR (500 MHz) spectrum of compound d4b in CDCl_3	277
Figure 153. $^{13}\text{C}\{^1\text{H}\}$ NMR (126 MHz) spectrum of compound d4b in CDCl_3	277
Figure 154. ^{11}B NMR (160 MHz) spectrum of compound d4b in CDCl_3	278
Figure 155. ^1H NMR (500 MHz) spectrum of compound d4c in CDCl_3	278
Figure 156. $^{13}\text{C}\{^1\text{H}\}$ NMR (126 MHz) spectrum of compound d4c in CDCl_3	279
Figure 157. ^{11}B NMR (160 MHz) spectrum of compound d4c in CDCl_3	279
Figure 158. ^1H NMR (500 MHz) spectrum of compound d4d in CDCl_3	280
Figure 159. $^{13}\text{C}\{^1\text{H}\}$ NMR (126 MHz) spectrum of compound d4d in CDCl_3	280
Figure 160. ^{11}B NMR (160 MHz) spectrum of compound d4d in CDCl_3	281
Figure 161. ^1H NMR (500 MHz) spectrum of compound d4e in CDCl_3	281
Figure 162. $^{13}\text{C}\{^1\text{H}\}$ NMR (126 MHz) spectrum of compound d4e in CDCl_3	282
Figure 163. ^{11}B NMR (160 MHz) spectrum of compound d4e in CDCl_3	282
Figure 164. ^1H NMR (400 MHz) spectrum of compound d4f in CDCl_3	283
Figure 165. $^{13}\text{C}\{^1\text{H}\}$ NMR (126 MHz) spectrum of compound d4f in CDCl_3	283
Figure 166. ^{11}B NMR (160 MHz) spectrum of compound d4f in CDCl_3	284
Figure 167. ^1H NMR (500 MHz) spectrum of compound d4g in CDCl_3	284
Figure 168. $^{13}\text{C}\{^1\text{H}\}$ NMR (126 MHz) spectrum of compound d4g in CDCl_3	285
Figure 169. ^{11}B NMR (160 MHz) spectrum of compound d4g in CDCl_3	285
Figure 170. ^1H NMR (500 MHz) spectrum of compound d4h in CDCl_3	286
Figure 171. $^{13}\text{C}\{^1\text{H}\}$ NMR (126 MHz) spectrum of compound d4h in CDCl_3	286
Figure 172. ^{11}B NMR (160 MHz) spectrum of compound d4h in CDCl_3	287

Figure 173. ^1H NMR (500 MHz) spectrum of compound d4i in CDCl_3	287
Figure 174. $^{13}\text{C}\{^1\text{H}\}$ NMR (126 MHz) spectrum of compound d4i in CDCl_3	288
Figure 175. ^{11}B NMR (160 MHz) spectrum of compound d4i in CDCl_3	288
Figure 176. Normalised absorption and emission spectra of compound e1 in CH_2Cl_2 .	295
Figure 177. Normalised absorption and emission spectra of compound e2a in CH_2Cl_2	295
Figure 178. Normalised absorption and emission spectra of compound e2b in CH_2Cl_2	296
Figure 179. ^1H NMR (500 MHz) spectrum of compound e1 in CDCl_3	297
Figure 180. $^{13}\text{C}\{^1\text{H}\}$ NMR (126 MHz) spectrum of compound e1 in CDCl_3	298
Figure 181. ^{11}B NMR (160 MHz) spectrum of compound e1 in CDCl_3	298
Figure 182. ^1H NMR (500 MHz) spectrum of compound e2a in CD_2Cl_2	299
Figure 183. $^{13}\text{C}\{^1\text{H}\}$ NMR (126 MHz) spectrum of compound e2a in CD_2Cl_2	299
Figure 184. ^{11}B NMR (160 MHz) spectrum of compound e2a in CD_2Cl_2	300
Figure 185. ^1H NMR (500 MHz) spectrum of compound e2b in CD_2Cl_2	300
Figure 186. $^{13}\text{C}\{^1\text{H}\}$ NMR (126 MHz) spectrum of compound e2b in CD_2Cl_2	301
Figure 187. ^{11}B NMR (160 MHz) spectrum of compound e2b in CD_2Cl_2	301

List of Schemes

Scheme 1. Example of Knorr pyrrole synthesis.	3
Scheme 2. Condensation of pyrroles and aryl aldehydes, followed by oxidation to generate free-base dipyrrens.	6
Scheme 3. MacDonald condensation of α -formyl pyrroles and α -unsubstituted pyrroles to generate dipyrren salts.	7
Scheme 4. Synthetic pathway for tellurophene-appended <i>F</i> -BODIPYs via Suzuki-Miyaura cross-coupling.	22
Scheme 5. Suzuki coupling employing a11 and a boronated <i>F</i> -BODIPYs towards the synthesis of a12	23
Scheme 6. Synthesis of 8-(4-(tellurophenyl)phenyl)-BODIPY b4	34
Scheme 7. Suzuki-Miyaura palladium cross-coupling reaction toward the synthesis of b10	46
Scheme 8. Synthesis of [<i>E</i>]-BODIPYs.	52
Scheme 9. Proposed synthetic scheme for substitution at the 3-position of various chalcogenophenes.	63
Scheme 10. Synthesis of [<i>Te</i>]-BODIPYs via nucleophilic substitution at boron.	71
Scheme 11. Proposed improved synthesis of [<i>Te</i>]-BODIPYs employing BCl ₃	81
Scheme 12. Synthetic route to compounds d4f	86
Scheme 13. Synthesis of alkyne functionalised estradiol e5	89
Scheme 14. Synthesis of estradiol-appended [<i>Te</i>]-BODIPY e1	90
Scheme 15. Alcohol protection of estradiol using MOMCl.	92
Scheme 16. Multistep oxidation of MOM-protected estradiol towards facilitation of reactivity at the 7-position.	93

Scheme 17. Synthesis of estradiols appended with alkyne functionality at the 7α -position.	94
Scheme 18. Synthetic route to compounds e6a and e6b	95
Scheme 19. Synthesis of 7α -position estradiol-appended [<i>Te</i>]-BODIPY e2a and e2b ...	95

Abstract

This thesis provides a comprehensive overview of the synthetic procedures for late-stage functionalisation of 4,4-difluoro-4-bora-3a,4a-diaza-s-indacenes (BODIPYs), specifically to append a tellurophene motif to unleash the photosensitisation capabilities of BODIPYs whilst providing a mass tag, *via* the tellurium atom, for mass cytometry.

The design and synthesis of the first tellurophene-appended BODIPY framework is realised. Investigational studies confirm tellurophene-appended BODIPYs exhibit desired photochemical characteristics for photosensitisation and the tellurium atom is traceable by mass cytometry. Tellurophenes are appended to BODIPYs *via* the boron centre and *via* the β - and *meso*-positions of the dipyrinato core. Further functionalisation involves appending the tellurophene-BODIPY framework to biological ligands, towards targeted therapy.

List of Abbreviations and Symbols Used

[O]	furan
[S]	thiophene
[Se]	selenophene
[Te]	tellurophene
$^1\text{O}_2$	singlet oxygen
amu	atomic mass unit
APCI	atmospheric-pressure chemical ionisation
app	apparent
BODIPY	boron dipyrromethene
BPin	pinacol borate
bs	Broad singlet
d	doublet
dd	doublet of doublets
DDQ	2,3-dichloro-5,6-dicyano-1,4-benzoquinone
dipyrin	dipyrromethene
dq	doublet of quartets
EDG	electron-donating group
ESI ⁺	electrospray ionisation (positive mode)
ESI ⁻	electrospray ionisation (negative mode)

EWG	electron-withdrawing group
HOMO	highest occupied molecular orbital
HRMS	high-resolution mass spectrometry
ISC	inter-system crossing
ITDB	2-isopropoxy-4,4,5,5-tetramethyl-1,3,2-dioxaborolane
LUMO	lowest unoccupied molecular orbital
m	multiplet
MC	mass cytometry
MIDA	<i>N</i> -methylinodiacetic acid
ms	mass spectrometry
neop	neopentyl
PDT	photodynamic therapy
PET/CT	positron emission tomography/computed tomography
PET/MRI	positron emission tomography/magnetic resonance imaging
PS	photosensitiser
q	quartet
Rongalite	sodium hydroxymethanesulfinate
ROS	reactive oxygen species
s	singlet or second
sh	shoulder
SPECT	single-photon emission computed tomography

t	triplet
TLC	thin-layer chromatography
v/v	volume per volume
XPhos	dicyclohexyl[2',4',6'-tris(propan-2-yl)[1,1'-biphenyl]-2-yl]phosphane
δ	chemical shift
ϵ	molar absorptivity
λ	wavelength
$\lambda_{\text{abs}}^{\text{max}}$	wavelength of maximum absorbance
$\lambda_{\text{em}}^{\text{max}}$	wavelength of maximum emission
Φ_{f}	quantum yield of fluorescence
Φ_{Δ}	singlet oxygen quantum yield

Acknowledgements

My first thanks go to the support staff at Dalhousie: Cathy Ryan, Danielle Pottie, Graham Dexter, Ihor Krasilia, Lea Gawne, Mike Boutilier, Mike Lumsden, Ryan MacKinnon, Ulli Werner-Zwanziger and Xiao Feng; all of whom played a crucial role in supporting me during my degree.

It has been a pleasure to work with amazing collaborators throughout my degree. I truly believe that collaboration is the path to great science as one cannot be an expert in every field of research. Special thanks to: Dr. Katherine Robertson from Saint Mary's University, not only is Kathy an expert in crystallography but has incredible passion for her work and loves to share her knowledge with others; to collaborators from University of Toronto, Matthew Tung and Dr. Andrew Beharry, who matched our excitement for our research and are experts in photodynamic therapy drug development; and to Sara Evans from Dalhousie, Sara is a very passionate researcher, and I am excited to see where our collaborative project will go.

Many thanks to my fellow group members: Dr. Adil Alkaş, Breanna Taylor, Em Sullivan, Emily Brown, Dr. Jim Hillborn, Dr. Liandrah Gapare, Mike Cotnam, Mmasinachi Atansi, Roberto Diaz-Rodriguez, Dr. Sarah Greening and Steve Sequeira. I would also like to thank my committee members for their support: Dr. Alex Speed, Dr. Norman Schepp and Dr. Stephen Bearne.

I would not be where I am today without the support from my friends and family. Thanks to my mother Charlene and father David for their unconditional love. To Nanny Campbell and Poppy Campbell as well as my number one fan Nan Baker. To my life partner Abby for her amazing support throughout this journey.

Finally, to Dr. Alison Thompson, thank you for your supervision these last years. You continually went above and beyond what is expected as a supervisor; you not only helped me with manuscripts, reports, scholarship applications, research, and scientific theory but have supported me with all aspects of life. You truly are an amazing role model.

Chapter 1. Introduction

1.1. Pyrroles: Structure and Synthesis

Heterocyclic scaffolds are ring structures that contain at least one atom that is not carbon (*e.g.*, nitrogen, oxygen, sulfur). Among them, nitrogen heterocycles stand out as privileged structural components of pharmaceuticals and natural products (*e.g.*, vitamins, hormones, and antibiotics). Perhaps the most famous examples of compounds containing nitrogen heterocycles are serotonin,¹ caffeine,² morphine,³ and codeine.⁴ A study by Njardarson *et al.* reported that 59% of U.S. FDA-approved small-molecule drugs contain a nitrogen heterocycle and, in those drugs, the average number of nitrogen atoms per drug molecule is 3.1.⁵ For medicinal chemists, interest in nitrogen-based heterocycles comes from the broad range of known biological activities, as well as the abundant applications that these systems have had in the pharmaceutical sciences and in drug development.⁶ The Thompson group has designed a research program based on pyrrole (**a1**, **Figure 1**) and pyrrole-containing compounds due to their interesting reactivity and properties/applications *e.g.*, photochemical,^{7,8} anti-cancer,⁹ anti-bacterial/anti-microbial,¹⁰ anti-viral,¹¹ etc. Perhaps of highest biological importance, pyrrole plays a critical role in compounds necessary to life such as heme (**a2**, **Figure 1**), chlorophyll (**a3**, **Figure 1**), and cytochromes (proteins containing a central heme core), which are all oligomers of pyrroles.¹²

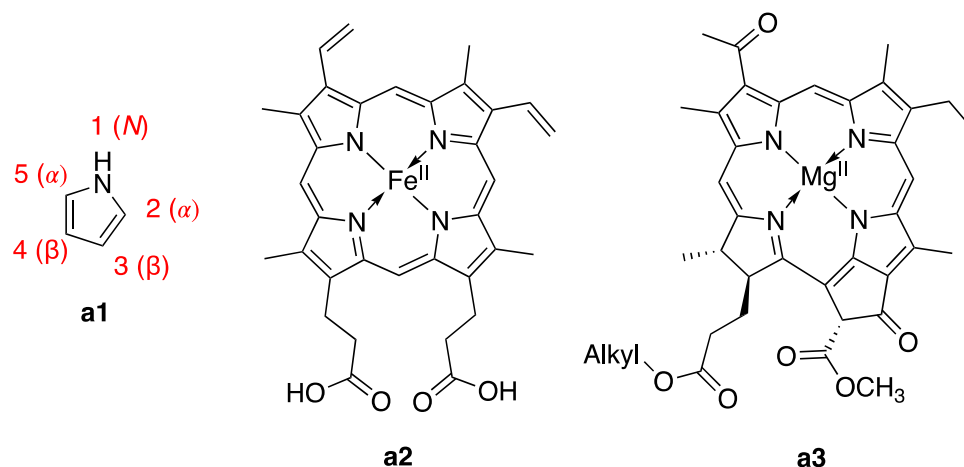


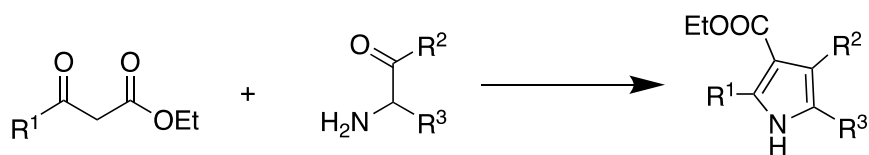
Figure 1. The numbering and common nomenclature of pyrrole (left). Chemical structure of heme (centre) and chlorophyll (right).

Pyrrole is an aromatic five-membered heterocycle by virtue of containing six pi electrons that are fully conjugated within a planar cyclic structure. As shown in **Figure 1**, the 2- and 5-positions of pyrrole are commonly referred to as the α -positions, the 3- and 4-positions are known as the β -positions, and the 1-position indicates the nitrogen atom.

Pyrroles have interesting electronic properties in that they are highly electron rich and are more nucleophilic at the α - and β - positions than the *N*-position.¹³ This is in contrast to pyridine, in which electrophilic addition favors the nitrogen atom. This relationship can be simply explained by considering the five resonance contributors of pyrrole: the favorable contributor results in a neutral pyrrole and other contributors are zwitterionic with the formal negative charge character being shared across the four carbon atoms. Collectively, this affords the α -position (and β -) a strong nucleophilic character when compared to the nitrogen atom upon which the formal positive charge character is located in these resonance contributors.

Pyrrole is highly susceptible to autooxidation when exposed to air, to thus generate a highly colored polymeric product.¹⁴ Furthermore, under acidic conditions pyrrole can be protonated at the ring, which can then undergo polymerisation.¹⁴ To combat this reactivity, a common practice is to install electron-withdrawing groups (EWGs) at the α - and/or β -positions, to greatly reduce both spontaneous polymerisation and ring protonation-mediated polymerisation.¹⁴ Consequently, many synthetic routes to functionalised pyrroles involve the formation of formyl-, acyl-, or carboxylate-substituted pyrroles.

Early synthetic routes towards pyrroles were studied in the late 19th century and contain many principles that are still employed today, *e.g.*, Hantzsch,¹⁵ Knorr,¹⁶ Paal-Knorr,^{17,18} and van Leusen.¹⁹ The Knorr pyrrole synthesis is most applicable for this report and produces stable pyrroles that feature carboxylates at the 3-position (**Scheme 1**). The Knorr synthesis employs a β -keto ester, which is converted to the corresponding imine. This imine can then be dissolved in a solution of acetic acid and reduced to the corresponding amine in the presence of zinc dust. The next step involves the condensation of the amine with the keto moiety of acetoacetate and followed by cyclisation.



Scheme 1. Example of Knorr pyrrole synthesis.

1.2. Dipyrrins

Early work extending the pyrrolic framework was focused on mimicking nature by synthesising tetrapyrrolic macrocycles such as porphyrins, *i.e.*, the synthetic analogue for the heme complex ligand, a major component of hemoglobin, the iron-containing oxygen-transport metalloprotein in the red blood cells.²⁰ Building on such porphyrin research, researchers began to take interest in 2,2'-dipyrromethenes (dipyrrins).²¹ However, despite the discovery of dipyrrins dating to the 20th Century, these systems were not popularised until Hans Fischer implemented them as critical precursors in the synthesis of porphyrins—work that was acknowledged when he won the Nobel prize in chemistry in 1930.²² Although Fischer's work sparked interest in dipyrrins, it was not until more recently that researchers have found uses for these dipyrroles outside of porphyrin chemistry. Dipyrrins are a member of the oligopyrrole family, containing just two pyrrolic units connected by a methylene bridge (**a4**, **Figure 2**). The two rings are formally non-equivalent as one contains a pyrrolic nitrogen and the other an iminic nitrogen, likening this unit to an aza-fulvene motif. Despite the two rings being formally inequivalent, on most useful timeframes rapid tautomerisation renders these rings equivalent. The numbering for dipyrrins is based on the porphyrin nomenclature in which the carbon atoms are labeled first, followed by the nitrogen atoms (**a4**, **Figure 2**). Like pyrrole, there is a common nomenclature that is more intuitive and will be used hereinafter: the 1- and 9-positions are referred to as the α -positions, 2-, 3-, 7-, and 8- are known as the β -positions and the 5-position is the *meso*-position.

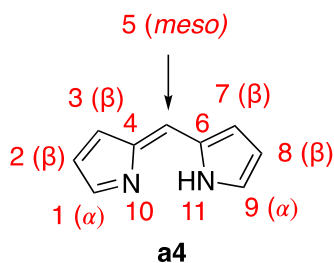
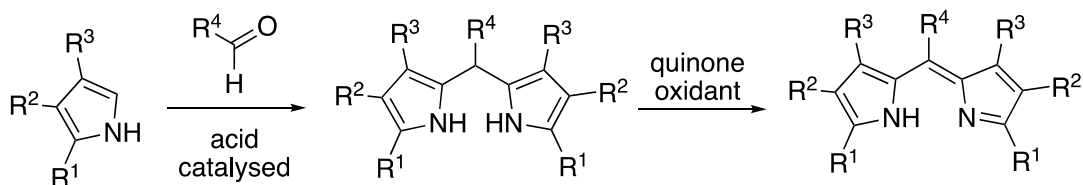


Figure 2. The numbering and common nomenclature of dipyrryn, **a4**.

The parent dipyrryn, *i.e.*, without substitution (α -, β - and *meso*-positions substituted with hydrogen), is highly susceptible to nucleophilic attack and not stable at ambient temperatures.²³ Fortunately, dipyrryns can be stabilised by addition of electron-withdrawing groups (EWGs). Furthermore, despite the viability of stability enhancement protocols, when the *meso*-position is left unsubstituted (*meso*-position substituted with hydrogen), many dipyrryns still lack stability in air. To enhance stability, it is commonplace for dipyrryns to be isolated as either the hydrobromide or hydrochloride salts, instead of the free-base form.²⁴ Moreover, it should be noted that the substitution pattern on dipyrryns often include alkyl groups which may seem in contrast to the stabilisation that is required; however, these arise by virtue of the Knorr-type pyrroles used to generate them.²³ Other approaches towards enhancing stability include complexation of the dipyrrynato unit to a boron difluoride group, generating 4,4-difluoro-4-bora-3a,4a-diaza-s-indacenes or "boron-dipyrromethenes" (hereinafter abbreviated to BODIPYs). Dipyrryns in the form of BODIPYs have significant stability in air, with the variant lacking any substitution about the pyrrolic units being isolated in 2009.²³

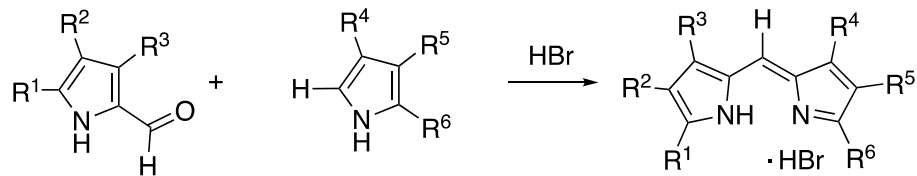
Classically, *meso*-substituted symmetrical free-base dipyrryns are synthesised by first generating a dipyrromethane (two pyrrole units bridged by $-\text{CH}_2-$) and then performing an

oxidation to generate the methylene, -CH-, unit. Dipyrrmethanes are commonly synthesised by condensing two equivalents of an α -free pyrrole in the presence of a carboxaldehyde under acid-catalysed conditions using hydrochloric acid,²⁵ acetic/propionic acid,²⁶ *p*-toluenesulphonic acid,²⁷ trifluoroacetic acid²⁸ or indium (III) chloride.²⁹ The dipyrrmethane species can then be oxidised using quinone oxidants such as 2,3-dichloro-5,6-dicyano-1,4-benzoquinone (DDQ) or *p*-chloranil (**Scheme 2**). This is a robust route for synthesis of symmetric dipyrins.



Scheme 2. Condensation of pyrroles and aryl aldehydes, followed by oxidation to generate free-base dipyrins.

Meso-unsubstituted dipyrins are regularly synthesised *via* MacDonald condensation, which condenses an α -formyl pyrrole and an α -unsubstituted pyrrole in the presence of hydrobromic acid (HBr) to generate the dipyrin as a salt (**Scheme 3**).³⁰ This is a robust route for synthesis of asymmetric dipyrins. Additionally, in the presence of formic acid and HBr, pyrrole α -carboxylates can be first hydrolysed to the carboxylic acid analogue, which then decarboxylates *in situ* to generate the α -free pyrrole. Two equivalents of this α -free pyrrole can then self-condense with formic acid to give the dipyrin salt.³⁰



Scheme 3. MacDonald condensation of α -formyl pyrroles and α -unsubstituted pyrroles to generate dipyrin salts.

Deprotonation of the dipyrin framework formally generates the resonance stabilised dipyrinato anion (**a5**, **Figure 3**). The dipyrinato unit is a bidentate chelating ligand, with the most famous case involving complexation to boron to generate the aforementioned BODIPY construct, first reported by Treibs and Kazar in 1968 (**a6**, **Figure 3**).³¹ However, the dipyrinato unit has also been reported to accept a variety of transition metal cations *e.g.*, nickel(II), copper(II), zinc (II), iron(III), cobalt(III), rhodium (III) and more to generate bis(dipyrinato)metal(II) (**a7**, **Figure 3**) and tris(dipyrinato)metal(III) complexes (**a8**, **Figure 3**).^{21,32}

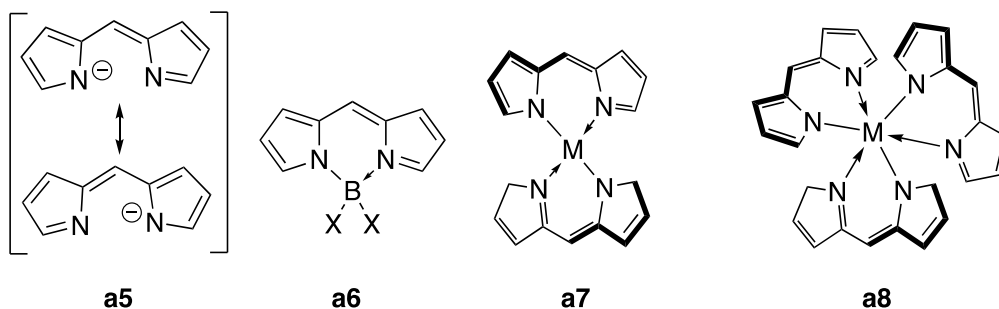


Figure 3. Dipyrinato, **a5**, resonance contributors. BODIPY, **a6**. Bis(dipyrinato)metal(II) complex, **a7**. Tris(dipyrinato)metal(II) complex, **a8**.

1.3. BODIPYs

Researchers have been enticed by BODIPYs, rather than other dipyrinato metal complexes, due to the photophysical properties of these boron-containing chromophores.

When compared to BODIPYs, most dipyrinato metal complexes have little to negligible fluorescent efficiencies.³²

Common nomenclature and numbering for BODIPYs (**a9**, **Figure 4**) is shared with *s*-indacene (**a10**, **Figure 4**), a compound with analogous bonding connectivity. Although the numbering is different than that of the parent dipyrin, BODIPYs share the same common nomenclature as dipyrin, *i.e.*, the 3- and 5- are referred to as the α -positions, 1-, 2-, 6-, and 7- are known as the β -positions and the 8-position is the *meso*-position (**a9**, **Figure 4**). BODIPYs can further be categorised by the atoms bound to the boron centre. Indeed, the complexation of the dipyrinato unit to $-\text{BF}_2$ gives what is commonly abbreviated as *F*-BODIPY. Many other BODIPYs are known: *aryl*-BODIPY,³³ *alkyl*-BODIPY,³⁴ *alkyne*-BODIPY,³⁵ *O*-BODIPY,³⁶ *Cl*-BODIPY³⁷ and more, with the substituents at boron varying accordingly.³⁸

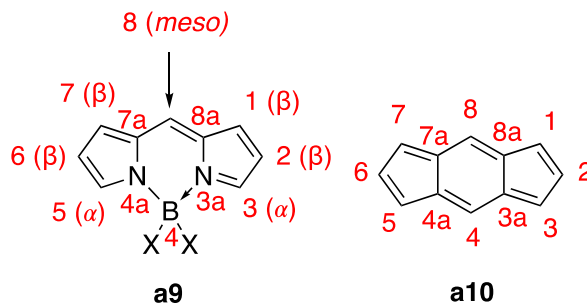


Figure 4. The numbering and common nomenclature of *X*-BODIPY, **a9**. The numbering of *s*-indacene, **a10**.

By far the most popular application of *F*-BODIPYs is their use as dyes.^{33,36,39–42} They have very strong visible UV-absorption properties and when irradiated, generally result in sharp emission peaks with high fluorescence quantum yields (Φ_f).⁴³ The photochemical properties of *F*-BODIPYs are generally tolerant to changes in environment such as polarity

and pH, and these compounds are reported to be stable under physiological conditions.⁴³ Even small substituent tuning of the *F*-BODIPY core can greatly impact the photophysical properties and thus *F*-BODIPYs have found use in multiple biological applications, *e.g.*, imaging reagents, labeling reagents,^{39,44,45} switches^{46,47} and sensors.^{48–51}

1.4. Multimodal (Hybrid) Cellular Imaging

A common problem in the field of biological imaging is that clinicians often have to settle for an imaging modality with high sensitivity, yet with relatively low resolution, or *vice versa*.⁵² To overcome this limitation, researchers have suggested to couple modalities that complement one another, thus generating a sharper overall image.⁵² Later termed multimodal or hybrid imaging techniques, these techniques began to gain traction when the first PET/CT (positron emission tomography/computed tomography) instrument, developed by Townsend *et al.*, became commercially available in 2001.⁵³ The next decade saw the development of many other multimodal approaches such as PET/MRI (positron emission tomography/magnetic resonance imaging),^{54,55} lipid-based approaches,^{56–58} quantum dots,^{59–63} iron oxide nanoparticles,^{64–66} macromolecular carriers^{67,68} and more recently, small-molecule probes.^{69–72} the latter of which is of interest in the Thompson group.

The tuning of pharmacokinetic properties for small-molecules is more accessible than for other *in vivo* multimodal probes as these systems are not bound to a macromolecular housing or involve nanoparticle conjugates, *e.g.*, the pharmacokinetic properties, such as metabolism of macromolecular carriers, is controlled solely by the macrostructure itself and not the probe.⁵² Moreover, a small probe can be tuned by synthetic functionalisation,

is more readily diffused through skin, and can be cleared by the renal system. In contrast, probes are cleared by the liver, which can cause problems affiliated with long-term liver retention and toxicity.⁵²

Small molecule multimodal probes were first popularised with the development of gadolinium (III) chelators, used as MRI contrast agents in humans,⁷³ coupled with fluorophores such as rhodamine or fluorescein (**Figure 5**).⁷¹ One challenge with conjugating multiple modalities is that most systems feature a 1:1 ratio of modalities in terms of each small-molecule. This can be limiting when the two different modalities have differing sensitivities.⁵²

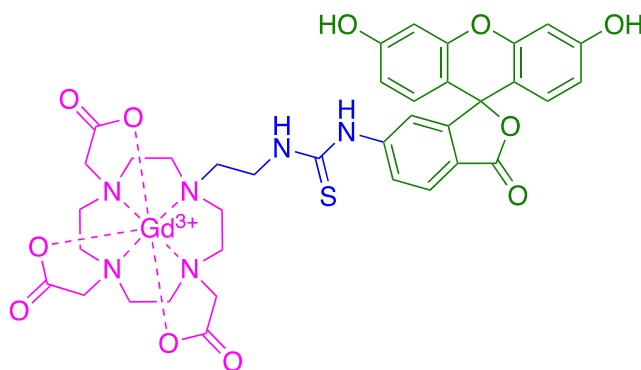


Figure 5. Chemical structure of Gd-DOTA-fluorescein: gadolinium-gadoteric acid complex, thiourea linker, and fluorescein.

An alternative approach towards a multimodal probe combines radioisotopes and fluorophores as their imaging techniques share similar sensitivity for *in vivo* applications.⁵² Many examples of installing chelated radioisotopes on small-molecule probes have been realised, including ⁶⁴Cu which is used for PET, ¹⁷⁷Lu used in SPECT and ¹¹¹In used for MRI.⁷⁴ Radioisotopes can be installed by iodinating *F*-BODIPYs directly with ¹²⁴I, generating a PET-fluorescence modality.^{57,69}

1.5. A Possible Theragnostic Approach Using Photodynamic Therapy

Recent breakthroughs, including the work involving ^{124}I ,^{69,75} saw development of small molecular probes with systems tuned for both diagnosis and treatment, to facilitate concurrent localisation and treatment of cancerous cells. This “see and treat” or theragnostic approach was first realised by tuning properties of dyes to act as photosensitisers (PS), for a treatment known commonly as photodynamic therapy (PDT). The use of theragnostic dyes is a clinically proven and powerful tool for applying an accurately assessed payload of PS to cancerous cells. Moreover, if the dye retains sufficient fluorescence, it can be used to identify the location of the drug, *i.e.*, multimodal imaging. The mechanism for cell death induced by PDT comprises of a nontoxic sensitizer drug in the ground state (PS) that is activated by absorbing highly focused and controlled light of an appropriate wavelength. The photosensitized drug, in the excited singlet state ($^1\text{PS}^*_n$), can then either lose energy and return to the ground state by relaxation *via* vibrational or emissive modes. Conversely, $^1\text{PS}^*_n$ can be promoted to the triplet state ($^3\text{PS}^*$) *via* intersystem crossing (ISC). From the $^3\text{PS}^*$, energy can be lost due to phosphorescence or, by virtue of the $^3\text{PS}^*$ having a longer half-life than $^1\text{PS}^*_n$, can interact with ground state oxygen ($^3\text{O}_2$) to form cytotoxic singlet oxygen ($^1\text{O}_2$) (**Figure 6**). Other reactive oxygen species (ROS) such as peroxide, superoxide anion, and hydroxyl radical can be formed *via* an electron transfer to $^3\text{O}_2$.⁷⁶

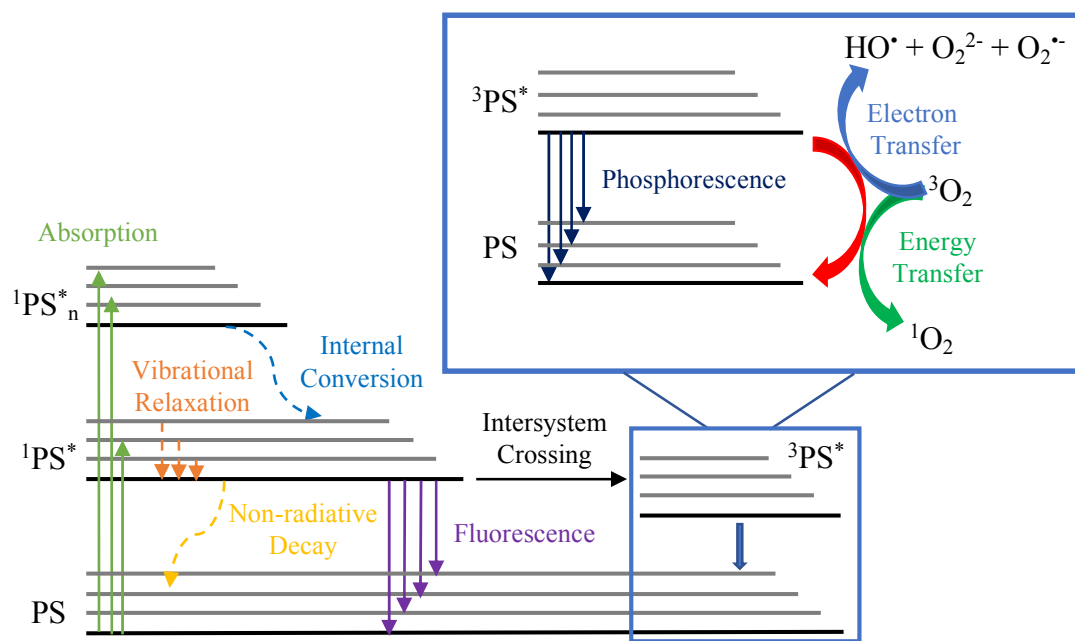


Figure 6. Representative photophysical pathways of photodynamic therapy. Modified from Kulbacka *et al.*⁷⁶

Inherently, PDT is less invasive than surgeries or radiation therapies,⁷⁷ is generally easily repeatable, has reduced tendency for development of drug resistance, and offers flexible delivery methods such as injection or topical application.⁷⁸ Notably, PS can only generate cytotoxic 1O_2 in the presence of an appropriate wavelength of light, which should be generally viewed as an advantage as it brings an inherent selectivity to the modality, *i.e.*, it can be viewed as an “on”-“off” drug treatment. This does, however, present a disadvantage since light will not penetrate beyond a few millimeters into human skin.^{78,79} As such, without use of a scope to administer light, PDT is limited to superficial tumors and drugs are generally designed to adhere to phototherapeutic window considerations, *i.e.*, PS absorbance between 600 and 1300 nm.⁷⁸ Moreover, due to the requirement for oxygen in an already oxygen deprived tumor tissue, PDT is a self-limiting modality in that it causes

its own inhibition.^{78,80} Another notable disadvantage to consider is that residual PS leads to light sensitivity following treatment,^{8,77,78} thus rapid clearance is critical for acceptable PDT drugs. Nevertheless, PDT remains attractive as a chemotherapeutic agent and an antimicrobial intervention.⁷⁷

There are many ways to modify fluorescent dyes to be PSs, *i.e.*, to promote $^1\text{PS}^*$ to $^3\text{PS}^*$ *via* ISC to generate high singlet oxygen quantum yield (Φ_{Δ}). Intrinsically, Φ_f must diminish to benefit Φ_{Δ} —albeit, it is favorable to retain some Φ_f for multimodal imaging purposes.^{76,77} However, Φ_{Δ} and Φ_f are not inversely proportional to one another owing to the fact that promotion from a singlet to a triplet excited state is a spin-forbidden process and as such occurs inefficiently for many PS.⁸¹ Moreover, the promotion to $^3\text{PS}^*$ does not guarantee energy transfer to ground-state oxygen.

Commonly, heavy-atoms are installed on or near chromophore systems such as *F*-BODIPYs to promote ISC. This functionalisation is performed at positions about the molecular core such that the planarity or conjugation of the dye is not disrupted, thus avoiding diminishment of crucial photophysical properties.⁸¹ There are many medically-approved PSs available to clinicians with varying degrees of heavy-atoms substitution, often halogens, that display a range of Φ_{Δ} .⁸¹ The heavy atom can either be placed directly on the chromophore (internal heavy-atom effect) or placed in the surrounding environment (external heavy-atom effect). The heavy-atom effect, and molecular motion, can consequently enhance non-radiative internal back-conversion and/or decay, thus reversing the effect of ISC. Fortunately, this can be mitigated by considering regiochemical placement of the heavy-atom as well as rigidifying the structure.⁸²

1.6. Mass Cytometry (MC)

Another method by which drugs or prodrugs can be located is cytometry. Cytometry is a general term for all techniques that detect and measure physical and chemical properties of a population of cells.⁸³ There are many imaging modalities used in cytometry—a popular example of this is flow cytometry, in which cells are labeled with a fluorescent dye and passed through a detector one at a time and thereby quickly gathering data on tens of thousands of cells.⁸⁴ Spectral overlap is an inherent problem in fluorescence cytometry as it limits the number of assays that can be run simultaneously due to the generally broad nature of dye emission. Spectral overlap, resulting from the use of multiple dyes, limits multilabel experiments, that might otherwise be used to concurrently monitor different physiological properties.⁸³ Experts in cytometry have said that fluorescence cytometry has obtained its limits and that recent developments in alternative methods such as mass cytometry (MC) have led to a post-fluorescence cytometry era.⁸³

MC, a relative newcomer in the cytometry field, is a clinically proven cellular imaging technique that employs small molecules with appended mass labels that can be tracked using mass spectrometry.^{75,83–86} For MC, cells are tagged, *via* covalent bond or chelation, elements that feature an easily accessible range of pure isotopes.⁸⁷ This sophisticated technique was designed to alleviate the challenges with the poor resolution of the more common flow cytometry techniques, and can display simultaneously over 40 cellular parameters at single-cell resolution. Thus, MC affords identification of cellular features at high resolution. Notable, MC has a slower rate of analysis than fluorescence cytometry (2 million compared to 25-60 million cells/h).⁸⁸ This slower rate is counteracted by

eliminating any single overlap, allowing for parameterisation of experiments by easily changing the isotope of the mass label; whilst maintaining a chemically identical yet isotopically distinct probe.

Ideal mass labels for MC require incorporation of heavy atoms (>100 amu), as to easily be tracked by mass spectrometry, with many available stable isotopes, enabling time/isotope-stamped control and information without affecting the pharmacokinetic profile.⁸⁸ Lanthanides are known for being the prototypical mass label for MC labels; however, the organotellurium motif was recently described by Nitz *et al.* as a suitable mass label for MC.^{85,86,89,90} Tellurium (Te) has a low toxicity profile, eight stable isotopes (five of which are commercially available in elemental form), no known roles in prokaryotic or eukaryotic cells^{89,91,92} and, like many other heavy-atom tags, has the inherent potential to promote ISC *via* the heavy-atom effect.⁹³ Moreover, and most importantly to the synthesis of small molecules containing this element, tellurium forms a stable bond with carbon and broadly follows the reactivity trends of other chalcogens.

Only a few *F*-BODIPYs featuring a Te-containing substituent are known, and most feature an alkyl- or aryl-telluroether motif.^{94–98} However, these compounds generally have poor stability, and a more robust tellurophene (abbreviated as [Te]) motif was proposed for the work described herein. Tellurophene, is a five-membered heterocycle containing a Te atom, and this motif was attached to BODIPY as described throughout this thesis. Being a member of the chalcogenophene family, tellurophene has useful chemical stability and synthetic feasibility, and maintains a limited toxicity profile that makes it a suitable scaffold for MC.⁸⁵

1.7. Late-Stage Functionalisation of *F*-BODIPYs

As the *F*-BODIPY core offers robust tolerance to functional group interconversion, late-stage incorporation of tellurophene appears feasible. Moreover, late-stage functionalisation, *i.e.*, modification of a preformed *F*-BODIPY, allows for relative ease of diversification *via* a convergent synthetic strategy. Although, there are many known approaches to functionalisation of *F*-BODIPYs, only those pertinent to the work described in this thesis will be introduced.

1.7.1. *Meso*-Position

Employing a *meso*-aryl substituent on *F*-BODIPYs lends well to further functionalisation through this group. Functionalisation of the *meso*-aryl substituents of *F*-BODIPYs has varying effect on the photochemical properties of the chromophore: often, no meaningful photochemical changes result from such substitution.⁹⁹ This comes by virtue of the highest occupied molecular orbital (HOMO) and lowest unoccupied molecular orbital (LUMO) of *meso*-aryl-substituted systems being located on the *F*-BODIPY core.^{81,100} Functionalisation of the *meso*-position is thus attractive for applications in which quantum yield of fluorescence (Φ_f) would ideally be maintained, *e.g.*,^{48,101} metal chelators^{102–105} and bioconjugation tags.^{50,51} The most accessible strategy to vary the substitution at the *meso*-positions is to do so *de novo*, *via* condensation of two equivalents of an α -free pyrrole with an aryl aldehyde, with subsequent oxidation and complexation to form *F*-BODIPYs.

1.7.2. Pre-functionalisation

Pre-functionalisation is an important step when designing synthetic pathways involving cross-coupling. Strategically placed substituents are used as leaving groups as well as

directing groups that often influence regio and stereochemistry.¹⁰⁶ To date, there are examples of late-stage functionalisation of *F*-BODIPYs via Migita-Kosugi-Stille,^{40–42,94,107,108} Suzuki-Miyaura,^{41,42,107–111} Mizoroki-Heck,^{41,42,42,112–114} Sonogashira,^{41,42,108,114–117} Buchwald-Hartwig¹¹⁸ and recently Negishi^{119,120} palladium-mediated cross-coupling reactions, all of which require suitable pre-functionalisation to generate requisite electrophilic and nucleophilic coupling partners (**Figure 7**).

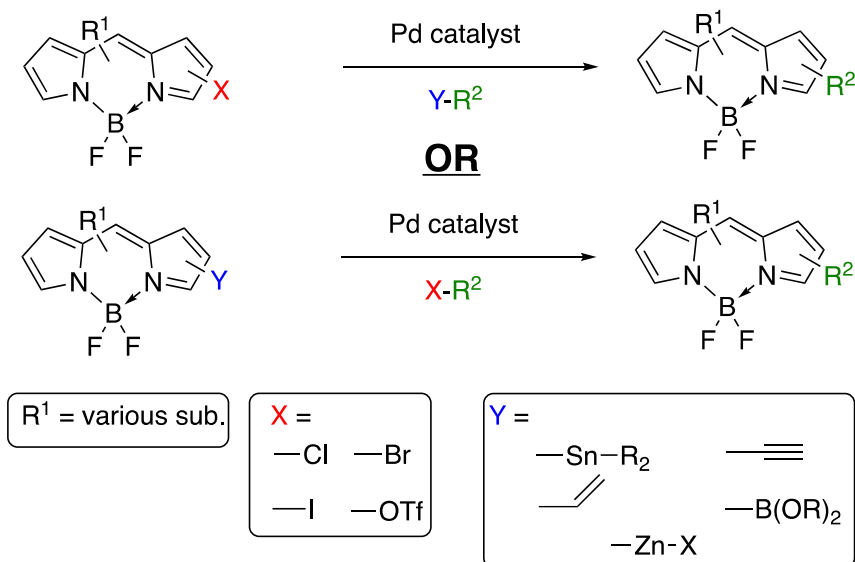


Figure 7. Palladium-catalysed functionalisation of *F*-BODIPYs with aryl coupling partners.

Towards the functionalisation of *F*-BODIPYs, electrophilic substitution reactions have shown utility for substitution at the pyrrolic positions. Interestingly, despite there being no definitive study on regioselectivity of unsubstituted *F*-BODIPY, perhaps due to the challenges of accessing the requisite unsubstituted dipyrin, the 2- and 6- positions are said to have the most negative charge character, and thus are the most susceptible to electrophilic attack.¹¹¹ It is common practice to block other positions with substituents and therefore avoid regiochemical complications. Pyrrolic sulfonation,¹²¹ either at the α - or β -

positions of *F*-BODIPY, was shown to have minimal effect of photophysical properties, whereas nitration¹²² and halogenation¹²³ result in a bathochromic shift of the maximum absorbance wavelength as well as a dramatic quench in fluorescence due to the heavy-atom effect. 3,5-Dihalogenation of *F*-BODIPYs is also possible since halogenation of dipyrromethanes is regiochemically preferred at the α -position to give the functionalised dipyrromethanes, which can later be oxidised and complexed with BF₂ to give the corresponding substituted *F*-BODIPY.¹²⁴

Boronic acid¹²⁵ and tin¹¹¹ derivatives of *F*-BODIPYs can easily be synthesised through lithiated intermediates of halogenated *F*-BODIPYs; and these pre-functionalised chromophores can be used as nucleophiles for Suzuki-Miyaura and Migita-Kosugi-Stille coupling, respectively. A few examples of *F*-BODIPYs featuring terminal alkene motifs are known, all of which were synthesised *via* Stille coupling of bromo- or iodo-substituted *F*-BODIPY with vinyl tin.¹²⁶ Of these halogenated *F*-BODIPYs, none were used as an electrophile for coupling chemistry as the simpler approach would involve use of a parent halogenated nucleophilic partner. Similarly, this coupling approach is amenable to the installation of terminal alkynes on *F*-BODIPYs, which are popular for bioconjugation. Terminal alkynes are often incorporated *de novo*, with condensation of pyrroles with acyl halides that feature appended alkyne functionality.¹²⁷

1.7.3. Palladium-Mediated Cross-Coupling of *F*-BODIPY

Five named palladium cross-coupling methods are known for late-stage functionalisation of *F*-BODIPY; however, only three have literature examples of successful coupling at every position (**Figure 8**). Little is known regarding the regioselectivity of *F*-BODIPY

cross-coupling, bar one study by Hao *et al.* that details the sub-stoichiometric arylation of 2,3,5,6-tetrabromo *F*-BODIPY and 1,2,3-tribromo *F*-BODIPY with various substituents in the *meso*-position.¹²⁸ Through these findings, the authors supported their hypothesis that for all electrophiles evaluated, the presence of steric bulk in the *meso*-position favors coupling of aryl nucleophiles to the α -positions; whereas the absence of steric bulk in the *meso*-position favors coupling of aryl nucleophiles to the β -positions.

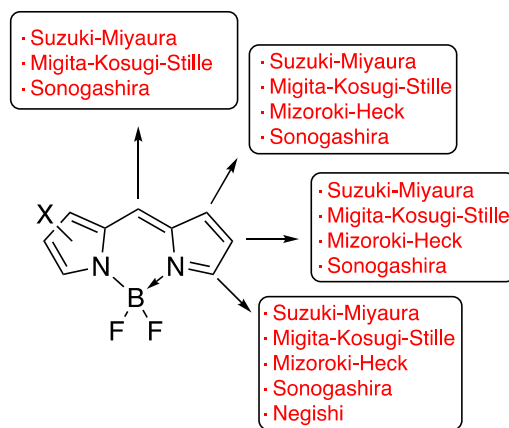


Figure 8. Regiochemical considerations of published palladium-mediated cross-coupling of halogenated *F*-BODIPYs.

1.7.4. Substitution at Boron

Substitution at boron is an attractive means by which to achieve late-stage functionalisation of BODIPYs. Functionalisation at the boron centre of *F*-BODIPYs has been exploited by employing nucleophiles such as Grignard reagents or lithiated organometallic reagents to install various functional groups, *e.g.*, aryl-, alkyl-, alkynyl-, alkoxy substituents.^{33,35,37,129–}

¹³¹ Substituents at the boron atom of BODIPYs have been used to help tune for desired photophysical properties of BODIPYs. Although BODIPYs bearing phenyl moieties at boron have been reported,¹³² there are few reports of compounds that feature heterocycles

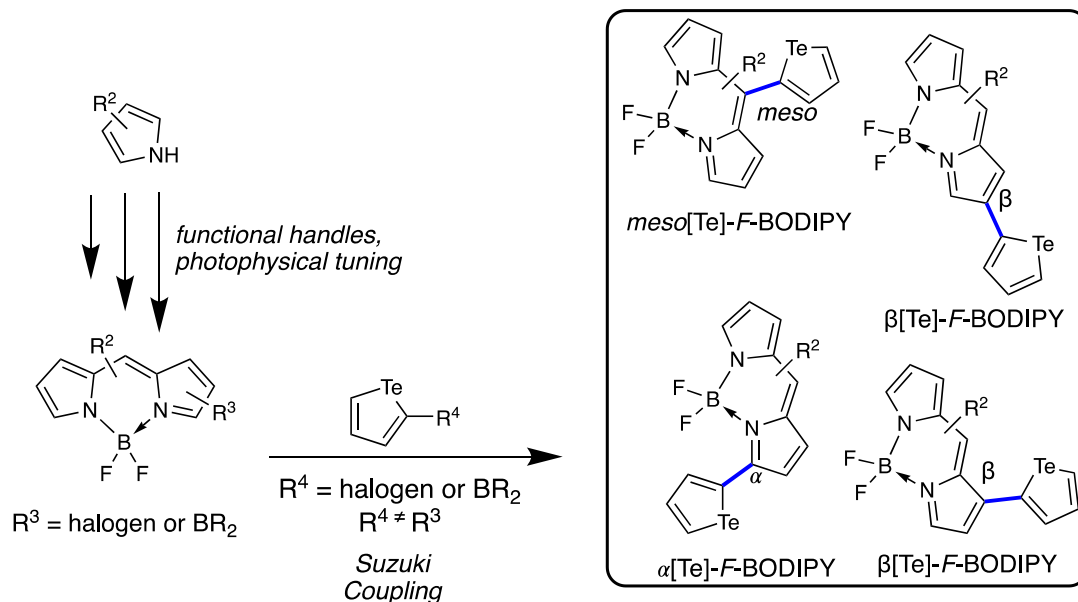
at boron.^{133–136} Chapter 3 and Chapter 4 will discuss nucleophilic substitution at the boron centre of *F*-BODIPYs with tellurophene: this work has displayed a powerful late-stage access to tellurophene-appended BODIPY photosensitisers.

1.8. Previous Work by Thompson-Group Members

Following a literature procedure,^{85,137} previous Thompson-group member Roberto Diaz-Rodriguez employed and optimised the synthesis of the parent tellurophene heterocycle.¹³⁸ Te^0 was reduced with sodium hydroxymethanesulfinate dihydrate (Rongalite) to form a water-soluble sodium telluride. Subsequent treatment with a commercially available trimethylsilyl-capped 1,3-butadiyne gave 2,5-bis(trimethylsilyl)tellurophene, which was deprotected *in situ* to give crude tellurophene.⁸⁵ This crude chalcogenophene was treated with bromine to give 1,1-dibromotellurophene as an insoluble orange solid, thus enabling purification by filtration. The reduction of 1,1-dibromotellurophene regenerated tellurophene that was isolated with increased purity.

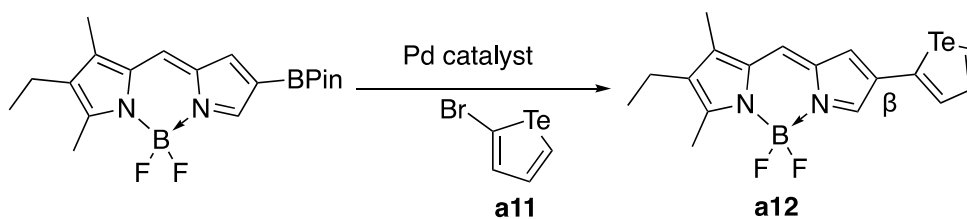
Early attempts towards tellurophene-appended *F*-BODIPYs followed a procedure¹³⁹ in which the chalcogenophene selenophene ([Se]) was installed at the *meso*-position by condensing dimethyl pyrrole with 2-formylselenophenyl to receive *meso*-selenophenyl dipyrromethane. When this work was attempted in the Thompson lab with tellurophene,¹³⁸ the dipyrromethane was afforded, but further oxidation to dipyrroin left a complex reaction mixture and the desired product was not recovered. It was clear that incorporation of tellurophene *via* a *de novo* synthesis might not be productive. As such, late-stage functionalisation of *F*-BODIPYs with prefunctionalised tellurophene was investigated *via* palladium-mediated cross-coupling chemistry.

Prior work regarding functionalisation of tellurophene involved the use of annulated tellurophenes, due to the belief that heavy chalcogenophenes had poor stability:¹³⁹ derivatisation consisted of halogenation,¹⁴⁰ acylation¹⁴¹ and alkylation¹⁴² chemistry of annulated tellurophenes. More recently, Rivard *et al.* described a useful metallacycle transfer process using prefunctionalised diynes to prepare pinacol borate (BPin) tellurophenes for use in Suzuki-Miyaura cross-coupling; however, these examples were still annulated.^{143,144} Stephens and Sweat developed 2-bromo and 2-stannous tellurophenes for use in Migita-Kosugi-Stille coupling and these stood as the only examples of cross-couplings on parent tellurophene,¹⁴⁵ prior to the work of Roberto Diaz-Rodriguez and myself, as reported herein. Previous work in the Thompson-group described Suzuki-Miyaura cross-coupling conditions for arylation of *F*-BODIPYs using pinacol boron *F*-BODIPYs as the nucleophilic partner and aryl bromides as the electrophilic partner:¹⁴⁶ a general approach for installing tellurophene on *F*-BODIPYs was developed (**Scheme 4**).



Scheme 4. Synthetic pathway for tellurophene-appended *F*-BODIPYs via Suzuki-Miyaura cross-coupling.

Roberto Diaz-Rodriguez, following a literature procedure,¹⁴⁰ subjected tellurophene to α -lithiation using *n*-butyllithium followed by subsequent bromination with 1,2-dibromotetrachloroethane to obtain 2-bromotellurophene (**a11**) in good yields. As a proof-of-principle, using the previously reported conditions,¹⁴⁶ **a11** was used in a coupling reaction with a β -BPin-*F*-BODIPY employing a Pd(0)/XPhos system to afford β -(2-tellurophenyl)-*F*-BODIPY (**a12**, **Figure 9**) in low yields after minor optimisation (**Scheme 5**). The photophysical properties of **a12** were explored: $\lambda_{\text{abs}}^{\text{max}} = 546 \text{ nm}$; emission spectrum was not obtained.



Scheme 5. Suzuki coupling employing **a11** and a borylated *F*-BODIPYs towards the synthesis of **a12**.

The success of preparing a tellurophene-appended *F*-BODIPY was further extended to a *meso*-(4-BPin)phenyl-*F*-BODIPY, as an example of positioning a remote tellurophene to study the effect of external heavy-atom effects. Using the same coupling conditions, **a11** was coupled to a *meso*-4-(BPIn)phenyl-*F*-BODIPY to afford *meso*-4-(2-tellurophenyl)phenyl-*F*-BODIPY (**a13**, **Figure 9**) in low yields. The photophysical properties of **a13** were explored: $\lambda_{\text{abs}}^{\text{max}} = 503 \text{ nm}$; $\lambda_{\text{em}}^{\text{max}} = 521 \text{ nm}$; $\Phi_{\text{f}} = 0.01$. Similarly, *meso*-mesityl-2,6-bis(2-tellurophenyl)-*F*-BODIPY (**a14**, **Figure 9**) was synthesised from the parent bis BPIn *F*-BODIPY in low yields. The photophysical properties of **a14** were explored: $\lambda_{\text{abs}}^{\text{max}} = 642 \text{ nm}$; $\lambda_{\text{em}}^{\text{max}} = 685 \text{ nm}$; $\Phi_{\text{f}} = 0.01$.

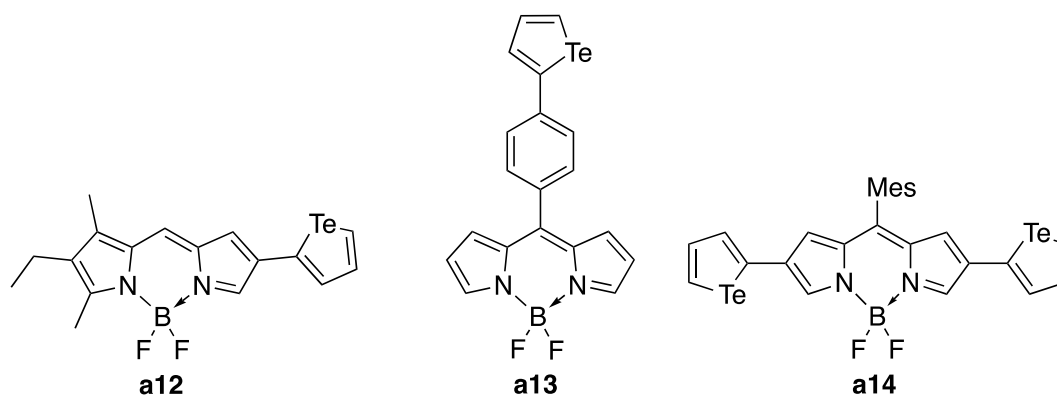


Figure 9. Tellurophene-appended *F*-BODIPYs previously synthesised by Roberto Diaz-Rodriguez *via* Suzuki-Miyaura cross-coupling of 2-bromotellurophene and borylated *F*-BODIPYs.¹⁴⁶

Roberto Diaz-Rodriguez, attempted to append 2-bromotellurophene at the α -position of α -borylated *F*-BODIPYs. However, several unsuccessful attempts to α -borylate *F*-BODIPYs met with expectation following reports that α -borylated BODIPYs are notoriously unstable, and that limited success regarding purification is encountered.¹⁴⁶ As such, the decision was made to transpose the electrophilic and nucleophilic functionalisation of these coupling partners, *i.e.*, prepare borylated tellurophene and halogenated *F*-BODIPY as coupling partners. Following an analogous procedure for the borylation of selenophene,¹⁴⁷ Roberto Diaz-Rodriguez subjected tellurophene to α -lithiation using *n*-butyllithium in a -78 °C bath, followed by borylation employing 2-isopropoxy-4,4,5,5-tetramethyl-1,3,2-dioxaborolane (ITDB), affording tellurophene-2-BPin (**a15**, **Figure 10**) in inconsistent purity and moderate yields. α -Substitution of an α -brominated *F*-BODIPY was attempted using two equivalents of **a15** and *meso*-mesityl-3,5-dibromo-*F*-BODIPY. However, only the mono α -tellurophene functionalised *F*-BODIPY (**a16**) was isolated at low yields (**Figure 10**). The photophysical properties of **a16** were explored: $\lambda_{\text{abs}}^{\text{max}} = 583 \text{ nm}$; $\lambda_{\text{em}}^{\text{max}} = 599 \text{ nm}$; $\Phi_{\text{f}} = 0.14$.

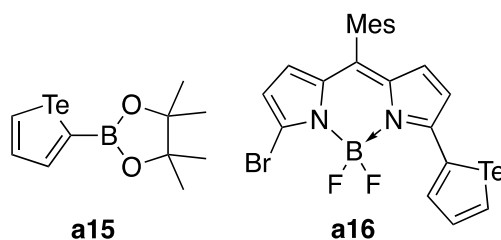
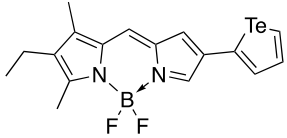
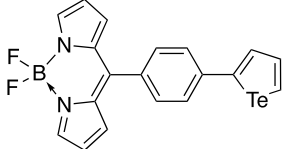
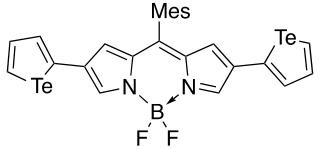
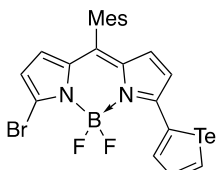


Figure 10. Borylated tellurophene analogue, **a15**, tellurophene-2-pincolborate. α -tellurophene-appended *F*-BODIPY, **a16**, previously synthesised by Roberto Diaz-Rodriguez *via* Suzuki-Miyaura cross-coupling of tellurophene-2-BPin and the corresponding dibrominated *F*-BODIPY.¹⁴⁶

Samples of all four tellurophene-appended *F*-BODIPYS (**a12**, **a13**, **a14**, **a16**) were then sent to the University of Toronto, to be evaluated for *in vitro* cytotoxicity in collaboration with Dr. Andrew Beharry. Note: only a summary of the results will be included as the experimental details are beyond the scope of this dissertation. First evaluating the ability of the four tellurophene-appended BODIPYs to effect photo-activated $^1\text{O}_2$ production, our collaborators employed an established method to detect $^1\text{O}_2$ using 1,3-diphenylisobenzofuran; this selective $^1\text{O}_2$ trap forms an endoperoxide that results in a decrease in absorbance at 410 nm.¹⁴⁸ Results of this study are summarised in **Table 1**. Photobleaching studies revealed minimal losses, suggesting these compounds exhibit high photostability in organic solvents. Once it was confirmed that these compounds produced $^1\text{O}_2$, and were photostable, they were evaluated for photocytotoxicity in cancer cells. Cells were incubated with varying concentrations of the four tellurophene-appended *F*-BODIPYs. Cell culture studies showed all compounds induced dose-dependent photocytotoxicity with nanomolar IC_{50} values. However, compounds **a12**, **a14** and **a16** exerted a high degree of dark toxicity with only minor increases of cytotoxicity under light. Furthermore, **a13**, exerted some dark toxicity but high phototoxicity, making it the best candidate for a photosensitiser. Mass cytometry experiments were later performed on **a13**, illustrating its ability to be tracked/monitored *via* using MC.⁷⁵

Table 1. Summary of preliminary study of tellurophene-appended *F*-BODIPYS as photosensitisers.

Compound	$\lambda_{\text{abs}}^{\text{max}}$ (nm)	$\lambda_{\text{em}}^{\text{max}}$ (nm)	Φ_{f}	Φ_{Δ}
a12 	546	n.d.	n.d.	0.42
a13 	503	521	0.01	0.26
a14 	642	685	0.01	0.19
a16 	583	599	0.14	0.53

n.d., not determined

1.9. Thesis Overview

Given the limitations of the synthetic route shown in **Scheme 5**, namely the low yields for coupling, my graduate research began with the need to optimise coupling conditions to afford **a13**. Chapter 2 discusses a convergent approach towards installation of tellurophene by performing late-stage functionalisation on the *F*-BODIPY core *via* palladium-catalysed cross-coupling. Much of this work is published and was reproduced herein. Chapter 2 also

details the limitations of the target tellurophene-appended BODIPY framework and includes attempts towards further optimisation.

Given the limitations of the tellurophene-appended BODIPYs discussed in Chapter 2, a new approach was desired. Chapter 3 discusses the installation of tellurophene motifs at the boron atom of BODIPYs *via* nucleophilic substitution. Upon the successful synthesis of the first BODIPY which featured two tellurophene motifs at boron (*[Te]*-BODIPY), it was realised that of chalcogenophenes, only the thienyl example was known. Thus, a systematic series of chalcogenophenes at the boron centre of BODIPYs was synthesised and (photo)chemical and (photo)physical trends were examined. The *[Te]*-BODIPY framework described in Chapter 3 exhibited several improvements relative to the compounds discussed in Chapter 2. This is published work and was reproduced herein.

The basis for the work in Chapter 4 was built on the utility of the *[Te]*-BODIPY framework and synthesis a series of compounds to evaluate the effects of substituent choice about the pyrrolic units on photosensitisation. This work ultimately led to a *[Te]*-BODIPY with improved properties and this published work was reproduced herein.

Chapter 5 discusses further functionalisation of the *[Te]*-BODIPYs, with the goal to append these compounds to biological ligands to improve selectivity of the photosensitisation event. The goal of this work is to develop a photosensitiser that, through conjugation with a ligand, targets cancer cells whilst sparing healthy cells.

Overall conclusions are given in Chapter 6 and supporting information for each chapter can be found in a corresponding appendix section.

Chapter 2. Palladium-Catalysed Cross-Coupling Towards Late-Stage Functionalisation of *F*-BODIPYs

2.1. Preface

Building on the work described in section 1.8 of this thesis, optimisation of the synthetic procedures and aspects of the photochemical evaluation of tellurophene-appended BODIPYs were needed. When I started on this project, I began by utilising a borylated tellurophene to couple with halogenated *F*-BODIPYs. This chapter contains a reproduced manuscript⁷⁵ (Section 2.2) that describes the first published route to a tellurophene-appended BODIPY.

The discussion starts by discussing the desire for a PDT agent with mass cytometry tracking capabilities. Then, the synthesis the tellurophene-appended BODIPY is provided. The work also includes a discussion regarding photochemical properties that are pertinent to PDT, *i.e.*, the photosensitisation and phototoxicity index. An evaluation of cytometry studies finalises the published work provided in this chapter.

After the reproduced manuscript, this chapter then discusses attempts towards optimisation of the synthesis of the published tellurophene-appended BODIPY system (Section 2.3). It was envisioned that a strategic increase in steric bulk surrounding the *meso*-aryl substituent would limit free rotation of the compound and thus decrease non-radiative decay of ¹PS*. The chapter ends with a conclusion and discussion of future perspectives (Section 2.4).

This chapter contains a publication that is wholly reproduced and edited for formatting and clarity of presentation (see Appendix G). Jacob W. Campbell designed and performed all

syntheses. Matthew T. Tung designed and performed all singlet oxygen and *in vitro* experiments. Roberto M. Diaz-Rodriguez helped conceptualise this work. X-ray crystallography was performed by Katherine N. Robertson. Andrew A. Beharry supervised Matthew T. Tung. Alison Thompson supervised Jacob W. Campbell and Roberto M. Diaz-Rodriguez. The publication was written by Jacob W. Campbell and Matthew M. Tung, then edited by all authors.

2.2. Introducing the Tellurophene-Appended BODIPY: PDT Agent With Mass Cytometry Tracking Capabilities

Reprinted and adapted with permission from:

Campbell, J. W.;^{†||} Tung, M. T.;^{‡||} Diaz-Rodriguez, R. M.;[†] Robertson, K. N.;[§] Beharry, A. A.;^{*} Thompson, A.^{†*} Introducing the Tellurophene-Appended BODIPY: PDT Agent With Mass Cytometry Tracking Capabilities. *ACS Med. Chem. Lett.* **2021**, 12, 12, 1925–1931. Copyright 2021 American Chemical Society. Appendix F.

[†] Department of Chemistry, Dalhousie University, Halifax, Nova Scotia B3H 4J3, Canada.

[‡] Department of Chemistry and Physical Sciences, University of Toronto, Mississauga, Ontario L5L 1C6, Canada.

[§] Department of Chemistry, Saint Mary's University, Halifax, Nova Scotia B3H 3C3, Canada.

^{||} Contributed equally

2.2.1. Abstract

The synthesis and characterisation of the first BODIPY appended to the five-membered heterocyclic tellurophene [Te] moiety is reported. By incorporating tellurophene at the *meso*-position, the tellurophene-appended BODIPY acts as a multi-modal agent, becoming a potent photosensitiser with a mass cytometry tag. To synthesise the compound, a method to enable late-stage Suzuki-Miyaura coupling was developed by preparing and isolating

tellurophene-2-BPin in a one-step procedure from the parent tellurophene: coupling with a *meso*-substituted BODIPY functionalised with a pendant aryl bromide provides the desired tellurophene-appended BODIPY. This compound demonstrated a singlet oxygen quantum yield of 0.26 ± 0.01 and produced a light dose-dependent cytotoxicity with nanomolar IC_{50} values against 2D-cultured HeLa cells and high efficacy against 3D-cultured HeLa tumour spheroids, proving to be a strong photosensitiser. The presence of the tellurophene moiety could be detected using mass cytometry, thus showcasing the ability of a tellurophene-appended BODIPY as a novel photodynamic therapy-mass cytometry theragnostic agent.

2.2.2. Introduction

Hybrid (or multi-modal) cellular imaging and/or therapeutic techniques employ complementary modalities in order to maximise resolution.^{52,54,69} Among the many approaches to multi-modal functions (*e.g.*, PET/CT,⁵³ PET/MRI,^{54,55} lipid-based approaches,^{56–58} quantum dots,^{59–63} iron oxide nanoparticles,^{64–66} and macromolecular carriers),^{67,68} small molecule probes^{69–72} stand out with advantages such as expedited clearance by the renal system, thus minimising toxicity associated with long-term liver retention, as well as facile tuning of properties through functionalisation.⁵² Recent breakthroughs in multi-modal small molecules involve systems that enable both diagnosis and treatment (*i.e.*, theranostics), or enable *in situ* localisation and treatment. This approach was first realised by tuning the fluorescent properties of dyes used in photodynamic therapy (PDT) such that cancerous cells can be located and given an accurately assessed payload of the drug.⁶⁹ Herein, the first mass cytometry/photosensitisation multi-modal agent incorporating tellurophene into a BODIPY scaffold designed for PDT is reported.

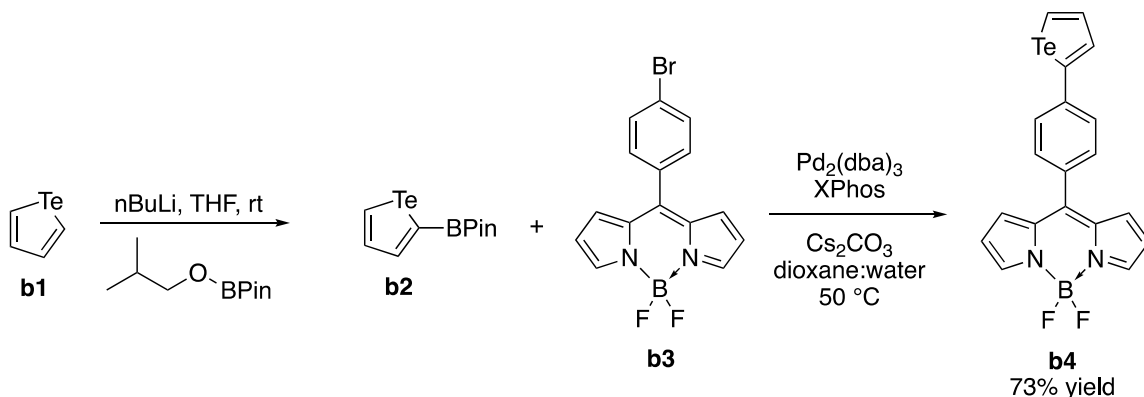
Mass cytometry (MC) is a clinically proven imaging technique that employs a small molecule appended with an isotopic mass label that can be tracked using mass spectrometry. Although a relative newcomer, MC is a valuable tool in the multi-modal imaging field owing to the diversity of compounds in which a mass label can be installed.^{83,88,149} Modern MC experiments can display simultaneous measurements of over 40 cellular parameters at single-cell resolution and, when used in union with flow cytometry, can help fill gaps in resolution encountered with less sophisticated imaging techniques.⁸⁸

PDT is a clinically approved treatment used as an alternative to highly invasive surgeries or radiation therapies:⁷⁷ in essence, a non-toxic sensitizer is activated by light of a therapeutically appropriate wavelength applied in a highly controlled manner. The photosensitized prodrug then interacts with oxygen to form cytotoxic singlet oxygen ($^1\text{O}_2$) and other reactive oxygen species (ROS) that effect death of cells in the immediate vicinity.¹⁵⁰ Notable advantages of PDT include repeatable application, cost effectiveness, and reduced drug resistance, alongside flexible delivery modes such as topical application or injection.⁷⁸ As such, combining multi-modal imaging techniques with PDT has the benefit of enhancing localisation of treatment through high resolution imaging, and provides a method to monitor the time taken for the drug to accumulate in target tissues.⁶⁹ Boron-dipyrromethene dyes (BODIPYs, 4-disubstituted-4-bora-3a,4a-diaza-s-indacenes) have been exhaustively investigated with regard to fluorescence quantum yield (Φ_f). More recently, BODIPYs have been tuned to facilitate intersystem crossing (ISC) from a singlet to a triplet excited state to enhance $^1\text{O}_2$ production.^{124,151,152} The BODIPY core can be tuned

via pyrrolic substitutions (at the α and/or β -positions) and/or *meso* substitution,¹²⁴ making this molecular framework particularly well-suited for adaption as a combined MC/PDT agent. The HOMO and LUMO of *meso*-aryl substituted BODIPYs are localised primarily on the dipyrrolic core, and thus substituents appended to the *meso*-arene are projected to have little effect on photo-induced $^1\text{O}_2$ production: therefore substitution at the *meso*-position offers promise for the incorporation of mass labels in a BODIPY equipped for monitoring, *via* MC, as well as PDT.¹⁵³ Furthermore, with BODIPYs often exhibiting very high fluorescence quantum yields, any residual emission could be used for complementary fluorescence imaging. With bromo-activated *meso*-substituted BODIPYs serving as common coupling partners,^{95–97,154–157} and with these skeletons typically exhibiting poor fluorescence (*e.g.*, $\Phi_f < 0.05$)^{158,159} and therefore potentially favouring high $^1\text{O}_2$ production, *meso*-aryl BODIPYs were selected for investigation as bifunctional PDT/MC agents.

The prototypical mass label for MC is a heavy element with many available isotopes such as to enable time/isotope-stamped administration and monitoring without altering physiological uptake and metabolism.⁸⁸ Although lanthanides are often used as MC labels, organotellurium motifs^{85,89} were identified as competent mass labels due to tellurium having a low toxicity profile, eight stable isotopes, no known biological role in prokaryotic or eukaryotic cells,^{89,91,92} and the potential to improve ISC through the heavy-atom effect.⁹³ There are a handful of reports of BODIPYs appended with alkyl or aryl telluroether functionalities,^{94–98,160} but many lack stability. Consequently, the 5-membered heterocyclic tellurophene motif, hereafter abbreviated as [Te], was selected for attachment to the

BODIPY framework. Early [Te] derivatisation consisted of halogenation,¹⁴⁰ acylation¹⁴¹ and alkylation¹⁴² chemistry of annulated [Te]s due to the poor reputation regarding the instability of heavy chalcogenophenes.¹³⁹ early-stage incorporation of the requisite functionality was essential, yet limiting, for the generation of analogs. More recently, elegant metallacycle transfer approaches using pre-functionalised diynes have been used to prepare borylated tellurophenes for Suzuki-Miyaura coupling.^{143,144} However, although stannylation of the [Te] heterocycle and consequent Stille coupling is known,^{145,161} there are no reports of the borylation of the parent heterocycle. In order to efficiently prepare [Te]-appended BODIPYs, a method for the synthesis of [Te]-2-BPin from the parent unsubstituted [Te] was developed for coupling with a bromo-activated BODIPY *via* Suzuki-Miyaura methods (**Scheme 6**). Natural abundance tellurium was used to enable methodology development, with the intention of using commercially available single-isotope elemental tellurium for applications work.



Scheme 6. Synthesis of 8-(4-(tellurophenyl)phenyl)-BODIPY **b4**.

2.2.3. Results and Discussion

To prepare the parent [Te] heterocycle,^{85,137} elemental tellurium was first reduced with sodium hydroxymethanesulfinate dihydrate (Rongalite) to form water-soluble sodium telluride. Subsequent treatment with trimethylsilyl-capped 1,3-butadiyne gave 2,5-bis(trimethylsilyl)[Te], which was deprotected *in situ* to give crude [Te] **b1**.¹³⁷ According to literature procedure, treatment of the crude chalcogenophene with bromine gave 1,1-dibromo[Te] as an insoluble orange solid to enable purification by filtration. Reduction of 1,1-dibromo[Te] gave the parent [Te] **b1**. Given the anticipated crystallinity and versatility of coupling,¹⁶² [Te]-2-BPin **b2** was selected as the target nucleophile for coupling with bromo-activated *meso*-aryl BODIPY **b3** as shown in **Scheme 6**. Through modification of procedures described for other heterocycles,¹⁴⁷ room temperature lithiation of [Te] with *n*-butyllithium, followed by borylation employing 2-isopropoxy-4,4,5,5-tetramethyl-1,3,2-dioxaborolane, afforded [Te]-2-BPin **b2** as a crystalline yellow solid in 72% yield after distillation. Slow evaporation of a diethyl ether solution of **b2** gave long acicular crystals. Analysis of the corresponding crystallographic data confirmed the structure of **b2** (**Figure 11**).

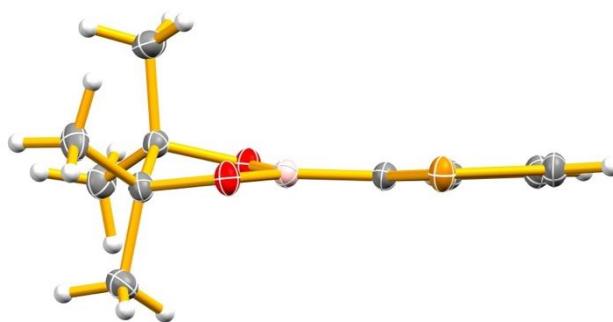


Figure 11. Side-on view of **b2** highlighting planarity of [Te].

The Suzuki-Miyaura coupling of **b2** and the bromo-activated BODIPY **b3** was catalysed employing a Pd(0)/XPhos system.¹⁴⁶ The crude product mixture was filtered to remove the catalyst, and the filtrate then subjected to chromatography on neutral alumina. Further purification by washing with pentane afforded 8-(4-(tellurophenyl)phenyl)-BODIPY **b4** as a crimson red air-stable solid in 73% yield (**Scheme 6**). Slow diffusion of hexanes layered over a dichloromethane solution of **b4** gave small single crystals. Analysis of the corresponding crystallographic data confirmed the structure of **b4** (**Figure 12**).

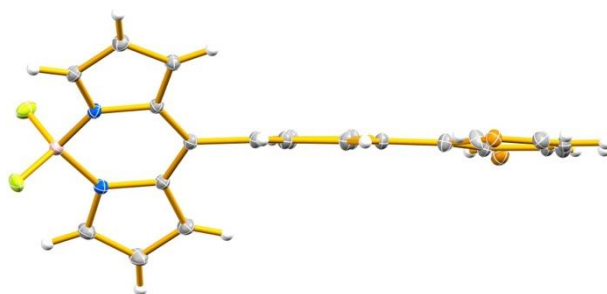


Figure 12. Side-on view of compound **b4**. Disorder removed for clarity.

The photophysical properties of **b4** were determined in CH₂Cl₂ at room temperature by first exciting at 500 nm whilst monitoring emission from 510 nm to 700 nm to determine the peak emission maximum ($\lambda_{em}^{max} = 526$ nm). The spectrofluorometer was then set to the excitation peak maximum and monitored from 350 nm to 521 nm to determine the peak absorbance maximum ($\lambda_{abs}^{max} = 503$ nm, **Figure 40**). Fluorescence quantum yield of **b4** was determined to be weak ($\Phi_f = 0.01$) using rhodamine B ($\Phi_f = 0.70$ in ethanol) as a standard. This weak fluorescence is anticipated to originate from non-radiative decay of the singlet excited state as a result of free-rotation of the meso-aryl substituent in addition to the presence of tellurium, the latter known to promote ISC from the excited singlet state

to the excited triplet state *via* the heavy-atom effect.⁹³ Since populating the triplet state may result in the generation of ROS, this was evaluated *via* irradiation of **b4** in the presence of 1,3-diphenylisobenzofuran (DPBF), an ¹O₂ sensor. If ¹O₂ is produced, DPBF forms an endoperoxide, causing a decrease in its absorbance at 410 nm.¹⁴⁸ Experiments were performed in MeOH containing 2% DMSO. Under these conditions, DPBF is monomeric and reactive¹⁴⁸ and **b4** exhibited only slight shifts in λ_{max} compared to aqueous solutions (**Figure 61**). Concentrations of compound **b4** were determined by calculating extinction coefficients ($\epsilon = 54822 \text{ M}^{-1}\text{cm}^{-1}$) in DMSO (**Figure 62**). Compound **b4** demonstrated a decrease in absorbance after irradiation *c.f.* background irradiation of DPBF alone, with a singlet oxygen quantum yield (Φ_{Δ}) of 0.26 ± 0.01 (**Figure 63**).

Although DPBF is selective for ¹O₂ and is commonly used to determine Φ_{Δ} ,^{163,164} it has been shown to react with other ROS, such as hydroxyl radicals and peroxides.^{148,165} To ensure that the degradation of DPBF was at least partly caused by ¹O₂, excess NaN₃, a ¹O₂ quencher,¹⁴⁸ was used in the DPBF assay whereby solutions containing NaN₃ degraded DPBF at a significantly slower rate, confirming that **b4** was indeed generating ¹O₂ (**Figure 64**). Furthermore, minimal photobleaching under these irradiation conditions was observed (**Figure 65**), demonstrating the high photostability of **b4** in MeOH.

Precursor **b3** generated minimal amounts of ¹O₂, indicating that the tellurophene moiety is critical to the photosensitisation exhibited by **b4** (**Figure 66**).

Given the ability of **b4** to generate ¹O₂ upon treatment with light, the capability to exert photocytotoxicity in cancer cells was explored. HeLa cells were incubated with varying

concentrations of **b4** in reduced serum media (Opti-MEM) for three hours, then either kept in the dark or irradiated for 5 min before culturing overnight. After this time, cell viability was determined using a standard MTT assay. Compound **b4** exerted some dark toxicity > 100 nM but high phototoxicity < 100 nM, yielding a phototoxic index of ~ 80 (dark IC₅₀ = 1.35 μM/light IC₅₀ = 0.017 μM (7.08 J/cm²)). Irradiation of **b4** for shorter times (1 min or 3 min) produced the expected light dose-dependency on photocytotoxicity (**Figure 13**). No background phototoxicity was observed upon irradiation of untreated cells (**Figure 67**).

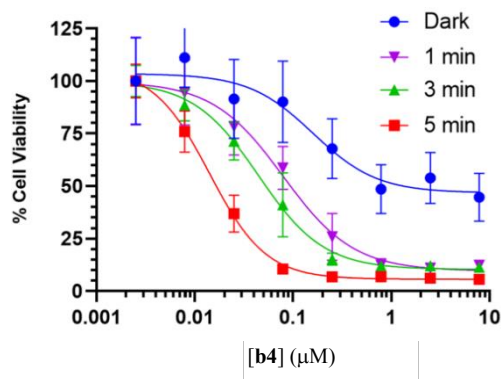


Figure 13. Cell Viability with **b4**. HeLa cells were incubated with 0–7.9 μM **b4** for 3 h and left either in the dark or irradiated for the given duration with a 525 nm green lamp (23.60 mW/cm²) IC₅₀ for dark condition = 1.35 μM, 1 min irradiation = 0.094 μM (1.42 J/cm²), 3 min irradiation = 0.053 μM (4.25 J/cm²), 5 min irradiation = 0.017 μM (7.08 J/cm²). Experiments were conducted in triplicate.

The ability of **b4** to exert phototoxicity by producing ROS was confirmed by intracellular imaging using the general ROS sensor, 2',7'-dichlorodihydrofluorescein diacetate (DCFDA). DCFDA is cell-permeable and, upon deacetylation by intracellular esterases and reaction with ROS, a green fluorescent product is produced.¹⁶⁶ HeLa cells treated with **b4** (25 nM) and DCFDA (10 μM) produced strong green fluorescence after irradiation over dark conditions (**Figure 14**). Control experiments with DCFDA (10 μM) alone, or **b4** (25 nM) alone, with/without irradiation (**Figure 68**) produced no fluorescence, further

demonstrating that irradiation of cells treated with **b4** is needed in order to produce ROS (**Figure 14**).

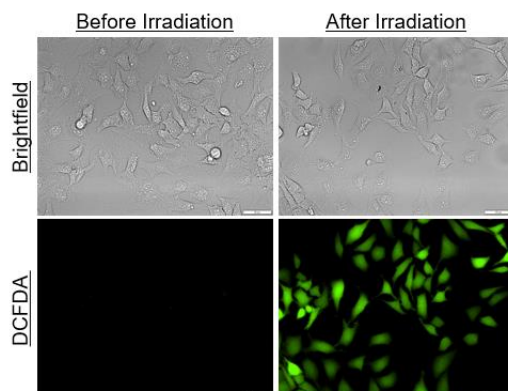


Figure 14. ROS Generation in HeLa Cells using DCFDA. HeLa cells were incubated with **b4** (25 μM) and DCFDA (10 μM) and fluorescence was monitored before and after 5-min irradiations with a 525 nm green lamp (23.60 mW/cm^2). Green fluorescence indicates the production of ROS in cells. 20x magnification, scale bar = 50 μm .

The mechanism of cell death was explored using Annexin V-FITC and propidium iodide (PI) staining. Annexin V binds phosphatidylserine, which is naturally found on the cytosolic side of the plasma membrane of healthy cells.⁸⁴ However, during apoptosis, phosphatidylserine translocates to the extracellular side of the plasma membrane, allowing Annexin V to bind and exhibit green fluorescence localised at the cell membrane.⁸⁴ PI is a non-cell permeable dye that fluoresces red when bound to DNA and is used as an indicator for cells dying by necrosis or in the late stages of apoptosis.^{84,167} Cells were treated with **b4** (1.25 μM) and irradiated for 5 min, then incubated for four hours and stained using the Annexin V/PI staining kit. Green fluorescence was observed indicating Annexin V binding, but minimal red fluorescence was observed (**Figure 15**), thus indicating the mechanism of death caused by light-activated **b4** to be through apoptosis.

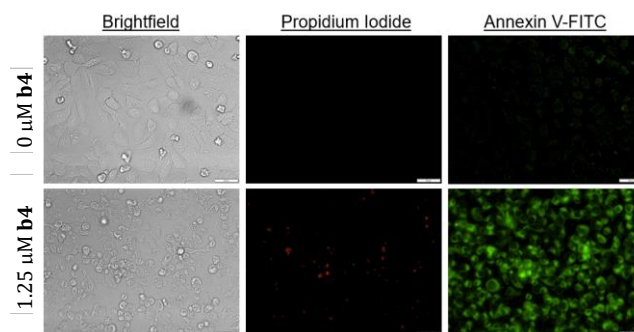


Figure 15. Mechanism of Cell Death. HeLa cells with no **b4** (top) or after incubation with **b4** (1.25 μM) and irradiated with 525 nm green lamp (bottom, 23.60 mW/cm^2) were stained with Annexin V-FITC and PI four h post-treatment. Green fluorescence was only observed after treatment, showcasing cell death occurring through apoptotic pathways. 10x magnification, scale bar = 100 μm .

3D cell cultures have been shown to represent the microenvironment within tumours by mimicking tumour morphology and physiology more accurately compared to 2D cell cultures.¹⁶⁸ To investigate the potential of compound **b4** as a therapeutic agent for solid tumours, HeLa spheroids were grown in Opti-MEM and incubated in the absence and presence (100 nM) of **b4** for 3 h: this concentration was chosen to match that resulting in the maximum phototoxic index observed in 2D cell cultures. Spheroids were then left in the dark or irradiated with a 525 nm green lamp (23.60 mW/cm^2) for 5 min and cultured overnight in the dark. ReadyProbesTM Cell Viability Imaging Kit, Blue/Green was used to determine cytotoxicity, whereby all cells have nuclei stained with blue fluorescence while only dead cells exhibit green fluorescence. Spheroids treated with **b4** and irradiated exhibited cell death (*i.e.*, bright green fluorescence) compared to controls containing **b4** without irradiation or untreated spheroids with/without irradiation (**Figure 16**).

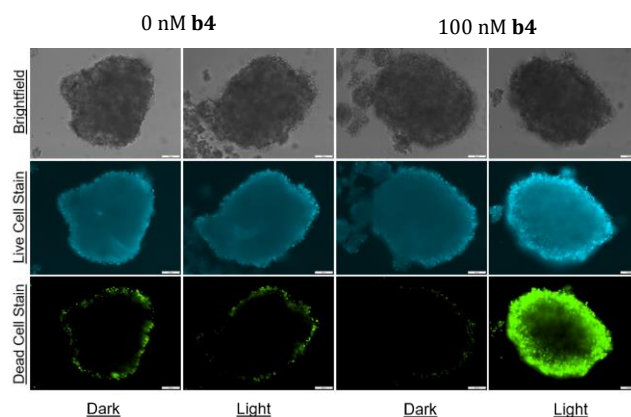


Figure 16. Cell Viability of HeLa Cell Spheroids. HeLa spheroids treated with/without 100 nM **b4** under 5 min-irradiations (525 nm, 23.60 mW/cm²) or dark conditions. (top row) brightfield images of HeLa spheroids; (middle row) nuclear staining of all cells; (bottom row) cell death monitored by green fluorescence. Only spheroids treated with 100 nM of **b4** and irradiated exhibited significant cell death (10x magnification, scale bars = 100 μ m).

Monitoring tellurium by mass cytometry would confirm the presence of **b4** within cells, provide time-points for accumulation, and demonstrate the potential to couple PDT with MC for cancer theragnostic applications. To prepare cells for MC, HeLa cells were treated with **b4** (25 nM – 4000 nM) for 3 h in the dark. Then, following a modified Maxpar Cell Surface Staining protocol, cells were prepared and analysed using a HeliosTM CyTOF system with 75×10^3 events collected per concentration. Just before the collection of data, cells were treated with industry-standard EQ calibration beads and data were normalised to account for signal drifts. Signals arising from ¹³⁰Te, the most abundant isotope of Te, were analysed. A positive linear relationship was observed between ¹³⁰Te signal intensity and increasing concentrations of **b4**, thereby confirming the presence of the tellurophene-appended BODIPY within the HeLa cells and demonstrating its potential as a theragnostic probe (**Figure 17**, **Figure 69**).

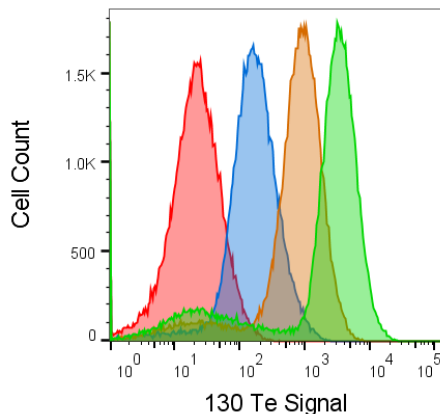


Figure 17. Mass cytometry of **b4** within HeLa cells. Overlaid histogram of ^{130}Te signals with increasing concentrations of **b4** (25 nM (red), 250 nM (blue), 1000 nM (orange) and 4000 nM (green)). Cells were incubated with different concentrations of **b4** for 3 h before preparing cells for MC.

2.2.4. Conclusions

To conclude, an efficient synthesis of a tellurophene-appended BODIPY is reported. The method uses borylated tellurophene and lends itself to coupling this motif with other biologically relevant species. The tellurophene-appended BODIPY is a capable photosensitiser and generates $^1\text{O}_2$. This compound demonstrated nanomolar IC_{50} under irradiation in HeLa cells, killing cells *via* apoptosis, with a large phototoxic index (~ 80). High efficacy against 3D-cultured HeLa spheroids was also demonstrated, illustrating capability as a potent photosensitiser. Mass cytometry studies confirmed the presence of Te within HeLa cells, further supporting the potential of tellurophene-appended BODIPYs as theragnostic agents. Future work will involve development of tellurophene-appended BODIPYs with optimised photophysical properties and introducing selectivity towards cancer cells to further demonstrate suitability as a multi-modal imaging and treatment agent.

2.2.5. Experimental

All experimental works for Section 2.2 were reproduced with permission and included in Appendix A.

2.3. Optimisation Studies

The *meso*-aryl tellurophene-appended BODIPY-based compound (**b4**) demonstrated the utility of a photosensitiser that was equipped with a mass cytometry handle. However, this system suffered from a moderate singlet oxygen quantum yield (Φ_{Δ} , 0.26 ± 0.01). In this section, the optimisation of **b4** will be discussed.

As mentioned in Section 1.5, molecular motion can provoke non-radiative decay, thus squandering both Φ_F and Φ_{Δ} . It was envisioned that this effect could be minimised by introducing steric bulk as large ortho groups on to the *meso*-aryl substituent, *i.e.*, limiting rotation and rigidifying the structure (**Figure 18**).

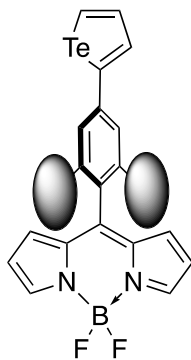


Figure 18. Tellurophene-appended *F*-BODIPY featuring bulky ortho groups on the *meso*-aryl substituent.

To test this hypothesis, bulky ortho groups were introduced *de novo* by varying the 4-bromobenzaldehyde in the synthesis of the requisite dipyrromethane. When planning a synthetic scope of the desired compounds for this project, it became abundantly clear that

sourcing suitable benzaldehyde starting materials from chemical supply companies would be challenging. 4-Bromo-2,6-difluorobenzaldehyde, 4-bromo-2-methylbenzaldehyde, 4-bromo-2-nitrobenzaldehyde, 4-bromo-2-chlorobenzaldehyde and 4-bromo-2-(trifluoromethyl)benzaldehyde were among the few commercially available starting materials for this work. This initial scope had a range of EWG, EDG, and relative steric bulk arranged based on A values ($H \approx F < Cl < Me < NO_2 < CF_3$).¹⁶⁹ Synthesising the corresponding *F*-BODIPYs from these aldehydes is an ongoing project. Initial success produced *meso*-(4-bromo-2,6-difluorophenyl)BODIPY, **b5**, and *meso*-(4-bromo-2-methylphenyl)BODIPY, **b6**, in adequate yields after optimisation of reaction conditions, while the pursuit of **b7**, **b8**, and **b9** is ongoing (**Figure 19**).

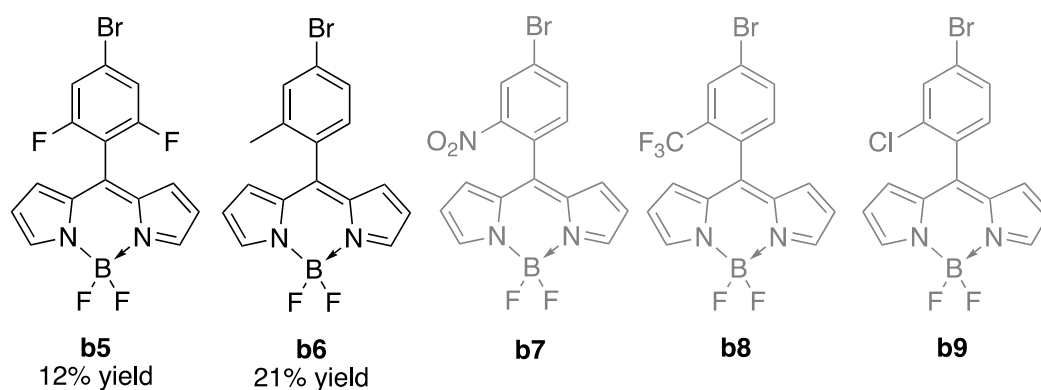


Figure 19. *F*-BODIPYs, featuring steric bulk at the ortho-position on the *meso*-aryl substituents. Chemical structures in grey represent ongoing studies.

Interestingly, the fluorine atoms of compound **b6** are no longer equivalent (unlike **b4** and **b5**) and result in a stunning AB quartet for the diastereotopic fluorine atoms. Further coupling in the way of the ^{19}F - ^{11}B interactions results in the four lines of equal integrals within each portion of the AB quartet (**Figure 20**). This pattern has been previously reported in the literature for similar compounds.⁹⁹ The presence of the methyl group results

in restriction of rotation around the BODIPY-aryl bond, thus resulting in a diastereomeric environment for each of the two fluoro-substituents.

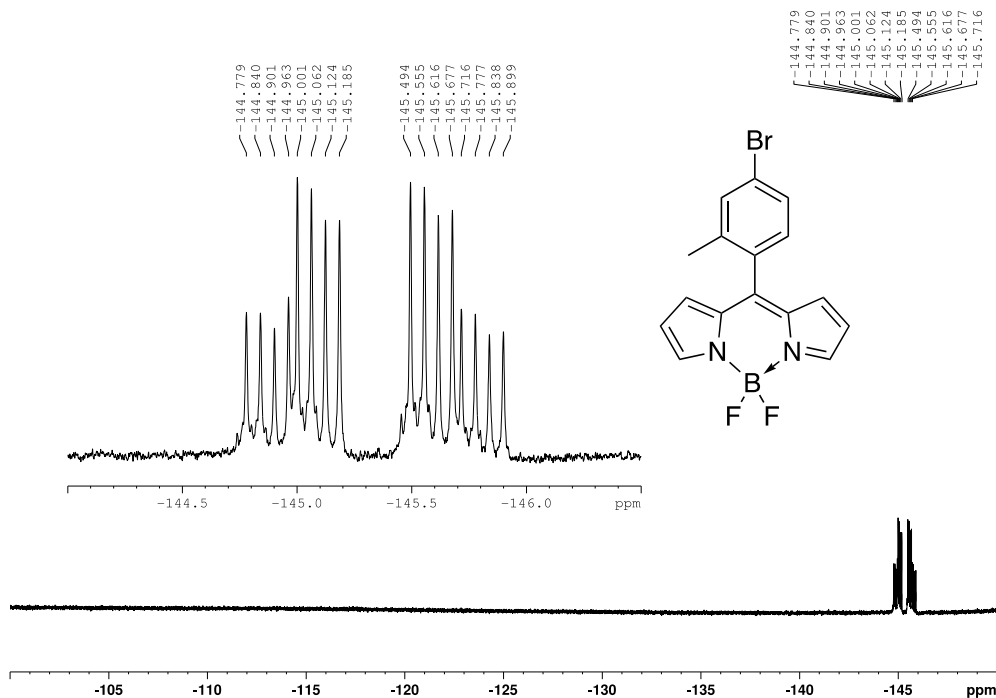
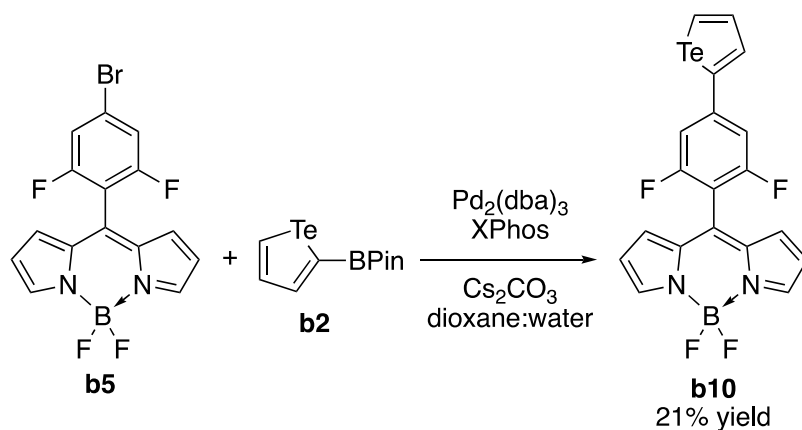


Figure 20. Fluorine NMR spectrum of **b6**, highlighting the doublet of quartets for each fluorine atom.

With some examples of bromo-substituted *F*-BODIPYs in hand, synthesis of desired tellurophene-appended BODIPYs was attempted. Using similar reaction conditions as published for compound **b4**,⁷⁵ **b5** was coupled with **b3** to afford the desired tellurophene-appended *F*-BODIPY, **b10**, in low yields after some optimisation (**Scheme 7**).



Scheme 7. Suzuki-Miyaura palladium cross-coupling reaction toward the synthesis of **b10**.

With this low yielding reaction, it became apparent that this catalyst system was not as potent for these systems as previously believed. This suspicion was maintained after failing to achieve, after many alterations of conditions, any conversion to desired product when employing the same catalyst system for **b6**. Moreover, according to analysis of the crude reaction mixture using NMR spectrometry, the decomposition of **b2** to tellurophene was observed. This is likely be attributed to protodeborylation, a common issue with organoboranes in the presence of water or other proton sources.¹⁶⁰

2.3.1. Experimental

Experimental works and supplementary data for this Section 2.3 can be found in Appendix B.

2.4. Chapter Conclusions and Future Perspectives

In conclusion, an efficient synthesis of the first tellurophene-appended *F*-BODIPY was published.⁷⁵ The method uses a borylated tellurophene and lends itself to coupling to various brominated *F*-BODIPY. Collaborators at the University of Toronto were able to demonstrate that the tellurophene-appended *F*-BODIPY was a capable photosensitiser and

generates $^1\text{O}_2$. Mass cytometry studies confirmed the presence of Te in cells, further supporting the potential of tellurophene-appended *F*-BODIPYs as theragnostic drugs.

To test the hypothesis that rigidifying the structure would limit vibrational relaxation and thus improve Φ_Δ , attempts were made to append the tellurophene-appended BODIPY framework with significant steric bulk *via a meso* aryl ring, *i.e.*, centrally between the two pyrrolic units of the BODIPY core. Unfortunately, this synthetic approach was found to be intolerant to many dipyrinato substrates. Future work for this project will address the need for a better catalyst system as well as better access to starting materials.

In general, if the tellurophene motif is to be widely adopted as a MC handle, then a robust coupling method must be realised. The Pd(0)/XPhos system used in this work showed some utility for appending the tellurophene motif to a BODIPY framework; however, this specific example does not show promise even with relatively similar substrates. Future works will explore Suzuki–Miyaura coupling of various borylated tellurophenes to various brominated aryl- and/or heteroaryl-substrates using alternative, perhaps more advanced, catalyst systems. Recently, in work by Denmark *et al.*,¹⁷⁰ researchers were able to perform heteroaryl-heteroaryl cross-coupling reactions of both pi-electron rich and pi-electron poor systems in good yields by employing a new generation palladium catalyst as well as some innovative additives. Citing the novelty of using trimethyl borate as an additive, researchers found that reaction rates increased due to the formation of boronate complexes *in situ*, thus increasing solubility and preventing catalyst poisoning. Another approach to consider is by Carrow *et al.* in which researchers employ an “on-cycle” precatalyst that is cited as being able to out-compete unwanted side-reactions such as the aforementioned

protodeborylation.¹⁶⁰ Moreover, the use of common organoboron analogues for pre-functionalisation of tellurophene can be explored. For example, the use of boronic acid, boronic acid *N*-methyliminodiacetic acid (MIDA) ester and neopentyl (neop) boronic acid may lead to improvements such as reduced protodeborylation.

Chapter 3. Nucleophilic Substitution of *F*-BODIPYs At Boron Towards the Synthesis of Chalcogenophene-BODIPYs

3.1. Preface

Optimisation of photophysical properties of the tellurophene-appended BODIPY system described in Chapter 2 proved synthetically challenging. Moreover, appending tellurophene to other positions on the BODIPY backbone had limited success (Section 1.8). One position, the boron centre, was yet to be explored for this project. Section 1.7.4 in this thesis details reactivity at the boron-atom and highlights some known BODIPY substitutions. This chapter contains a reproduced manuscript¹⁷¹ (Section 3.2) that describes the first published route towards appending two tellurophene motifs, and later other chalcogenophenes, at the boron centre of BODIPYs *via* nucleophilic substitution of a parent *F*-BODIPY. A series of chalcogenophene BODIPYs, *i.e.*, [*Te*]-, [*Se*]-, [*S*]- and [*O*]-BODIPYs, is established and photochemical and structural trends are discussed.

This chapter contains a publication that is wholly reproduced and edited for formatting and clarity of presentation (see Appendix G). Jacob W. Campbell led conceptualised of the project as well as designed and performed all synthesis. Matthew T. Tung designed and performed all singlet oxygen and *in vitro* experiments. X-ray crystallography was performed by Katherine N. Robertson. Andrew A. Beharry supervised Matthew T. Tung. Alison Thompson supervised Jacob W. Campbell. The publication was written by Jacob W. Campbell and Matthew M. Tung then edited by all authors.

3.2. BODIPYs with Chalcogenophenes at Boron: Synthesis and Properties

Reprinted and adapted with permission from:

Campbell, J. W.;[†] Tung, M. T.;[‡] Robertson, K. N.;^{§*} Beharry, A. A.;^{‡*} Thompson, A.^{†*}
BODIPYs with Chalcogenophenes at Boron: Synthesis and Properties. *J. Org. Chem.* **2023**,
88, 12, 10655-10661. Copyright 2023 American Chemical Society (Appendix F).

[†] Department of Chemistry, Dalhousie University, Halifax, Nova Scotia B3H 4J3, Canada.

[‡] Department of Chemistry and Physical Sciences, University of Toronto, Mississauga,
Ontario L5L 1C6, Canada.

[§] Department of Chemistry, Saint Mary's University, Halifax, Nova Scotia B3H 3C3,
Canada.

3.2.1. Abstract

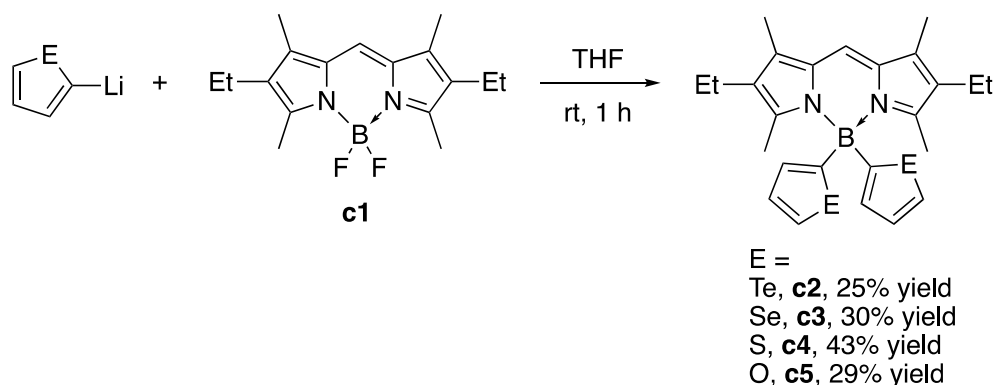
Reported herein is the synthesis and characterisation of a systematic series of BODIPYs bearing heterocycles at boron. To synthesise this series, chalcogenophenes (furan, thiophene, selenophene and tellurophene) were lithiated and then used as nucleophiles to attack the boron centre of a parent *F*-BODIPY. Compounds in the series were compared with respect to the photophysical and structural properties, and trends discussed. By virtue of the “heavy-atom effect”, as the mass of the heterocycle appended to the BODIPY core increases, compounds exhibit higher quantum yields of singlet oxygen. The BODIPY with

tellurophene at boron exhibits the highest quantum yield ($0.68 \Phi_{\Delta}$) in the series, and reduced emission ($0.01 \Phi_f$).

3.2.2. Introduction

Boron-dipyrromethene dyes (BODIPYs, 4-disubstituted-4-bora-3*a*,4*a*-diazas-indacenes) have garnered significant attention as photoactive species. This interest comes by virtue of the high structural tunability of BODIPYs, enabling applications in the fields of labeling reagents,^{39,44,45} switches,^{46,47} chemosensors,^{48–51} photodynamic therapy (PDT) agents,^{75,81,124} solar capture¹⁷² and laser dyes.¹⁷³ The stability of 4,4-difluoroBODIPYs (*F*-BODIPYs), along with their relative ease of synthesis, has resulted in these systems being extensively studied.⁴³ However, despite the popularity of this motif, discussion of systematic substitution effects remains scarce.^{174–178} Recently, BODIPYs have been functionalised by reaction at the boron centre with nucleophiles such as Grignard reagents or lithiated organo-metallic reagents. This facilitates the installation of substituents (other than fluorine) at the boron centre of the BODIPY framework (*e.g.*, aryl-, alkyl-, alkynyl-, alkoxy substituents) thus enhancing tunability of the wide range of desirable photophysical properties displayed by BODIPYs.^{33,35,37,129–131} however, there are few reports rationalising these trends.^{24,179,180} Moreover, despite the ability to arylate at boron with phenyl groups, there are few reported BODIPYs featuring heterocycles, herein denoted as [*E*], at the boron centre:^{133–136} thienyl-substituted systems are the sole examples. To address the surprising dearth of BODIPYs with heterocycles at boron, we present a complete series of B-(2-chalcogenophenyl)-substituted [*E*]-BODIPYs bearing tellurophene, selenophene, thiophene and furan at boron (**Scheme 8**), using 2,6-diethyl-4,4-difluoro-1,3,5,7-

tetramethylBODIPY (**c1**) as the dipyrinato skeleton. Photophysical and structural trends are discussed, with a particular focus on probing factors by which the BODIPY framework can be tuned to provide suitable photodynamic therapy (PDT) agents, an application which requires singlet oxygen generation rather than remarkable emission properties: main aims centre around optimisation of singlet oxygen generation, photostability, and cell viability. We report *[E]*-BODIPYs bearing tellurophene, selenophene, thiophene and furan at boron (**Scheme 8**), using 2,6-diethyl-4,4-difluoro-1,3,5,7-tetramethylBODIPY, **c1**, as the dipyrinato skeleton.¹²⁹



Scheme 8. Synthesis of *[E]*-BODIPYs.

3.2.3. Results and Discussion

We recently showed that 2-tellurophenyllithium serves as the precursor to a borylated-tellurophene capable of appending the tellurophene moiety *via* cross-coupling reactions.⁷⁵ Building on this utility, we hypothesised that 2-tellurophenyllithium could instead be used in nucleophilic substitutions at the boron centre of *F*-BODIPYs, thus providing access to tellurophene-appended BODIPYs and enabling a thorough study of BODIPYs with a heterocyclic system at boron. To prepare 2-tellurophenyllithium, *n*-butyllithium (2.2

equiv.) was slowly added to a stirring solution of tellurophene⁷⁵ (2 equiv.) in THF, under nitrogen, to generate a pale-yellow solution. A solution of the *F*-BODIPY **c1** (1 equiv.) in THF was then slowly added to the solution of 2-tellurophenyllithium, at room-temperature (**Scheme 8**). Progress of the reaction was evident *via* a rapid colour change from dark green (for the parent *F*-BODIPY) to dark red (for the tellurophene-substituted system), and *via* TLC through loss of the highly fluorescent *F*-BODIPY starting material. Aqueous workup and column chromatography over silica afforded BODIPY **c2**, bearing two tellurophene groups at boron, as a scarlet solid. Mass spectrometry for this compound revealed the anticipated complex isotope patterns for natural-abundance tellurium, with two tellurophene motifs incorporated for each dipyrinato unit. Loss of ¹⁹F NMR signal, plus acquisition and analysis of ¹H, ¹¹B, ¹³C and ¹²⁵Te NMR spectra, confirmed the synthesis of **c2**, with characteristic tellurium satellites evident in the ¹H NMR spectrum.

Adding to the known BODIPYs bearing thiophene at boron,^{133–136} we complemented the B-tellurophenyl framework of **c2** by synthesising analogues featuring the other Group 6 heterocycles (**Scheme 8**). The selenophene derivative **c3**, and the thiophene derivative **c4**, were prepared in a manner analogous to that of **c2** using the requisite lithiated heterocycles. As before, the progress of the reactions was observed by noting the change of colour from dark green to dark red as the substitution proceeded. Successful isolation of the thienyl- and selenophenyl-substituted BODIPYs was confirmed by analysis of the ¹H, ¹¹B and ¹³C NMR spectra corresponding to each product. Slow evaporation of either *n*-hexane or cyclohexane solutions of **c2**, **c3** and **c4** gave small acicular crystals in all cases. Analysis of the crystallographic data confirmed the structures of these compounds.

With BODIPYs bearing Te, Se, and S chalcogenophenes at boron in hand, we turned our focus to the B-substitution of **c1** with furan. However, attempts to synthesise and isolate **c5** (Scheme 8) following the same method as had been successful for **c2-c4** produced a complex product mixture suggestive of decomposition. Synthesis of **c5** instead required cooling the reaction mixture to 0°C *via* use of an ice-bath. Thus, the chalcogenic series was complete: BODIPYs bearing tellurophene, selenophene, thiophene, and furan at boron.

As a consequence of concerns regarding the stability of furan-containing **c5** that arose during synthesis and purification, the robustness of **c2-c5** was established before the photophysical and structural properties of the series were studied. Compounds **c2-c5** were all found to be stable in the solid state upon a week-long exposure to atmospheric conditions. Furthermore, solutions of compounds **c2-c4** in cyclohexane were stable upon heating to reflux temperature in air, with no observable changes according to NMR spectroscopic analysis. Conversely, the same analysis revealed the decomposition of **c5** when subjected to elevated temperatures under air.

Although compounds **c2-c4** were easily crystallised, many attempts to crystallise the furan analogue, **c5**, failed. One attempt, carried out in air, resulted in a crystal suitable for X-ray analysis. The crystal was found to be compositionally disordered. A two-component model was used to describe this disorder. Rather than the anticipated furan heterocycle at boron, and in support of our observations regarding decomposition, both components surprisingly featured ether-type chains at this position (see the SI **Figure 117** for crystal structure of compound **c6**).

Further attempts to crystallise **c5** were performed under a nitrogen atmosphere. Use of an impure sample of **c5** gave a compositionally disordered single crystal described *via* a four-component model (crystal structure of compound **c7** in the SI). Two components (see **Figure 21**, left) featured all the atoms and connectivity of **c5**, and differed only through the orientation of the furan rings at boron. The other two components (**Figure 21**, right) bore an additional furan ring at the *meso* (C5) position of the dipyrinato framework and also differed from each other through the orientation of the furan rings at boron. Through this work with **c5** we highlighted the differing reactivity of the furanyl ring derivative, relative to the other heterocycles in the chalcogenophenyl series. Indeed, none of the other compounds demonstrated instability during synthesis or purification.

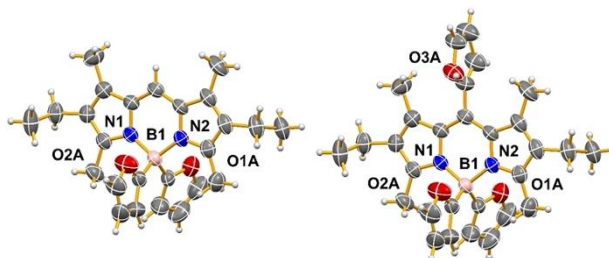


Figure 21. The minor (left, matching **c5**) and major (right) components of the model used to refine the structure of a crystal grown from a reaction mixture obtained after attempts to synthesise **c5**. Disorder of the furan rings has been removed. Thermal ellipsoids are drawn at the 50% probability level and only selected atoms have been labelled.

The series of compounds (*[O]*-, *[S]*-, *[Se]*- and *[Te]*-BODIPYs) was investigated crystallographically, with **c2** being the only structure in the series that was found not to be substantially disordered (**Figure 22**). The presence of significant disorder made determining any trends in the metrical parameters (bond lengths and angles) challenging (**Table 12** in the SI). Consequently, simple gas-phase calculations were carried out on the

parent 5-membered heterocycles (tellurophene, selenophene, thiophene, furan) to identify trends that might manifest in the X-ray crystallographic analysis of the BODIPYs bearing these heterocycles at boron (SI page 207). The calculations reveal that, unlike for the S, Se and Te congeners, furan has the most negative region of electrostatic potential located on the heteroatom itself. This helps to rationalise the instability of **c5**.

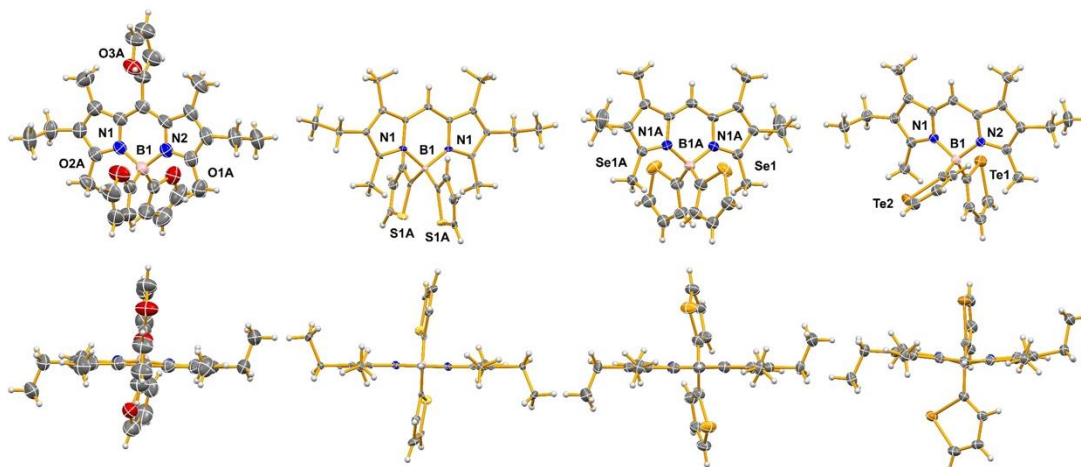


Figure 22. Structures of **c7** (one of the major components featuring three furan rings), **c4**, **c3** and **c2** (left to right), highlighting heterocyclic ring orientations at boron (top) and dipyrroin planarity (bottom). Disorder (where present) has been removed for clarity with only the major component shown. Thermal ellipsoids are drawn at the 50% probability level and only selected atoms have been labelled.

Trends in the NMR spectra for the series **c2-c5** include the relationship between chemical shifts and the identity of the heterocycle at boron. The ^{11}B chemical shift of the parent *F*-BODIPY **c1** is 0.76 ppm.¹⁸¹ ^{11}B spectra of compounds **c2-c5** show a downfield shifting trend of the chemical shift of the central boron atom from E = O to Te, indicative that the chalcogenophene affects the nature of the B-N bond (

Figure 102). Notwithstanding polarisation of bonds due to electronegativity effects, the observed trend in the chemical shift of the central boron atom demonstrates the increasing influence of the paramagnetic shielding effect of the heavy elements.^{182,183} As expected, reported BODIPYs with thiophene at boron¹³⁴ exhibit similar ¹¹B chemical shifts (-3.61 ppm, and featuring a different dipyrinato framework) to that of **c4** (-3.30 ppm).

Photophysical properties of the compounds in this series are given in **Table 2**. First, we compare the spectral characteristics of the new [*E*]-BODIPYs to those of the parent *F*-BODIPY **c1**. Upon substitution at boron with chalcogens, a bathochromic shift in $\lambda_{\text{abs}}^{\text{max}}$ is observed from E = O to Te (**Figure 83**). All extinction coefficients decrease relative to the parent *F*-BODIPY,¹⁸⁴ with compound **c5** exhibiting approximately half the molar absorptivity (ϵ) of the other [*E*]-BODIPYs. The $\lambda_{\text{em}}^{\text{max}}$ values follow the same relative trend as $\lambda_{\text{abs}}^{\text{max}}$ with Stokes shift values remaining largely consistent across all compounds. As expected, the parent *F*-BODIPY exhibits the highest quantum yield of fluorescence (Φ_f) in the series, with Φ_f decreasing as the atomic mass of the appended heterocycle increases ([O] > [S] > [Se] > [Te]) in accordance with heavy-atom effects.

Table 2. Photophysical data for **c1-c5** in CH₂Cl₂ solution.

Compound	λ_{absmax} (nm)	ϵ (M ⁻¹ cm ⁻¹)	λ_{emmax} (nm)	S.S. (nm)	Φ_{f}	Φ_{Δ}^{a}
c1 , <i>F</i> -BODIPY	530	103000	538	8	0.98	0.13
c2 , [<i>Te</i>]-	528	66000	537	9	0.01	0.68
c3 , [<i>Se</i>]-	526	77000	533	7	0.38	0.63
c4 , [<i>S</i>]-	524	66000	532	8	0.85	0.21
c5 , [<i>O</i>]-	522	35000	529	7	0.88	0.24

S.S., Stokes' shift; ^acalculated in 2% DMSO and MeOH

Singlet oxygen quantum yields (Φ_{Δ}) of the [*E*]-BODIPYs were evaluated using 1,3-diphenylisobenzofuran (DPBF), a selective singlet oxygen (¹O₂) sensor which decreases in absorbance upon reaction with ¹O₂ (**Figure 23**).¹⁴⁸ Experiments were conducted in 2% MeOH/DMSO, matching absorbances of the BODIPYs at 530 nm and irradiating samples with a 530 nm LED (2.15 mW/cm²). Eosin Y (EosY), a known green light-absorbing photosensitizer ($\Phi_{\Delta} = 0.42$ in MeOH),¹⁸⁵ was chosen as a standard while DPBF alone, with irradiation, was used as a control for any background degradation under the applied irradiation conditions. Measured Φ_{Δ} are presented in **Table 2** (see supplementary data for calculations). All [*E*]-BODIPY compounds **c2-c5** exhibited ¹O₂ generation, with compounds **c4** and **c5** generating significantly less than **c2** and **c3**. This difference is attributed to different mechanisms of intersystem crossing (ISC) with **c4** and **c5** achieving ISC according to El Sayed's rules, *i.e.*, coupling a spin flip with an orbital change.¹⁸⁶⁻¹⁸⁸ Compounds **c2** and **c3**, would effect ISC *via* the heavy-atom effect courtesy of the presence of Te and Se, respectively.¹⁸⁹ Photostability was also evaluated in 2% DMSO/MeOH, using

a 530 nm LED (2.15 mW/cm^2) as the excitation source. Spectra for compounds **c3-c5** exhibited no noticeable change over 5 min, but those corresponding to the analysis of **c2** revealed a slight decrease in absorbance over time (**Figure 24**).

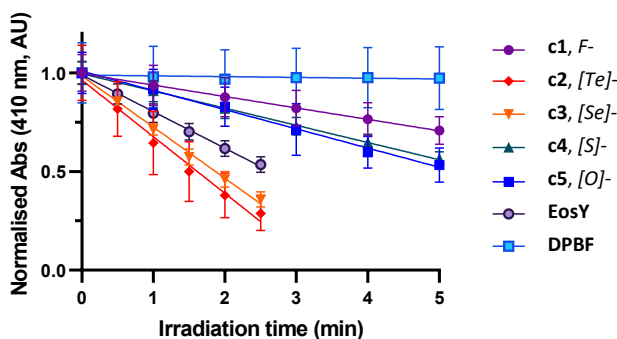


Figure 23. Singlet oxygen generation of BODIPYs detected by DPBF in 2% DMSO/MeOH under 530 nm irradiation (2.15 mW/cm^2). EosY was chosen as the standard and DPBF alone was irradiated as a control. Experiments were conducted in triplicate.

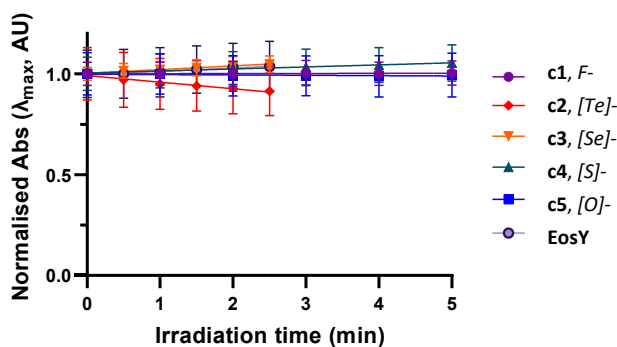


Figure 24. Photostability of $[E]$ -BODIPYs and parent F -BODIPY in 2% DMSO/MeOH. Absorbance was monitored at the λ_{max} during irradiation with a 530 nm LED (2.15 mW/cm^2).

To confirm cell permeability, HeLa cells were treated with $1 \mu\text{M}$ of the respective $[E]$ -BODIPY and imaged after incubation using a EGFP filter set (**Figure 25**). All $[E]$ -BODIPYs were fluorescent, although compound **c2** displayed only very weak fluorescence above the background (**Figure 89**). Consequently, all the $[E]$ -BODIPYs have potential as

diagnostic agents, in addition to their use in photodynamic therapy, courtesy of their fluorescence (**c3-c5**) and their potential as multi-channel probes of use in mass cytometry given the ability to incorporate single-isotope tellurium (*e.g.*, **c2**).⁷⁵

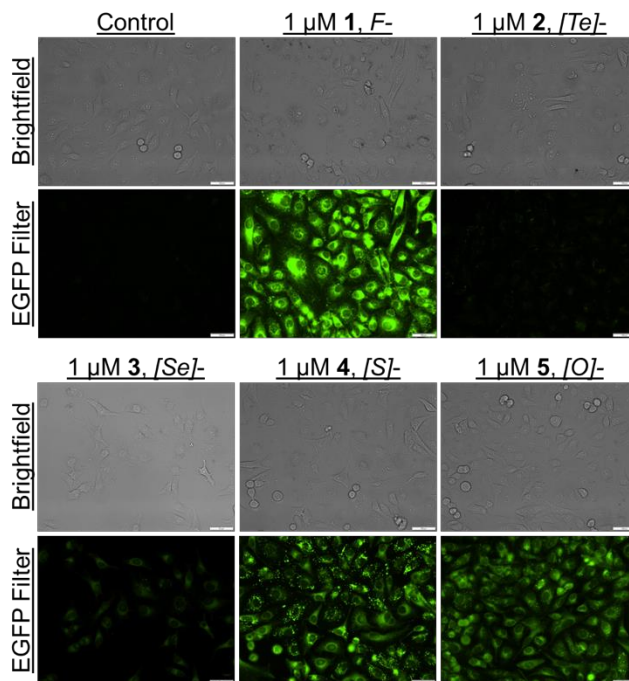


Figure 25. Fluorescent images of HeLa cells incubated with $[E]$ -BODIPY ($1 \mu\text{M}$) for 3 h, obtained using an EGFP filter set (Ex 450-490 nm, Em 500-550 nm), 20x magnification, scale bar = $50 \mu\text{m}$.

Given the ability of **c2-c5** to effect $^1\text{O}_2$ production, the phototoxicity of the $[E]$ -BODIPYs was determined using the MTT assay in HeLa cells. Various concentrations of compounds **c1-c5** were incubated with HeLa cells for 3 h, washed, and either kept in the dark or irradiated with a 525 nm lamp (5 min, 15.60 mW/cm^2 , 4.68 J/cm^2) before culturing overnight. MTT assays were conducted in triplicate to evaluate cell viability (**Figure 26**), and the resultant absolute IC_{50} values are shown in **Table 3**. The F -BODIPY control compound **1** did not exhibit substantial dark or light toxicity under the concentrations tested

(< 10 μM). Under irradiation (4.68 J/cm²), all *[E]*-BODIPYs exhibited nanomolar IC₅₀ values, with **c4** having an IC₅₀ of 25 nM and **c2** and **c3** each having an IC₅₀ of 6 nM. The dark toxicity of the *[E]*-BODIPYs were all above the concentrations evaluated, except for **c3** which had a dark IC₅₀ of 520 nM. Overall, compounds **c2** (heavy-atom effect) and **c4** (El Sayed's rules) show promise for further studies given their low nanomolar light IC₅₀ values and low dark toxicities observed up to 1 μM .

Table 3. Absolute IC₅₀ values of BODIPYs **c1-c5**.

Compound	Dark IC ₅₀ (μM)	Light IC ₅₀ (μM) ^a
c1 , <i>F</i> -BODIPY	> 10.0	> 10.0
c2 , <i>[Te]</i> -	> 1.00	0.006
c3 , <i>[Se]</i> -	0.520	0.006
c4 , <i>[S]</i> -	> 1.00	0.025
c5 , <i>[O]</i> -	> 3.16	0.689

^a525-nm lamp used for 5 min (15.60 mW/cm², 4.68J/cm²)

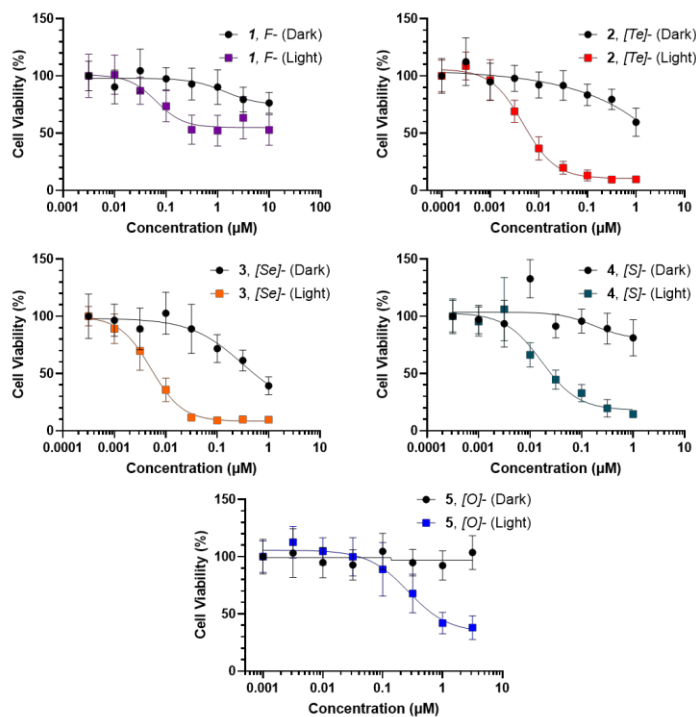


Figure 26. Cell viability with $[E]$ -BODIPYs. HeLa cells were incubated with varying concentrations of compounds for three h and left either in the dark or irradiated with a 525-nm green lamp (5 min, 15.60 mW/cm², 4.68 J/cm²). Experiments were conducted in triplicate.

3.2.4. Conclusions

To conclude, a systematic series of chalcogenophenes (O, S, Se, Te) bound to the boron centre of BODIPYs is reported and investigated spectroscopically and crystallographically. The $[E]$ -BODIPYs were synthesised *via* nucleophilic substitution of the fluorine atoms of a parent *F*-BODIPY with 2-lithiated chalcogenophenes. Parameters associated with suitability as PDT agents were evaluated, with the conclusion that compounds **c2** and **c4** were the most capable sensitisers in the series by virtue of their low light IC₅₀ values, low dark toxicities, and good cell viability. Access to the Group 6 heterocycles enabled a detailed analysis of the electronic and size effects upon the properties of the $[E]$ -BODIPYs within the series: such a systematic assessment is a rarity within the BODIPY field. The

ability of the heterocyclic moiety to tune photodynamic therapeutic effects was demonstrated. Future work will build on this series by substitution at other positions of the chalcogenophenyl substituent, along with systematic exploration of other systems bearing heterocycles at boron.

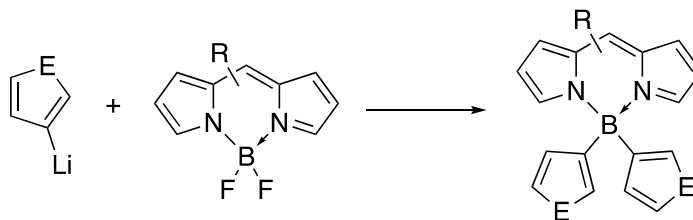
3.2.5. Experimental

All experimental works were reproduced with permission and included in Appendix C.

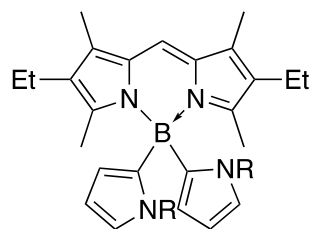
3.3. Chapter Conclusions and Future Perspectives

The synthesis and characterisation of a series of BODIPYs featuring a chalcogenophenes at the boron centre were explored. The goal of this work was to monitor the photophysical and structural trends of BODIPYs when there is substantial atomic masses appended to the boron centre. The parent *F*-BODIPY was reacted with lithiated chalcogenophenes to afford the desired compounds. The [*Te*]-BODIPY synthesised exhibits the highest quantum yield ($\Phi_{\Delta} = 0.68 \pm 0.08$).

With the success in synthesising a comprehensive chalcogenophene [*E*]-BODIPY series, future work should focus on substitution at the 3-position of the chalcogenophene (**Scheme 9**), and further extending this series to include various *N*-substituted pyrroles such as *N*-H, *N*-Boc and *N*-Me pyrrole (**Figure 27**) to study the effect on PDT.



Scheme 9. Proposed synthetic scheme for substitution at the 3-position of various chalcogenophenes.



R = H, Me or Boc

Figure 27. Proposed *[N]*-BODIPYs featuring various substituents on the nitrogen atom.

Chapter 4. Synthesis of a Series of [Te]-BODIPYs

4.1. Preface

This chapter contains a reproduced manuscript¹⁹⁰ (Section 4.2). In Chapter 3 photochemical properties of chalcogenophene BODIPYs were discussed, with particular emphasis given to properties that are related to photosensitisation. The [Te]-BODIPY system, as described therein, was found to be the most potent system for photosensitisation. In this chapter, the scope of [Te]-BODIPYs is explored, and photochemical and structural trends are discussed.

This chapter contains a publication that is wholly reproduced and edited for formatting and clarity of presentation (see Appendix G). Jacob W. Campbell conceptualised the project as well as designed and performed all synthesis. Matthew T. Tung designed and performed all singlet oxygen and *in vitro* experiments. Breanna B. Taylor assisted Jacob W. Campbell. Andrew A. Beharry supervised Matthew T. Tung. Alison Thompson supervised Jacob W. Campbell and Breanna B. Taylor. The publication was written by Jacob W. Campbell and Matthew M. Tung and edited by all authors.

4.2. A Series of Potent BODIPY Photosensitisers Featuring Tellurophene Motifs at Boron

Reprinted and adapted with permission from:

Campbell, J. W.;[†] Tung, M. T.;[‡] Taylor, B. B;[†] Beharry, A. A.;^{‡*} Thompson, A.^{†*} *Org. Biomol. Chem.* **2024**, 22, 4157–4162. Copyright 2024 The Royal Society of Chemistry (Appendix F).

[†] Department of Chemistry, Dalhousie University, Halifax, Nova Scotia B3H 4J3, Canada.

[‡] Department of Chemistry and Physical Sciences, University of Toronto, Mississauga, Ontario L5L 1C6, Canada.

4.2.1. Abstract

This article describes the synthesis and photophysical properties of a series of BODIPY photosensitisers that feature tellurophene motifs appended at the boron centre. These compounds were obtained *via* nucleophilic substitution of various *F*-BODIPYs with lithiated tellurophene. The synthetic scope, photophysical characteristics and photosensitisation properties are discussed. Structural modifications around the BODIPY core resulted in an eight-fold improvement in light IC₅₀ values compared to previous designs.

4.2.2. Introduction

Photodynamic therapy (PDT) is a clinically proven modality for killing cancer cells.^{77,191}

The mechanism of cytotoxicity relies on a photosensitiser (PS) that, upon irradiation, absorbs light. This promotes the PS to an excited singlet ($^1\text{PS}^*$) state that ideally undergoes intersystem crossing (ISC) to the excited triplet ($^3\text{PS}^*$) state, rather than relaxation *via* vibrational or emissive modes. With the sufficiently long $^3\text{PS}^*$ lifetime, collision with molecular oxygen ($^3\text{O}_2$) generates cytotoxic singlet oxygen ($^1\text{O}_2$) and other reactive oxygen species *in situ*, and results in a photodynamic therapeutic effect.⁷⁶

The photophysical tunability of boron-dipyrromethane dyes (*e.g.*, *F*-BODIPYs, 4,4-difluoro-4-bora-3a,4a-diaza-*s*-indacene) lends well to PDT, and thus *F*-BODIPYS are well-documented as PDT agents.^{8,75,124,151,171,192} The design principles aligning with tuning for photosensitisation aim to promote ISC to the $^3\text{PS}^*$ state, with the maintenance of modest fluorescence deemed useful for theragnostic purposes.⁸ A structural modification known to promote ISC involves the incorporation of a heavy-atom near or on the chromophore,¹⁸⁷ with the resulting ISC enhancement originating from greater spin-orbital coupling. Indeed, introduction of halogens is a proven approach by which to tune *F*-BODIPYs away from typically dominant fluorophoric properties and instead to enhance ISC and PDT effects.^{81,100,176,193} Despite the utility of these design principles, structure-activity relationships involving fluorophoric, photosensitising, and other photochemical properties are typically fickle in terms of predictability, and thus the examination of a broad range of derivatives is typically necessary. These design principles were described in our previous work which melded the heavy-atom effect of a tellurium atom with the photophysical

capabilities of the BODIPY core. Furthermore, the presence of tellurium not only promoted ISC but also provided a mass label for tracking using mass cytometry (MC). MC is a method used to analyse the physical and chemical characteristics of cells *via* the incorporation of a mass label conjugated or appended to organic molecules.⁸⁸ Mass cytometry reagent development is predominantly focussed on incorporating heavy-atoms, typically lanthanides, as metal-chelates into small organic molecules or antibodies.⁸⁸ However, the tellurium atom shows promise as a mass label given its eight stable isotopes and a desirable physiological profile.^{85,86,90,194} Moreover, given that tellurium–carbon bonds are generally stable, this heavy atom mass label can be incorporated into small molecules by synthetic routes that are well mapped out courtesy of many decades of development involving other group-16 elements.^{85,90,94,98} Indeed, tellurophene, a tellurium-containing heterocycle that is a member of the chalcogenophene family, has been developed as a promising component for small molecule incorporation.^{86,194,195}

Our previous work discussed the utility of appending tellurophene to BODIPYs and involved two synthetic approaches. The first involved a Suzuki coupling reaction between an organoboron-functionalised tellurophene nucleophile and an electrophilic BODIPY (**d1**, **Figure 28**).⁷⁵ This system acted as a proof-of-principle for tellurophene-appended BODIPY-based photosensitisers; however, this system suffered from a moderate singlet oxygen quantum yield ($\Phi_{\Delta} = 0.26 \pm 0.01$). To test the hypothesis that rigidifying the structure would limit vibrational relaxation and thus improve Φ_{Δ} , we further appended the tellurophene-appended BODIPY framework with significant steric bulk *via* a *meso* aryl ring, *i.e.*, centrally between the two pyrrolic units of the BODIPY core. Unfortunately, this

synthetic approach was found to be intolerant to many dipyrinato substrates and it became clear that a more effective approach to functionalisation was needed.

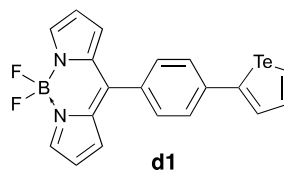


Figure 28. Tellurophene-appended BODIPY *via* Suzuki coupling.

We recently described a new system in which we appended chalcogenophenes (furan, thiophene, selenophene and tellurophene) to the core of a BODIPY *via* nucleophilic substitution at the boron atom of an *F*-BODIPY.¹⁷¹ The synthesis involved using lithiated heterocycles and thereby avoided the need to activate the B–F bond *via* the use of Lewis acids, or effect prior halogen exchange at boron.^{33,37,136,196,197} When comparing the photophysical data of all compounds in the series we found that the tellurophene-appended [Te]-BODIPY **d2** (**Figure 29**) exhibited the highest Φ_{Δ} (0.68 ± 0.08). Incorporating tellurophene at the boron atom of BODIPYs thus led to an improvement of desirable photophysical properties for a theragnostic photosensitiser. Herein, we demonstrate tellurophene incorporation at boron for a variety of BODIPYs. Furthermore, we discuss parameters that are pertinent to photosensitiser capabilities (Φ_{Δ} , photostability, cell viability), and review the tolerance and limitations of the synthetic approach.

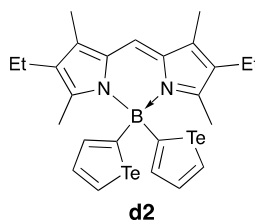


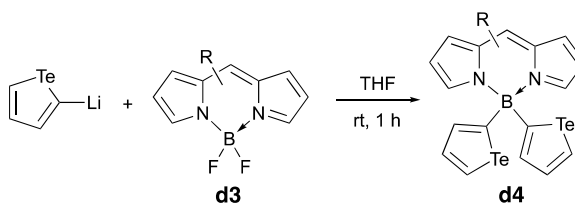
Figure 29. Tellurophene-appended BODIPY *via* nucleophilic substitution at boron.

4.2.3. Results and Discussion

To analyse a series of *[Te]*-BODIPYs, the synthesis of the corresponding *F*-BODIPYs (**d3**, **Scheme 10**) was realised. The suite of *F*-BODIPYs was designed to evaluate the tolerance of the nucleophilic substitution at boron by varying the substituents on the dipyrinato core. *F*-BODIPYs with various alkyl, aryl, halogen, and other substituents were synthesised by first condensing pyrroles with carbonyl-containing reagents in the presence of acid catalysts to form dipyrromethanes which were oxidised as necessary, and then complexed to boron difluoride to give *F*-BODIPYs. Conversely, for some substrates, a direct route to dipyrin was used in which formyl pyrroles were condensed with α -free pyrroles to give dipyrin salts that were then complexed to boron difluoride.

With the requisite *F*-BODIPYs in hand, and working in a nitrogen-filled glovebox, 2-tellurophenyllithium was generated *in situ* by adding *n*-butyllithium (2.4 equiv.) dropwise to a stirring solution of tellurophene (2.2 equiv.) in THF at room temperature.¹⁷¹ After five minutes, and in order to promote double-substitution of the fluoro substituents, the requisite *F*-BODIPYs (**d3**, **Scheme 10**) were added dropwise over five minutes to the pale-yellow stirring solution of 2-tellurophenyllithium. The resulting solution was stirred for one hour at room temperature. Aqueous workup, followed by column chromatography gave the desired *[Te]*-BODIPYs (**d4**, **Scheme 10**) as scarlet red solids in moderate to low yields. The relative ease of chromatography of the compounds varied dramatically. For example, *F*-BODIPYs with fewer substituents on the dipyrinato core were found to have off-target reactivity that provided complex reaction mixtures of compounds with similar retention factors. All chemical structures were supported by analysis of ¹H, ¹³C, and ¹¹B NMR

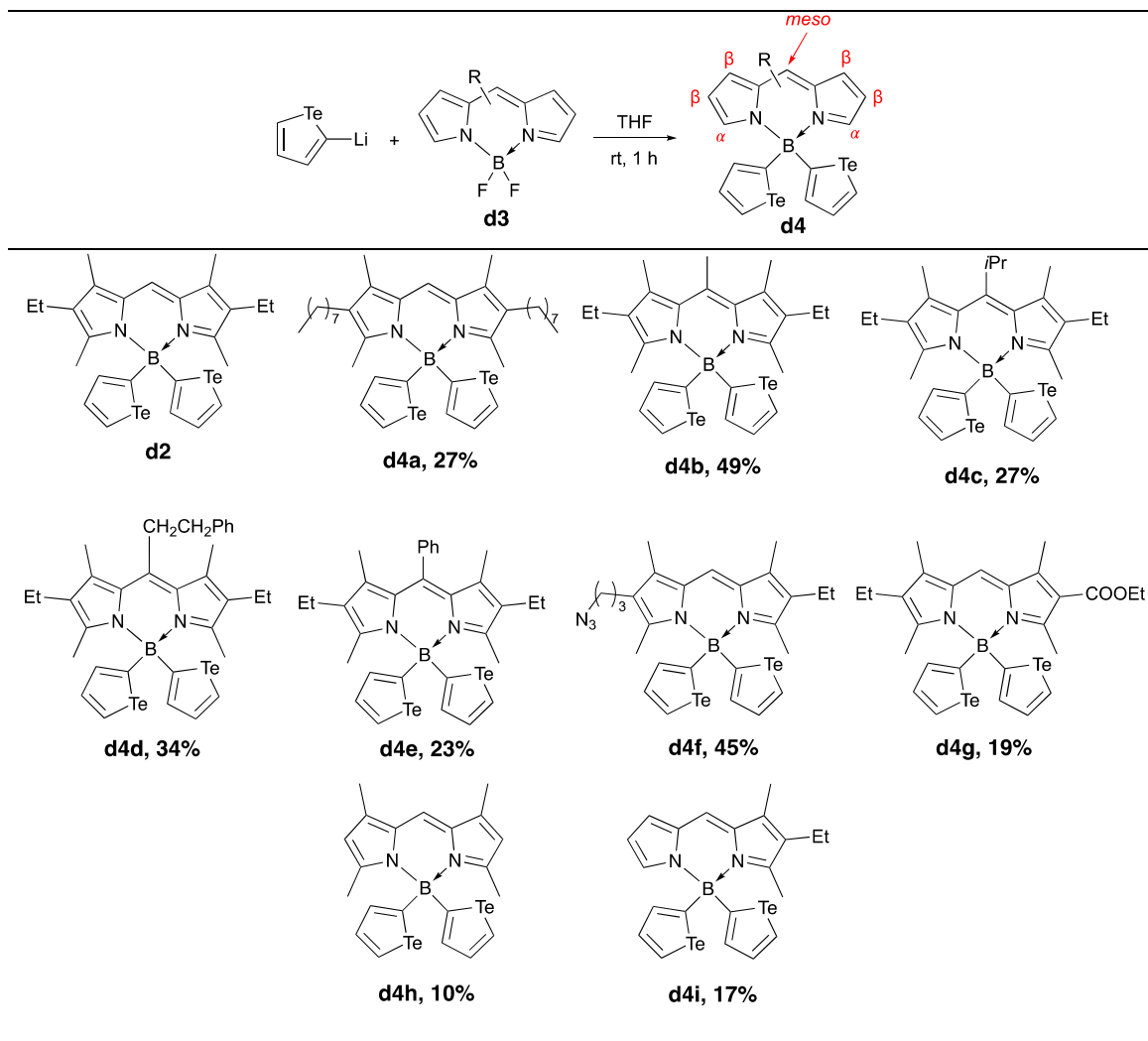
spectra and by observing a loss of ^{19}F NMR signal. Furthermore, the anticipated complex isotope pattern was observed in mass spectral data, owing to the many tellurium isotopes.



Scheme 10. Synthesis of $[\text{Te}]$ -BODIPYs via nucleophilic substitution at boron.

Employing this synthetic method, a series of $[\text{Te}]$ -BODIPYs that feature various substituents on the dipyrrolic backbone was synthesised (**Table 4**). The properties of the ethyl-substituted $[\text{Te}]$ -BODIPY **d2** have been established,¹⁷¹ and it was found that replacing ethyl chains with octyl chains (**d4a**) had little effect on the system in terms of yields and ease of purification. Similarly, alkyl groups are well tolerated in the *meso* position of the dipyrrolic core, as demonstrated by the isolation of the methyl and isopropyl examples **d4b** and **d4c**, respectively. Functionality at the *meso* position successfully extended to the incorporation of alkyl phenyl (**d4d**) and phenyl (**d4e**) moieties. Examples with synthetically useful functional group handles were then targeted. For example, the azide-containing $[\text{Te}]$ -BODIPY **d4f** was produced by treatment of the corresponding *F*-BODIPY with 2-tellurolithium: an ester-functionalised $[\text{Te}]$ -BODIPY **d4g** was similarly prepared.

Table 4. Synthetic scope of nucleophilic substitution of tellurophene at boron of various BODIPYs.



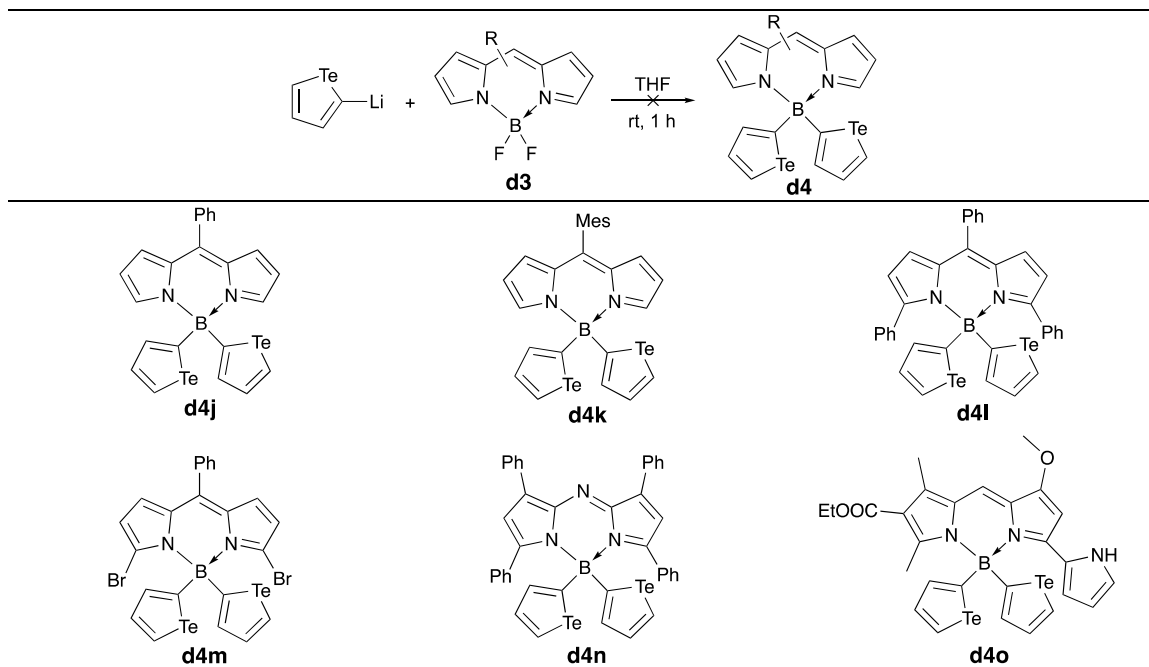
Challenges and reduced yields arose when attempts were made to synthesise *[Te]*-BODIPYs that had fewer substituents on the dipyrinato backbone. One such example, **d4h**, involved a *F*-BODIPY that was unsubstituted at the *meso* and at two of the β -positions on the dipyrinato core. TLC analyses and ^1H NMR data for the crude reaction mixture suggested the presence of many compounds which was an indication of off-target

substitution at other positions on the dipyrinato backbone. A similar result was observed for the asymmetric system **d4i** which features one entirely unsubstituted pyrrolic unit. Although these two examples were successfully purified, reduced regioselectivity for unsubstituted systems is apparent. Attempts to improve nucleophilic substitution at the desired position included cooling the reaction mixture to -78 °C for both the lithiation of tellurophene and the addition of *F*-BODIPY, as well as diluting the reaction mixtures: however, undesired off-target reactivity prevailed.

F-BODIPYs with unsubstituted positions were challenging in terms of substitution at boron with tellurophene (**Table 5**). In the crude reaction mixture, a loss of ¹⁹F NMR signal was observed. However, mass spectrometry analysis for the two reactions suggested only a complex mixture of decomposition products, as was supported *via* TLC and ¹H NMR analysis. This was attributed to the oxidatively unstable nature of the unsubstituted dipyrinato cores. Challenges were also encountered when attempting to effect substitution at boron by tellurophene for *F*-BODIPYs bearing larger steric bulk at the α -positions on the dipyrinato core. When *F*-BODIPYs featuring α -phenyl and α -bromo substituents (**d4l** and **d4m**, respectively) were used, the reaction did not reach completion, but rather the starting material *F*-BODIPY could be recovered from the reaction mixture. These results suggest that this system not only suffers from poor regioselectivity for the nucleophilic substitution, but also that substitution at boron is hindered by steric bulk at the α -positions on the dipyrinato core. Further addition of steric bulk, such as in the use of the tetra-phenyl substituted *aza*-BODIPY (**d4n**), resulted in no reaction and almost all starting material was recovered. The use of a highly substituted natural product derivative, prodigiosin BF₂

complex (**d4o**), was attempted and showed little to no reactivity for nucleophilic substitution at boron.

Table 5. Challenging substrates for incorporation of tellurophene at boron of BODIPYs.



With the successfully synthesised $[Te]$ -BODIPYs in hand, photophysical properties (absorbance, fluorescence, extinction coefficient (ϵ), and Φ_{Δ}) were determined (**Table 6** and **Table 14**). Absorbances and fluorescence quantum yields (Φ_f) were determined for **d4a-d4i** initially in CH_2Cl_2 (**Figure 126** to **Figure 134**). Similarly to the reported $[Te]$ -BODIPYs, **d1** and **d2**, the determined Φ_f values were minimal and no noticeable fluorescence was observed in aqueous conditions.^{75,171} Although aggregation-induced emission (AIE) has been observed for BODIPYs featuring aryl groups at the *meso*-position and thiophenes, or spiro-linked aryl groups, at boron, investigation of AIE properties for a

series of BODIPYs appended with tellurophenes at boron would require an alternative synthetic approach given the challenges encountered herein regarding **d4j-d4l**.^{33,136,198} The absorbance properties for all compounds were also measured in solutions of 1% DMSO in MeOH and 1% DMSO in PBS to determine the wavelengths for ¹O₂ determination and *in cellulo* experiments, respectively. In MeOH, the λ_{max} of absorption for compounds for **d2** and for **d4a-d4f** were between 517–529 nm, in line with other alkyl-substituted BODIPYs.⁴³ With unsubstituted dipyrinato cores or electron-withdrawing groups, *F*-BODIPYs generally exhibit a blue shifted λ_{max} of absorption, as noted for compounds **d4g-d4i** which absorb between 506–508 nm.⁴³ Under aqueous environments, all [*Te*]-BODIPYs exhibited a red shifted absorption of ~4-18 nm as seen in **Figure 30a** and **Figure 135**.

Table 6. *In vitro* and *in cellulo* data for [Te]-BODIPYs

	$\lambda_{\text{max}}^{\text{abs}}$ (MeOH, nm)	ϵ (DMSO, $\text{M}^{-1}\text{cm}^{-1}$)	Φ_{Δ} (MeOH)	Dark IC_{50} (μM)	Light IC_{50} (μM) ^b	Phototoxicity Index
d2	526	55700	0.68 ± 0.08	> 10.0	0.039 ± 0.013	> 256
d4a	529	83100	0.48 ± 0.05	13.1 ^a	0.421 ± 0.118	31
d4b	517	96800	0.54 ± 0.03	> 10.0	0.009 ± 0.002	> 1110
d4c	528	85600	0.17 ± 0.01	> 10.0	0.047 ± 0.018	> 213
d4d	521	90800	0.85 ± 0.11	> 10.0	0.054 ± 0.025	> 185
d4e	521	72900	0.82 ± 0.09	> 10.0	0.042 ± 0.013	> 238
d4f	526	70000	0.45 ± 0.02	> 10.0	0.016 ± 0.008	> 625
d4g	506	75500	0.55 ± 0.07	13.2 ^a	0.005 ± 0.002	2640
d4h	506	86200	0.57 ± 0.08	> 10.0	0.005 ± 0.001	> 2000
d4i	508	33100	0.47 ± 0.04	> 10.0	0.017 ± 0.004	> 588

^a Dark IC_{50} values were extrapolated from the graph (the highest concentrations tested were 10 μM). ^b A 525-nm lamp was used for irradiations (5 min, 15.60 mW/cm², 4.68 J/cm²)

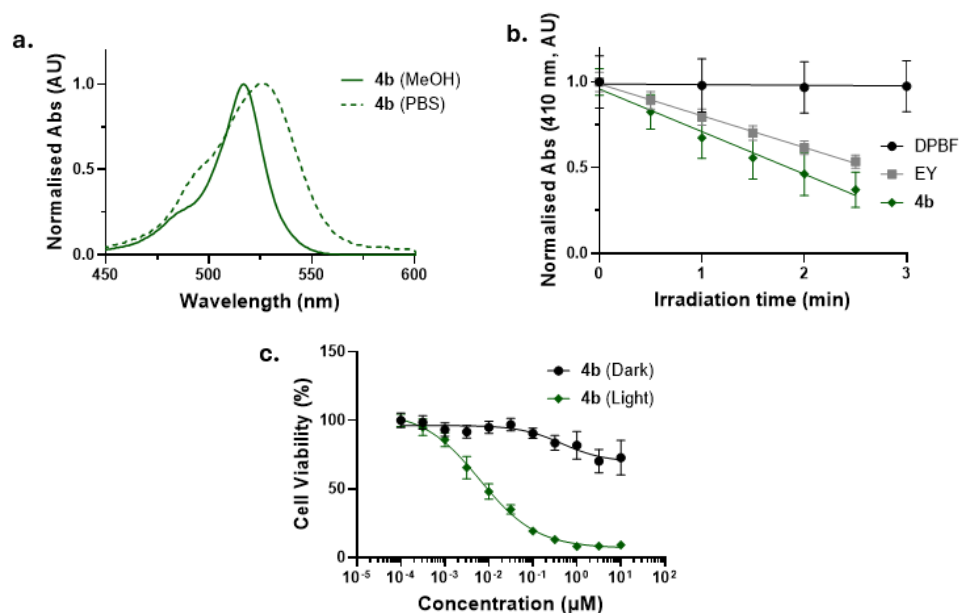


Figure 30. Photophysical characterisations of **d4b**. (a) Normalised absorbance of **d4b** in solutions of 1% DMSO in MeOH and 1% DMSO in PBS. (b) Singlet oxygen generation of **d4b** detected by DPBF in 1% DMSO in MeOH with 530 nm irradiation (2.15 mW/cm²), n = 3. (c) Cell viability of HeLa cells incubated with varying concentrations of **d4b** under dark or light (525 nm, 4.68 J/cm²) conditions, n = 9.

The Φ_{Δ} values were determined using 1,3-diphenylisobenzofuran (DPBF), a selective $^1\text{O}_2$ sensor that exhibits a decreased absorbance at 410 nm upon reaction with $^1\text{O}_2$. Eosin Y (EY) is a known PS with a Φ_{Δ} of 0.42 in MeOH¹⁸⁵ and was used as the standard for all [Te]-BODIPYs studied herein. For compounds **d4a-d4f** absorbances were matched at 530 nm, while compounds **d4g-d4i** were matched at 490 nm, and irradiated with the respective LEDs. The degradation of DPBF was observed for all compounds (**Figure 30b** and **Figure 136**) and the Φ_{Δ} values were determined. All [Te]-BODIPYs produced moderate to high Φ_{Δ} values (0.45–0.85) except for **d4c** ($\Phi_{\Delta} = 0.17 \pm 0.01$). This can be rationalised by the presence of the isopropyl group at the *meso* position on **d4c**. Indeed, other researchers demonstrated that the presence of isopropyl groups on the *meso* position of BODIPYs causes decreased quantum yields of fluorescence *via* nonradiative decay from the excited

state.¹⁹⁹ Therefore, it is proposed that compound **d4c** exhibits low ¹O₂ generation through similar relaxation pathways. The photostabilities of the [Te]-BODIPYs were also evaluated by monitoring the change in absorbance at the λ_{max} of absorbance over the irradiation period. All compounds demonstrated slight degradation except for **d4c**, likely due to decreased ¹O₂ generation (**Figure 137**).

With the promising *in vitro* data in hand, the properties of the [Te]-BODIPYs were evaluated in a cervical cancer cell line. All concentrations were determined based on the ϵ value in DMSO (**Table 6** and **SI**). To summarise, 10,000 HeLa cells were seeded into 96 well plates overnight in Dulbecco's Modified Eagle Medium (DMEM) before washing with phosphate-buffered saline (PBS) and incubation with the respective compounds for three hours in minimal essential medium (Opti-MEM). The cells were then washed with PBS and either kept in the dark or irradiated with a 525-nm lamp (4.68 J/cm²) for 5 min in DMEM. After incubation overnight, an MTT cell viability assay (n = 9) was performed to determine the dark and light toxicities of each compound (**Figure 30c** and **Figure 138**). The absolute IC₅₀ values are reported in **Table 6**. The dark toxicity observed for all compounds was greater than the highest concentrations tested (10 μ M) while the light IC₅₀ values of all compounds demonstrated either single or double-digit nanomolar IC₅₀ values except for **d4a** (light IC₅₀ = 0.421 μ M). The increase in light-activated IC₅₀ between **d4a** and the other [Te]-BODIPYs is likely a result of decreased solubility caused by the long hydrophobic alkyl chains at the β -positions of the dipyrinato core present in **d4a**. Furthermore, and notwithstanding the need for caution when attempting to align photochemical properties with molecular structure, incorporation of functionality onto the

BODIPY core (**d4g**) and/or tuning hydrophobicity (**d4g**) results in significantly improved photosensitisation properties as seen *via* light IC₅₀ values. With the exception of **d4a** (PI = 31), all compounds had a phototoxic index (PI) of > 185. Although comparisons of PI between studies can be difficult, due to variations in cell type, irradiation powers and experimental conditions,²⁰⁰ other researchers determined the PI of two known PSs, Photofrin and Hypericin, under similar conditions.²⁰¹ Using HeLa cells and similar irradiation powers (5 J/cm² as opposed to the 4.68 J/cm² used in this study) the PI values of Photofrin and Hypericin were found to be > 4.3 and > 12, respectively,²⁰¹ *i.e.*, much lower than the PIs determined in this study, and thus demonstrating the potential of [*Te*]-BODIPYs as an alternative PS for PDT.

4.2.4. Conclusions

The synthesis and characterisation of BODIPY-based PSs appended with tellurophenes at the boron centre are reported. These compounds were synthesised *via* nucleophilic substitution of the fluoro substituents of *F*-BODIPYs with 2-lithiated tellurophenes. Various parent *F*-BODIPYs were used in order to determine the scope of substitution, and modifications on the *meso* and β -positions on the dipyrinato core were found to be generally tolerated. However, the use of *F*-BODIPYs with unsubstituted positions about the dipyrinato core led to undesirable side reactions while the presence of bulky substituents on the α -position reduced reactivity.

The [*Te*]-BODIPYs all retained similar absorbances and ϵ values as expected of BODIPY-based fluorophores. The incorporation of tellurophenes at boron resulted in a decrease in Φ_f values and generated PSs with modest to high Φ_Δ values. PI values are comparable to

known PSs, demonstrating that *[Te]*-BODIPYs as potential PSs for PDT. Structural modification resulted in an eight-fold improvement in light IC₅₀ values (compare **d2** with **d4g** and **d4h**). Future work will explore the incorporation of chemical handles, such as the azide in **d4f**, as a strategy by which to incorporate targeted selectivity towards cancerous cells.

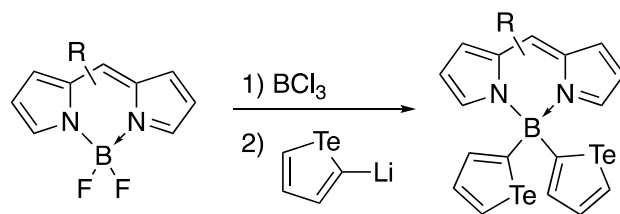
4.2.5. Experimental

All experimental works were reproduced with permission and included in Appendix D.

4.3. Chapter Conclusions and Future Perspectives

To conclude this chapter, the synthesis and characterisation of a series of *[Te]*-BODIPYs featuring a variety of substituents on the BODIPY backbone were explored. The goal of this work was to analyse the photophysical properties and attempt to identify emergent structural trends. The desired compounds were synthesised by reacting the corresponding *F*-BODIPYs with lithiated tellurophene. Some *[Te]*-BODIPY compounds exhibited more favorable photophysical properties for PDT than compounds showcased in Chapter 2 and Chapter 3.

A previous publication from the Thompson group outlines the conversion of *F*-BODIPYs to *Cl*-BODIPYs as a method of increasing reactivity at the boron centre to afford *alkyl*- and *alkoxy*-BODIPYs that were not possible in one step. This one-pot procedure employs boron trichloride (BCl₃) to substitute the fluorine atoms for the chloride analogue *in situ*, followed by either the addition of Grignard or lithio organo-metallic reagent to afford the desired product. This method could be explored for the synthesis of *[Te]*-BODIPYs and may lead to an improvement in yields (**Scheme 11**).



Scheme 11. Proposed improved synthesis of [Te]-BODIPYs employing BCl_3 .

Chapter 5. Synthesis of Estradiol *[Te]*-BODIPYs

5.1. Introduction

Previous chapters discussed the development of potent *[Te]*-BODIPY photosensitisers with excellent phototoxicity indices. The next logical step to further explore our system is to incorporate targeted selectivity to enhance the accumulation of photosensitiser in specific cancerous cells. Owing to the enormous efforts from the scientific community towards the development of chemotherapy drugs, there is an extensive body of research and a seemingly endless number of resources to aid in chemotherapeutic drug development. Most chemotherapeutic drugs function on the premise of killing cells that grow and divide quickly.²⁰² Although this is an extremely effective modality of cancer treatment that has saved countless lives, it does have negative side-effects such as causing damage to and death of healthy fast-growing cells, *e.g.*, mouth and intestine lining, as well as hair-growth cells.²⁰² Recently, through the study of cancer cell genomes, as well as a cancer cell initiation and metastasis, researchers have identified a multitude of proteins and enzymes to target *via* chemotherapeutic drugs.^{203,204} These target proteins and enzymes can be exploited, *via* drug design, to create chemotherapeutics to help mitigate the risk to healthy cells. These so called “targeted therapy drugs” differ from traditional chemotherapeutic drugs in that they ideally pose limited risk to healthy cells. There are a number of modalities available to kill cancer cells using a targeted approach, *e.g.*, drugs that trigger an immune system response,²⁰⁵ block specific chemical signals which are vital for growth,²⁰⁶ change

specific proteins that are vital for cell viability,²⁰⁴ and stop the formation of new blood vessels.²⁰⁷ Though these approaches have been proven effective, the work in this chapter follows an approach to targeted therapy that is perhaps more simplistic in which a cytotoxic species is merely carried to cancer cells using pharmacodelivery vehicles/ligands.²⁰⁸

Antibodies²⁰⁸ and polymers²⁰⁹ have been used to preferentially target sites of disease and, with conjugation to cytotoxic drugs, have helped deliver these cytotoxic payloads. Antibodies exhibit specificity to a respective target antigen, whereas polymers rely on the facilitation of enhanced accumulation within a tumor to mitigate undesired off-target toxicity. Another approach, the use of endogenous ligands, relies on the overexpression of a protein or enzyme in cancer cells.²⁰⁸ This can be exploited as a ligand for said protein or enzyme and can help transport a payload to the cancerous cell. There are a number of reported targets that are highly expressed in cancer cells yet with low expression in healthy cells. Some of these targets have ligands that can be used to differentiate between pathological and normal cells, *e.g.*, folate receptor proteins,²¹⁰ glucose transporter proteins,²¹¹ and estrogen receptor (ER) proteins.^{212,213} While the ligands for these examples are small molecules, it should be noted that the same strategy extends to analogous work for peptide,²¹⁴ aptamers,²¹⁵ and antibodies.²¹⁶

Borrowing from the practice of bioconjugation for appending small molecules to peptides, a number of methods can be employed to form a ligand-payload linkage through covalent bonding. Moreover, once a reaction has been selected to append these molecules of interest, the relative spacer length can be adjusted, and this has been shown to have a significant impact on the biological activity of the resulting material (**Figure 31**).^{217,218} There are

several common bioconjugation reactions, each requiring particular coupling partner functionalisation as shown in **Figure 32**.²¹⁹

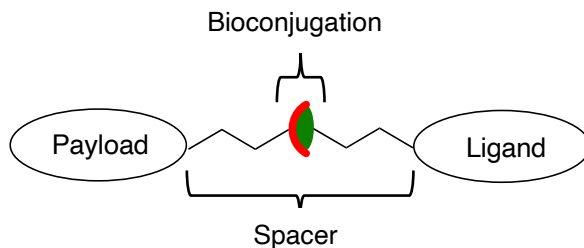


Figure 31. Bioconjugate cartoon highlighting all components.

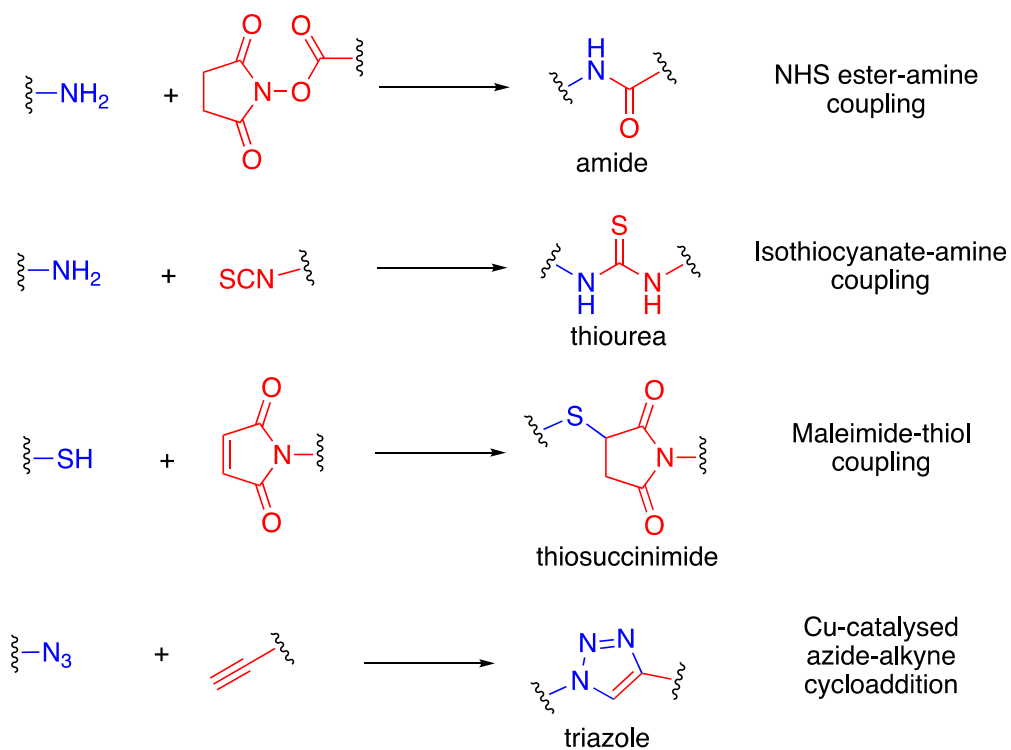


Figure 32. Examples of bioconjugation strategies.

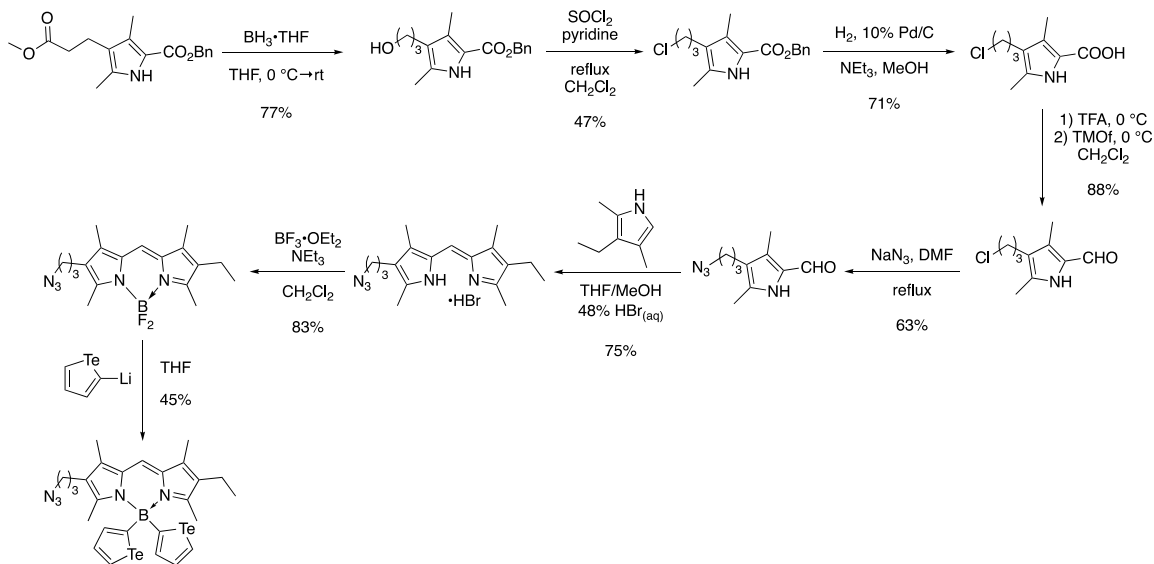
This chapter will discuss the design, synthesis, purification, and characterisation of a cytotoxic payload-appended to a ligand that is overexpressed in cancer cells.

5.2. Design Principles and Targets

With our success in optimising photosensitisers such as tellurophene-appended *F*-BODIPYs⁷⁵ and [*Te*]-BODIPYs,¹⁷¹ the next advancement for this project involves appending them to biological ligands as a strategy by which to target cancerous cells. While any of the bioconjugation strategies could be employed for this work, there is one method, the Nobel prize winning CuAAC reaction, that stands out as the powerhouse in bioconjugation reactions.²²⁰ Moreover, the CuAAC reaction was used recently in the Thompson group for bioconjugation chemistry for appending ligands to prodigiosenes.²²¹ Prodigiosenes, the synthetic analogue of the natural product prodigiosin, are a class of compounds that has been of great interest to the Thompson group for many years. Prodigiosenes have known anticancer properties,^{222,223} as well as other biological activities and, as such, previous Thompson group members have appended prodigiosenes to porphyrin,²²⁴ estrone,²²⁴ tamoxifen,^{221,224} estradiol^{221,225} and folate²²⁶ in attempts to increase the relative bioavailability of prodigiosenes. In one project, the aforementioned CuAAC reaction was used to form the first click-appended prodigiosene conjugates.²²¹ This conjugation approach, using estradiol as the targeting ligand, represented an approach that was deemed attractive for conjugating tellurophene-appended BODIPYs with a targeting biological ligand.

In this chapter, with the requisite azide coupling partner already in hand (**d4f**),¹⁹⁰ focus will centre on functionalisation of estradiol with an alkyne motif and subsequent conjugation with **d4f**. The reaction sequence towards compounds **d4f** is shown in **Scheme 12**. Estradiol is composed of four fused rings, and this framework is a core characteristic of the steroid

class of molecules (**Figure 33**). Moreover, estradiol is one of the major endogenous estrogens and is an agonist of the ER, a receptor that is overexpressed in certain types of cancers.²²⁷ There are many positions at which researchers have chosen to functionalise estradiol, but ideally this would occur at a position that does not negatively affect or inhibit the binding of estradiol to the ER.



Scheme 12. Synthetic route to compounds d4f.

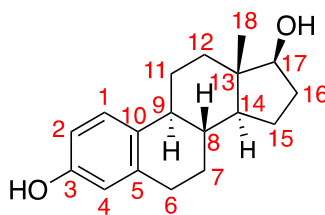


Figure 33. 17 β -Estradiol highlighting numbering.

Functionalisation at the phenolic position (3-position), *i.e.*, forming a propargyloxyphenyl analogue (**e1**, **Figure 34**), would be synthetically the most accessible. However, conjugation at this position is likely to affect binding to the ER. The natural ligand binds

to the ERs *via* hydrogen bonding, therefore substitution at the phenolic position will likely reduce binding affinity.^{228,229} Nevertheless, conjugation at this position will provide a system suitable for use as a proof-of-principle. Despite the many other intermolecular binding forces (London forces and dipole interactions) playing a role in binding, interrupting hydrogen bonding would likely have the most dramatic change in binding affinity. There are many examples in the literature that show functionalisation at the 11- and 7-positions, more specifically the 11 β - and 7 α -positions.^{228–231} For a multitude of reasons, the 11 β -position is synthetically more challenging to access than the 7 α -position; therefore, it was decided that conjugation at the phenolic position would be accompanied by attempts to conjugate at the 7 α -position, using an approach previously published by the Thompson group.²²¹ An alkynyl functionality would be introduced onto the 7 α -position of estradiol, ready for a reaction with an azide *via* the CuAAC reaction. This approach presents an opportunity to study the effect of linker chain lengths between estradiol and [Te]-BODIPY components. The alkyne functional group on estradiol can be appended using a propargyl reagent that has both an alkyl chain spacer and the ability to append it to estradiol. For this work, we envisioned using propargyl alkylating reagents with two different chain lengths (nine- and three-carbon chain). This would result in two propargyl-functionalised estradiols that would, when conjugated to **d4f**, result in the desired structures and feature nine- and three-carbon spacers between the ligand and the cytotoxic payload (**e2a** and **e2b**, respectively, **Figure 34**).

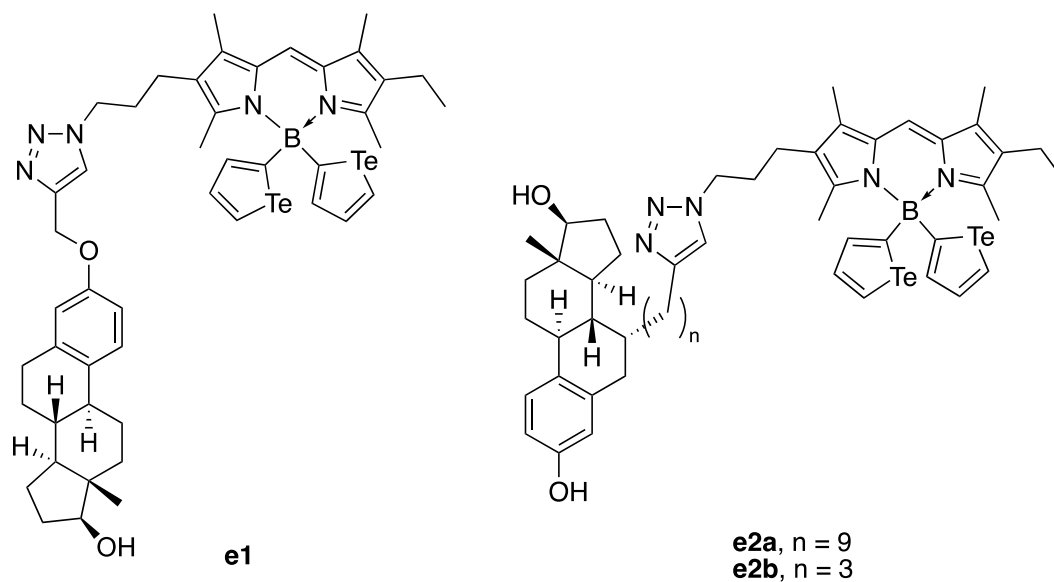
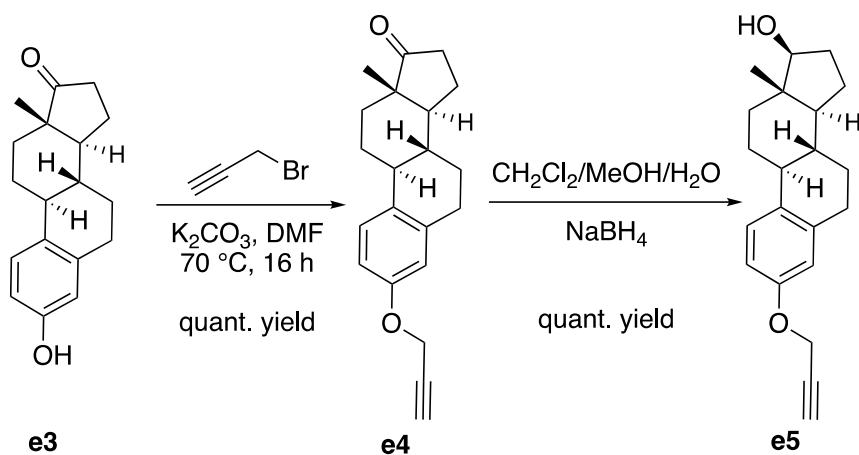


Figure 34. Estradiol-appended [Te]-BODIPY targets.

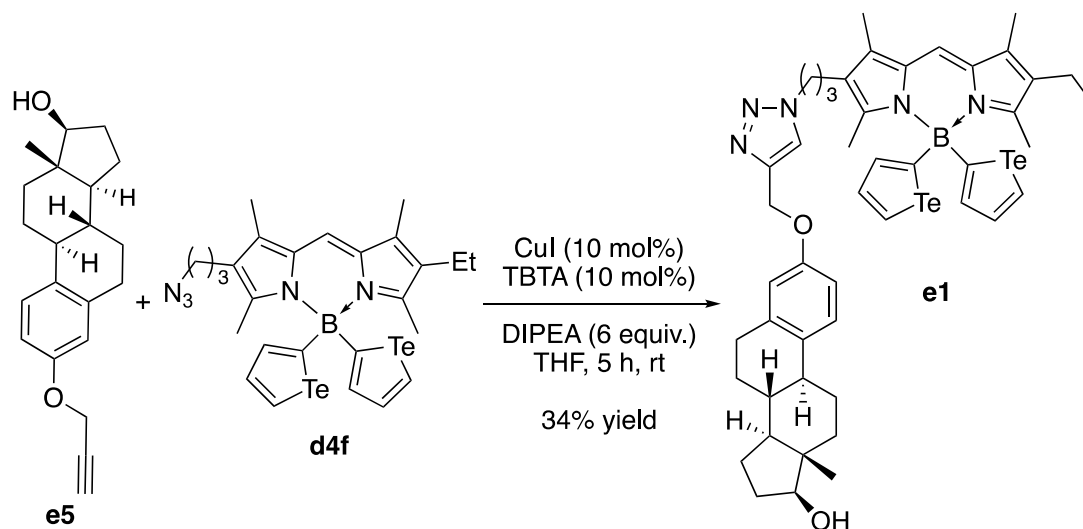
5.3. Discussion

As mentioned above, functionalisation at the phenolic position of estradiol can be achieved readily (**Scheme 13**). Following a literature procedure,²³² estrone (**e3**), which already has the C17 secondary alcohol protected as the carbonyl analogue, was reacted with propargyl bromide in the presence of potassium carbonate to form the propargyloxyphenyl analogue **e4** in quantitative yield with no purification required. Next, this species was reduced with sodium borohydride to produce the alkyne-appended estradiol **e5** in high yield.



Scheme 13. Synthesis of alkyne functionalised estradiol **e5**.

Next, with the requisite alkyne-functionalised estradiol **e5** in hand, the CuAAC coupling of this compound with the previously synthesised azide-functionalised *[Te]*-BODIPY **d4f** was attempted (Scheme 14). Following a literature procedure for similar substrates,²²¹ **e5** and **d4f** were reacted in the presence of copper iodide, tris(benzyltriazolylmethyl)amine and Hünig's base to afford the desired estradiol-appended *[Te]*-BODIPY **e1** in moderate yield after column chromatography. This compound was then shared with collaborators for evaluation of its ability to act as a targeted photosensitiser for breast cancer cells and other cells that over-express estrogen receptors.



Scheme 14. Synthesis of estradiol-appended [Te]-BODIPY **e1**.

With the successful synthesis of the first estradiol-appended [Te]-BODIPY, focus was then shifted to the synthesis of the targets featuring substitution at the 7 α -position. The synthetic sequence from estradiol (**Figure 33**) to the desired alkyne-functionalised estradiol (**Figure 35**) is not trivial. Although a propargyl alkylating motif can be employed to install the desired alkyne at the 7 α -position, the 7 α -position is not the most reactive position on estradiol. As such, the activation of the 7 α -position of estradiol is necessary. The reactive benzylic position (6-position, **Figure 33**) can be masked by oxidation to make a benzylic ketone and direct reactivity to the 7-position for subsequent steps.

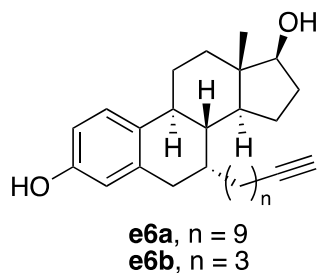
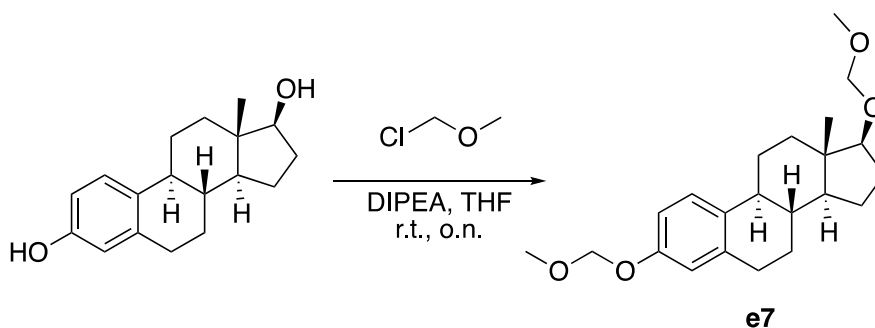


Figure 35. Target alkyne-functionalised estradiol.

Firstly, the two alcohol groups must be protected so that the alkylating agent will react preferentially at the 7-position. There are many different alcohol protecting groups (esters, silyl ethers, benzyl ethers, acetals, etc.); however, selecting a protecting group that is stable when needed yet labile when deprotection is required necessitates planning. Next, oxidation at the 6-position will ensure that subsequent reactivity occurs at the desired 7-position. Once alkylation at the 7-position is complete, the masking ketone can be reduced and the protecting groups on the alcohols removed.

The estradiol protecting group strategy of choice for previous work in the Thompson group involved the chloromethyl methyl ether (MOMCl) reagent.²²¹ In that work, estradiol was subjected to a large excess of MOMCl, along with Hünig's base in tetrahydrofuran and heated at reflux temperature overnight to afford the desired product in high yields and purity (**Scheme 15**). Unfortunately, MOMCl is now a controlled substance due to a contaminant in technical grade MOMCl, called bis(chloromethyl) ether, which is a highly carcinogenic molecule that causes lung cancer (likely *via* a mechanism of cross-linking cells).²³³ Even if we were able to source and accept the inherent risk in using this reagent, it is prohibitively expensive, and therefore other protecting group options were explored for this work.



Scheme 15. Alcohol protection of estradiol using MOMCl.

Protecting group stability tables were used to select suitable hydroxyl protecting groups that would be stable during our desired synthetic steps—yet labile when needed.²³⁴ These tables show that tetrahydropyranyl ethers (THP) and *tert*-butyldimethylsilyl ethers (TBS) share similar stabilities to that of MOM and as such are suitable candidates for protecting estradiol (**Figure 36**). Attempts were made towards the synthesis of THP- and TBS-protected estradiol. Despite many attempts and the use of various reaction conditions, the use of both of these protecting groups was ultimately abandoned as the desired protected estradiols were never evident in the purified reaction mixture. When discussing other protecting group strategies with Dr. Alex Speed (Dalhousie University Chemistry), a safer way to use MOMCl was suggested. Following a literature procedure used for similar substrates,²³⁵ MOMCl was generated *in situ* by reacting dimethoxymethane and acetyl chloride in the presence of zinc bromide in toluene. To this solution containing MOMCl, a solution of estradiol was charged *via* syringe, followed by *N,N*-diisopropylethylamine. After the reaction was deemed complete by TLC analysis, the reaction was quenched with a saturated aqueous ammonium chloride solution to ensure full decomposition of MOMCl. Column chromatography was performed to afford **e7** in good yield on a multigram scale.

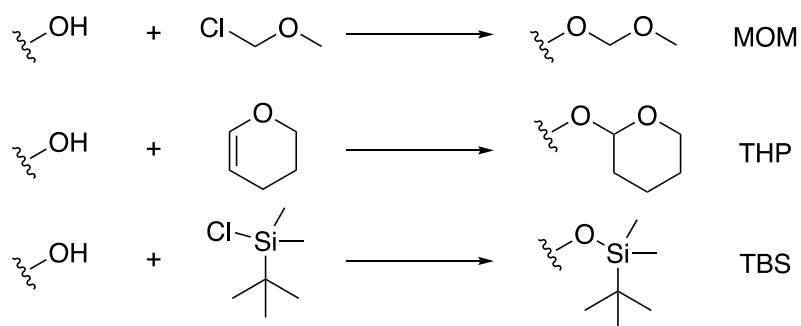
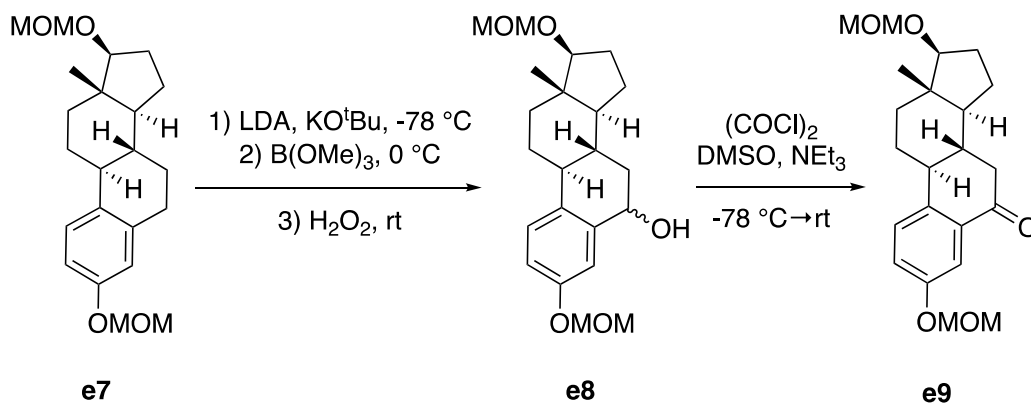


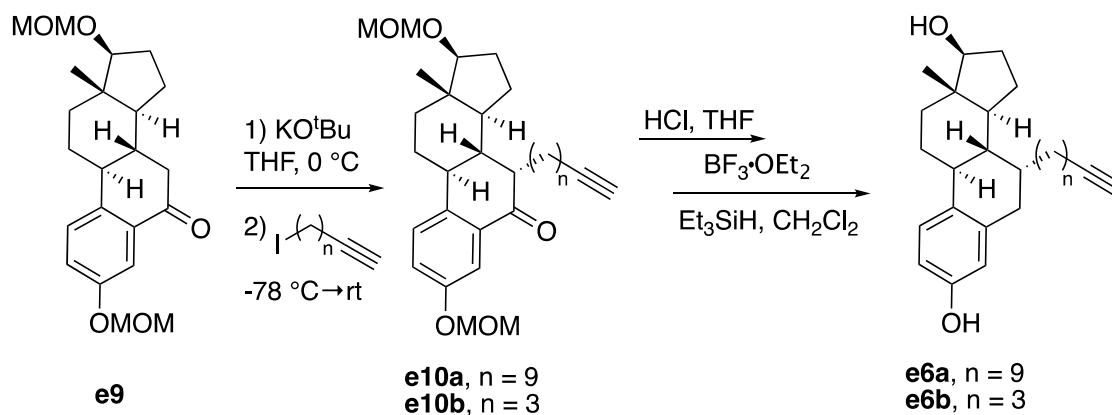
Figure 36. Protecting group strategies for C3 and C17 alcohol protection of estradiol.

With the MOM-protected estradiol **e7** in hand, the benzylic position was oxidised to an alcohol and subsequently oxidised again to a ketone (**Scheme 16**). A hydroboration oxidation was employed for the first oxidation. The borylation was achieved by first deprotonating the benzylic position using a mixture of bulky bases, lithium diisopropylamide (generated *in situ* from freshly distilled diisopropylamine and *n*-butyllithium) and potassium *tert*-butoxide. Oxidation with hydrogen peroxide gave compound **e8** in moderate yields after column chromatography. This compound was then oxidised, using a Swern oxidation procedure, to generate **e9** in good yields after column chromatography.

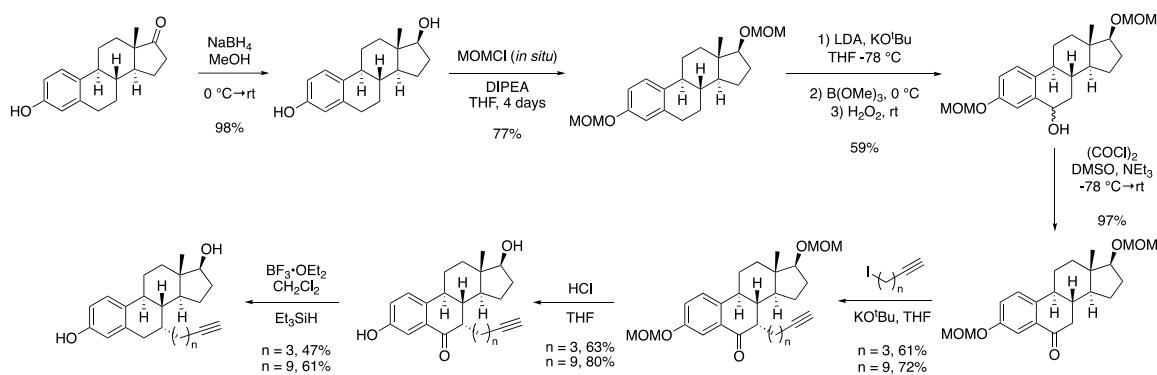


Scheme 16. Multistep oxidation of MOM-protected estradiol towards facilitation of reactivity at the 7-position.

With the alcohol groups protected and the benzylic position masked, **e9** then underwent alkylation with propargyl iodides bearing two different chain lengths. This was performed by cooling a THF solution containing **e9** via use of a liquid nitrogen/acetone bath before adding potassium *tert*-butoxide followed by the alkylating agent.²²¹ Products featuring nine- (**e10a**) and three-carbon chain spacers (**e10b**) were formed in moderate yield after column purification (**Scheme 17**). The MOM protecting groups on the alcohol are acid labile and were readily removed by stirring a solution of either **e10a** or **e10b** in THF/HCl at room temperature. Deprotection was achieved with full conversion, and without the need for purification of the afforded product. Next, the benzylic ketone was reduced *via* the use of triethylsilane in the presence of boron trifluoride diethyl etherate to afford the desired 7 α -functionalised alkyne estradiols with nine- (**e6a**) and three-carbon (**e6b**) chains as spacers. The reaction sequence towards compounds **e6a** and **e6b** is shown in **Scheme 18**.

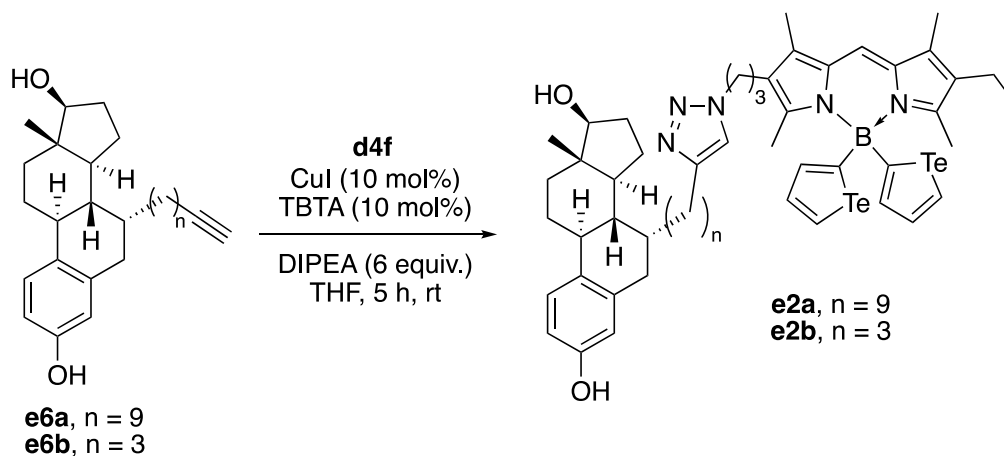


Scheme 17. Synthesis of estradiols appended with alkyne functionality at the 7 α -position.



Scheme 18. Synthetic route to compounds **e6a** and **e6b**.

With the requisite 7α -position alkyne-functionalised estradiols (**e6a** and **e6b**) in hand, the CuAAC coupling of these compounds with the previously synthesised azide-functionalised $[Te]$ -BODIPY **d4f** was attempted. Following a literature procedure for similar substrates,²²¹ the estradiols and **d4f** were reacted in the presence of copper iodide, tris(benzyltriazolylmethyl)amine (TBTA), and Hünig's base. The desired estradiol-appended $[Te]$ -BODIPY **e2a** ($n = 9$) and **e2b** ($n = 3$) were thus afforded in low yields after column chromatography. It should be noted that many precipitation procedures were required, following chromatography, in order to isolate the pure material (**Scheme 19**).



Scheme 19. Synthesis of 7α -position estradiol-appended $[Te]$ -BODIPY **e2a** and **e2b**.

The photophysical properties of these compounds were then evaluated and the results are summarised in **Table 7**. Furthermore, our collaborators studied important photophysical factors that are pertinent to photosensitisers such as singlet oxygen yield, photostability and cell viability. The molar absorptivity decreased for all estradiol-appended *[Te]*-BODIPY compounds, with respect to **4df**. This was expected as the appended estradiol contributes significantly to the molecular weight but does not contribute to the extent of the chromophoric unit. However, **e1** exhibited an increase in singlet oxygen production with respect to **4df**, whereas **e2a** and **e2b** exhibited a decrease. It was hypothesised that this observation might be attributed to the oxidative stability of the photosensitisers in the presence of singlet oxygen. However, when the photostability of this series was measured, all compounds proved stable over the timeframe of the experiment. Next, collaborators incubated two different cell lines with each photosensitiser and cell viabilities (cell death) were measured. Both cell lines are epithelial-like. However, one cell line, MCF7, is from human breast which has estradiol receptors while the other, MDA, does not. Our collaborators conducted a study in which the two cell lines were incubated with **e1**, **e2a**, or **e2b**, then either irradiated with light or analysed for cell viability directly after incubation. The purpose of this experiment was to evaluate the light versus dark toxicity of the photosensitisers and also determine if the photosensitisers were more toxic to cells that express estradiol receptors. Preliminary results for this work showed that these compounds have good dark versus light toxicity properties. However, there was no discernable difference in cell viability between the cell lines. From the initial IC₅₀ results it seems that **e1** and **e2b** were taken up by the cells; however, as evident by low cell death, it appears

that **e2a** is not cell permeable. Although these reports are disappointing, they serve to demonstrate that targeting was unsuccessful and that conjugation to another ligand is needed in order to overcome challenges with targeting.

Table 7. Photophysical data for estradiol-appended *[Te]*-BODIPYs in CH₂Cl₂ solution.

Compound	λ_{absmax} (nm)	ϵ (M ⁻¹ cm ⁻¹)	λ_{emmax} (nm)	S.S. (nm)	Φ_f	Φ_{Δ}^a
4df	526	60000	543	17	0.01	0.45
e1	526	47000	540	14	0.01	0.65
e2a	526	40000	539	13	0.01	0.38
e2b	526	40000	542	16	0.01	0.32

S.S., Stokes' shift; ^acalculated in 2% DMSO and MeOH

5.4. Experimental

Experimental works and supplementary data for this chapter can be found in Appendix E.

5.5. Chapter Conclusions and Future Perspectives

With the goal of synthesising a targeted chemotherapeutic drug, this work represents the continuation of previous photosensitisers systems. In this chapter the synthesis and characterisation of estradiol-appended *[Te]*-BODIPY photosensitisers is reported. The conjugation reaction employed to append the photosensitiser and ligand components was CuAAC coupling. The azide coupling partner was previously synthesised; however, alkyne functionalised estradiols were synthesised and discussed herein. Conjugation was achieved through the estradiol phenolic (C3) position as well as the more advantageous 7 α -position, the latter of which was appended using two linkers that differed in length. Through collaboration, the properties of these three photosensitisers were evaluated *in vitro* with cell lines that do and do not express ERs and results were compared. It was found that, similar to our other reported *[Te]*-BODIPYs, that the estradiol-appended *[Te]*-BODIPYs exhibit good light versus dark toxicities. However, the cytotoxicity exhibited in the ER-positive cell line was not superior to that observed in the MDA cell line.

From these initial findings it was hypothesised that the cause of poor selectivity is likely due to the transportation mechanism for the photosensitiser to get into the cell. Like all steroids, estrogens diffuse readily across the cell membrane *via* passive diffusion.²³⁶ Molecules will move from an area of high concentration to an area of low concentration; therefore, if a cell line has overexpressed ERs, then more ligand will diffuse into the cells.²³⁶ As the compounds discussed in this chapter exhibit similar cytotoxicities in ER-positive and ER-negative cell lines, appending this ligand to *[Te]*-BODIPYs was unsuccessful as a strategy by which to achieve targeted cytotoxicity.

To address this drug transportation concern, future work towards a *[Te]*-BODIPY targeted therapy drug should focus on appending ligands that enter cells *via* other mechanisms. Folic acid (**Figure 37**), for instance, is the endogenous ligand for the folate receptor protein and is transported into cells *via* an endocytosis mechanism.²³⁷ Folate receptor proteins, are over expressed in a number of epithelial cancers *e.g.*, breast, cervical, colorectal and ovarian.

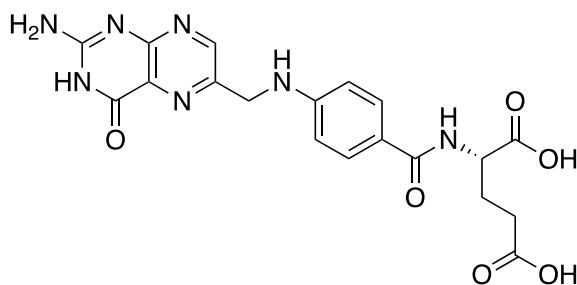


Figure 37. Chemical structure of folic acid.

There are several approaches towards functionalisation of folic acid for conjugation to drugs. A recent publication from the Thompson group²²⁶ attached prodigiosenes bearing folic acid *via* amide bond-forming reactions. This process is laborious in that folic acid has many reactive sites, that must be protected, in addition to the site of interest being activated. In the previous work, this was achieved *via* an approach that first removed the L-glutamic acid portion of folic acid. Installation of protecting and activating groups on both halves of the molecule the proceeded, before re-attaching the folic acid *via* amide bond. If this approach were to be attempted for this research, once the challenging steps to achieve the conjugation-ready folic acid were performed, a *[Te]*-BODIPY photosensitiser equipped with a linker ready for amide bond formation would also need to be synthesised. Once the

desired amide is achieved the protecting groups could be removed to afford a folic acid appended *[Te]*-BODIPY photosensitiser (**Figure 38**).

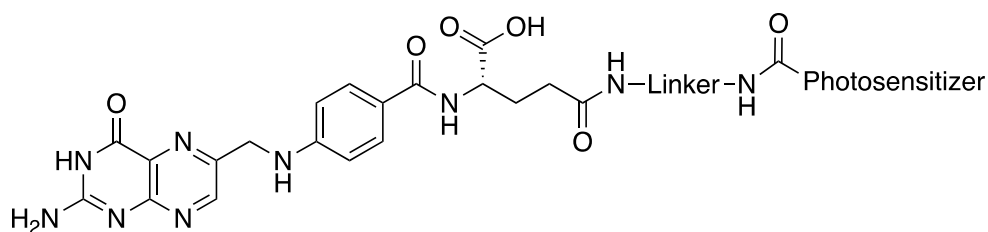


Figure 38. Potential target folic acid appended photosensitiser *via* amide bond forming reactions.

Considering our relative success to synthesise and utilise an azide functionalised *[Te]*-BODIPY for CuAAC conjugation, it would perhaps be less challenging to instead synthesise a folic acid that has alkyne functionality. Similar to amide bond conjugation, there are numerous reports of approaches to synthesise an alkyne-functionalised folic acid.^{238–240} Many of these involve laborious reactions to mask and activate specific positions. However, one report stands out as it presents a direct synthesis to afford an alkyne-containing folic acid in high yields with one amide reaction and without the need for reconstruction.²⁴¹ This procedure and CuAAC coupling, could be applicable to afford a folic acid appended *[Te]*-BODIPY photosensitiser (**Figure 39**). This target represents a potential targeted photosensitiser drug with a transportation mechanism that differs from our reported estradiol-appended *[Te]*-BODIPYs and may serve to improve the selectivity for this system.

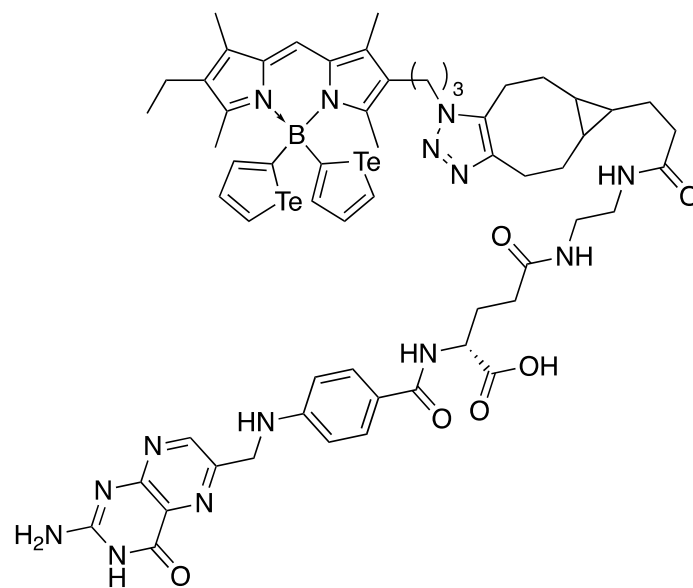


Figure 39. Potential target folic acid appended photosensitiser *via* CuAAC bond forming reactions.

Chapter 6. Overall Conclusions

The work described in this thesis, as a mixture of both reproduced manuscripts and non-published works, has focused on the development of tellurophene-appended BODIPYs. Various approaches were taken towards tellurophene-appended BODIPYs that exhibited a range of photochemical properties. Chapter 1 discussed pertinent information that led to the conceptualisation of this work, introduced relevant topics and outlined past work performed by previous Thompson-group members and others.

Chapter 2, which includes a reproduced manuscript, discussed the design, synthesis, and characterisation of a *meso*-aryl appended BODIPY. This first in class compound was shown to be a moderate photosensitiser ($\Phi_{\Delta} = 0.26 \pm 0.01$) and exhibit a moderate phototoxic index (~ 80). Moreover, mass cytometry studies were performed that confirmed the presence of Te within HeLa cells, further supporting the potential of tellurophene-appended BODIPYs as theragnostic agents. This chapter then discussed non-published work that aimed to address the low quantum yield of singlet oxygen that this system exhibited. This optimisation study remains unfinished as access to the desired compounds proved challenging—suggested future works relate to overcome these challenges.

Chapter 3, which includes a reproduced manuscript, discussed an alternative approach, *via* nucleophilic substitution at boron with lithiated tellurophene, for appending tellurophene to BODIPYs. The design, synthesis, and characterisation of this class of compound, dubbed *[Te]*-BODIPYs, was realised. Then, a series was established by extending to other

chalcogenophenes, *i.e.*, *[Se]*-, *[S]*- and *[O]*-BODIPY analogues, and trends were discussed with particular interest to the observed photochemical properties. As the mass of the chalcogenophenes appended to the BODIPY core increased, the compounds exhibited higher Φ_{Δ} . The *[Te]*-BODIPY example exhibited the highest quantum yield ($\Phi_{\Delta} = 0.68 \pm 0.08$) in the series and an improved phototoxic index (> 256) over the compound reported in Chapter 2. Suggested future works include preparation of *[E]*-BODIPYs appended through the β -position and further extending this series to include pyrroles such as *N*-H, *N*-Boc and *N*-Me examples.

Chapter 4, which includes a reproduced manuscript, discussed further development of the *[Te]*-BODIPY system by changing substituents on the BODIPY backbone. Notably, one example with an alkyl phenyl substituent in the *meso*-position exhibited impressive photosensitisation properties and the ability to induce the production of singlet oxygen ($\Phi_{\Delta} = 0.85 \pm 0.11$). Moreover, by virtue of an eight-fold increase in light toxicity, improvements in phototoxicity indices were demonstrated, *e.g.*, 2640 for one example. Other notable examples are *[Te]*-BODIPYs functionalised with substituents on the BODIPY backbone that can be exploited for further functionalisation, *i.e.*, azide and ester. Suggested future work to improve yields involves the conversion of *F*-BODIPYs to *Cl*-BODIPYs before reacting with lithiated tellurophene.

Chapter 5 discussed taking potent *[Te]*-BODIPY photosensitisers and incorporating functionality to selectively target cancer cells. A *[Te]*-BODIPY with an azide substituent on the BODIPY backbone was appended, *via* copper-catalysed azide-alkyne cycloaddition, to estradiols at various positions. Incorporation of the estradiol ligand was thought to make

the photosensitisers more toxic to cells which overexpress estrogen receptors, *i.e.*, MCF7 versus MCA breast cancer cells. Unfortunately, the cytotoxicity exhibited in the MCF7 (ER-positive) cell line was not superior to that observed in the MDA cell line. Citing selectivity issues related to cell transportation mechanisms, suggested future work involves the study of [*Te*]-BODIPYs appended to folates.

References

- (1) Ferreira, P. M. T.; Maia, H. L. S.; Monteiro, L. S. Synthesis of 2,3,5-Substituted Pyrrole Derivatives. *Tetrahedron Lett.* **2002**, *43* (25), 4491–4493.
- (2) Deidda, D.; Lampis, G.; Fioravanti, R.; Biava, M.; Porretta, G. C.; Zanetti, S.; Pompei, R. Bactericidal Activities of the Pyrrole Derivative BM212 against Multidrug-Resistant and Intramacrophagic *Mycobacterium Tuberculosis* Strains. *Antimicrob. Agents Chemother.* **1998**, *42* (11), 3035–3037.
- (3) Schaefer, E. J.; McNamara, J. R.; Asztalos, B. F.; Tayler, T.; Daly, J. A.; Gleason, J. L.; Seman, L. J.; Ferrari, A.; Rubenstein, J. J. Effects of Atorvastatin Versus Other Statins on Fasting and Postprandial C-Reactive Protein and Lipoprotein-Associated Phospholipase A2 in Patients With Coronary Heart Disease Versus Control Subjects. *Am. J. Cardiol.* **2005**, *95* (9), 1025–1032.
- (4) Leppert, W.; Zajackowska, R.; Wordliczek, J. The Role of Oxycodone/Naloxone in the Management of Patients with Pain and Opioid-Induced Constipation. *Expert Opin. Pharmacother.* **2019**, *20* (5), 511–522.
- (5) Vitaku, E.; Smith, D. T.; Njardarson, J. T. Analysis of the Structural Diversity, Substitution Patterns, and Frequency of Nitrogen Heterocycles among U.S. FDA Approved Pharmaceuticals: Miniperspective. *J. Med. Chem.* **2014**, *57* (24), 10257–10274.
- (6) Heravi, M. M.; Zadsirjan, V. Prescribed Drugs Containing Nitrogen Heterocycles: An Overview. *RSC Adv.* **2020**, *10* (72), 44247–44311.
- (7) Kue, C. S.; Ng, S. Y.; Voon, S. H.; Kamkaew, A.; Chung, L. Y.; Kiew, L. V.; Lee, H. B. Recent Strategies to Improve Boron Dipyrromethene (BODIPY) for Photodynamic Cancer Therapy: An Updated Review. *Photochem. Photobiol. Sci.* **2018**, *17* (11), 1691–1708.
- (8) Callaghan, S.; Senge, M. O. The Good, the Bad, and the Ugly – Controlling Singlet Oxygen through Design of Photosensitizers and Delivery Systems for Photodynamic Therapy. *Photochem. Photobiol. Sci.* **2018**, *17* (11), 1490–1514.

- (9) Jeelan Basha, N.; Basavarajaiah, S. M.; Shyamsunder, K. Therapeutic Potential of Pyrrole and Pyrrolidine Analogs: An Update. *Mol. Divers.* **2022**.
- (10) Rawat, P.; Gautam, A.; Singh, R. N. Synthesis, Spectral, Structural and Antimicrobial Activities of Ethyl-4-{-[-(1-(2-(4-Nitrobenzoyl)Hydrazono)Ethyl)]-3,5-Dimethyl-1H-Pyrrole-2-Carboxylate. *J. Mol. Struct.* **2022**, *1255*, 132405.
- (11) Zhdanova, K. A.; Savelyeva, I. O.; Ezhov, A. V.; Zhdanov, A. P.; Zhizhin, K. Yu.; Mironov, A. F.; Bragina, N. A.; Babayants, A. A.; Frolova, I. S.; Filippova, N. I.; Scliankina, N. N.; Scheglovitova, O. N. Novel Cationic Meso-Arylporphyrins and Their Antiviral Activity against HSV-1. *Pharmaceuticals* **2021**, *14* (3), 242.
- (12) Li Petri, G.; Spanò, V.; Spatola, R.; Holl, R.; Raimondi, M. V.; Barraja, P.; Montalbano, A. Bioactive Pyrrole-Based Compounds with Target Selectivity. *Eur. J. Med. Chem.* **2020**, *208*, 112783.
- (13) Jones, A.; Bean, G. The Chemistry of Pyrroles. In *Organic Chemistry: A Series of Monographs*; Academic Press: New York, NY, 1977; Vol. 34, pp 1–525.
- (14) Ram, V. J.; Sethi, A.; Nath, M.; Pratap, R. *The Chemistry of Heterocycles*; Elsevier Ltd: Amsterdam, 2017.
- (15) Hantzsch, A. Neue Bildungsweise von Pyrrolderivaten [New Methods of Forming Pyrrole Derivatives]. *Berichte Dtsch. Chem. Ges.* **1890**, *23* (1), 1474-1476.
- (16) Knorr, L. Synthese von Pyrrolderivaten [Synthesis of Pyrrole Derivatives]. *Berichte Dtsch. Chem. Ges.* **1884**, *17* (2), 1635–1642.
- (17) Paal, C. Ueber Die Derivate Des Acetophenonacetessigesters Und Des Acetylacetessigesters. *Berichte Dtsch. Chem. Ges.* **1884**, *17* (2), 2756–2767.
- (18) Knorr, L. Synthese von Furfuranderivaten Aus Dem Diacetbernsteinsäureester [Synthesis of Furan Derivatives from the [Diethyl] Ester of 2,3-Diacetyl-Succinic Acid]. *Berichte Dtsch. Chem. Ges.* **1884**, *17* (2), 2863–2870.
- (19) Oldenziel, O. H.; Van Leusen, D.; Van Leusen, A. M. Chemistry of Sulfonylmethyl Isocyanides. 13. A General One-Step Synthesis of Nitriles from Ketones Using Tosylmethyl Isocyanide. Introduction of a One-Carbon Unit. *J. Org. Chem.* **1977**, *42* (19), 3114–3118.

- (20) Amanullah, S.; Ghosh, C.; Dey, S. G.; Dey, A. Heme Proteins – Structure and Function. In *Fundamentals of Porphyrin Chemistry*; 2022; pp 709–742.
- (21) Wood, T. E.; Thompson, A. Advances in the Chemistry of Dipyrrins and Their Complexes. *Chem. Rev.* **2007**, *107* (5), 1831–1861.
- (22) Fischer, H.; Treibs, A.; Zeile, K. The Mechanism of Iron Introduction into Porphyrins and Isolation of Crystalline Hemes. *Z Physiol Chem* **1931**, *195*, 1–27.
- (23) Tram, K.; Yan, H.; Jenkins, H. A.; Vassiliev, S.; Bruce, D. The Synthesis and Crystal Structure of Unsubstituted 4,4-Difluoro-4-Bora-3a,4a-Diaza-s-Indacene (BODIPY). *Dyes Pigments* **2009**, *82* (3), 392–395.
- (24) Groves, B. R.; Crawford, S. M.; Lundrigan, T.; Matta, C. F.; Sowlati-Hashjin, S.; Thompson, A. Synthesis and Characterisation of the Unsubstituted Dipyrrin and 4,4-Dichloro-4-Bora-3a,4a-Diaza-s-Indacene: Improved Synthesis and Functionalisation of the Simplest BODIPY Framework. *Chem Commun* **2013**, *49* (8), 816–818.
- (25) Kataev, E. A.; Müller, C.; Kolesnikov, G. V.; Khrustalev, V. N. Guanidinium-Based Artificial Receptors for Binding Orthophosphate in Aqueous Solution: Guanidinium-Based Artificial Receptors for Binding Orthophosphate. *Eur. J. Org. Chem.* **2014**, *2014* (13), 2747–2753.
- (26) Swavey, S.; DeBeer, M.; Li, K. Photoinduced Interactions of Supramolecular Ruthenium(II) Complexes with Plasmid DNA: Synthesis and Spectroscopic, Electrochemical, and DNA Photocleavage Studies. *Inorg. Chem.* **2015**, *54* (7), 3139–3147.
- (27) Singh, R. N.; Rawat, P.; Kumar, A.; Kant, P.; Srivastava, A. Spectral Analysis, Chemical Reactivity and First Hyperpolarizability Evaluation of a Novel 1,9-Bis(2-Cyano-2-Ethoxycarbonylvinyl)-5-(2-Furyl)-Dipyrrromethane: Experimental and Theoretical Approaches. *Spectrosc. Lett.* **2015**, *48* (4), 235–250.
- (28) Mahanta, S. P.; Panda, P. K. 5,10-Diacetylcalix[4]Pyrroles: Synthesis and Anion Binding Studies. *Org Biomol Chem* **2014**, *12* (2), 278–285.
- (29) Esipova, T. V.; Vinogradov, S. A. Synthesis of Phosphorescent Asymmetrically π -Extended Porphyrins for Two-Photon Applications. *J. Org. Chem.* **2014**, *79* (18), 8812–8825.

- (30) MacDonald, S.; Bullock, E.; Arsenault, G. Pyrromethanes and Porphyrins Therefrom. *J. Am. Chem. Soc.* **1960**, *82* (16), 4384–4389.
- (31) Kreuzer, F.-H.; Treibs, A. Difluorboryl-Komplexe von Di- Und Tripyrrylmethenen. *Eur. J. Org. Chem.* **1968**, *718* (1), 208–223.
- (32) Sakamoto, R.; Iwashima, T.; Tsuchiya, M.; Toyoda, R.; Matsuoka, R.; Kögel, J. F.; Kusaka, S.; Hoshiko, K.; Yagi, T.; Nagayama, T.; Nishihara, H. New Aspects in Bis and Tris(Dipyrinato)Metal Complexes: Bright Luminescence, Self-Assembled Nanoarchitectures, and Materials Applications. *J. Mater. Chem. A* **2015**, *3* (30), 15357–15371.
- (33) Goze, C.; Ulrich, G.; Mallon, L. J.; Allen, B. D.; Harriman, A.; Ziessel, R. Synthesis and Photophysical Properties of Borondipyrromethene Dyes Bearing Aryl Substituents at the Boron Center. *J. Am. Chem. Soc.* **2006**, *128* (31), 10231–10239.
- (34) Bonardi, L.; Ulrich, G.; Ziessel, R. Tailoring the Properties of Boron–Dipyrromethene Dyes with Acetylenic Functions at the 2,6,8 and 4-B Substitution Positions. *Org. Lett.* **2008**, *10* (11), 2183–2186.
- (35) Ziessel, R.; Goze, C.; Ulrich, G. Design and Synthesis of Alkyne-Substituted Boron in Dipyrromethene Frameworks. *Synthesis* **2007**, *6*, 936.
- (36) Sánchez-Carnerero, E. M.; Moreno, F.; Maroto, B. L.; Agarrabeitia, A. R.; Ortiz, M. J.; Vo, B. G.; Muller, G.; Moya, S. de la. Circularly Polarized Luminescence by Visible-Light Absorption in a Chiral *O*-BODIPY Dye: Unprecedented Design of CPL Organic Molecules from Achiral Chromophores. *J. Am. Chem. Soc.* **2014**, *136* (9), 3346–3349.
- (37) Lundrigan, T.; Crawford, S. M.; Cameron, T. S.; Thompson, A. *Cl*-BODIPYs: A BODIPY Class Enabling Facile B-Substitution. *Chem Commun* **2012**, *48* (7), 1003–1005.
- (38) Kee, H. L.; Kirmaier, C.; Yu, L.; Thamyongkit, P.; Youngblood, W. J.; Calder, M. E.; Ramos, L.; Noll, B. C.; Bocian, D. F.; Scheidt, W. R.; Birge, R. R.; Lindsey, J. S.; Holten, D. Structural Control of the Photodynamics of Boron–Dipyrin Complexes. *J. Phys. Chem. B* **2005**, *109* (43), 20433–20443.

- (39) Wagner, R. W.; Lindsey, J. S. Boron-Dipyrromethene Dyes for Incorporation in Synthetic Multi-Pigment Light-Harvesting Arrays. *Pure Appl. Chem.* **1996**, *68* (7), 1373–1380.
- (40) Wang, H.; Fronczek, F. R.; Vicente, M. G. H.; Smith, K. M. Functionalization of 3,5,8-Trichlorinated BODIPY Dyes. *J. Org. Chem.* **2014**, *79* (21), 10342–10352.
- (41) Rohand, T.; Qin, W.; Boens, N.; Dehaen, W. Palladium-Catalyzed Coupling Reactions for the Functionalization of BODIPY Dyes with Fluorescence Spanning the Visible Spectrum. *Eur. J. Org. Chem.* **2006**, *2006* (20), 4658–4663.
- (42) Leen, V.; Leemans, T.; Boens, N.; Dehaen, W. 2- and 3-Monohalogenated BODIPY Dyes and Their Functionalized Analogues: Synthesis and Spectroscopy. *Eur. J. Org. Chem.* **2011**, *2011* (23), 4386–4396.
- (43) Loudet, A.; Burgess, K. BODIPY Dyes and Their Derivatives: Syntheses and Spectroscopic Properties. *Chem. Rev.* **2007**, *107* (11), 4891–4932.
- (44) Yee, M.; Fas, S. C.; Stohlmeyer, M. M.; Wandless, T. J.; Cimprich, K. A. A Cell-Permeable, Activity-Based Probe for Protein and Lipid Kinases. *J. Biol. Chem.* **2005**, *280* (32), 29053–29059.
- (45) Katayama, M.; Nakane, R.; Matsuda, Y.; Kaneko, S.; Hara, I.; Sato, H. Determination of Progesterone and 17-Hydroxyprogesterone by High Performance Liquid Chromatography after Pre-Column Derivatization with 4,4-Difluoro-5,7-Dimethyl-4-Bora-3a,4a-Diaza-s-Indacene-3-Propionohydrazide. *The Analyst* **1998**, *123* (11), 2339–2342.
- (46) Triefflinger, C.; Rurack, K.; Daub, J. “Turn ON/OFF Your LOV Light”: Borondipyrromethene-Flavin Dyads as Biomimetic Switches Derived from the LOV Domain. *Angew. Chem. Int. Ed.* **2005**, *44* (15), 2288–2291.
- (47) Golovkova, T. A.; Kozlov, D. V.; Neckers, D. C. Synthesis and Properties of Novel Fluorescent Switches. *J. Org. Chem.* **2005**, *70* (14), 5545–5549.
- (48) Baki, C. N.; Akkaya, E. U. Boradiazaindacene-Appended Calix[4]Arene: Fluorescence Sensing of pH Near Neutrality. *J. Org. Chem.* **2001**, *66* (4), 1512–1513.

- (49) Turfan, B.; Akkaya, E. U. Modulation of Boradiazaindacene Emission by Cation-Mediated Oxidative PET. *Org. Lett.* **2002**, *4* (17), 2857–2859.
- (50) DiCesare, N.; Lakowicz, J. R. Fluorescent Probe for Monosaccharides Based on a Functionalized Boron-Dipyrromethene with a Boronic Acid Group. *Tetrahedron Lett.* **2001**, *42* (52), 9105–9108.
- (51) Zhang, X.; Wang, H.; Li, J.-S.; Zhang, H.-S. Development of a Fluorescent Probe for Nitric Oxide Detection Based on Difluoroboradiaza-s-Indacene Fluorophore. *Anal. Chim. Acta* **2003**, *481* (1), 101–108.
- (52) Louie, A. Multimodality Imaging Probes: Design and Challenges. *Chem. Rev.* **2010**, *110* (5), 3146–3195.
- (53) Townsend, D. W.; Beyer, T.; Blodgett, T. M. PET/CT Scanners: A Hardware Approach to Image Fusion. *Semin. Nucl. Med.* **2003**, *33* (3), 193–204.
- (54) Cherry, S.; Louie, A.; Jacobs, R. The Integration of Positron Emission Tomography With Magnetic Resonance Imaging. *Proc. IEEE* **2008**, *96* (3), 416–438.
- (55) Schlemmer, H.-P.; Pichler, B.; Schmand, M.; Burbar, Z.; Michel, C.; Ladebeck, R.; Jattke, K.; Townsend, D.; Nahmias, C.; Jacob, P.; Heiss, W.-D.; Claussen, C. Simultaneous MRI/PET Imaging of the Human Brain: Feasibility Study. *Radiology* **2008**, *248* (3), 1028–1035.
- (56) Al-Jaml, W.; Kostarelos, K. Liposome-Nanoparticle Hybrids for Multimodal Diagnostic and Therapeutic Applications. *Nanomed.* **2007**, *2* (1), 85–98.
- (57) Zheng, J.; Muhanna, N.; De Souza, R.; Wada, H.; Chan, H.; Akens, M. K.; Anayama, T.; Yasufuku, K.; Serra, S.; Irish, J.; Allen, C.; Jaffray, D. A Multimodal Nano Agent for Image-Guided Cancer Surgery. *Biomaterials* **2015**, *67*, 160–168.
- (58) Zheng, J.; Liu, J.; Dunne, M.; Jaffray, D. A.; Allen, C. In Vivo Performance of a Liposomal Vascular Contrast Agent for CT and MR-Based Image Guidance Applications. *Pharm. Res.* **2007**, *24* (6), 1193–1201.
- (59) Chan, W. C. Quantum Dot Bioconjugates for Ultrasensitive Nonisotopic Detection. *Science* **1998**, *281* (5385), 2016–2018.

- (60) Bruchez Jr., M. Semiconductor Nanocrystals as Fluorescent Biological Labels. *Science* **1998**, *281* (5385), 2013–2016.
- (61) Wu, X.; Liu, H.; Liu, J.; Haley, K. N.; Treadway, J. A.; Larson, J. P.; Ge, N.; Peale, F.; Bruchez, M. P. Immunofluorescent Labeling of Cancer Marker Her2 and Other Cellular Targets with Semiconductor Quantum Dots. *Nat. Biotechnol.* **2003**, *21* (1), 41–46.
- (62) Dubertret, B. In Vivo Imaging of Quantum Dots Encapsulated in Phospholipid Micelles. *Science* **2002**, *298* (5599), 1759–1762.
- (63) Jaiswal, J. K.; Mattoussi, H.; Mauro, J. M.; Simon, S. M. Long-Term Multiple Color Imaging of Live Cells Using Quantum Dot Bioconjugates. *Nat. Biotechnol.* **2003**, *21* (1), 47–51.
- (64) Banerjee, S. S.; Chen, D.-H. A Multifunctional Magnetic Nanocarrier Bearing Fluorescent Dye for Targeted Drug Delivery by Enhanced Two-Photon Triggered Release. *Nanotechnology* **2009**, *20* (18), 185103.
- (65) Maxwell, D. J.; Bonde, J.; Hess, D. A.; Hohm, S. A.; Lahey, R.; Zhou, P.; Creer, M. H.; Piwnicka-Worms, D.; Nolte, J. A. Fluorophore-Conjugated Iron Oxide Nanoparticle Labeling and Analysis of Engrafting Human Hematopoietic Stem Cells. *Stem Cells* **2008**, *26* (2), 517–524.
- (66) Min Yeo, K.; Ji Gao, C.; Ahn, K.-H.; Su Lee, I. Superparamagnetic Iron Oxide Nanoparticles with Photoswitchable Fluorescence. *Chem. Commun.* **2008**, No. 38, 4622.
- (67) Tu, C.; Osborne, E. A.; Louie, A. Y. Synthesis and Characterization of a Redox- and Light-Sensitive MRI Contrast Agent. *Tetrahedron* **2009**, *65* (7), 1241–1246.
- (68) Uzgiris, E. E.; Sood, A.; Bove, K.; Grimmond, B.; Lee, D.; Lomnes, S. A Multimodal Contrast Agent for Preoperative MR Imaging and Intraoperative Tumor Margin Delineation. *Technol. Cancer Res. Treat.* **2006**, *5* (4), 301–309.
- (69) Pandey, S. K.; Gryshuk, A. L.; Sajjad, M.; Zheng, X.; Chen, Y.; Abouzeid, M. M.; Morgan, J.; Charamisinau, I.; Nabi, H. A.; Oseroff, A.; Pandey, R. K. Multimodality Agents for Tumor Imaging (PET, Fluorescence) and Photodynamic Therapy. A Possible “See and Treat” Approach. *J. Med. Chem.* **2005**, *48* (20), 6286–6295.

- (70) Bhushan, K. R.; Misra, P.; Liu, F.; Mathur, S.; Lenkinski, R. E.; Frangioni, J. V. Detection of Breast Cancer Microcalcifications Using a Dual-Modality SPECT/NIR Fluorescent Probe. *J. Am. Chem. Soc.* **2008**, *130* (52), 17648–17649.
- (71) Mishra, A.; Pfeuffer, J.; Mishra, R.; Engelmann, J.; Mishra, A. K.; Ugurbil, K.; Logothetis, N. K. A New Class of Gd-Based DO3A-Ethylamine-Derived Targeted Contrast Agents for MR and Optical Imaging. *Bioconjug. Chem.* **2006**, *17* (3), 773–780.
- (72) Hüber, M. M.; Staubli, A. B.; Kustedjo, K.; Gray, M. H. B.; Shih, J.; Fraser, S. E.; Jacobs, R. E.; Meade, T. J. Fluorescently Detectable Magnetic Resonance Imaging Agents. *Bioconjug. Chem.* **1998**, *9* (2), 242–249.
- (73) Meyer, D.; Schaefer, M.; Bommemain, B. Gd-DOTA, A Potential MRI Contrast Agent: Current Status of Physicochemical Knowledge. *Investigative Radiol.* **1988**, *23* (1), 232–235.
- (74) Li, C.; Wang, G.; Qi, J.; Cherry, S. Three-Dimensional Fluorescence Optical Tomography in Small-Animal Imaging Using Simultaneous Positron-Emission-Tomography. *Opt. Lett.* **2009**, *34* (19), 2933–2935.
- (75) Campbell, J. W.; Tung, M. T.; Diaz-Rodriguez, R. M.; Robertson, K. N.; Beharry, A. A.; Thompson, A. Introducing the Tellurophene-Appended BODIPY: PDT Agent with Mass Cytometry Tracking Capabilities. *ACS Med. Chem. Lett.* **2021**, *12* (12), 1925–1931.
- (76) Kwiatkowski, S.; Knap, B.; Przystupski, D.; Saczko, J.; Kędzierska, E.; Knap-Czop, K.; Kotlińska, J.; Michel, O.; Kotowski, K.; Kulbacka, J. Photodynamic Therapy – Mechanisms, Photosensitizers and Combinations. *Biomed. Pharmacother.* **2018**, *106*, 1098–1107.
- (77) Dougherty, T. J.; Gomer, C. J.; Henderson, B. W.; Jori, G.; Kessel, D.; Korbelik, M.; Moan, J.; Peng, Q. Photodynamic Therapy. *J. Natl. Cancer Inst.* **1998**, *90* (12), 17.
- (78) Gunaydin, G.; Gedik, M. E.; Ayan, S. Photodynamic Therapy—Current Limitations and Novel Approaches. *Front. Chem.* **2021**, *9*, 691697.

- (79) Stolik, S.; Delgado, J. A.; Pérez, A.; Anasagasti, L. Measurement of the Penetration Depths of Red and near Infrared Light in Human “Ex Vivo” Tissues. *J. Photochem. Photobiol. B* **2000**, *57* (2–3), 90–93.
- (80) Vaupel, P.; Thews, O.; Hoeckel, M. Treatment Resistance of Solid Tumors. *Med. Oncol.* **2001**, *18* (4), 243–260.
- (81) Gorman, A.; Killoran, J.; O’Shea, C.; Kenna, T.; Gallagher, W. M.; O’Shea, D. F. In Vitro Demonstration of the Heavy-Atom Effect for Photodynamic Therapy. *J. Am. Chem. Soc.* **2004**, *126* (34), 10619–10631.
- (82) Leonard, K. A.; Nelen, M. I.; Anderson, L. T.; Gibson, S. L.; Hilf, R.; Detty, M. R. 2,4,6-Triarylchalcogenopyrylium Dyes Related in Structure to the Antitumor Agent AA1 as in Vitro Sensitizers for the Photodynamic Therapy of Cancer. *J. Med. Chem.* **1999**, *42* (19), 3942–3952.
- (83) Bendall, S. C.; Nolan, G. P.; Roederer, M.; Chattopadhyay, P. K. A Deep Profiler’s Guide to Cytometry. *Trends Immunol.* **2012**, *33* (7), 323–332.
- (84) Crowley, L. C.; Marfell, B. J.; Scott, A. P.; Waterhouse, N. J. Quantitation of Apoptosis and Necrosis by Annexin V Binding, Propidium Iodide Uptake, and Flow Cytometry. *Cold Spring Harb. Protoc.* **2016**, *2016* (11), pdb.prot087288.
- (85) Park, H.; Edgar, L. J.; Lumba, M. A.; Willis, L. M.; Nitz, M. Organotellurium Scaffolds for Mass Cytometry Reagent Development. *Org. Biomol. Chem.* **2015**, *13* (25), 7027–7033.
- (86) Bassan, J.; Willis, L. M.; Vellanki, R. N.; Nguyen, A.; Edgar, L. J.; Wouters, B. G.; Nitz, M. TePhe, a Tellurium-Containing Phenylalanine Mimic, Allows Monitoring of Protein Synthesis in Vivo with Mass Cytometry. *Proc. Natl. Acad. Sci.* **2019**, *116* (17), 8155–8160.
- (87) Lou, X.; Zhang, G.; Herrera, I.; Kinach, R.; Ornatsky, O.; Baranov, V.; Nitz, M.; Winnik, M. A. Polymer-Based Elemental Tags for Sensitive Bioassays. *Angew. Chem. Int. Ed.* **2007**, *46* (32), 6111–6114.
- (88) Spitzer, M. H.; Nolan, G. P. Mass Cytometry: Single Cells, Many Features. *Cell* **2016**, *165* (4), 780–791.

- (89) Edgar, L. J.; Vellanki, R. N.; McKee, T. D.; Hedley, D.; Wouters, B. G.; Nitz, M. Isotopologous Organotellurium Probes Reveal Dynamic Hypoxia In Vivo with Cellular Resolution. *Angew. Chem. Int. Ed.* **2016**, *55* (42), 13159–13163.
- (90) Edgar, L. J.; Vellanki, R. N.; Halupa, A.; Hedley, D.; Wouters, B. G.; Nitz, M. Identification of Hypoxic Cells Using an Organotellurium Tag Compatible with Mass Cytometry. *Angew. Chem. Int. Ed.* **2014**, *53* (43), 11473–11477.
- (91) Ba, L. A.; Döring, M.; Jamier, V.; Jacob, C. Tellurium: An Element with Great Biological Potency and Potential. *Org. Biomol. Chem.* **2010**, *8* (19), 4203.
- (92) Yarema, M. C. Acute Tellurium Toxicity From Ingestion of Metal-Oxidizing Solutions. *PEDIATRICS* **2005**, *116* (2), e319–e321.
- (93) C. Hoover, G.; S. Seferos, D. Photoactivity and Optical Applications of Organic Materials Containing Selenium and Tellurium. *Chem. Sci.* **2019**, *10* (40), 9182–9188.
- (94) Palao, E.; Slanina, T.; Klán, P. Construction of the Carbon–Chalcogen (S, Se, Te) Bond at the 2,6-Positions of BODIPY via Stille Cross-Coupling Reaction. *Chem. Commun.* **2016**, *52* (80), 11951–11954.
- (95) Peña-Cabrera, E.; Aguilar-Aguilar, A.; González-Domínguez, M.; Lager, E.; Zamudio-Vázquez, R.; Godoy-Vargas, J.; Villanueva-García, F. Simple, General, and Efficient Synthesis of Meso-Substituted Borondipyrromethenes from a Single Platform. *Org. Lett.* **2007**, *9* (20), 3985–3988.
- (96) Gupta, N.; Reja, S. I.; Bhalla, V.; Gupta, M.; Kaur, G.; Kumar, M. A Bodipy Based Fluorescent Probe for Evaluating and Identifying Cancer, Normal and Apoptotic C6 Cells on the Basis of Changes in Intracellular Viscosity. *J. Mater. Chem. B* **2016**, *4* (11), 1968–1977.
- (97) Hu, R.; Gómez-Durán, C. F. A.; Lam, J. W. Y.; Belmonte-Vázquez, J. L.; Deng, C.; Chen, S.; Ye, R.; Peña-Cabrera, E.; Zhong, Y.; Wong, K. S.; Tang, B. Z. Synthesis, Solvatochromism, Aggregation-Induced Emission and Cell Imaging of Tetraphenylethene-Containing BODIPY Derivatives with Large Stokes Shifts. *Chem. Commun.* **2012**, *48* (81), 10099.

- (98) Manjare, S. T.; Kim, Y.; Churchill, D. G. Selenium- and Tellurium-Containing Fluorescent Molecular Probes for the Detection of Biologically Important Analytes. *Acc. Chem. Res.* **2014**, *47* (10), 2985–2998.
- (99) Farfán-Paredes, M.; González-Antonio, O.; Tahuilan-Anguiano, D. E.; Peón, J.; Ariza, A.; Lacroix, P. G.; Santillan, R.; Farfán, N. Physicochemical and Computational Insight of ^{19}F NMR and Emission Properties of *Meso*-(*o*-Aryl)-BODIPYs. *New J. Chem.* **2020**, *44* (45), 19459–19471.
- (100) Watley, R. L.; Awuah, S. G.; Bio, M.; Cantu, R.; Gobeze, H. B.; Nesterov, V. N.; Das, S. K.; D'Souza, F.; You, Y. Dual Functioning Thieno-Pyrrole Fused BODIPY Dyes for NIR Optical Imaging and Photodynamic Therapy: Singlet Oxygen Generation without Heavy Halogen Atom Assistance. *Chem. - Asian J.* **2015**, *10* (6), 1335–1343.
- (101) Werner, T.; Huber, C.; Heintl, S.; Kollmannsberger, M.; Daub, J.; Wolfbeis, O. S. Novel Optical pH-Sensor Based on a Boradiaza-Indacene Derivative. *Fresenius J. Anal. Chem.* **1997**, *359* (2), 150–154.
- (102) Qi, X.; Jun, E. J.; Xu, L.; Kim, S.-J.; Joong Hong, J. S.; Yoon, Y. J.; Yoon, J. New BODIPY Derivatives as OFF–ON Fluorescent Chemosensor and Fluorescent Chemodosimeter for Cu^{2+} : Cooperative Selectivity Enhancement toward Cu^{2+} . *J. Org. Chem.* **2006**, *71* (7), 2881–2884.
- (103) Bricks, J. L.; Kovalchuk, A.; Trieflinger, C.; Nofz, M.; Büschel, M.; Tolmachev, A. I.; Daub, J.; Rurack, K. On the Development of Sensor Molecules That Display Fe^{III} -Amplified Fluorescence. *J. Am. Chem. Soc.* **2005**, *127* (39), 13522–13529.
- (104) Wu, Y.; Peng, X.; Guo, B.; Fan, J.; Zhang, Z.; Wang, J.; Cui, A.; Gao, Y. Boron Dipyrromethene Fluorophore Based Fluorescence Sensor for the Selective Imaging of $\text{Zn}(\text{II})$ in Living Cells. *Org. Biomol. Chem.* **2005**, *3* (8), 1387.
- (105) Wang, J.; Qian, X. A Series of Polyamide Receptor Based PET Fluorescent Sensor Molecules: Positively Cooperative Hg^{2+} Ion Binding with High Sensitivity. *Org. Lett.* **2006**, *8* (17), 3721–3724.
- (106) Brückl, T.; Baxter, R. D.; Ishihara, Y.; Baran, P. S. Innate and Guided C–H Functionalization Logic. *Acc. Chem. Res.* **2012**, *45* (6), 826–839.

- (107) Zhao, N.; Xuan, S.; Fronczek, F. R.; Smith, K. M.; Vicente, M. G. H. Stepwise Polychlorination of 8-Chloro-BODIPY and Regioselective Functionalization of 2,3,5,6,8-Pentachloro-BODIPY. *J. Org. Chem.* **2015**, *80* (16), 8377–8383.
- (108) Leen, V.; Yuan, P.; Wang, L.; Boens, N.; Dehaen, W. Synthesis of *Meso* - Halogenated BODIPYs and Access to *Meso* -Substituted Analogues. *Org. Lett.* **2012**, *14* (24), 6150–6153.
- (109) Savoldelli, A.; Meng, Q.; Paolesse, R.; Fronczek, F. R.; Smith, K. M.; Vicente, M. G. H. Tetrafluorobenzo-Fused BODIPY: A Platform for Regioselective Synthesis of BODIPY Dye Derivatives. *J. Org. Chem.* **2018**, *83* (12), 6498–6507.
- (110) Ortiz, M. J.; Agarrabeitia, A. R.; Duran-Sampedro, G.; Bañuelos Prieto, J.; Lopez, T. A.; Massad, W. A.; Montejano, H. A.; García, N. A.; Lopez Arbeloa, I. Synthesis and Functionalization of New Polyhalogenated BODIPY Dyes. Study of Their Photophysical Properties and Singlet Oxygen Generation. *Tetrahedron* **2012**, *68* (4), 1153–1162.
- (111) Zhao, N.; Xuan, S.; Byrd, B.; Fronczek, F. R.; Smith, K. M.; Vicente, M. G. H. Synthesis and Regioselective Functionalization of Perhalogenated BODIPYs. *Org. Biomol. Chem.* **2016**, *14* (26), 6184–6188.
- (112) Prusty, D. K.; Herrmann, A. A Fluorogenic Reaction Based on Heavy-Atom Removal for Ultrasensitive DNA Detection. *J. Am. Chem. Soc.* **2010**, *132* (35), 12197–12199.
- (113) Gai, L.; Mack, J.; Lu, H.; Yamada, H.; Kuzuhara, D.; Lai, G.; Li, Z.; Shen, Z. New 2,6-Distyryl-Substituted BODIPY Isomers: Synthesis, Photophysical Properties, and Theoretical Calculations. *Chem. - Eur. J.* **2014**, *20* (4), 1091–1102.
- (114) Leen, V.; Miscoria, D.; Yin, S.; Filarowski, A.; Molisho Ngongo, J.; Van der Auweraer, M.; Boens, N.; Dehaen, W. 1,7-Disubstituted Boron Dipyrromethene (BODIPY) Dyes: Synthesis and Spectroscopic Properties. *J. Org. Chem.* **2011**, *76* (20), 8168–8176.
- (115) Jiao, L.; Yu, C.; Uppal, T.; Liu, M.; Li, Y.; Zhou, Y.; Hao, E.; Hu, X.; Vicente, M. G. H. Long Wavelength Red Fluorescent Dyes from 3,5-Diiodo-BODIPYs. *Org. Biomol. Chem.* **2010**, *8* (11), 2517.

- (116) Maity, A.; Sarkar, A.; Sil, A.; B. N., S. B.; Patra, S. K. Synthesis, Photophysical and Concentration-Dependent Tunable Lasing Behavior of 2,6-Diacetylenyl-Functionalized BODIPY Dyes. *New J. Chem.* **2017**, *41* (6), 2296–2308.
- (117) Misra, R.; Dhokale, B.; Jadhav, T.; Mobin, S. M. The Quenching of Fluorescence as an Indicator of Donor-Strength in Meso Arylethynyl BODIPYs. *Dalton Trans.* **2014**, *43* (12), 4854.
- (118) Alnoman, R. B.; Stachelek, P.; Knight, J. G.; Harriman, A.; Waddell, P. G. Synthesis of 2-aminoBODIPYs by Palladium Catalysed Amination. *Org. Biomol. Chem.* **2017**, *15* (36), 7643–7653.
- (119) Duran-Sampedro, G.; Palao, E.; Agarrabeitia, A. R.; Moya, S. de la; Boens, N.; Ortiz, M. J. Negishi Reaction in BODIPY Dyes. Unprecedented Alkylation by Palladium-Catalyzed C–C Coupling in Boron Dipyrromethene Derivatives. *RSC Adv* **2014**, *4* (37), 19210–19213.
- (120) Palao, E.; Duran-Sampedro, G.; de la Moya, S.; Madrid, M.; García-López, C.; Agarrabeitia, A. R.; Verbelen, B.; Dehaen, W.; Boens, N.; Ortiz, M. J. Exploring the Application of the Negishi Reaction of HaloBODIPYs: Generality, Regioselectivity, and Synthetic Utility in the Development of BODIPY Laser Dyes. *J. Org. Chem.* **2016**, *81* (9), 3700–3710.
- (121) Morgan, L.; Boyer, J. Borondifluoride Compounds Unesful in Photodynamic Therapy and Production of Laster Light. 5446157.
- (122) Pavlopoulos, T.; Joseph, B.; Shah, M.; Thangaraj, K.; Soong, M.-L. Laser Action from 2,6,8-Position Trisubstituted 1,3,5,7-Tetramethylpyrromethene-BF₂ Complexes. *Appl. Opt.* **1990**, *29* (27), 3885–3886.
- (123) Haugland, R.; Kang, H. Chemically Reactive Dipyrrometheneboron Difluoride Dyes. US4774339A.
- (124) Bassan, E.; Gualandi, A.; Cozzi, P. G.; Ceroni, P. Design of BODIPY Dyes as Triplet Photosensitizers: Electronic Properties Tailored for Solar Energy Conversion, Photoredox Catalysis and Photodynamic Therapy. *Chem. Sci.* **2021**, *12* (19), 6607–6628.

- (125) Hayashi, Y.; Yamaguchi, S.; Cha, W. Y.; Kim, D.; Shinokubo, H. Synthesis of Directly Connected BODIPY Oligomers through Suzuki–Miyaura Coupling. *Org. Lett.* **2011**, *13* (12), 2992–2995.
- (126) Ahrens, J.; Birte, H.; Anne, S.; Matthias, T.; Martin, B. Conjugated BODIPY DYEimers by Metathesis Reactions. *Eur. J. Chem.* **2014**, *20*, 2901–2912.
- (127) Yalagala, R. S.; Mazinani, S. A.; Maddalena, L. A.; Stuart, J. A.; Yan, F.; Yan, H. Microwave-Assisted Syntheses of BODIPY–Sugar Conjugates through Click Chemistry and Conjugate Assembly into Liposomes. *Carbohydr. Res.* **2016**, *424*, 15–20.
- (128) Feng, Z.; Jiao, L.; Feng, Y.; Yu, C.; Chen, N.; Wei, Y.; Mu, X.; Hao, E. Regioselective and Stepwise Syntheses of Functionalized BODIPY Dyes through Palladium-Catalyzed Cross-Coupling Reactions and Direct C–H Arylations. *J. Org. Chem.* **2016**, *81* (15), 6281–6291.
- (129) Lundrigan, T.; Thompson, A. Conversion of *F* -BODIPYs to *Cl* -BODIPYs: Enhancing the Reactivity of *F* -BODIPYs. *J. Org. Chem.* **2013**, *78* (2), 757–761.
- (130) Davies, L. H.; Stewart, B.; Harrington, R. W.; Clegg, W.; Higham, L. J. Air-Stable, Highly Fluorescent Primary Phosphanes. *Angew. Chem. Int. Ed.* **2012**, *51* (20), 4921–4924.
- (131) Nagai, A.; Miyake, J.; Kokado, K.; Nagata, Y.; Chujo, Y. Highly Luminescent BODIPY-Based Organoboron Polymer Exhibiting Supramolecular Self-Assemble Structure. *J. Am. Chem. Soc.* **2008**, *130* (46), 15276–15278.
- (132) Gapare, R. L.; Thompson, A. Substitution at Boron in BODIPYs. *Chem. Commun.* **2022**, *58* (53), 7351–7359.
- (133) Choi, S. H.; Kim, K.; Jeon, J.; Meka, B.; Bucella, D.; Pang, K.; Khatua, S.; Lee, J.; Churchill, D. G. Optical Effects of *S* -Oxidation and M^{n+} Binding in *Meso* -Thienyl Dipyrrin Systems and of Stepwise Bromination of 4,4-Difluoro-8-(2,5-Dibromo-3-Thienyl)-4-Bora-3a,4a-Diaza-*s*-Indacene. *Inorg. Chem.* **2008**, *47* (23), 11071–11083.

- (134) Choi, S. H.; Pang, K.; Kim, K.; Churchill, D. G. Cu^{2+} Colorimetric Sensing and Fluorescence Enhancement and Hg^{2+} Fluorescence Diminution in “Scorpionate”-like Tetrathienyl-Substituted Boron–Dipyrrins. *Inorg. Chem.* **2007**, *46* (25), 10564–10577.
- (135) Kim, K.; Choi, S. H.; Jeon, J.; Lee, H.; Huh, J. O.; Yoo, J.; Kim, J. T.; Lee, C.-H.; Lee, Y. S.; Churchill, D. G. Control of On–Off or Off–On Fluorescent and Optical $[\text{Cu}^{2+}]$ and $[\text{Hg}^{2+}]$ Responses via Formal Me/H Substitution in Fully Characterized Thienyl “Scorpionate”-like BODIPY Systems. *Inorg. Chem.* **2011**, *50* (12), 5351–5360.
- (136) Wang, Z.; Guo, X.; Kang, Z.; Wu, Q.; Li, H.; Cheng, C.; Yu, C.; Jiao, L.; Hao, E. Aryl-Boron-Substituted BODIPYs: Direct Access via Aluminum-Chloride-Mediated Arylation from Arylstannanes and Tuning the Optoelectronic Properties. *Org. Lett.* **2023**, in press.
- (137) Lohner, W.; Praefcke, K. Organic Tellurium Compounds, IV: An Improved Synthesis of Tellurophene. *Chem. Ber.* **1978**, *111* (11), 3745–3746.
- (138) Diaz-Rodriguez, R. Some Aspects of the Inorganic and Organometallic Chemistry of Dipyrrins. MSc thesis, Dalhousie, Halifax NS, 2020.
- (139) Rhoden, C. R. B.; Zeni, G. New Development of Synthesis and Reactivity of Seleno- and Tellurophenes. *Org. Biomol. Chem.* **2011**, *9* (5), 1301.
- (140) Inoue, S.; Jigami, Tetsuya; Nozoe, H.; Aso, Y.; Ogura, F.; Otsubo, T. Syntheses, Spectroscopic Properties, and Polymerizations of 2,2'-Bitellurophene, 2,2':5',2"-Tertellurophene, and Related Hybrid Terchalcogenophenes. *Heterocycles* **2000**, *52* (1), 159–170.
- (141) Talbot, J.; Piette, J.; Renson, M. Three Substituted Benzo[b]Tellurophenes. *Bull. Soc. Chim. Belg.* **1980**, *89* (9), 763–771.
- (142) Gschwend, H.; Rodriguez, H. Heteroatom-Facilitate Lithiations. *Org. React.* **1979**, *26*.
- (143) Braun, C. A.; Martinek, N.; Zhou, Y.; Ferguson, M. J.; Rivard, E. Using Boryl-Substitution and Improved Suzuki–Miyaura Cross-Coupling to Access New Phosphorescent Tellurophenes. *Dalton Trans.* **2019**, *48* (27), 10210–10219.

- (144) He, G.; Kang, L.; Torres Delgado, W.; Shynkaruk, O.; Ferguson, M. J.; McDonald, R.; Rivard, E. The Marriage of Metallacycle Transfer Chemistry with Suzuki–Miyaura Cross-Coupling To Give Main Group Element-Containing Conjugated Polymers. *J. Am. Chem. Soc.* **2013**, *135* (14), 5360–5363.
- (145) Sweat, D.; Stephens, C. Synthesis and Stille Cross-Coupling Reactions of 2-(Tributylstannyl)- and 2,5-Bis(Trimethylstannyl)Tellurophene. *Synthesis* **2009**, *2009* (19), 3214–3218.
- (146) Smith, C. D.; Thompson, A. The Suzuki–Miyaura Reaction of BPin-Substituted F-BODIPYs with Aryl Halides. *Can. J. Chem.* **2021**, *99* (3), 287–294.
- (147) Haid, S.; Mishra, A.; Uhrich, C.; Pfeiffer, M.; Bäuerle, P. Dicyanovinylene-Substituted Selenophene–Thiophene Co-Oligomers for Small-Molecule Organic Solar Cells. *Chem. Mater.* **2011**, *23* (20), 4435–4444.
- (148) Entradas, T.; Waldron, S.; Volk, M. The Detection Sensitivity of Commonly Used Singlet Oxygen Probes in Aqueous Environments. *J. Photochem. Photobiol. B* **2020**, *204*, 111787.
- (149) Hartmann, F. J.; Bendall, S. C. Immune Monitoring Using Mass Cytometry and Related High-Dimensional Imaging Approaches. *Nat. Rev. Rheumatol.* **2020**, *16* (2), 87–99.
- (150) Digby, E. M.; Sadovski, O.; Beharry, A. A. An Activatable Photosensitizer Targeting Human NAD(P)H: Quinone Oxidoreductase 1. *Chem. – Eur. J.* **2020**, *26* (12), 2713–2718.
- (151) Kamkaew, A.; Lim, S. H.; Lee, H. B.; Kiew, L. V.; Chung, L. Y.; Burgess, K. BODIPY Dyes in Photodynamic Therapy. *Chem Soc Rev* **2013**, *42* (1), 77–88.
- (152) Zhao, J.; Xu, K.; Yang, W.; Wang, Z.; Zhong, F. The Triplet Excited State of Bodipy: Formation, Modulation and Application. *Chem. Soc. Rev.* **2015**, *44* (24), 8904–8939.
- (153) Li, W.; Li, L.; Xiao, H.; Qi, R.; Huang, Y.; Xie, Z.; Jing, X.; Zhang, H. Iodo-BODIPY: A Visible-Light-Driven, Highly Efficient and Photostable Metal-Free Organic Photocatalyst. *RSC Adv.* **2013**, *3* (32), 13417.

- (154) Yin, Z.; Tam, A. Y.-Y.; Wong, K. M.-C.; Tao, C.-H.; Poon, C.-T.; Wu, L.; Yam, V. W.-W. Functionalized BODIPY with Various Sensory Units – a Versatile Colorimetric and Luminescent Probe for pH and Ions. **2012**, 11.
- (155) Xochitiotzi-Flores, E.; Islas-Mejía, A. A.; García-Ortega, H.; Romero-Ávila, M.; Mendez-Stivalet, J. M.; Carreón-Castro, M. del P.; Santillan, R.; Maldonado-Domínguez, M.; Arcos-Ramos, R.; Farfán, N. On the Structure of Meso-Substituted F-BODIPYs and Their Assembly in Molecular Crystals: An Experimental-Theoretical Approach. *J. Organomet. Chem.* **2016**, 805, 148–157.
- (156) Tsujimoto, K.; Ogasawara, R.; Nakagawa, T.; Fujiwara, H. Photofunctional Conductors Based on TTF-BODIPY Dyads Bearing *p*-Phenylene and *p*-Phenylenevinylene Spacers: Photofunctional Conductors Based on TTF-BODIPY Dyads. *Eur. J. Inorg. Chem.* **2014**, 2014 (24), 3960–3972.
- (157) Tsujimoto, K.; Ogasawara, R.; Fujiwara, H. Photocurrent Generation Based on New Tetrathiafulvalene–BODIPY Dyads. *Tetrahedron Lett.* **2013**, 54 (10), 1251–1255.
- (158) Taniguchi, M.; Lindsey, J. S. Database of Absorption and Fluorescence Spectra of >300 Common Compounds for Use in Photochem CAD. *Photochem. Photobiol.* **2018**, 94 (2), 290–327.
- (159) Taniguchi, M.; Du, H.; Lindsey, J. S. PhotochemCAD 3: Diverse Modules for Photophysical Calculations with Multiple Spectral Databases. *Photochem. Photobiol.* **2018**, 94 (2), 277–289.
- (160) Chen, L.; Francis, H.; Carrow, B. P. An “On-Cycle” Precatalyst Enables Room-Temperature Polyfluoroarylation Using Sensitive Boronic Acids. *ACS Catal.* **2018**, 8 (4), 2989–2994.
- (161) Torres Delgado, W.; Shahin, F.; Ferguson, M. J.; McDonald, R.; He, G.; Rivard, E. Selective Placement of Bromide and Pinacolboronate Groups about a Tellurophene: New Building Blocks for Optoelectronic Applications. *Organometallics* **2016**, 35 (12), 2140–2148.
- (162) Barcellos, A. M.; Sacramento, M.; da Costa, G. P.; Perin, G.; João Lenardão, E.; Alves, D. Organoboron Compounds as Versatile Reagents in the Transition Metal-Catalyzed C–S, C–Se and C–Te Bond Formation. *Coord. Chem. Rev.* **2021**, 442, 214012.

- (163) Demirbař, Ü.; Bayrak, R.; Dilber, G.; Menteře, E.; Akçay, H. T. Novel Triazole Substituted Phthalocyanines Showing High Singlet Oxygen Quantum Yields. *J. Lumin.* **2019**, *206*, 199–204.
- (164) Günsel, A.; Güzel, E.; Bilgiçli, A. T.; Atmaca, G. Y.; Erdođmuř, A.; Yarasir, M. N. Synthesis and Investigation of Photophysicochemical Properties of Novel Ketone-Substituted Gallium (III) and Indium (III) Phthalocyanines with High Singlet Oxygen Yield for Photodynamic Therapy. *J. Lumin.* **2017**, *192*, 888–892.
- (165) Źamojć, K.; Zdrowowicz, M.; Rudnicki-Velasquez, P. B.; Krzymiński, K.; Zaborowski, B.; Niedziałkowski, P.; Jacewicz, D.; Chmurzyński, L. The Development of 1,3-Diphenylisobenzofuran as a Highly Selective Probe for the Detection and Quantitative Determination of Hydrogen Peroxide. *Free Radic. Res.* **2017**, *51* (1), 38–46.
- (166) Lebel, C. P.; Ischiropoulos, H.; Bondy, S. C. Evaluation of the Probe 2',7'-Dichlorofluorescein as an Indicator of Reactive Oxygen Species Formation and Oxidative Stress. *Chem Res Toxicol* **1992**, *5*, 227–231.
- (167) Rieger, A. M.; Nelson, K. L.; Konowalchuk, J. D.; Barreda, D. R. Modified Annexin V/Propidium Iodide Apoptosis Assay For Accurate Assessment of Cell Death. *J. Vis. Exp. JoVE* **2011**, No. 50, 2597.
- (168) Edmondson, R.; Broglie, J.; Adcock, A.; Yang, L. Three-Dimensional Cell Culture Systems and Their Applications in Drug Discovery and Cell-Based Biosensors. *Assay Drug Dev. Technol.* **2014**, *12* (4), 207–218.
- (169) Ruzziconi, R.; Spizzichino, S.; Lunazzi, L.; Mazzanti, A.; Schlosser, M. B Values as a Sensitive Measure of Steric Effects. *Chem. - Eur. J.* **2009**, *15* (11), 2645–2652.
- (170) Kassel, V. M.; Hanneman, C. M.; Delaney, C. P.; Denmark, S. E. Heteroaryl–Heteroaryl, Suzuki–Miyaura, Anhydrous Cross-Coupling Reactions Enabled by Trimethyl Borate. *J. Am. Chem. Soc.* **2021**, *143* (34), 13845–13853.
- (171) Campbell, J. W.; Tung, M. T.; Robertson, K. N.; Beharry, A. A.; Thompson, A. BODIPYs with Chalcogenophenes at Boron: Synthesis and Properties. *J. Org. Chem.* **2023**, *88* (15), 10655–10661.

- (172) Singh, S. P.; Gayathri, T. Evolution of BODIPY Dyes as Potential Sensitizers for Dye-Sensitized Solar Cells: Sensitizers for Dye-Sensitized Solar Cells. *Eur. J. Org. Chem.* **2014**, 2014 (22), 4689–4707.
- (173) Xu, Z.; Yuan, Y.; Zuguang, Y.; Heping, Z. Laser Action from 1,3,5,7-Tetramethyl-2,6-Diethyl-8- n-Propyl Pyrromethene-BF₂. *Opt. Soc. Am.* **2002**, 19 (6), 1349–1354.
- (174) Mukherjee, S.; Thilagar, P. Effect of Alkyl Substituents in BODIPYs: A Comparative DFT Computational Investigation. *RSC Adv.* **2015**, 5 (4), 2706–2714.
- (175) Schellhammer, K. S.; Li, T.-Y.; Zeika, O.; Körner, C.; Leo, K.; Ortmann, F.; Cuniberti, G. Tuning Near-Infrared Absorbing Donor Materials: A Study of Electronic, Optical, and Charge-Transport Properties of Aza-BODIPYs. *Chem. Mater.* **2017**, 29 (13), 5525–5536.
- (176) Rey, Y. P.; Abradelo, D. G.; Santschi, N.; Strassert, C. A.; Gilmour, R. Quantitative Profiling of the Heavy-Atom Effect in BODIPY Dyes: Correlating Initial Rates, Atomic Numbers, and ¹O₂ Quantum Yields: Quantitative Profiling of the Heavy-Atom Effect in BODIPY Dyes: Correlating Initial Rates, Atomic Numbers, and ¹O₂ Quantum Yields. *Eur. J. Org. Chem.* **2017**, 2017 (15), 2170–2178.
- (177) Wang, D.-G.; Zhang, L.-N.; Li, Q.; Yang, Y.; Wu, Y.; Fan, X.; Song, M.; Kuang, G.-C. Dimeric BODIPYs with Different Linkages: A Systematic Investigation on Structure-Properties Relationship. *Tetrahedron* **2017**, 73 (49), 6894–6900.
- (178) Wu, Z.; Fujita, H.; Magdaong, N. C. M.; Diers, J. R.; Hood, D.; Allu, S.; Niedzwiedzki, D. M.; Kirmaier, C.; Bocian, D. F.; Holten, D.; Lindsey, J. S. New Molecular Design for Blue BODIPYs. *New J. Chem.* **2019**, 43 (19), 7233–7242.
- (179) Wang, M.; Vicente, M. G. H.; Mason, D.; Bobadova-Parvanova, P. Stability of a Series of BODIPYs in Acidic Conditions: An Experimental and Computational Study into the Role of the Substituents at Boron. *ACS Omega* **2018**, 3 (5), 5502–5510.
- (180) Slanina, T.; Shrestha, P.; Palao, E.; Kand, D.; Peterson, J. A.; Dutton, A. S.; Rubinstein, N.; Weinstain, R.; Winter, A. H.; Klán, P. In Search of the Perfect Photocage: Structure–Reactivity Relationships in *Meso*-Methyl BODIPY Photoremovable Protecting Groups. *J. Am. Chem. Soc.* **2017**, 139 (42), 15168–15175.

- (181) Lundrigan, T.; Baker, A. E. G.; Longobardi, L. E.; Wood, T. E.; Smithen, D. A.; Crawford, S. M.; Cameron, T. S.; Thompson, A. An Improved Method for the Synthesis of *F*-BODIPYs from Dipyrins and Bis(Dipyrin)s. *Org. Lett.* **2012**, *14* (8), 2158–2161.
- (182) James, E. C.; Jura, M.; Kociok-Köhn, G.; Raithby, P. R.; Sharp, E. L.; Wilson, P. J. Communication in Platinum Ethynylchalcogenophenes. *Inorg. Chem.* **2007**, *46* (18), 7232–7234.
- (183) Vícha, J.; Novotný, J.; Komorovsky, S.; Straka, M.; Kaupp, M.; Marek, R. Relativistic Heavy-Neighbor-Atom Effects on NMR Shifts: Concepts and Trends Across the Periodic Table. *Chem. Rev.* **2020**, *120* (15), 7065–7103.
- (184) Kuznetsova, R. T.; Aksenova, Yu. V.; Tel'minov, E. N.; Samsonova, L. G.; Maier, G. V.; Kopylova, T. N.; Yutanova, S. L.; Antina, E. V.; Berezin, M. B.; Guseva, G. B. Spectral, Luminescent, Photochemical, and Laser Properties of a Series of Boron Fluoride Complexes of Dipyrrolylmethenes in Solutions. *Opt. Spectrosc.* **2012**, *112* (5), 746–754.
- (185) Redmond, R. W.; Gamlin, J. N. A Compilation of Singlet Oxygen Yields from Biologically Relevant Molecules. *Photochem. Photobiol.* **1999**, *70* (4), 391–475.
- (186) Nguyen, V.-N.; Qi, S.; Kim, S.; Kwon, N.; Kim, G.; Yim, Y.; Park, S.; Yoon, J. An Emerging Molecular Design Approach to Heavy-Atom-Free Photosensitizers for Enhanced Photodynamic Therapy under Hypoxia. *J. Am. Chem. Soc.* **2019**, *141* (41), 16243–16248.
- (187) Nguyen, V.-N.; Yan, Y.; Zhao, J.; Yoon, J. Heavy-Atom-Free Photosensitizers: From Molecular Design to Applications in the Photodynamic Therapy of Cancer. *Acc. Chem. Res.* **2021**, *54* (1), 207–220.
- (188) Baba, M. Intersystem Crossing in the $^1N\pi^*$ and $^1\Pi\pi^*$ States. *J. Phys. Chem. A* **2011**, *115* (34), 9514–9519.
- (189) Hoover, G. C.; Seferos, D. S. Photoactivity and Optical Applications of Organic Materials Containing Selenium and Tellurium. *Chem. Sci.* **2019**, *10* (40), 9182–9188.

- (190) Campbell, J. W.; Tung, M. T.; Taylor, B. B.; Beharry, A. A.; Thompson, A. A Series of Potent BODIPY Photosensitisers Featuring Tellurophene Motifs at Boron. *Org. Biomol. Chem.* **2024**, No. 22, 4157–4162.
- (191) Correia, J. H.; Rodrigues, J. A.; Pimenta, S.; Dong, T.; Yang, Z. Photodynamic Therapy Review: Principles, Photosensitizers, Applications, and Future Directions. *Pharmaceutics* **2021**, *13* (9), 1332.
- (192) Gu, K.; Lin, G.; Zhu, Y.; Ji, X.; Li, J.; Dong, X.; Zhao, W. Anchoring BODIPY Photosensitizers Enable Pan-Microbial Photoinactivation. *Eur. J. Med. Chem.* **2020**, *199*, 112361.
- (193) Al Anshori, J.; Slanina, T.; Palao, E.; Klán, P. The Internal Heavy-Atom Effect on 3-Phenylselanyl and 3-Phenyltellanyl BODIPY Derivatives Studied by Transient Absorption Spectroscopy. *Photochem. Photobiol. Sci.* **2016**, *15* (2), 250–259.
- (194) Willis, L. M.; Park, H.; Watson, M. W. L.; Majonis, D.; Watson, J. L.; Nitz, M. Tellurium-Based Mass Cytometry Barcode for Live and Fixed Cells. *Cytometry A* **2018**, *93* (7), 685–694.
- (195) Jia Bu, Y.; Nitz, M. Incorporation of TePhe into Expressed Proteins Is Minimally Perturbing. *ChemBioChem* **2021**, *22* (14), 2449–2456.
- (196) Liu, S.; Lin, T.-P.; Li, D.; Leamer, L.; Shan, H.; Li, Z.; Gabbai, F. P.; Conti, P. S. Lewis Acid-Assisted Isotopic ^{18}F - ^{19}F Exchange in BODIPY Dyes: Facile Generation of Positron Emission Tomography/Fluorescence Dual Modality Agents for Tumor Imaging. *Theranostics* **2013**, *3* (3), 181–189.
- (197) Murase, S.; Tominaga, T.; Kohama, A. Pyrromethene Metal Complex and Light Emitting Device Composition and Light Emitting Devices Using the Same. Eur. Pat., 1253151A1, October 30, 2002.
- (198) Yuan, K.; Wang, X.; Møllerup, S. K.; Kozin, I.; Wang, S. Spiro-BODIPYs with a Diaryl Chelate: Impact on Aggregation and Luminescence. *J. Org. Chem.* **2017**, *82* (24), 13481–13487.
- (199) Choi, H. W.; Lee, U.; Song, J. K. Optical Features of AGGREGATION-INDUCED Emission in BODIPY With Isopropyl Meso Group. *Bull. Korean Chem. Soc.* **2021**, *42* (4), 567–570.

- (200) Berlanda, J.; Kiesslich, T.; Engelhardt, V.; Krammer, B.; Plaetzer, K. Comparative in Vitro Study on the Characteristics of Different Photosensitizers Employed in PDT. *J. Photochem. Photobiol. B* **2010**, *100* (3), 173–180.
- (201) Heinemann, F.; Karges, J.; Gasser, G. Critical Overview of the Use of Ru(II) Polypyridyl Complexes as Photosensitizers in One-Photon and Two-Photon Photodynamic Therapy. *Acc. Chem. Res.* **2017**, *50* (11), 2727–2736.
- (202) Blass, B. *Basic Principles of Drug Discovery and Development*, 2nd ed.; Academic Press: London, 2021.
- (203) Evans, L. *Cancer Drug Discovery and Development*; Hayle Medical: New York, NY, 2020.
- (204) Zhong, L.; Li, Y.; Xiong, L.; Wang, W.; Wu, M.; Yuan, T.; Yang, W.; Tian, C.; Miao, Z.; Wang, T.; Yang, S. Small Molecules in Targeted Cancer Therapy: Advances, Challenges, and Future Perspectives. *Signal Transduct. Target. Ther.* **2021**, *6* (1), 201.
- (205) Hafeez, U.; Gan, H. K.; Scott, A. M. Monoclonal Antibodies as Immunomodulatory Therapy against Cancer and Autoimmune Diseases. *Curr. Opin. Pharmacol.* **2018**, *41*, 114–121.
- (206) Chen, Y.; Law, P.; Loh, H. Inhibition of PI3K/Akt Signaling: An Emerging Paradigm for Targeted Cancer Therapy. *Curr. Med. Chem.* **5** (6), 575–589.
- (207) El-Kenawi, A. E.; El-Remessy, A. B. Angiogenesis Inhibitors in Cancer Therapy: Mechanistic Perspective on Classification and Treatment Rationales. *Br. J. Pharmacol.* **2013**, *170* (4), 712–729.
- (208) Cazzamalli, S.; Corso, A. D.; Neri, D. Targeted Delivery of Cytotoxic Drugs: Challenges, Opportunities and New Developments. *CHIMIA* **2017**, *71* (10), 712.
- (209) Ding, L.; Agrawal, P.; Singh, S. K.; Chhonker, Y. S.; Sun, J.; Murry, D. J. Polymer-Based Drug Delivery Systems for Cancer Therapeutics. *Polymers* **2024**, *16* (6), 843.
- (210) Ebrahimnejad, P.; Sodagar Taleghani, A.; Asare-Addo, K.; Nokhodchi, A. An Updated Review of Folate-Functionalized Nanocarriers: A Promising Ligand in Cancer. *Drug Discov. Today* **2022**, *27* (2), 471–489.

- (211) Zhang, C.-W.; Zhang, J.-G.; Yang, X.; Du, W.-L.; Yu, Z.-L.; Lv, Z.-Y.; Mou, X.-Z. Carbohydrates Based Stimulus Responsive Nanocarriers for Cancer-Targeted Chemotherapy: A Review of Current Practices. *Expert Opin. Drug Deliv.* **2022**, *19* (6), 623–640.
- (212) Morioka, M.; Kamizono, A.; Takikawa, H.; Mori, A.; Ueno, H.; Kadowaki, S.; Nakao, Y.; Kato, K.; Umezawa, K. Design, Synthesis, and Biological Evaluation of Novel Estradiol–Bisphosphonate Conjugates as Bone-Specific Estrogens. *Bioorg. Med. Chem.* **2010**, *18* (3), 1143–1148.
- (213) Farzaneh, S.; Zarghi, A. Estrogen Receptor Ligands: A Review (2013–2015). *Sci. Pharm.* **2016**, *84* (3), 409–427.
- (214) Samec, T.; Boulos, J.; Gilmore, S.; Hazelton, A.; Alexander-Bryant, A. Peptide-Based Delivery of Therapeutics in Cancer Treatment. *Mater. Today Bio* **2022**, *14*, 100248.
- (215) Gao, F.; Yin, J.; Chen, Y.; Guo, C.; Hu, H.; Su, J. Recent Advances in Aptamer-Based Targeted Drug Delivery Systems for Cancer Therapy. *Front. Bioeng. Biotechnol.* **2022**, *10*, 972933.
- (216) Dumontet, C.; Reichert, J. M.; Senter, P. D.; Lambert, J. M.; Beck, A. Antibody–Drug Conjugates Come of Age in Oncology. *Nat. Rev. Drug Discov.* **2023**, *22* (8), 641–661.
- (217) Burridge, K. M.; Page, R. C.; Konkolewicz, D. Bioconjugates – From a Specialized Past to a Diverse Future. *Polymer* **2020**, *211*, 123062.
- (218) Boutureira, O.; Bernardes, G. J. L. Advances in Chemical Protein Modification. *Chem. Rev.* **2015**, *115* (5), 2174–2195.
- (219) Pellico, J.; Gawne, P. J.; T. M. de Rosales, R. Radiolabelling of Nanomaterials for Medical Imaging and Therapy. *Chem. Soc. Rev.* **2021**, *50* (5), 3355–3423.
- (220) Hong, V.; Presolski, S. I.; Ma, C.; Finn, M. G. Analysis and Optimization of Copper-Catalyzed Azide–Alkyne Cycloaddition for Bioconjugation. *Angew. Chem. Int. Ed.* **2009**, *48* (52), 9879–9883.
- (221) Marchal, E.; Figliola, C.; Thompson, A. Prodigiosenes Conjugated to Tamoxifen and Estradiol. *Org. Biomol. Chem.* **2017**, *15* (25), 5410–5427.

- (222) Montaner, B.; Pérez-Tomás, R. Prodigiosin-Induced Apoptosis in Human Colon Cancer Cells. *Life Sci.* **2001**, *68* (17), 2025–2036.
- (223) Pérez-Tomás, R.; Montaner, B.; Llagostera, E.; Soto-Cerrato, V. The Prodigiosins, Proapoptotic Drugs with Anticancer Properties. *Biochem. Pharmacol.* **2003**, *66* (8), 1447–1452.
- (224) Hawco, C. L. A.; Marchal, E.; Uddin, Md. I.; Baker, A. E. G.; Corkery, D. P.; Dellaire, G.; Thompson, A. Synthesis and Biological Evaluation of Prodigiosene Conjugates of Porphyrin, Estrone and 4-Hydroxytamoxifen. *Bioorg. Med. Chem.* **2013**, *21* (19), 5995–6002.
- (225) Marchal, E.; Uddin, Md. I.; Hawco, C. L. A.; Thompson, A. Synthesis of Prodigiosene–Estrogen Conjugates: Optimization of Protecting Group Strategies and Anticancer Properties. *Can. J. Chem.* **2015**, *93* (5), 526–535.
- (226) Figliola, C.; Marchal, E.; Groves, B. R.; Thompson, A. A Step-Wise Synthetic Approach Is Necessary to Access γ -Conjugates of Folate: Folate-Conjugated Prodigiosenes. *RSC Adv.* **2019**, *9* (25), 14078–14092.
- (227) Maynadier, M.; Nirdé, P.; Ramirez, J.-M.; Cathiard, A. M.; Platet, N.; Chambon, M.; Garcia, M. Role of Estrogens and Their Receptors in Adhesion and Invasiveness of Breast Cancer Cells. In *Hormonal Carcinogenesis V*; Li, J. J., Li, S. A., Mohla, S., Rochefort, H., Maudelonde, T., Eds.; Springer New York: New York, NY, 2008; pp 485–491.
- (228) Jordan, C. Antiestrogens and Selective Estrogen Receptor Modulators as Multifunctional Medicines. 1. Receptor Interactions. *J. Med. Chem.* **2003**, *46* (6), 883–908.
- (229) Jordan, C. Antiestrogens and Selective Estrogen Receptor Modulators as Multifunctional Medicines. 2. Clinical Considerations and New Agents. *J. Med. Chem.* **2003**, *46* (7), 1081–1111.
- (230) Spera, D.; Cabrera, G.; Fiaschi, R.; Carlson, K. E.; Katzenellenbogen, J. A.; Napolitano, E. Estradiol Derivatives Bearing Sulfur-Containing Substituents at the 11 β or 7 α Positions: Versatile Reagents for the Preparation of Estrogen Conjugates. *Bioorg. Med. Chem.* **2004**, *12* (16), 4393–4401.

- (231) Cyrus, K.; Wehenkel, M.; Choi, E.; Lee, H.; Swanson, H.; Kim, K. Jostling for Position: Optimizing Linker Location in the Design of Estrogen Receptor-Targeting PROTACs. *ChemMedChem* **2010**, *5* (7), 979–985.
- (232) Ramírez-López, P.; De La Torre, M. C.; Montenegro, H. E.; Asenjo, M.; Sierra, M. A. A Straightforward Synthesis of Tetrameric Estrone-Based Macrocycles. *Org. Lett.* **2008**, *10* (16), 3555–3558.
- (233) Rogers, D. T. *Environmental Compliance Handbook: Report on Carcinogens, Fifteenth Edition*, 1st ed.; CRC Press: Boca Raton, 2022.
- (234) Greene, T.; Wuts, P. *Protective Groups in Organic Synthesis*, Third.; John Wiley and Sons, Inc.: New York, 1999.
- (235) Berliner, M.; Belecki, K. SYNTHESIS OF ALPHA-HALO ETHERS FROM SYMMETRIC ACETALS AND in Situ METHOXYMETHYLATION OF AN ALCOHOL. *Org. Synth.* **2007**, *84*, 102.
- (236) Stillwell, W. Chapter 20 - Bioactive Lipids. In *An Introduction to Biological Membranes (Second Edition)*; Stillwell, W., Ed.; Elsevier, 2016; pp 453–478.
- (237) Zhao, R.; Diop-Bove, N.; Visentin, M.; Goldman, I. D. Mechanisms of Membrane Transport of Folates into Cells and Across Epithelia. *Annu. Rev. Nutr.* **2011**, *31*, 177–201.
- (238) Destito, G.; Yeh, R.; Rae, C. S.; Finn, M. G.; Manchester, M. Folic Acid-Mediated Targeting of Cowpea Mosaic Virus Particles to Tumor Cells. *Chem. Biol.* **2007**, *14* (10), 1152–1162.
- (239) Mindt, T. L.; Müller, C.; Melis, M.; De Jong, M.; Schibli, R. “Click-to-Chelate”: In Vitro and In Vivo Comparison of a ^{99m}Tc(CO)₃-Labeled N(τ)-Histidine Folate Derivative with Its Isostructural, Clicked 1,2,3-Triazole Analogue. *Bioconjug. Chem.* **2008**, *19* (8), 1689–1695.
- (240) Fischer, C. R.; Müller, C.; Reber, J.; Müller, A.; Krämer, S. D.; Ametamey, S. M.; Schibli, R. [¹⁸F]Fluoro-Deoxy-Glucose Folate: A Novel PET Radiotracer with Improved in Vivo Properties for Folate Receptor Targeting. *Bioconjug. Chem.* **2012**, *23* (4), 805–813.

- (241) Trindade, A. F.; Frade, R. F. M.; Maçôas, E. M. S.; Graça, C.; Rodrigues, C. A. B.; Martinho, J. M. G.; Afonso, C. A. M. “Click and Go”: Simple and Fast Folic Acid Conjugation. *Org. Biomol. Chem.* **2014**, *12* (20), 3181–3190.
- (242) Gottlieb, H. E.; Kotlyar, V.; Nudelman, A. NMR Chemical Shifts of Common Laboratory Solvents as Trace Impurities. *J. Org. Chem.* **1997**, *62* (21), 7512–7515.
- (243) Koelmann, C.; Sladky, F. Ultrasonic Activation of Chalcogen-Chalcogen Bonds: Synthesis of Bis(Organoyltellurenyl) Selenides and Sulfides, (R₂Te)₂(Se,S). *Organometallics* **1991**, *10* (7), 2101–2102.
- (244) Beh, M. H. R.; Douglas, K. I. B.; House, K. T. E.; Murphy, A. C.; Sinclair, J. S. T.; Thompson, A. Robust Synthesis of F-BODIPYs. *Org. Biomol. Chem.* **2016**, *14* (48), 11473–11479.
- (245) Sengupta, S.; Pandey, U. K. Dual Emissive Bodipy–Benzodithiophene–Bodipy TICT Triad with a Remarkable Stokes Shift of 194 Nm. *Org. Biomol. Chem.* **2018**, *16* (12), 2033–2038.
- (246) Lager, E.; Liu, J.; Aguilar-Aguilar, A.; Tang, B. Z.; Peña-Cabrera, E. Novel Meso - Polyarylamine-BODIPY Hybrids: Synthesis and Study of Their Optical Properties. *J. Org. Chem.* **2009**, *74* (5), 2053–2058.
- (247) Williams, A. T. R.; Winfield, S. A.; Miller, J. N. Relative Fluorescence Quantum Yields Using a Computer-Controlled Luminescence Spectrometer. *The Analyst* **1983**, *108* (1290), 1067.
- (248) Brouwer, A. M. Standards for Photoluminescence Quantum Yield Measurements in Solution (IUPAC Technical Report). *Pure Appl. Chem.* **2011**, *83* (12), 2213–2228.
- (249) *APEX 3*; Bruker AXS Inc.: Madison, Wisconsin, USA, 2018.
- (250) *SAINT*; Bruker AXS Inc.: Madison, Wisconsin, USA, 2016.
- (251) Sheldrick, G.M. *SHELXT* – Integrated space-group and crystal-structure determination. *Acta Cryst.* **2015**, *A71*, 3-8.
- (252) Sheldrick, G. Crystal Structure Refinement with SHELXL. *Acta Crystallographica* **2015**, No. C71, 3–8.

- (253) Macrae, C.; Bruno, J.; Chisholm, J.; Edgington, P.; McCabe, P.; Rodriguez-Monge, L.; Taylor, R.; van de Streek, J.; Wood, P. Mercury CSD 2.0 - New Features for the Visualization and Investigation of Crystal Structures. *Appl. Crystallogr.* **2008**, No. 41, 466–470.
- (254) Spek, A. Single-Crystal Structure Validation with the Program PLATON. *Appl. Crystallogr.* **2003**, No. 36, 7–13.
- (255) Atif Mahammed; Kepeng Chen; Jenya Vestfrid; Jianzhang Zhao; Zeev Gross. Phosphorus Corrole Complexes: From Property Tuning to Applications in Photocatalysis and Triplet–Triplet Annihilation Upconversion. *Chem. Sci.* **2019**, 10 (29), 7091–7103.
- (256) Yutanova, S. L.; Berezin, M. B.; Semeikin, A. S.; Antina, E. V.; Guseva, G. B.; V'yugin, A. I. Thermal Oxidative Degradation of the Functionally Substituted 2,2'-Dipyrrolylmethenes Hydrobromides and Difluoroborates. *Russ. J. Gen. Chem.* **2013**, 83 (3), 545–551.
- (257) SADABS (Bruker, 2016) Bruker AXS Inc., Madison, Wisconsin, USA.
- (258) Sheldrick, G. M. (2008) CELL_NOW, University of Göttingen, Germany.
- (259) Spartan'20, version 1.3.0 (Wavefunction Inc., 2019) Irvine, California, USA.
- (260) Braun, C. A.; Ferguson, M. J.; Rivard, E. Tellura(Benzo)Bithiophenes: Synthesis, Oligomerization, and Phosphorescence. *Inorg. Chem.* **2021**, 60 (4), 2672–2679.
- (261) Lash, T. D.; Chen, S. Syntheses of Per-15N Labeled Etioporphyrins I–IV and a Related Tetrahydrobenzoporphyrin for Applications in Organic Geochemistry and Vibrational Spectroscopy. *Tetrahedron* **2005**, 61 (49), 11577–11600.
- (262) Yang, L.; Huang, Z.; Li, G.; Cao, R.; Wang, C.; Xiao, J.; Xue, D. Synthesis of Phenols: Organophotoredox/Nickel Dual Catalytic Hydroxylation of Aryl Halides with Water. 1.
- (263) Al-Sheikh Ali, A.; Cipot-Wechsler, J.; Cameron, T. S.; Thompson, A. Formation of Vinylic Dipyrroles by the Deprotonation of *Meso*-Alkyl and *Meso*-Benzyl Dipyrroin HCl Salts. *J. Org. Chem.* **2009**, 74 (7), 2866–2869.

- (264) Nguyen, A. L.; Fronczek, F. R.; Smith, K. M.; Vicente, M. G. H. Synthesis of 4,4'-Functionalized BODIPYs from Dipyrrens. *Tetrahedron Lett.* **2015**, *56* (46), 6348–6351.
- (265) Telitel, S.; Blanchard, N.; Schweizer, S.; Morlet-Savary, F.; Graff, B.; Fouassier, J.-P.; Lalevée, J. BODIPY Derivatives and Boranil as New Photoinitiating Systems of Cationic Polymerization Exhibiting a Tunable Absorption in the 400–600 nm Spectral Range. *Polymer* **2013**, *54* (8), 2071–2076.
- (266) Zlatić, K.; Bogomolec, M.; Cindrić, M.; Uzelac, L.; Basarić, N. Synthesis, Photophysical Properties, Anti-Kasha Photochemical Reactivity and Biological Activity of Vinyl- and Alkynyl-BODIPY Derivatives. *Tetrahedron* **2022**, *124*, 132995.
- (267) Nepomnyashchii, A. B.; Bröring, M.; Ahrens, J.; Bard, A. J. Synthesis, Photophysical, Electrochemical, and Electrogenated Chemiluminescence Studies. Multiple Sequential Electron Transfers in BODIPY Monomers, Dimers, Trimers, and Polymer. *J. Am. Chem. Soc.* **2011**, *133* (22), 8633–8645.
- (268) Crawford, S. M.; Al-Sheikh Ali, A.; Cameron, T. S.; Thompson, A. Synthesis and Characterization of Fluorescent Pyrrolyldipyrrinato Sn(IV) Complexes. *Inorg. Chem.* **2011**, *50* (17), 8207–8213.
- (269) *Dichloromethane ACS reagent, = 99.5, Yes amylene 40-150ppm stabilizer 75-09-2*. <http://www.sigmaaldrich.com/> (accessed 2024-01-31).
- (270) Scott, T. A. Refractive Index of Ethanol–Water Mixtures and Density and Refractive Index of Ethanol–Water–Ethyl Ether Mixtures. *J. Phys. Chem.* **1946**, *50* (5), 406–412.
- (271) Crawford, S. M.; Thompson, A. Conversion of 4,4-Difluoro-4-Bora-3a,4a-Diaza-*s*-Indacenes (*F*-BODIPYs) to Dipyrrens with a Microwave-Promoted Deprotection Strategy. *Org. Lett.* **2010**, *12* (7), 1424–1427.
- (272) Verbelen, B.; Leen, V.; Wang, L.; Boens, N.; Dehaen, W. Direct Palladium-Catalysed C–H Arylation of BODIPY Dyes at the 3- and 3,5-Positions. *Chem. Commun.* **2012**, *48* (73), 9129.

Appendix A. Chapter 2, Section 2.2 Supporting Information

A.1. Experimental Procedures

A.1.1. General Remarks

Reagents were commercially available and used without further purification unless otherwise discussed. Anhydrous solvents were purchased from Millipore Sigma or Acros Organics, and used without further drying. Manipulations requiring inert atmospheres were conducted under nitrogen and using Schlenk line procedures or glovebox techniques unless otherwise discussed. Nuclear magnetic resonance (NMR) spectra were recorded using Bruker AVANCE 500 MHz or 300 MHz spectrometers. ^1H chemical shifts are reported in ppm relative to tetramethylsilane using the solvent residual as an internal standard ($\delta = 7.26$ for chloroform, 5.32 for dichloromethane).¹ ^{13}C chemical shifts are reported in ppm relative to tetramethylsilane, referenced to the resonances of CDCl_3 ($\delta = 77.2$ ppm) or CD_2Cl_2 ($\delta = 53.84$ ppm) and were proton decoupled.¹ Trace impurities and residual solvent peaks were determined using tables developed by Nudlam *et al.*²⁴² Coupling constants are reported in Hertz (Hz) and spin multiplicities are reported using the following symbols: s (singlet), bs (broad singlet), d (doublet), dd (doublet of doublets), t (triplet), q (quartet), m (multiplet) and app (apparent). ^{11}B chemical shifts are reported in ppm, externally referenced to boron trifluoride diethyl etherate ($\delta = 0.00$). ^{19}F chemical shifts are reported in ppm, externally referenced to CFCl_3 ($\delta = 0.00$). NMR spectra were processed using Bruker TopSpin 4.0 software. ^{125}Te NMR spectra were recorded using a Bruker AVANCE

300 MHz spectrometer; chemical shifts are reported in ppm relative to Me_2Te_2 , externally referenced to diphenyl ditelluride ($\delta = 422$ ppm).²⁴³ Thin layer chromatography was performed using commercially prepared silica gel plates or alumina plates and visualised using long- or shortwave UV lamps. Column chromatography was performed either on 230-400 mesh silica or 58 Å neutral alumina. The relative proportions of solvents mentioned in column chromatography refer to a volume-to-volume ratio. Absorption spectra were recorded in dichloromethane using a Varian Cary 100 Bio spectrophotometer using a quartz cuvette. Fluorescence spectra were recorded in dichloromethane using a Shimadzu RF-5301PC fluorimeter using a quartz cuvette. Mass spectra were recorded using a Bruker microTOF Focus Mass Spectrometer.

A.1.2. Synthesis of tellurophene, **b1**

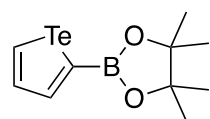


Using a modified version of literature procedures,^{85,137} a 500 mL two-neck round-bottom flask equipped with a water condenser was oven-dried and then evacuated and backfilled with inert gas. To this, distilled water (150 mL) was added followed by sodium hydroxide (17.0 g, 425 mmol) with stirring to dissolve. Powdered tellurium (4.0 g, 42 mmol, 200 mesh) was added, followed by sodium hydroxymethanesulfinate dihydrate (31.0 g, 200 mmol). This suspension was stirred vigorously and heated to reflux temperature until suspended tellurium powder was no longer observed (approximately 1 hr). The solution was deep purple in colour, and a bright light was used to confirm complete tellurium dissolution. The mixture was then allowed to cool down to approximately 60 °C. 1,4-Bis(trimethylsilyl)-1,3-butadiyne (8.2 g, 42 mmol) was suspended in 100% ethanol (100 mL), and the solution was poured into the stirring solution of sodium telluride. The

reaction mixture was then stirred at 60 °C for 1.5 h. Next, the solution was allowed to cool to room temperature and poured into a 1 L separatory funnel and extracted with diethyl ether (3× 150 mL). The organic layers were combined, dried over sodium sulfate, and filtered through a glass wool plug into a 1 L round-bottom flask, before concentrating under reduced pressure to roughly 150 mL (the weakest possible vacuum was applied to minimise co-evaporation of tellurophene). A stir-bar was added to the flask along with a pressure-equalising dropping funnel. To the dropping funnel, bromine (10.0 mL, 200 mmol) was added. In order to control the rate of this exothermal reaction the stopcock was opened until a drop-wise addition was achieved. Once all bromine had been added, the reaction was allowed to cool, and the orange solids then collected on fritted glass *via* suction filtration. This orange solid, 1,1-dibromotellurophene, could be stored for short periods of time under an inert atmosphere and in a freezer. A solution of sodium sulfite (Na₂SO₃) (21.0 g, 170 mmol) and potassium carbonate (16.0 g, 116 mmol) in distilled water (250 mL) was **freshly prepared** and transferred into a 500 mL separatory funnel. Diethyl ether (≈75 mL) was added directly into the separatory funnel, followed by the 1,1-dibromotellurophene as a powder (Note: adding as a powder alleviated challenges caused by the limited solubility properties of 1,1-dibromotellurophene). The separatory funnel was capped and shaken vigorously reducing 1,1-dibromotellurophene to tellurophene. The organic layer was collected, and the aqueous fraction was extracted with additional diethyl ether (3× 50 mL). The combined organic layers were dried over sodium sulfate, filtered into a round-bottom flask, and concentrated under reduced pressure (the weakest possible vacuum was applied to avoid co-evaporation of tellurophene). The oil was further purified *via* simple distillation

under reduced pressure to afford the desired compound as a pale-yellow oil (1.96 g, 39%) (Note: care was taken to rinse the distillation apparatus with diethyl ether in an effort to maximise yield; residual ether was removed under reduced pressure). ^1H NMR (500 MHz, CDCl_3) δ 9.03-8.96 (m with Te satellites, 2H), 7.81-7.93 (m with Te satellites, 2H). $^{125}\text{Te}\{^1\text{H}\}$ NMR (95 MHz, CDCl_3) δ 777.9. This data is in accordance with those previously reported.¹³⁷

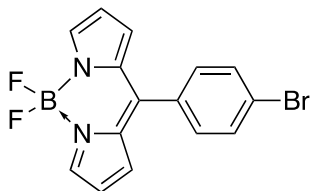
A.1.3. Synthesis of 2-(pinacolatoboron)tellurophene, **b2**



Inside a nitrogen-filled glovebox, tellurophene (**b1**) (250 mg, 1.37 mmol) and dry tetrahydrofuran (4 mL) were stirred in a 15 mL vial at room temperature until complete dissolution was achieved (5 min). *n*-Butyllithium (956 μL , 1.6 M in hexanes, 1.51 mmol) was added dropwise *via* syringe, and the vial then capped. The reaction mixture was stirred for 1 hr, and then quenched with 2-isopropoxy-4,4,5,5-tetramethyl-1,3,2-dioxaborolane (340 μL , 1.67 mmol). The capped quenched reaction mixture was stirred overnight (16 h). The crude reaction mixture was then taken out of the glovebox and extracted with dichloromethane (20 mL). The organic layer was washed with saturated ammonium chloride (3 \times 20 mL), water (1 \times 20 mL), and brine (1 \times 20 mL). The organic layer was dried over sodium sulfate and concentrated under reduced pressure. The crude product was purified by Kugelrohr distillation (155 $^\circ\text{C}$, 9.0 mm Hg) to afford the title compound as pale-yellow crystals (305 mg, 72%). ^1H NMR (300 MHz, CDCl_3) δ 9.34 (d, J = 6.5 Hz, 1H), 8.51 (d, J = 3.8 Hz, 1H), 8.01 (dd, J = 6.5, 3.8 Hz, 1H), 1.34 (s, 12H). ^{11}B NMR (160 MHz, CD_2Cl_2) δ 31.2 (s). ^{13}C (126 MHz, CD_2Cl_2) δ 149.6,

147.3, 140.3, 134.2, 84.5, 25.0. HRMS-ESI⁺ m/z [$M^+ + H$] calc. for $C_{10}H_{15}BO_2^{130}Te$: 309.0300; found: 309.0297.

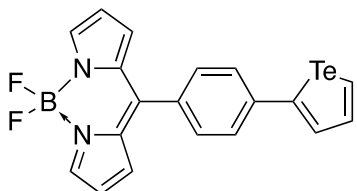
A.1.4. Synthesis of 8-(4-bromophenyl)BODIPY, b3



Using a modified version of literature procedures,⁵⁻⁸ in a 250 mL round-bottom flask 4-bromobenzaldehyde (1.00 g, 4.52 mmol) was added to nitrogen-sparged 0.018 M HCl (100 mL) and the mixture then stirred under a nitrogen atmosphere. Freshly distilled pyrrole (0.94 mL, 13.6 mmol) was transferred drop-wise *via* syringe into the flask and the reaction mixture was stirred for 3 h. The crude reaction mixture was extracted into dichloromethane (3 × 100 mL) and the combined organic fractions were washed with water, dried over sodium sulfate and concentrated under reduced pressure. The resulting crude oil was purified *via* column chromatography over silica, loading as a solution and first eluting with 1% triethylamine in hexanes until all unreacted pyrrole was eluted. Then, a gradient of 0 → 25% ethyl acetate in hexanes was employed until all dipyrromethane was eluted. The fractions were concentrated under reduced pressure and an aliquot was taken to confirm unreacted starting materials were not present according to analysis using ¹H NMR spectroscopy. The crude dipyrromethane was dissolved in dry dichloromethane (40 mL) under a nitrogen atmosphere. 2,3-Dichloro-5,6-dicyano-1,4-benzoquinone (2.0 g, 9.0 mmol) was added, and the reaction mixture was stirred at room temperature overnight (16 h). Triethylamine (3.8 mL, 27 mmol) was then added to the reaction mixture, *via* syringe, followed by boron trifluoride diethyl etherate (5.0 mL, 40 mmol). After stirring the reaction mixture for 1.5 h, second aliquots of triethylamine (3.8 mL, 27.12 mmol) and boron trifluoride diethyl

etherate (5.0 mL, 40.68 mmol) were added, followed by stirring for a further 1.5 h.²⁴⁴ The crude reaction mixture was filtered through a silica gel plug, eluting with dichloromethane, and the resulting mixture was evaporated under reduced pressure. Then, the residue was taken up in ether and washed with 1 M HCl (5× 50 mL), and 6 M HCl (1× 50 mL). The organic layer was dried over sodium sulfate and concentrated under reduced pressure to afford dark purple crystalline material (1.11 g, 59%). ¹H NMR (500 MHz, CD₂Cl₂) δ 7.96 (bs, 2H), 7.68 (d, *J* = 8.3 Hz, 2H), 7.45 (d, *J* = 8.3 Hz, 2H), 6.90 (apparent d, *J* = 4.2 Hz, 2H), 6.56 (apparent d, *J* = 4.2 Hz, 2H). This data is in accordance with those reported.^{146,245,246}

A.1.5. Synthesis of 8-(4-(tellurophenyl)phenyl)BODIPY, **b4**



2-(Pinacolatoboron)tellurophene (**b2**) (120 mg, 0.39 mmol),

8-(4-bromophenyl)BODIPY (**b3**) (150 mg, 0.43 mmol),

Pd₂(dba)₃ (16 mg, 16 μmol), XPhos (16 mg, 31 μmol) and

cesium carbonate (704 mg, 1.96 mmol) were stirred to combine in a 4 mL vial. The vial was evacuated and purged with nitrogen before dioxane (3 mL) and distilled water (300 μL) were added. The vial was capped, stirred, and heated to 50 °C for 4 h. Second aliquots of Pd₂(dba)₃ (16 mg, 16 μmol) and XPhos (16 mg, 31 μmol) were then added, before stirring the reaction overnight (16 h). The reaction mixture was filtered through Celite, eluting with dichloromethane, and then evaporated under reduced pressure. The crude material was purified *via* column chromatography on neutral alumina, *via* wet-loading and elution with 0 → 25% v/v ethyl acetate in hexanes. To remove further impurities, the resulting crude solids were suspended in pentane and loaded into a Pasteur pipette equipped with a

Kimwipe plug. The solids were washed multiple times with pentane, then eluted through the plug with dichloromethane. The sample was concentrated under reduced pressure to afford the desired product as a crimson solid (128 mg, 73% yield). $R_f = 0.18$ (20% v/v ethyl acetate/hexanes). ^1H NMR (500 MHz, CD_2Cl_2) δ 8.97 (dd, $J = 6.8, 1.0$ Hz, 1H), 8.00 (dd, $J = 4.1, 1.0$ Hz), 7.93 (bs, 2H), 7.89 (dd, $J = 6.8$ Hz, 4.1, 1H), 7.67 (d, $J = 8.2$ Hz, 2H) 7.59 (d, $J = 8.2$ Hz, 2H), 7.05 (app d, $J = 4.0$ Hz, 2H), 6.60 (app d, $J = 4.0$ Hz, 2H). ^{11}B NMR (160 MHz, CD_2Cl_2) δ 0.23 (t, $J = 26$ Hz). ^{19}F NMR (471 MHz, CD_2Cl_2) -145.5 (q, $J = 29$ Hz). $^{13}\text{C}\{^1\text{H}\}$ NMR (126 MHz, CD_2Cl_2) δ 148.2, 147.5, 144.2, 143.2, 139.3, 135.2, 133.2, 131.91, 131.85, 128.0, 127.3, 119.0 (note: two overlapping signals). $^{125}\text{Te}\{^1\text{H}\}$ NMR (95 MHz, CD_2Cl_2) δ 778.0. HRMS-APCI⁺ m/z [$\text{M}^+ - \text{F}$] calc. for $\text{C}_{19}\text{H}_{13}\text{BFN}_2^{130}\text{Te}$: 429.0213; found: 429.0217.

A.2. Photophysical Characterisation

Using a modified version of a literature procedure,²⁴⁷ photophysical properties of **b4** were determined in dichloromethane solution at room temperature. $\lambda_{\text{abs}}^{\text{max}} = 503$ nm (482 nm shoulder), $\lambda_{\text{em}}^{\text{max}} = 521$ nm, $\Phi_f = 0.01$, Stokes shift = 18 nm. Fluorescence quantum yield (Φ_f) was determined according to the equation: $\Phi_{\text{unk}} = (\Phi_{\text{std}})(n/n_{\text{std}})^2(I_{\text{unk}}/I_{\text{std}})(A_{\text{std}}/A_{\text{unk}})$,²⁴⁸ where Φ is the quantum yield, I is the area under the peaks in the fluorescence spectra, A is the absorbance at the excitation wavelength, and n is the refractive index (dichloromethane = 1.425, ethanol = 1.357). Rhodamine B ($\Phi_f = 0.70$ in ethanol)¹⁵⁸ was chosen as the standard. Fluorescence spectra were recorded using an excitation wavelength

of 490 nm. Quantum yield measurements were determined in dilute solutions ($\lambda_{\text{abs}}^{\text{max}} \leq 0.1$) to avoid inner filter effects and are the composites of ten scans in all cases.

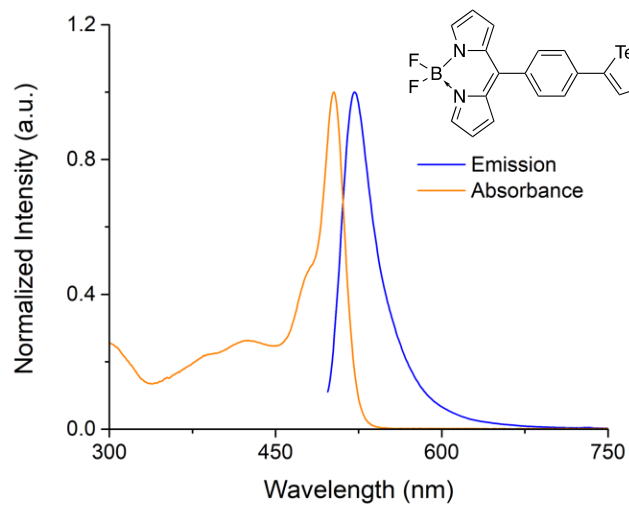


Figure 40. Normalised absorption and emission spectra of compound **b4** in dichloromethane.

A.3. Nuclear Magnetic Resonance Spectra

Figure 41. ^1H NMR spectrum of compound **b1** in CDCl_3

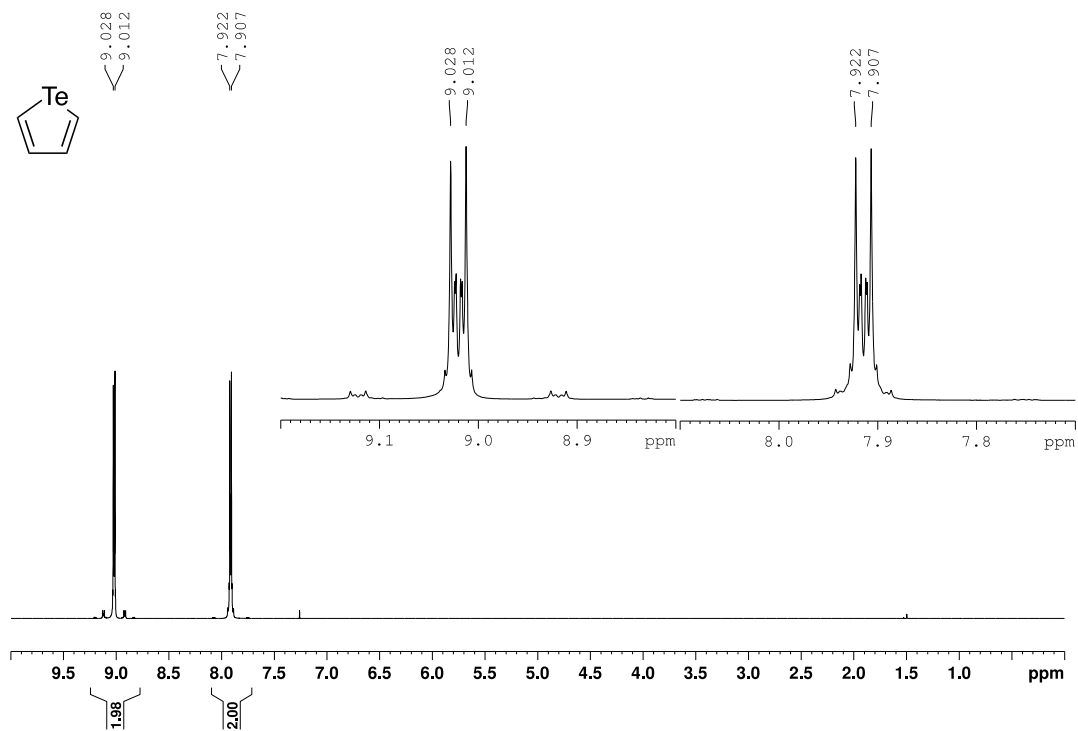


Figure 42. $^{125}\text{Te}\{^1\text{H}\}$ NMR spectrum of compound **b1** in CDCl_3

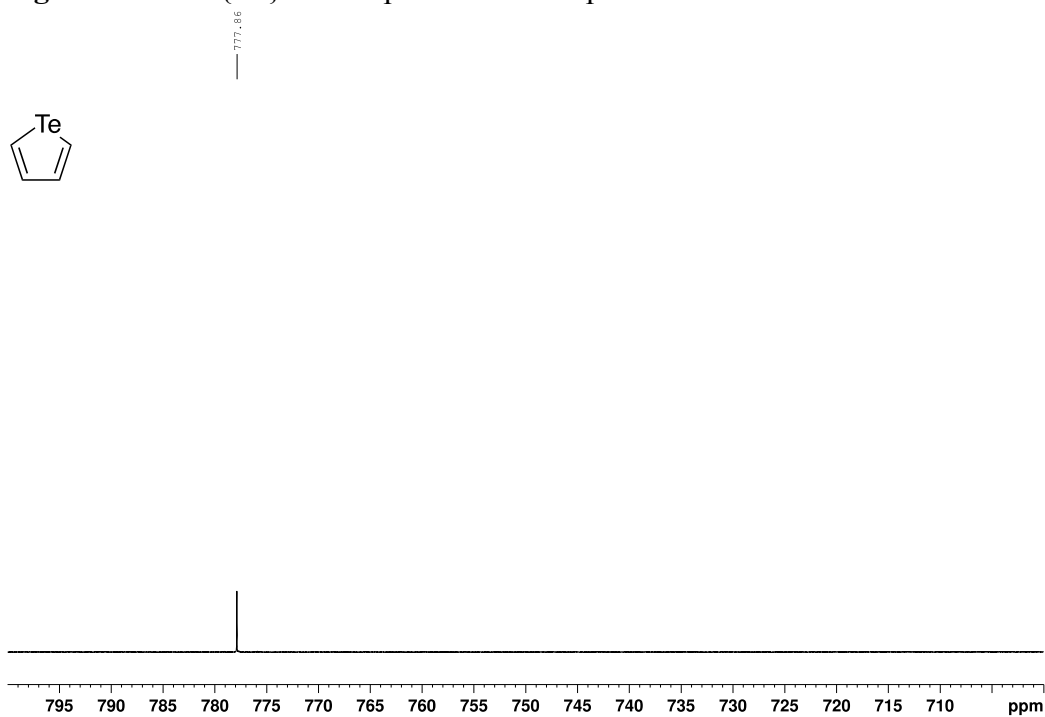


Figure 43. ^1H NMR spectrum of compound **b2** in CDCl_3

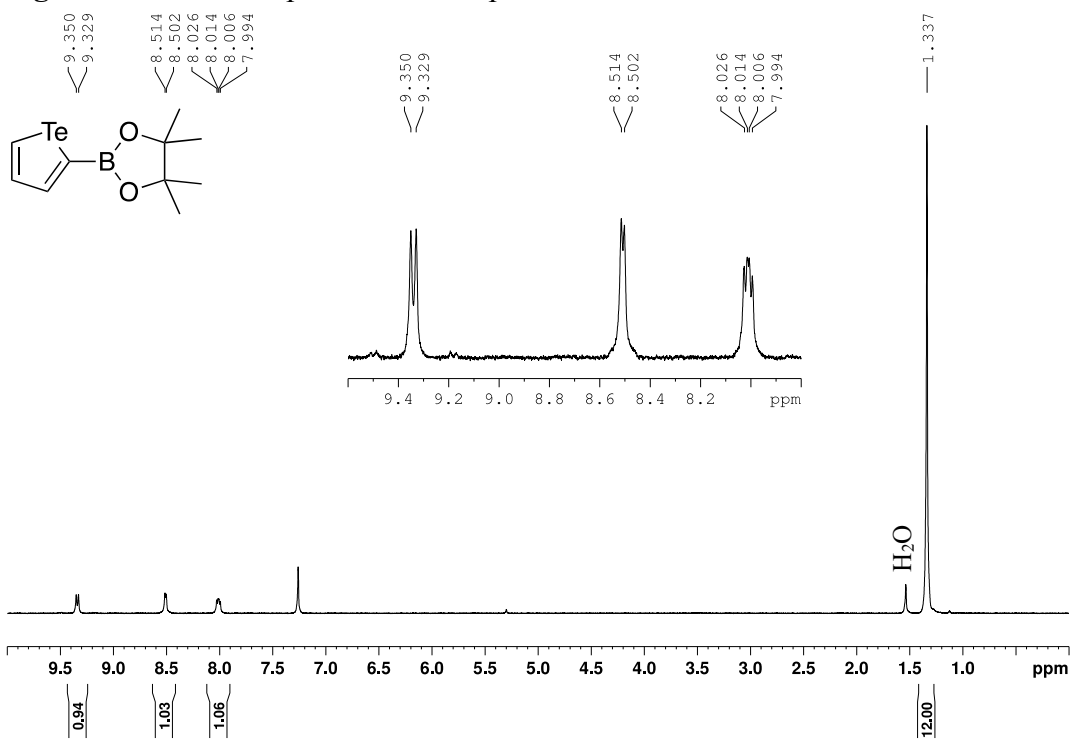


Figure 44. $^{13}\text{C}\{^1\text{H}\}$ NMR spectrum of compound **b2** in CD_2Cl_2

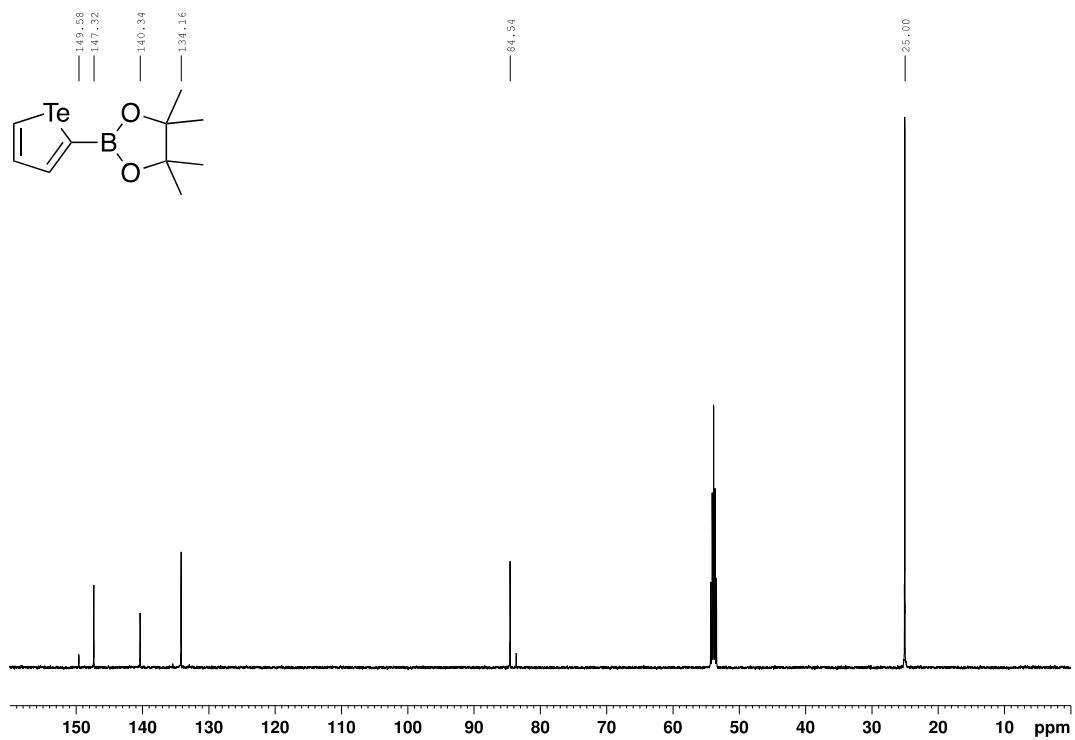


Figure 45. ^{11}B NMR spectrum of compound **b2** in CD_2Cl_2

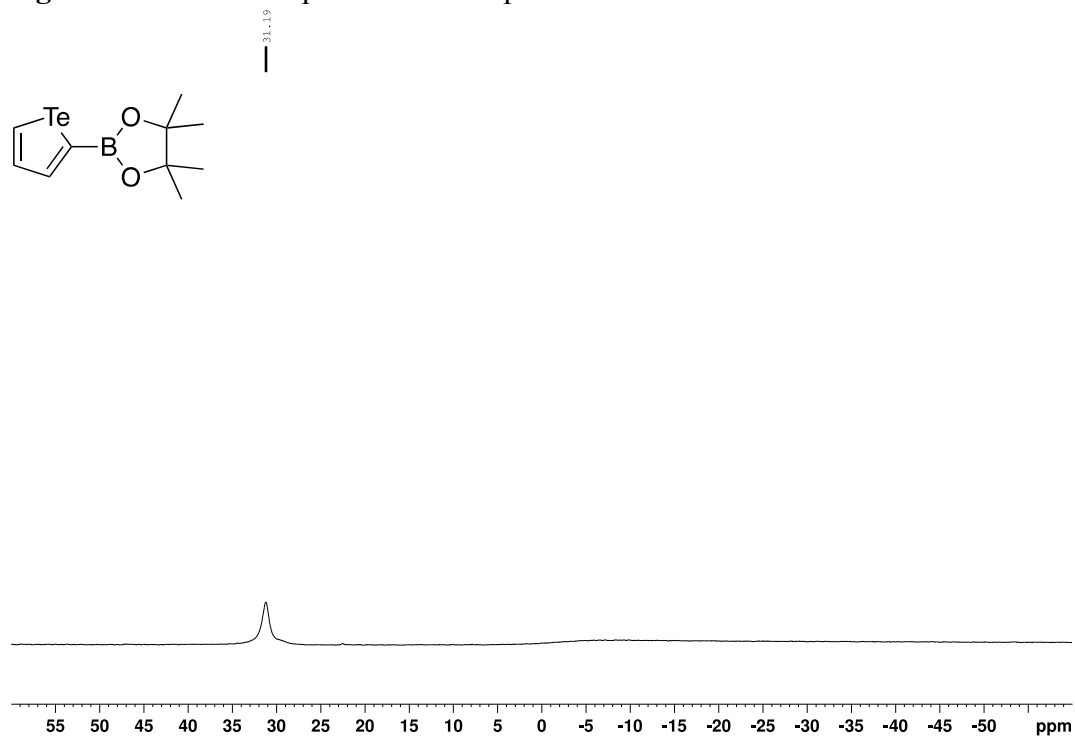


Figure 46. ^1H NMR spectrum of compound **b3** in CDCl_3

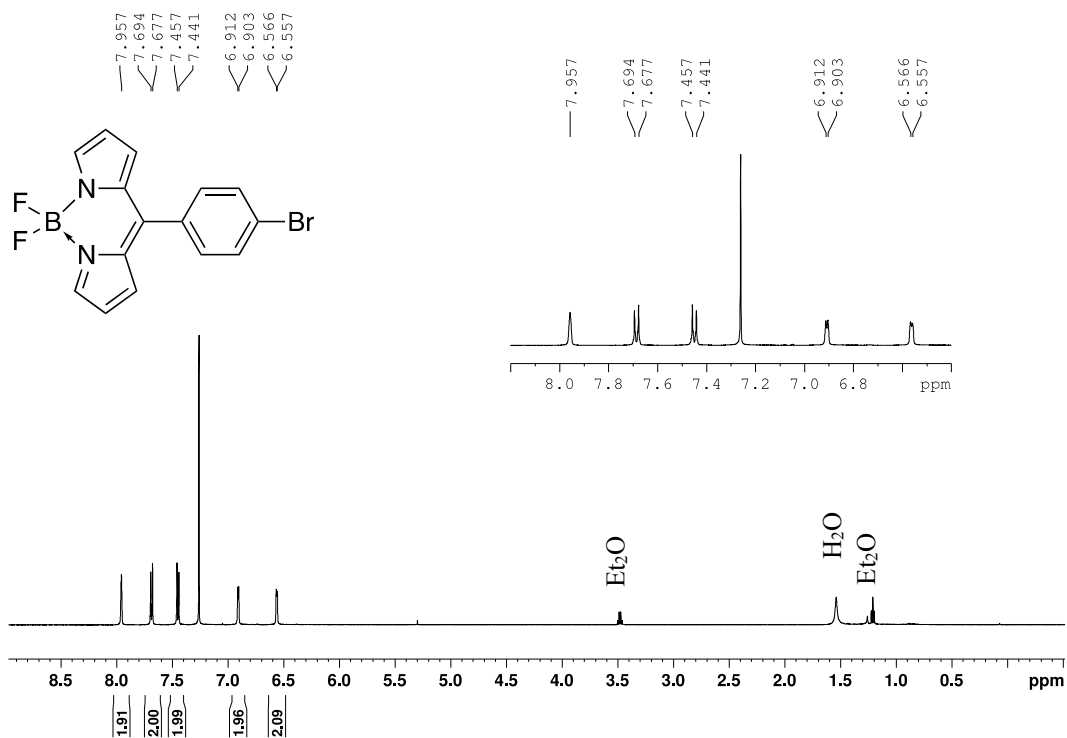


Figure 47. ^1H NMR spectrum of compound **b4** in CD_2Cl_2

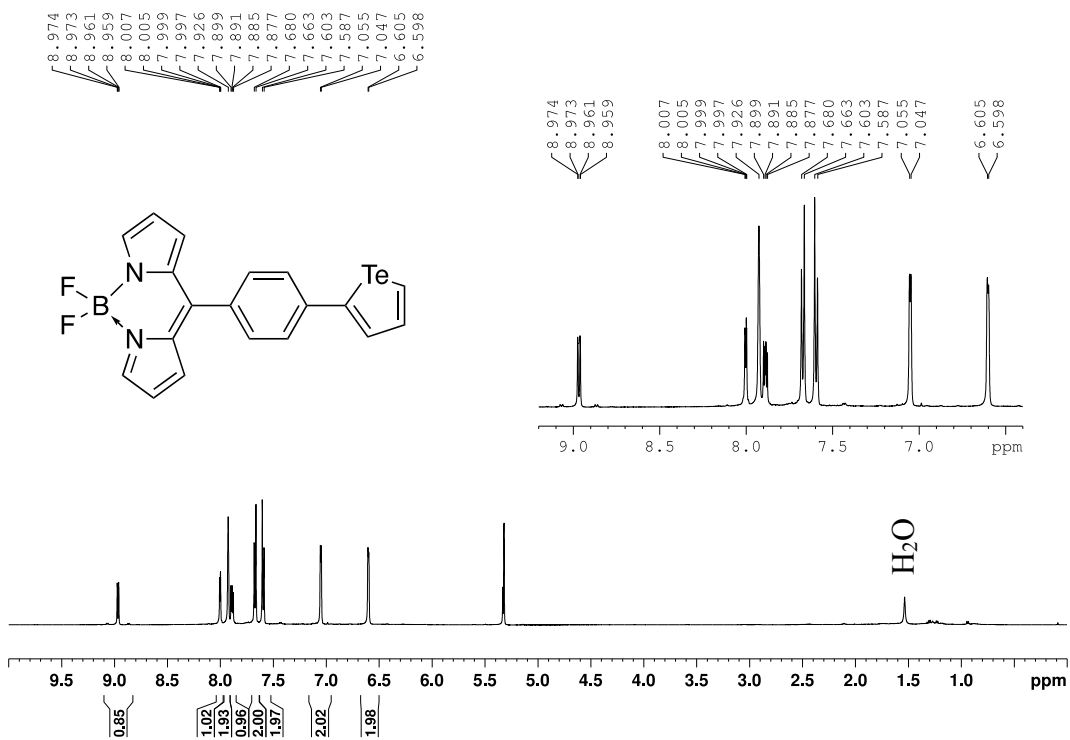


Figure 48. $^{13}\text{C}\{^1\text{H}\}$ NMR spectrum of compound **b4** in CD_2Cl_2

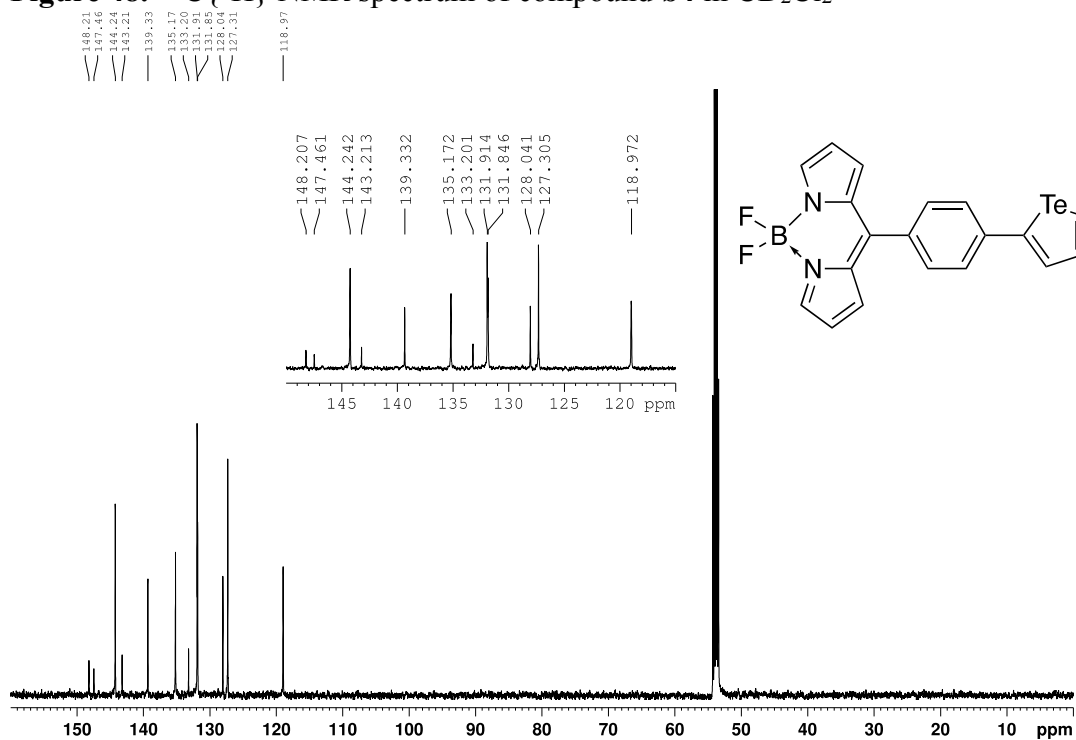


Figure 49. ^{11}B NMR spectrum of compound **b4** in CD_2Cl_2

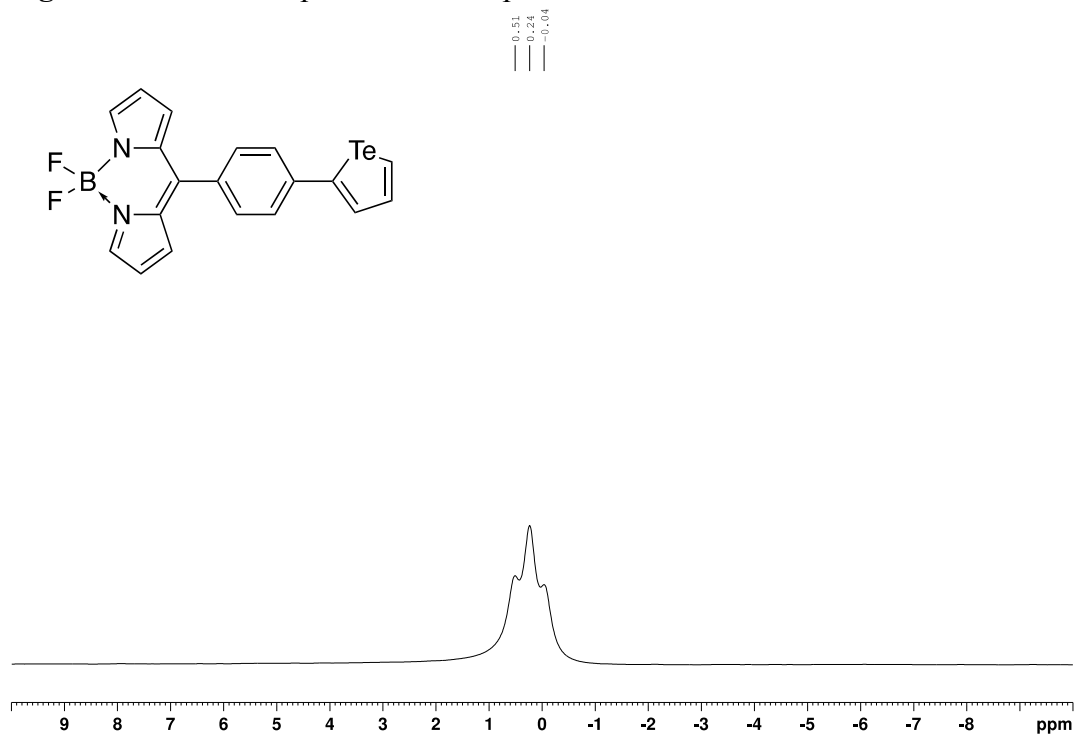


Figure 50. ^{19}F NMR spectrum of compound **b4** in CD_2Cl_2

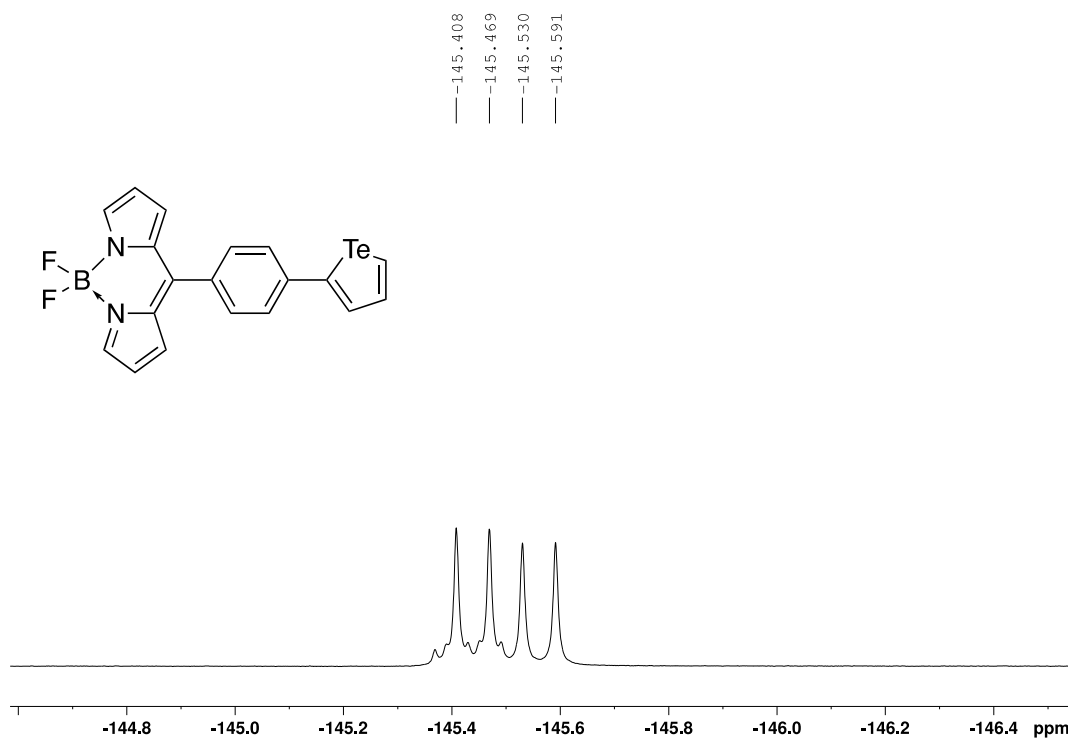


Figure 51. HSQC NMR (126 MHz, 500 MHz) spectrum of compound **b4** in CD_2Cl_2

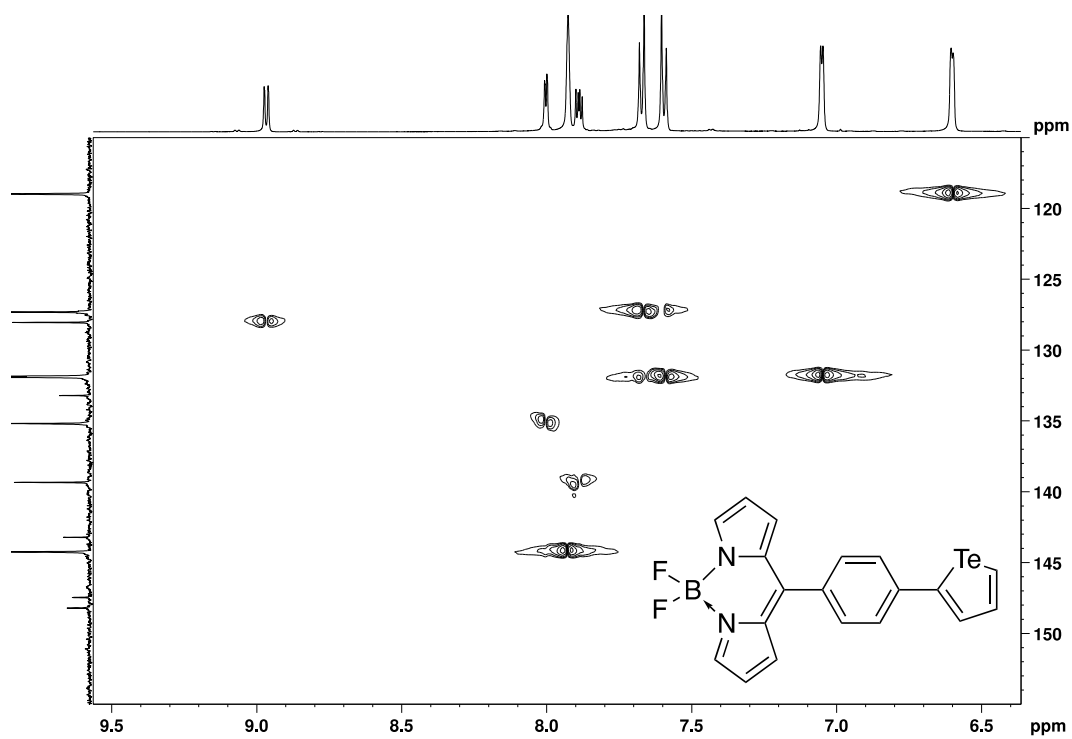
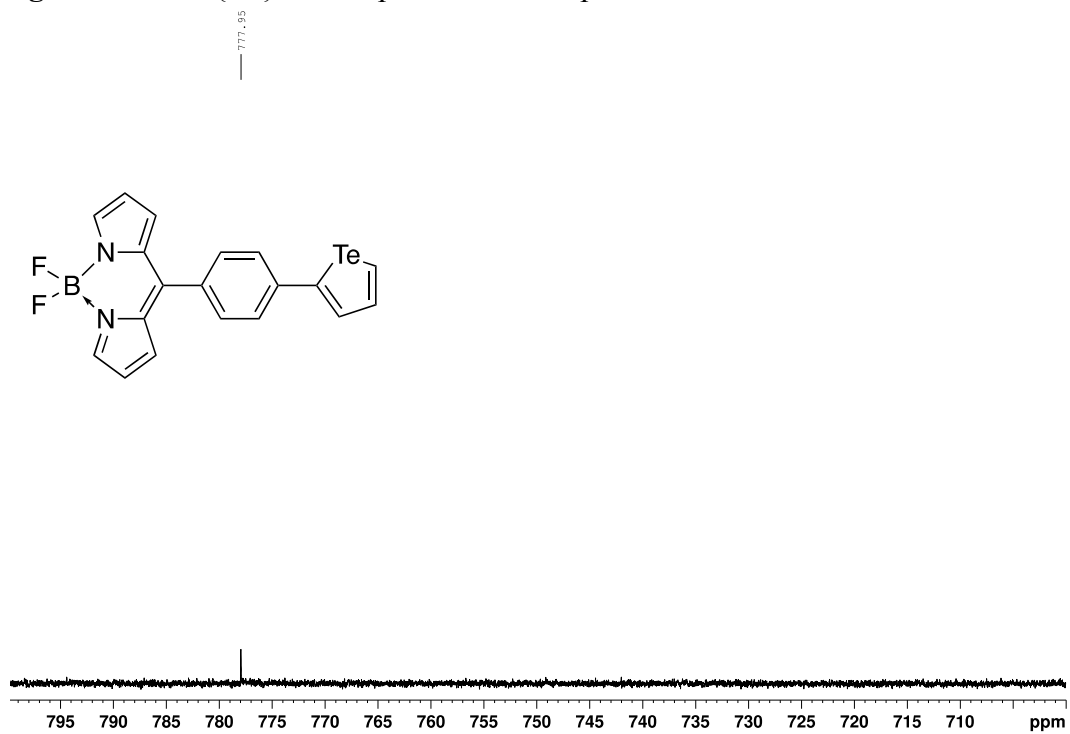


Figure 52. $^{125}\text{Te}\{^1\text{H}\}$ NMR spectrum of compound **b4** in CD_2Cl_2



A.4. Crystallographic Information

The crystal chosen was attached to the tip of a MicroLoop with paratone-N oil. Measurements were made on a Bruker D8 VENTURE diffractometer equipped with a PHOTON III CMOS detector using monochromated Mo K α radiation ($\lambda = 0.71073 \text{ \AA}$) from an Incoatec microfocus sealed tube at either 125 K (**b2**) or 100 K (**b4**).²⁴⁹ The initial orientation and unit cell were indexed using a least-squares analysis of the reflections collected from a 180° phi-scan, 1 second per frame and 1° per frame. For data collection, a strategy was calculated to maximise data completeness and multiplicity, in a reasonable amount of time, and then implemented using the Bruker Apex 3 software suite.²⁴⁹ The crystal to detector distance was set to 4 cm and 10 second frames were collected. Cell refinement and data reduction were performed with the Bruker SAINT²⁵⁰ software, which corrects for beam inhomogeneity, possible crystal decay, Lorentz and polarisation effects. A multi-scan absorption correction was applied (SADABS).²⁵¹ The structures were solved using SHELXT-2014²⁵² and were refined using a full-matrix least-squares method on F^2 with SHELXL-2018.²⁵² The refinements were unremarkable. The non-hydrogen atoms were refined anisotropically. The hydrogen atoms bonded to carbon were included at geometrically idealised positions and were not refined. The isotropic thermal parameters of these hydrogen atoms were fixed at 1.2 U_{eq} of the parent carbon atom or 1.5 U_{eq} for methyl hydrogens.

All diagrams were prepared using the program Mercury CSD 4.3.²⁵³ The data has been deposited with the Cambridge Crystallographic Data Centre. The deposition numbers for each compound are given in **Table 8**.

2-(Pinacolatoboron)tellurophene, b2

Two reflections (2 0 0; -1 1 2) were removed from the refinement, as they were partially obscured by the beam stop. Data was collected to maximum θ angle of 47.18° (0.48 Å resolution). However, the data was cut off at 0.55 Å (40.25°) during refinement using a SHEL instruction.

A rigid bond restraint (DELU) was applied to the Te-C bonds to keep the anisotropic displacement parameters in the direction of the bonds more equal.

8-(4-(Tellurophenyl)phenyl)BODIPY, b4

The final model refined for this structure included a two-part disorder of the 5-membered ring containing the tellurium centre. In essence, the molecule could crystallise with the 5-membered ring containing the tellurium facing in either direction, so that the tellurium atom in each ring is on the right or left side. The occupancies of the two components of the disorder were modelled and they refined to a ratio of 89.94 and 10.06% with errors of 0.05%. To refine the disorder, the two rings were restrained to have similar geometries using a SAME command in SHELXL and the atoms of the two rings were restrained to have similar thermal parameters.

One reflection (1 2 0) was removed from the final refinement as it showed poor agreement between F_{obs}^2 and F_{calc}^2 . The SHELXL calculated Flack and Parson's parameters were 0.020(10) and 0.014(3), respectively. Because these parameters were not quite zero, the structure was refined as a two-component inversion twin with BASF refining to 0.019(10). This result is supported by values calculated for the Hooft and Parson's parameters using the program Platon.²⁵⁴ These values came out to 0.012(1) and 0.029(3), respectively. All

of this suggests that the correct absolute configuration has been chosen and that the structure is not actually twinned.

Table 8. Crystal data and structure refinement details.

Identification code	b2	b4
CCDC deposition number	2092928	2092927
Empirical formula	C ₁₀ H ₁₅ BO ₂ Te	C ₁₉ H ₁₃ BF ₂ N ₂ Te
Formula weight	305.63	445.72
Crystal system	Monoclinic	Orthorhombic
Space group	P2 ₁ /c	Pna2 ₁
Unit cell dimensions (Å and °)	a = 12.7386(6) b = 8.0013(4) c = 12.4763(6) α = 90 β = 110.4540(10) γ = 90	a = 14.0159(5) b = 15.9383(5) c = 7.3025(2) α = 90 β = 90 γ = 90
Volume (Å ³)	1191.48(10)	1631.30(9)
Z	4	4
Density (calculated, Mg/m ³)	1.704	1.815
Absorption coefficient (mm ⁻¹)	2.470	1.848
F(000)	592	864
Crystal size (mm ³)	0.200 x 0.156 x 0.129	0.368 x 0.232 x 0.146
Theta range of data (°)	3.065 to 40.246	2.556 to 47.144

Identification code	b2	b4
Index ranges (h, k, l)	-23/23, -14/14, -	-28/28, -32/32, -15/15
	22/22	
Reflections collected	107188	231231
Independent reflections	7454	14917
R(int)	0.0251	0.0372
Completeness to 25.242° (%)	97.5	98.9
Max. and min. transmission	0.1306 and 0.0603	0.7493 and 0.6452
Data / restraints / parameters	7454 / 3 / 131	14917 / 119 / 273
Goodness-of-fit on F ²	1.044	1.087
Final R indices [I>2σ(I)]	R1 = 0.0159	R1 = 0.0202
	wR2 = 0.0455	wR2 = 0.0524
R indices (all data)	R1 = 0.0171	R1 = 0.0237
	wR2 = 0.0464	wR2 = 0.0543
Absolute structure parameter	n.a.	0.019(10)
Largest diff. peak and hole (e.Å ⁻³)	0.535 and -1.335	0.597 and -0.880

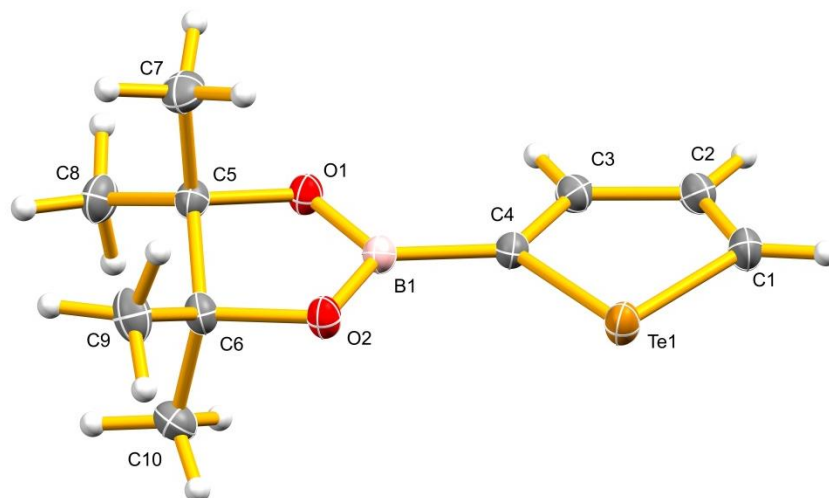


Figure 53. Structure of compound **b2**. Thermal ellipsoids have been drawn at the 50% probability level. Hydrogen atoms have not been labelled.

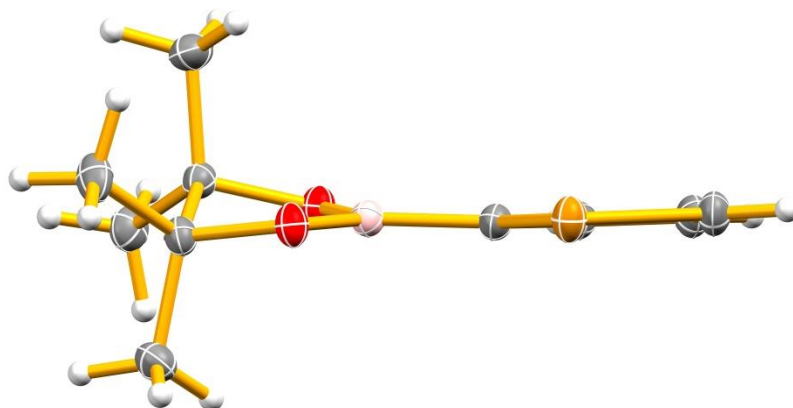


Figure 54. Side-on view of compound **b2**.

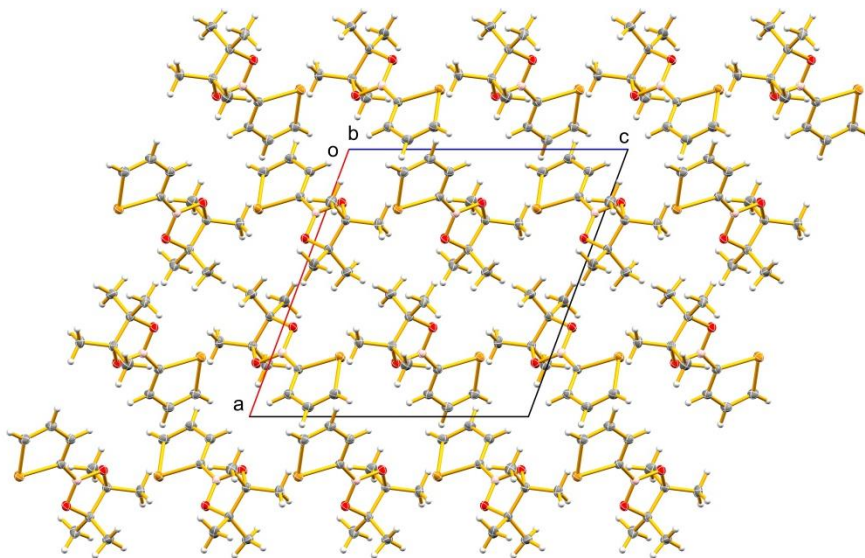


Figure 55. Packing diagram for compound **b2** viewed down the Y-axis.

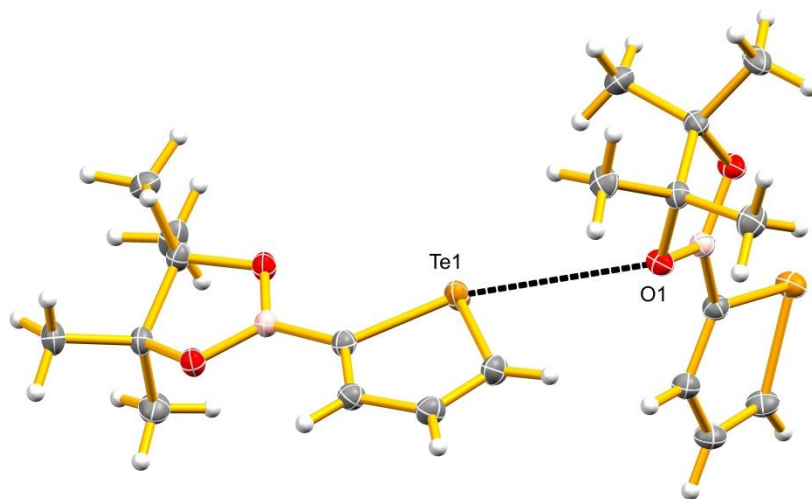


Figure 56. Intermolecular interactions to the sum of the van der Waals radii of the Te atom in compound **b2**. Only the atoms involved in the interactions have been labelled.

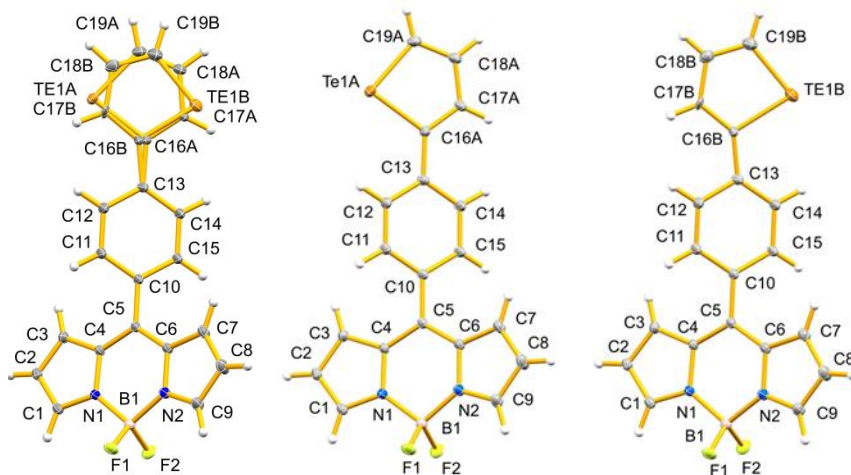


Figure 57. Structure of compound **b4**. The two-part disorder of compound **b4** (left) has been modelled by two ordered parts, part A 89.94(5) % and part B 10.06 % (centre and right, respectively). Thermal ellipsoids have been drawn at the 50% probability level. Hydrogen atoms have not been labelled.

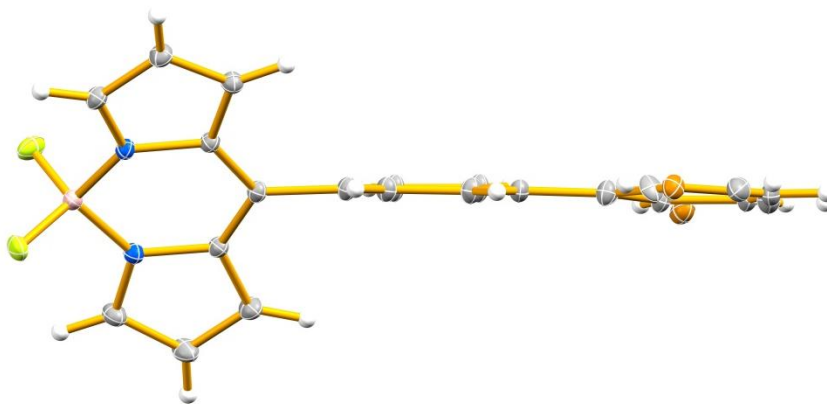


Figure 58. Side-on view of compound **b4**.

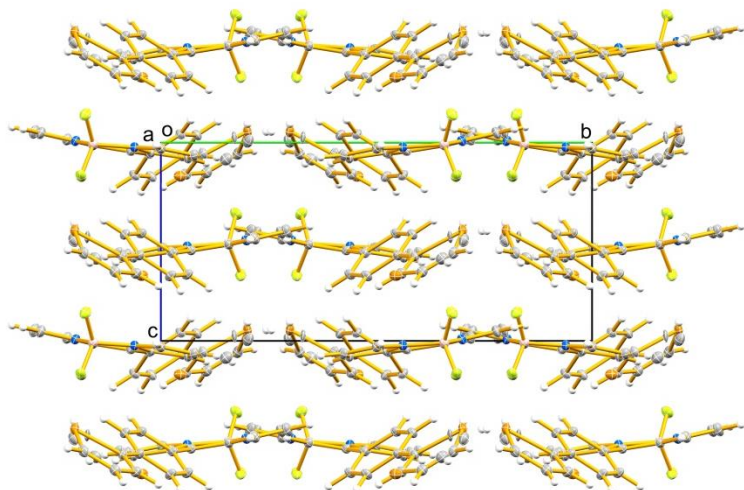


Figure 59. Packing diagram for compound **b4** viewed down the X-axis.

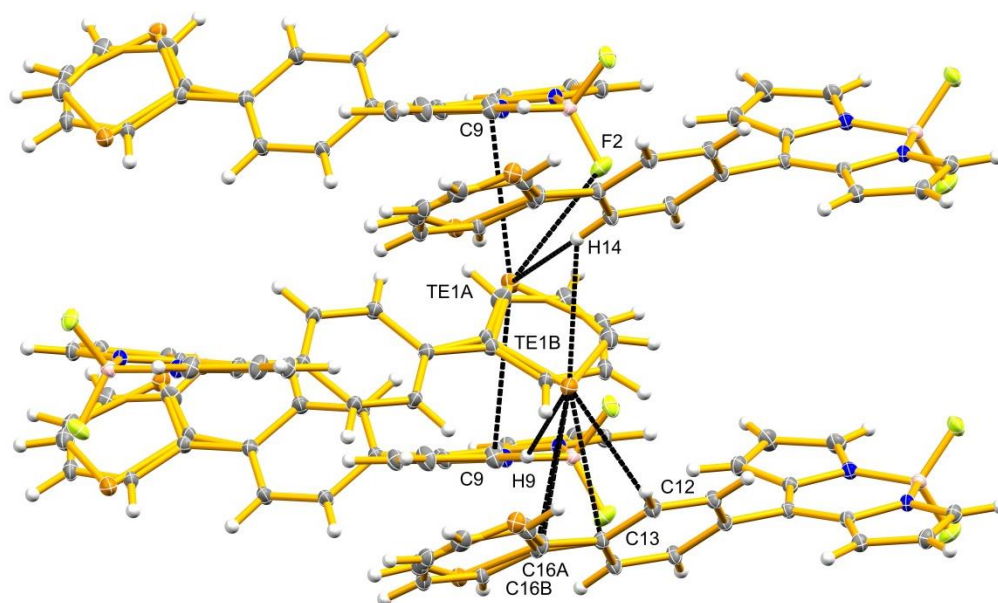


Figure 60. Intermolecular interactions to the sum of the van der Waals radii of the Te atoms in one central molecule of compound **b4**. Only the atoms involved in the interactions have been labelled.

A.5. Singlet Oxygen Detection Experiments

A.5.1. Spectra General Considerations

Absorbance spectra were obtained with a Shimadzu UV-1800 UV Spectrophotometer. All spectra were recorded in a 60 μL or an 800 μL quartz cuvette, both with a 1.0 cm path length from Starna Scientific Ltd.

A.5.2. UV-Vis Absorbance Spectra

Absorbance spectra were obtained in both phosphate buffered saline (PBS) and in MeOH with 2% DMSO. Concentrated stock of **b4** was made in DMSO, and diluted to a final concentration of 2% DMSO into either a 60 μL or 800 μL cuvette for PBS and MeOH, respectively. The solutions were diluted until absorbance of the λ_{max} was between 0.2 – 1 AU and then normalised to 1 AU at the λ_{max} .

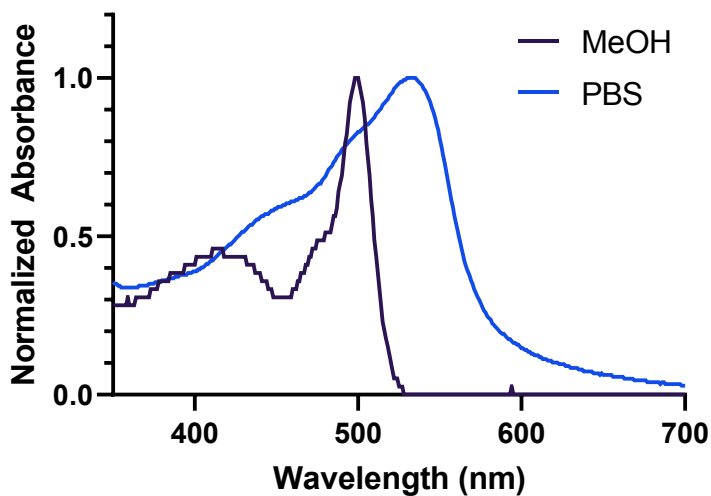


Figure 61. Absorbance of compound **b4** in MeOH and PBS with 2% DMSO. λ_{max} values were 499 nm in MeOH and 532 nm in PBS, respectively.

A.5.3. Determination of Molar Extinction Coefficients (ϵ) in DMSO Using Quantitative NMR

Compound **b4** was dissolved in 392 μL DMSO- d_6 and 8 μL of a 500 μM stock solution of 1,4-dioxane in DMSO- d_6 was added. This provided a final concentration of 10 μM 1,4-dioxane as a standard. The sample was then analysed using a Bruker 400 MHz NMR spectrometer. 1,4-Dioxane has only one peak at δ 3.57 ppm, representing 8 protons whereas a single peak for compound **b4** (δ 6.71 ppm, 2 protons) was chosen and used in the equation below:

$$M_a = (M_b) \left(\frac{\text{integral}_a / \text{protons}_a}{\text{integral}_b / \text{protons}_b} \right)$$

Where: M = molarity, a = compound **b4**, b = 1,4-dioxane

The equation allows us to calculate the concentration of probe within the sample by taking a ratio of integrals and comparing it to the concentration of 1,4-dioxane. Each sample was then serially diluted with DMSO and had their absorbances measured in a 60 μL cuvette. Monitoring at the λ_{max} , a slope of the absorbance vs concentration was generated to determine the molar extinction coefficient (ϵ) using the Beer-Lambert Law ($A = \epsilon bc$, where b is 1cm). All measurements were repeated in triplicate.

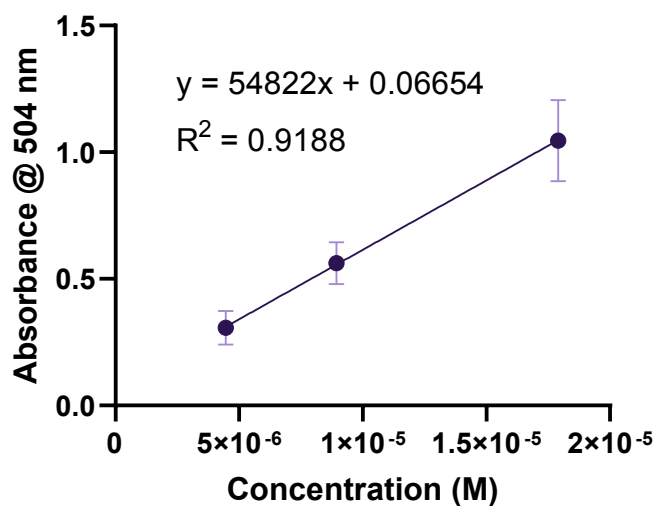


Figure 62. Determination of molar extinction coefficient of compound **b4** in DMSO

A.5.4. Singlet Oxygen Quantum Yield Experiments

An initial experiment was performed to confirm the generation of singlet oxygen ($^1\text{O}_2$) using 1,3-diphenylisobenzofuran (DPBF) as the $^1\text{O}_2$ sensor. Concentrated DMSO stock of **b4** was diluted to $1 \mu\text{M}$ in MeOH with 2% DMSO in an $800 \mu\text{L}$ cuvette. $110 \mu\text{M}$ of DPBF was then added and the sample was irradiated with a 490 nm LED to obtain slopes of the degradation of DPBF. The singlet oxygen quantum yield (Φ_Δ) for **b4** was determined by comparing it to eosin Y (EY, $\Phi_\Delta = 0.42$ in MeOH)¹⁸⁵ as a reference standard. The absorbances for **b4** and eosin Y were matched within 10% at the irradiation wavelength. Control experiments using just DPBF and irradiation alone were also conducted to monitor DPBF degradation under irradiation conditions. Finally, to calculate the Φ_Δ , the following equation was used.²⁵⁵

$$\Phi_{\Delta unk} = \Phi_{\Delta std} \left(\frac{1 - 10^{-A_{std}}}{1 - 10^{-A_{unk}}} \right) \left(\frac{m_{unk}}{m_{std}} \right)$$

Where: unk = unknown, std = standard, A = absorbance, m = slope of DPBF degradation

The equation does not consider refractive indexes or irradiation power as experiments were conducted under the same solutions and LED (**Table 10**). The absorbances between the standard and compound **b4** were corrected for in the equation and the slopes were used after subtracting the background of DPBF degrading under irradiation alone. Quenching experiments were done using the same irradiation conditions and concentrations of **b4** and DPBF as above and introducing a final concentration of 10 mM NaN₃ into the solution. All measurements were done with n = 6.

Table 9. LED specifications used for singlet oxygen experiments

Compound	LED Used	Wavelength (nm)	FWHM	Power (mW/cm ²)
b3	M490L4	490	26	28.0
b4	M490L4	490	26	17.0

LED were purchased from Thorlabs. Power of LEDs determined using a Newport Optical Power Meter Model 1916-R at a 1 cm distance from LEDs.

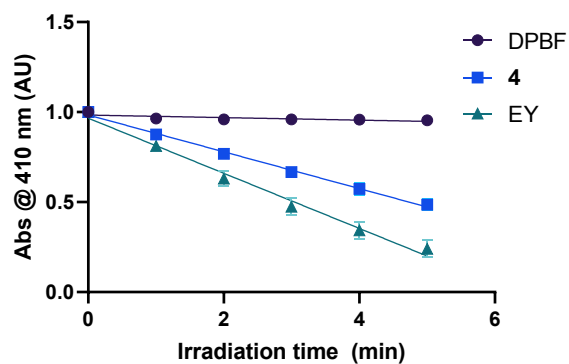


Figure 63. Singlet oxygen generation of compound **b4** (1 μ M) was compared to Eosin Y in MeOH with irradiation at 490 nm (17.0 mW/cm²) at room temperature. Experiments were conducted n = 6 times.

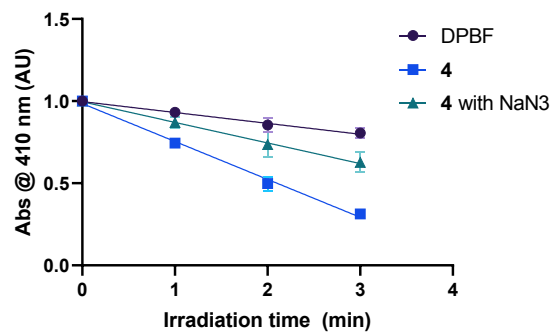


Figure 64. Quenching of ¹O₂ production of compound **b4** with NaN₃ in MeOH at room temperature (1 μ M) under irradiation at 490 nm (17.0 mW/cm²). Experiments were conducted in triplicate.

A.5.5. Photostability of BODIPY compounds

Photostability experiments were conducted using the same conditions and LED as the Φ_{Δ} experiments above. Compound **b4** was diluted to 1 μM in 2% DMSO and MeOH and irradiated using the respective LED. The λ_{max} was monitored and plotted to observe if any photobleaching had occurred. No substantial degradation was noticed, and all measurements were conducted in triplicate.

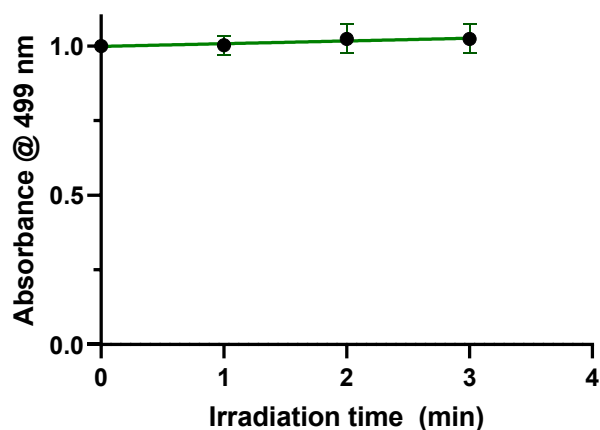


Figure 65. Photostability of compound **b4** (1 μM) under irradiation at 490 nm (17.0 mW/cm^2) in MeOH at room temperature. Experiments were conducted in triplicate.

A.5.6. Singlet Oxygen Determination of Compound **b3**

Experiments were conducted similar to compound **b4**, using DPBF as the $^1\text{O}_2$ sensor. Compound **b3** was diluted to 2 μM in MeOH with 2% DMSO in an 800 μL cuvette. 110 μM of DPBF was then added and the sample was irradiated with the 490 nm LED at a higher intensity than **b4** to obtain the slopes of degradation of DPBF. Compared to EY, the $^1\text{O}_2$ generation was minimal.

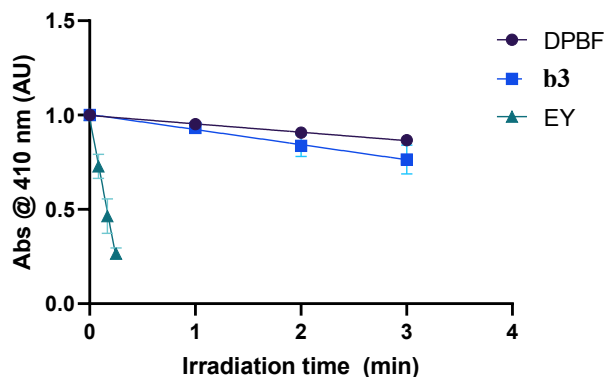


Figure 66. Singlet oxygen generation of compound **b3** (2 μ M) was compared to Eosin Y in MeOH with irradiation at 490 nm (28.0 mW/cm²) at room temperature. Minimal ¹O₂ was detected, and experiments were conducted in triplicate.

A.6. Cell Assays and Viability

A.6.1. Cell Culture General Notes

HeLa cells were maintained in a 75 cm² culture flask (NuncTM EasYFlaskTM 75 cm² NunclonTM Delta Surface) at 37 °C and 5% CO₂ atmosphere in a Thermo Scientific Forma Steri-Cycle CO₂ Incubator. The cells were grown in Dulbecco's Modified Eagle Medium (DMEM) with sodium pyruvate, 4.5 g/L glucose and L-glutamine (Wisent Inc.) supplemented with 10% fetal bovine serum and 1% antibiotics/antimycotics (complete growth medium). Unless otherwise stated, all incubations were conducted in the incubator using DMEM.

A.6.2. Cell viability Assays

HeLa cells were seeded at a density of 25,000 cells per well in four separate 96-well plates (Thermo Scientific Nunclon™ Delta Surface) and incubated with 200 μ L DMEM overnight. The following day, the media was removed, and the cells were washed with D-PBS and replaced with 200 μ L Opti-Minimal Essential Medium (Opti-MEM™, Thermo Scientific). Compound **b4** was then added at their respective concentrations (0 – 7.9 μ M), to a final DMSO concentration of 1% and incubated for 3 hours. After incubation, cells were washed with D-PBS and replaced with 200 μ L of DMEM. One plate was kept in the dark while the other three plates were irradiated with a 525 nm lamp for 1, 3, and 5 minutes respectively before incubating the cells overnight. On the following day, 20 μ L of a 5 mg/mL solution of thiazolyl blue tetrazolium bromide (MTT) in D-PBS was added to each well and incubated for 3 hours. The media was then removed and 150 μ L DMSO was added to dissolve the formazan products. Plates were then read at 565 nm using a BioTek Synergy™ HTX Multi-Mode Microplate Reader. Absorbance values were then used to calculate the cell viability using the following equation and all viability experiments were conducted in triplicate. Cell viability with 1% DMSO incubation and irradiation alone were also conducted in triplicate to show toxicity is only present with compound.

$$Cell\ Viability = \left(\frac{A_{sample}}{A_{control}} \right) (100\%)$$

Table 10. Lamp specifications used for cell experiments

Compound	Lamp Used	Wavelength (nm)	FWHM	Power (mW/cm ²)
b4	525 nm Lamp	525	N/A	23.60

The lamp used was a Philips LED 90 W equivalent PAR38 Green Lamp (Model # 473736). Power of the lamp were determined using a Newport Optical Power Meter Model 1916-R at a 1 cm distance from LEDs.

Table 11. IC₅₀ of compound **b4**

Conditions	IC ₅₀ (μM)	Light Fluence Rates (J/cm ²)	Phototoxic Index
Dark	1.35	N/A	N/A
1 min Irradiation	0.094	1.42	14
3 min Irradiation	0.053	4.25	25
5 min Irradiation	0.017	7.08	79

Absolute IC₅₀'s are reported. Compound **b4** was left in the dark or irradiated for 5 minutes with the light source. Experiments were conducted in triplicate.

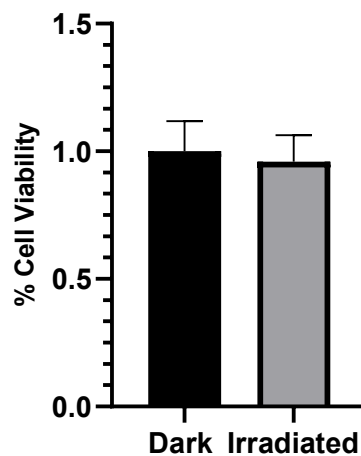


Figure 67. Cell viability of HeLa cells under 5-min irradiations and in the dark. No phototoxicity was observed under irradiation conditions with the 525 nm lamp (23.60 mW/cm²). Experiments were done in triplicate.

A.6.3. Determining Reactive Oxygen Species Generation Within Cells

HeLa cells were seeded at a density of 40,000 cells per well in an 8-well chamber (Thermo Scientific Lab-Tek™ Chambered #1.0 Borosilicate Coverglass System) and incubated with 250 µL DMEM overnight. The following day, the cells were washed with D-PBS once and replaced with 250 µL Opti-MEM containing 0-100 nM **b4**. Plates were incubated for 3 hours before washing with D-PBS and incubating the cells for 30 minutes with 250 µL of Opti-MEM with 10 µM 2',7'-dichlorofluorescein diacetate (DCFDA). Cells were then washed once with D-PBS and replaced with 250 µL Opti-MEM. Cells were imaged, then irradiated with a 525 nm green lamp (23.60 mW/cm²) for 5 minutes and imaged again. All fluorescence microscopy images and brightfield images were taken on an Olympus 1X73 inverted microscope. Olympus CellSens Dimension V1.19 software was used to analyse and adjust the images. The filter cube used to image the DCFDA had a 440 – 470 nm excitation bandpass filter, a 495 nm dichroic mirror and a 525–550 nm emission bandpass filter.

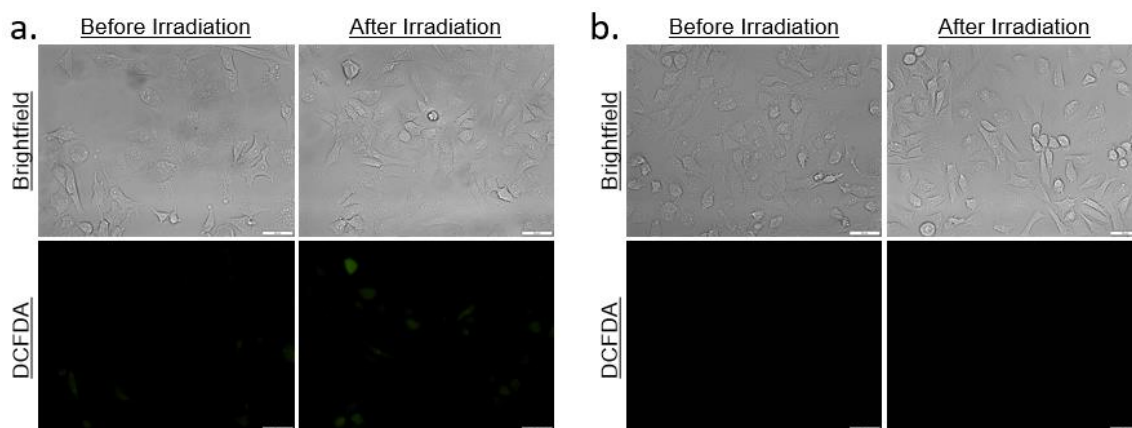


Figure 68. Controls for intracellular ROS detection. (a) Cell incubated with 10 μM DCFDA before and after 5-minute irradiation with 525 nm lamp ($23.60 \text{ mW}/\text{cm}^2$) (b) Cells incubated with 25 nM **b4** without DCFDA before and after 5-minute irradiation with 525 nm lamp ($23.60 \text{ mW}/\text{cm}^2$).

A.6.4. Mechanism of Cell Death

HeLa cells were seeded at a density of 40,000 cells per well in an 8-well chamber (Thermo Scientific Lab-Tek™ Chambered #1.0 Borosilicate Coverglass System) and incubated with 250 μL DMEM overnight. The following day, the cells were washed with D-PBS once and replaced with 250 μL Opti-MEM containing 1.25 μM **b4** (1% DMSO). Plates were incubated for 3 hours before washing once with D-PBS and replacing media with DMEM. Each well was irradiated for 5 minutes using the 525 nm green lamp ($23.60 \text{ mW}/\text{cm}^2$) and left for four hours in the incubator. From here, Invitrogen eBioscience™ Annexin V Apoptosis Detection Kit FITC (Cat # 88-8005-72) was used, and the protocol is summarised here. Cells were washed with cold D-PBS and replaced with 250 μL 1X binding buffer. 5 μL Annexin V-FITC was added and incubated for 10 minutes. Cells were washed with 1X binding buffer and placed back into 250 μL 1X binding buffer. 5 μL

propidium iodide staining solution was added and cells were incubated for another 10 minutes. Cells were washed one more time with 1X binding buffer and imaged in 250 μ L 1X binding buffer.

Imaging was conducted using two filter sets: the DCFDA filter set described above, and a filter cube with a 503-557 nm excitation bandpass filter, a 580 dichroic mirror, and a 600-700 emission bandpass filter. The DCFDA filter was used to analyse the Annexin V-FITC fluorophore while the second filter set was used to image the propidium iodide.

A.6.5. Cell Spheroid

HeLa cells were seeded at a density of 1000 cells per well in two different Nunclon™ Sphera™ 96-Well, Nunclon Sphera-Treated, U-Shaped-Bottom Microplates in 150 μ L Opti-MEM with 1% antibiotics/antimycotics. Cells were left to grow in the incubator for three days until they reached an appropriate size monitored by brightfield imaging. Stocks of **b4** were made ranging from 0-200 nM in Opti-MEM (1% DMSO). 50 μ L of Opti-MEM was removed from each well carefully to not disturb the spheroids and 100 μ L of the **b4** stocks were added to the respective wells to a final concentration ranging from 0-100 nM. Spheroids were incubated for 3 hours and irradiated for 5 minutes using the 525 nm green lamp (23.60 mW/cm²) and left overnight. The next day, ReadyProbes™ Cell Viability Imaging Kit (Blue/Green) was used following the protocol. Four drops of each viability stain were added to 1 mL of Opti-MEM. 100 μ L was carefully removed from each well and 100 μ L of viability stain solution was added and incubated for 15 minutes at room temperature. Cells were directly imaged without any washes.

Two filter sets were used to image the cells, the DCFDA filter cube explained above and a Semrock DAPI-50-LP-A-OFF-ZERO filter cube with a 337 nm (50 nm bandwidth) single band exciter, a 409 nm long pass emitter, and a 409 nm single band dichroic mirror. The DCFDA filter cube was used to image the green fluorophore while the DAPI filter cube was used to image the blue viability dye.

A.7. Mass Cytometry

HeLa cells were seeded at a density of 300,000 cells per well in a 6 well plate (Thermo Scientific Nunclon™ Delta Surface) with 2 mL DMEM overnight. Cells were then washed with D-PBS once and replaced with 1 mL Opti-MEM (1% DMSO) containing the respective concentration of **b4** (25 – 4000 nM). Cells were incubated for 3 hours in the dark before following a modified Fluidigm Maxpar Cell Surface Staining protocol. All consumables and protocols were obtained from the Centre for Advanced Single Cell Analysis at SickKids hospital.

To summarise, cells were resuspended into a V-bottom FACS staining tube and counted (~1 million cells per concentration). Cells were then pelleted, the solvent was removed and cells were resuspended and washed with 2 mL D-PBS. Cells were once again pelleted, the solvent was aspirated and resuspended in 100 µL D-PBS at room temperature. 100 µL of 2 µM cisplatin stock was added to each tube and samples were incubated for 5 minutes at room temperature. To quench the cisplatin, 2 mL of CSM CyTOF Staining Media (SM) was added and cells were pelleted. The solvent was removed and cells were washed once with D-PBS before pelleting again. To each tube, 1 mL of 75 nM iridium solution (PBS/SAP containing 1.6% FA) was added and incubated overnight at 4°C. The next day,

cells were pelleted, aspirated and washed with 3 mL SM. The cells were then treated 3 times with D-PBS (pelleted, solvent removed and washed) before pelleting and removing the remaining solvent. The dry cell pellets were then placed on ice and transported to the CyTOF facility and run on the Helios (CyTOF).

75 thousand events were collected for each concentration and all data obtained were normalised against industry-standard EQ beads to correct for signal variation from the instrument. The data was then analysed using the FlowJo software to generate an overlaid histogram and determine the mean ^{130}Te intensities at each concentration of **b4**.

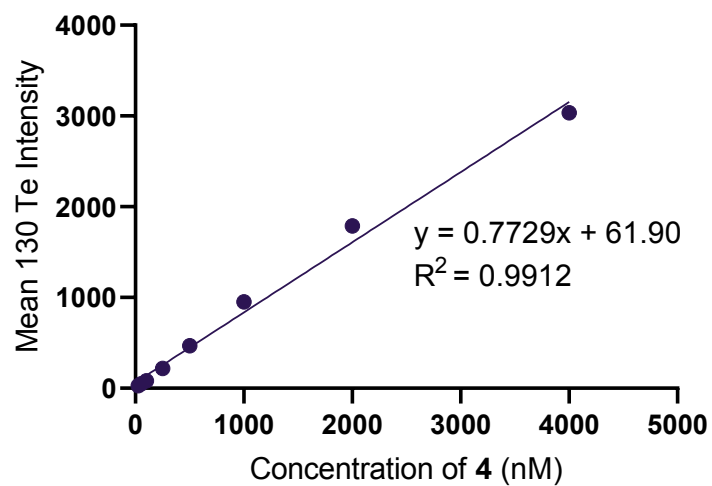


Figure 69. A plot of ^{130}Te intensities versus concentration of **4**. 75 thousand events were taken per concentration.

Appendix B. Chapter 2, Section 2.3 Supporting Information

B.1. General Remarks

Reagents were commercially available and used without further purification unless otherwise discussed. Pyrrole was distilled under reduced pressure and stored in a nitrogen-filled Schlenk flask in the freezer. Anhydrous solvents were purchased from Millipore Sigma or Acros Organics and used without further drying. Manipulations requiring inert atmospheres were conducted under nitrogen and using Schlenk line procedures. Nuclear magnetic resonance (NMR) spectra were recorded using Bruker AVANCE 500 MHz or 300 MHz spectrometers. ^1H chemical shifts are reported in ppm relative to tetramethylsilane using the solvent residual as an internal standard ($\delta = 7.26$ for chloroform).²⁴² ^{13}C chemical shifts are reported in ppm relative to tetramethylsilane, referenced to the resonances of CDCl_3 ($\delta = 77.2$ ppm) and were proton decoupled.²⁴² Trace impurities and residual solvent peaks were determined using tables developed by Nudelman *et al.*²⁴² Coupling constants were reported in Hertz (Hz) and spin multiplicities were reported using the following symbols: s (singlet), bs (broad singlet), d (doublet), dd (doublet of doublets), t (triplet), m (multiplet), and app (apparent). ^{11}B chemical shifts are reported in ppm, externally referenced to boron trifluoride diethyl etherate ($\delta = 0.00$). ^{19}F chemical shifts are reported in ppm, externally referenced to CFCl_3 ($\delta = 0.00$). NMR spectra were processed using Bruker TopSpin 4.0 software. ^{125}Te NMR spectra were recorded using a Bruker AVANCE 300 MHz spectrometer; chemical shifts are reported in

ppm relative to Me₂Te₂, externally referenced to diphenyl ditelluride ($\delta = 422$ ppm).²⁴³ Thin layer chromatography was performed using commercially prepared silica gel plates or alumina plates and visualised using long- or shortwave UV lamps. Column chromatography was performed either on 230-400 mesh silica or 58 Å neutral alumina. The relative proportions of solvents mentioned in column chromatography refer to a volume-to-volume ratio. Mass spectra were recorded using a Bruker microTOF Focus Mass Spectrometer.

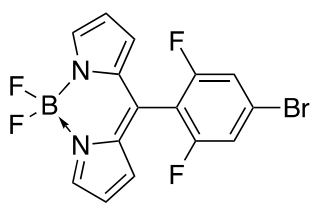
B.2. Experimental

B.2.1. General Procedure for the Synthesis of 8-(4-bromophenyl)BODIPYs, GP1

Using a modified version of literature procedures,^{146,244–246} in a 250 mL round-bottom flask the corresponding aldehyde (1.00 g, 1 equiv.) was added to nitrogen-sparged 0.018 M HCl (100 mL) and the mixture then stirred under a nitrogen atmosphere. Freshly distilled pyrrole (3 equiv.) was transferred drop-wise *via* syringe into the flask and the reaction mixture was stirred for 3 h (all reactions were performed at room temperature unless otherwise stated). The crude reaction mixture was extracted into dichloromethane (3 × 100 mL) and the combined organic fractions were washed with water, dried over sodium sulfate and concentrated under reduced pressure. The resulting crude oil was purified *via* column chromatography over silica, loading in dry silica and first eluting with 1% triethylamine in hexanes until all unreacted pyrrole was eluted. Then, a gradient of 0 → 25% ethyl acetate in hexanes was used until all dipyrromethane was eluted. The fractions were concentrated under reduced pressure and an aliquot was taken to confirm the absence of starting materials using ¹H NMR spectroscopy. The mass of dipyrromethane was recorded and used

to calculate equivalences for the following steps. The crude dipyrromethane was dissolved in dry dichloromethane (40 mL) under a nitrogen atmosphere. 2,3-Dichloro-5,6-dicyano-1,4-benzoquinone (2 equiv.) was added, and the reaction mixture was stirred at room temperature overnight (16 h). Triethylamine (6 equiv.) was then added to the reaction mixture, *via* syringe, followed by boron trifluoride diethyl etherate (9 equiv.). After stirring the reaction mixture for 1.5 h, second aliquots of triethylamine (6 equiv.) and boron trifluoride diethyl etherate (9 equiv.) were added, followed by stirring for a further 1.5 h.²⁴⁴ The crude reaction mixture was filtered through a silica gel plug, eluting with dichloromethane, and the resulting mixture was evaporated under reduced pressure. Then, the residue was taken up in ether and washed with 1 M HCl (5× 50 mL), and 6 M HCl (1× 50 mL). The organic layer was dried over sodium sulfate and concentrated down under reduced pressure. This solution was then filtered through a basic alumina plug and finally concentrated to dryness under reduced pressure to afford dark purple crystalline material.

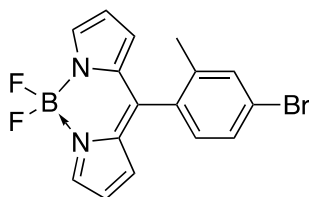
B.2.2. Synthesis of 8-(4-bromo-2,6-difluorophenyl)BODIPY, **b5**



Following **GP1**, 4-bromo-2,6-difluorobenzaldehyde (1.0 g, 4.52 mmol) was reacted with pyrrole (0.94 mL, 13.6 mmol) under weakly acidic conditions to afford the corresponding dipyrromethane after column purification (0.63 g, 1.87 mmol). The BODIPY was formed by first oxidation using 2,3-dichloro-5,6-dicyano-1,4-benzoquinone (0.85 g, 3.74 mmol) and complexation using triethylamine (3.1 mL, 22.4 mmol) and boron trifluoride diethyl etherate (4.1 mL, 33.6 mmol) over two additions to afford the title compound (210 mg, 12% yield) as a dark purple crystalline solid after aqueous workup and a basic alumina

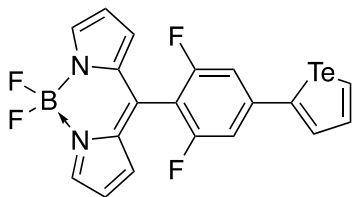
plug. ^1H NMR (500 MHz, CDCl_3) δ 7.95 (bs, 2H), 7.30 (d, $J = 6.6$ Hz, 2H), 6.82 (app d, $J = 4.0$ Hz, 2H), 6.54 (app d, $J = 4.0$ Hz, 2H). ^{11}B NMR (160 MHz, CDCl_3) δ 0.50 (t, $J = 26$ Hz). ^{19}F NMR (470 MHz, CDCl_3) δ 107.0 (d, $J = 6.6$ Hz), -145.5 (q, $J = 29$ Hz). $^{13}\text{C}\{^1\text{H}\}$ NMR (126 MHz, CDCl_3), better NMR data required. HRMS-ESI $^+$ m/z [$\text{M}^+ + \text{Na}$] calc. for $\text{C}_{15}\text{H}_8\text{BBBrF}_4\text{N}_2\text{Na}$: 404.9792; found: 404.9796.

B.2.3. Synthesis of 8-(4-bromo-2-methylphenyl)BODIPY, **b6**



Following **GP1**, 4-bromo-2-methylbenzaldehyde (1.0 g, 5.02 mmol) was reacted with pyrrole (4.52 mL, 15.1 mmol) under weakly acidic conditions at 55 °C to afford the corresponding dipyrromethane after column purification (675 mg, 2.14 mmol). The BODIPY was formed by first oxidation using 2,3-dichloro-5,6-dicyano-1,4-benzoquinone (0.97 g, 4.28 mmol), followed by complexation using triethylamine (3.58 mL, 25.7 mmol) and boron trifluoride diethyl etherate (4.75 mL, 38.5 mmol) over two additions to afford the title compound (384 mg, 21%) as a dark purple crystalline solid after aqueous workup and a basic alumina plug. ^1H NMR (500 MHz, CDCl_3) δ 7.94 (bs, 2H), 7.51 (d, $J = 1.2$ Hz, 1H), 7.45 (dd, $J = 1.2, 8.2$ Hz, 1H), 7.16 (d, $J = 8.2$ Hz, 1H), 6.70 (app d, $J = 4.0$ Hz, 2H), 6.51 (app d, $J = 4.0$ Hz, 2H), 2.23 (s, 3H). ^{11}B NMR (160 MHz, CDCl_3) δ 0.28 (bs). ^{19}F NMR (470 MHz, CDCl_3) δ -144.95 (dq, $J_{\text{B-F(a)}} = 28$ Hz, $J_{\text{F-F}} = 104$ Hz), -145.6 (dq, $J_{\text{B-F(b)}} = 28$ Hz, $J_{\text{F-F}} = 104$ Hz). $^{13}\text{C}\{^1\text{H}\}$ NMR (126 MHz, CDCl_3), better NMR data required. HRMS required.

B.2.4. Synthesis of 8-(2,6-difluoro-4-(tellurophenyl)phenyl)BODIPY, **b10**



2-(Pinacolatoboron)tellurophene (**b2**) (30 mg, 0.10 mmol),

8-(4-bromo-2,6-difluorophenyl)BODIPY (**b5**) (41 mg, 0.11 mmol), Pd₂(dba)₃ (4 mg, 4 μmol), XPhos (4 mg, 8 μmol) and

cesium carbonate (163 mg, 0.50 mmol) were stirred to combine in a 4 mL vial. The vial was evacuated and purged with nitrogen before dioxane (3 mL) and distilled water (300 μL) were added. The vial was capped, stirred, and heated to 50 °C for 4 h. Second aliquots of Pd₂(dba)₃ (16 mg, 16 μmol) and XPhos (16 mg, 31 μmol) were then added, before stirring the reaction overnight (16 h). The reaction mixture was filtered through Celite, eluting with dichloromethane, and then evaporated under reduced pressure. The crude material was purified *via* column chromatography on neutral alumina, *via* wet-loading and elution with 0 → 20% v/v ethyl acetate in hexanes. To remove further impurities, the resulting crude solids were suspended in pentane and loaded into a Pasteur pipette equipped with a Kimwipe plug. The solids were washed multiple times with pentane, then eluted through the plug with dichloromethane. The sample was concentrated under reduced pressure to afford the desired product as a crimson solid (11 mg, 21% yield). R_f = 0.19 (20% v/v ethyl acetate/hexanes). ¹H NMR (500 MHz, CDCl₃) δ 9.06 (d with Te satellites, *J* = 6.4 Hz, 1H), 8.03-7.96 (m, 3H), 7.93 (dd, *J* = 6.4, 4.0 Hz, 1H), 7.23 (d, *J* = 8.6 Hz, 2H), 6.94 (app d, *J* = 3.2 Hz, 2H), 6.58 (app d, *J* = 3.2 Hz, 2H). ¹¹B NMR (160 MHz, CDCl₃) δ 0.27 (t, *J* = 26 Hz). ¹⁹F NMR (471 MHz, CDCl₃) δ -108.6 (d, *J* = 8.6), 145.0 (q, *J* = 26 Hz). ¹³C {¹H} NMR (126 MHz, CDCl₃) δ 161.4, 159.4, 145.5, 139.0, 136.0, 135.4, 133.6, 130.9, 129.6, 119.2, 110.3, 110.1 (note: two overlapping signals). ¹²⁵Te {¹H} NMR (95 MHz,

CDCl₃) δ 778.0. HRMS-APCI⁺ *m/z* [M⁺ - F] calc. for C₁₉H₁₁BF₃N₂¹³⁰Te: 465.0024; found:
465.0007.

B.3. Nuclear Magnetic Resonance Spectra

Figure 70. ^1H NMR (500 MHz) spectrum of compound **b5** in CDCl_3

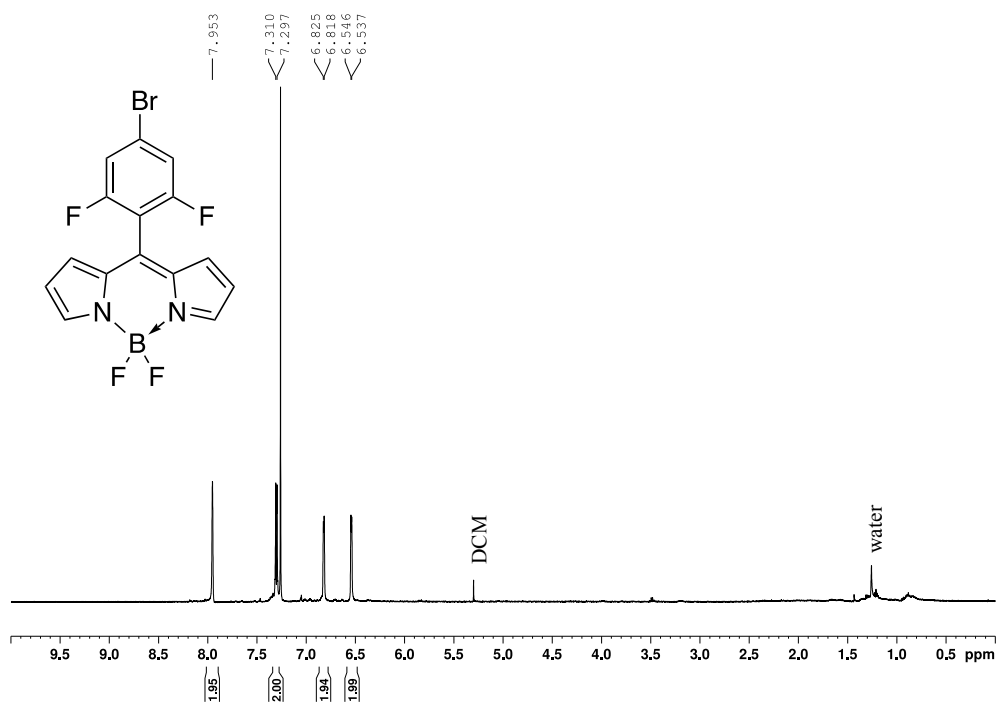


Figure 71. $^{13}\text{C}\{^1\text{H}\}$ NMR (126 MHz) spectrum of compound **b5** in CDCl_3 .

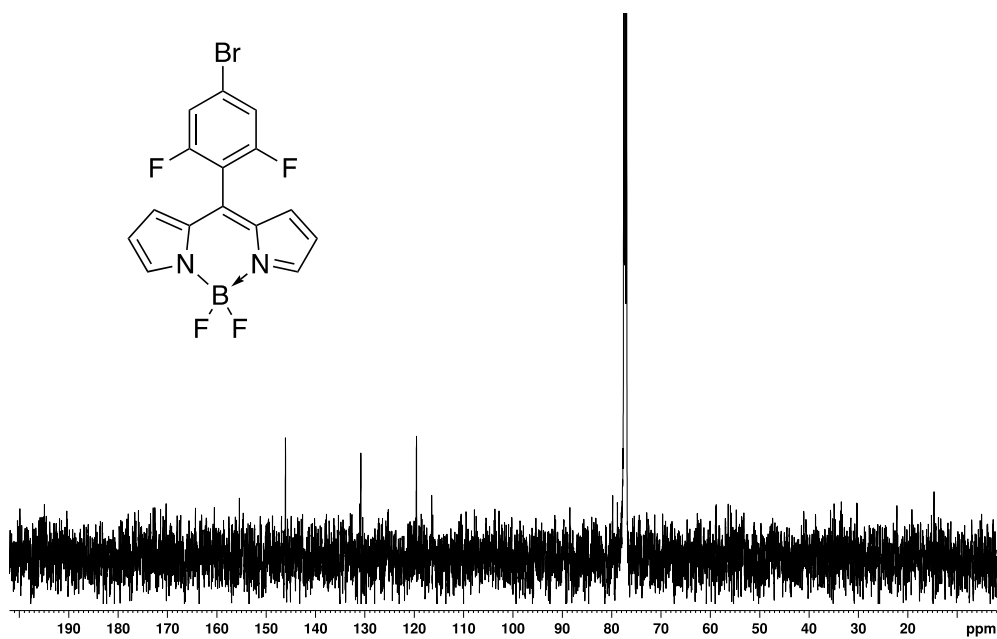


Figure 72. ^{11}B NMR (160 MHz) spectrum of compound **b5** in CDCl_3

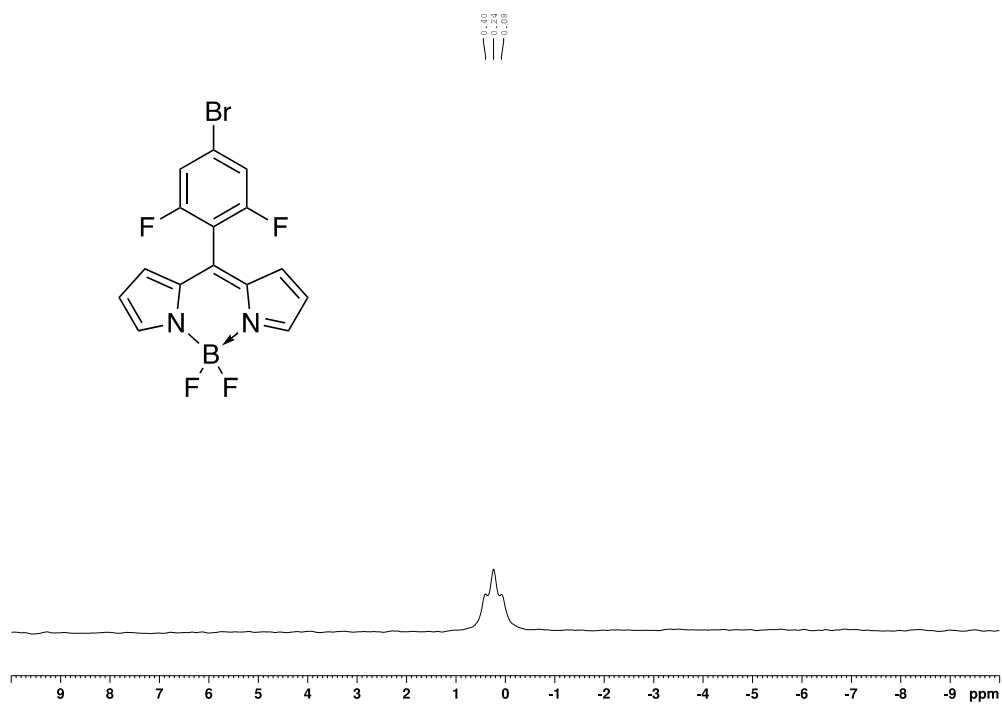


Figure 73. ^{19}F NMR (470 MHz) spectrum of compound **b5** in CDCl_3

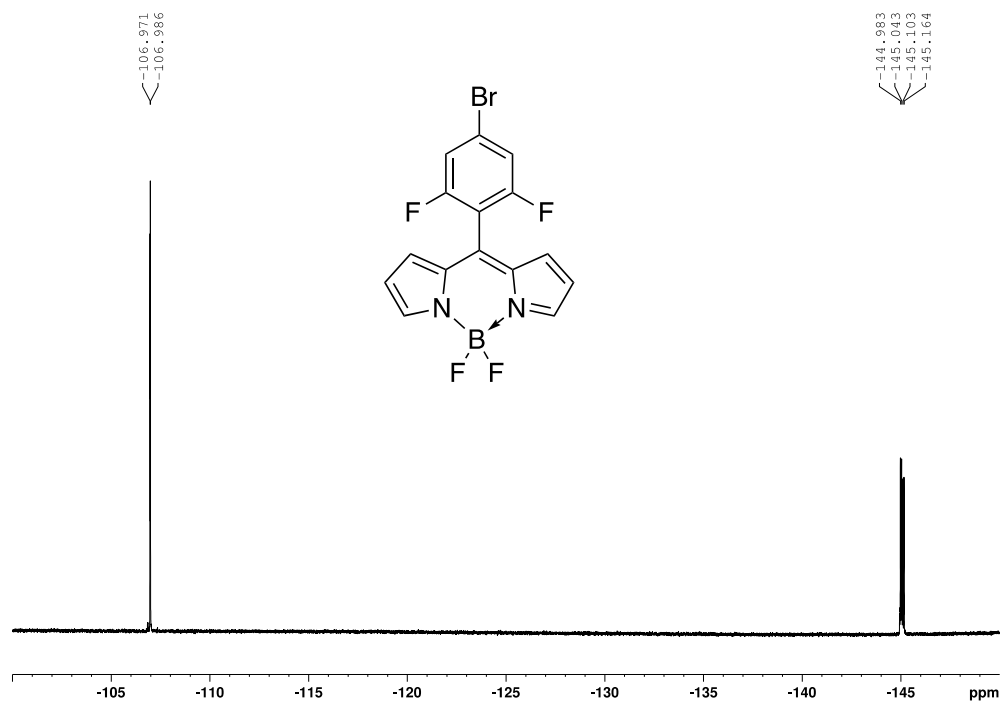


Figure 74. ^1H NMR (500 MHz) spectrum of compound **b6** in CDCl_3

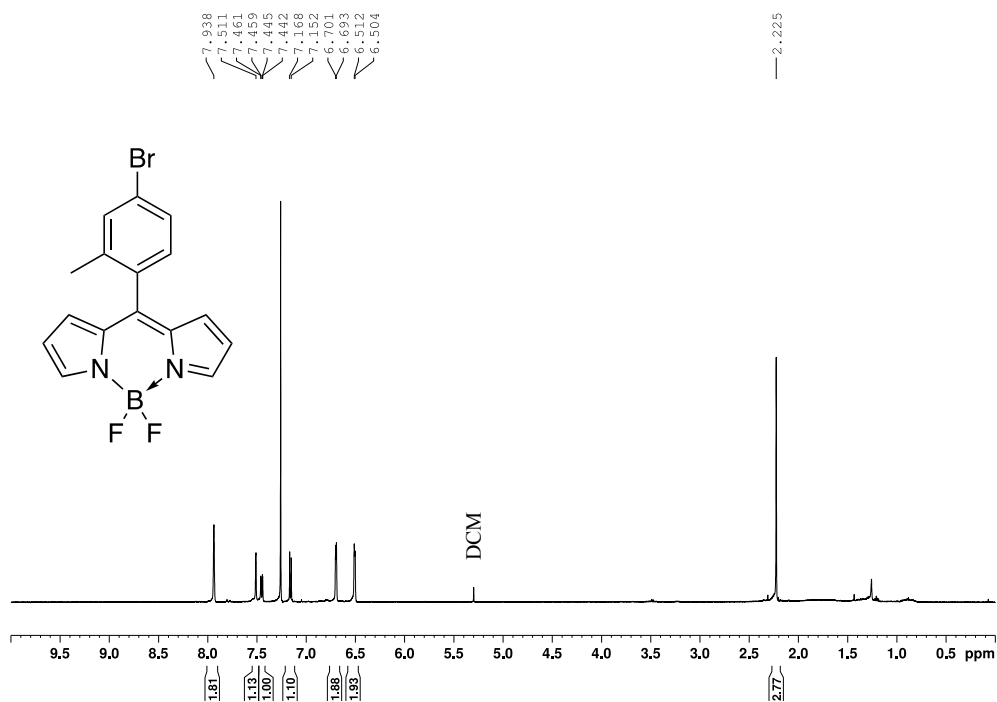


Figure 75. $^{13}\text{C}\{^1\text{H}\}$ NMR (126 MHz) spectrum of compound **b6** in CDCl_3

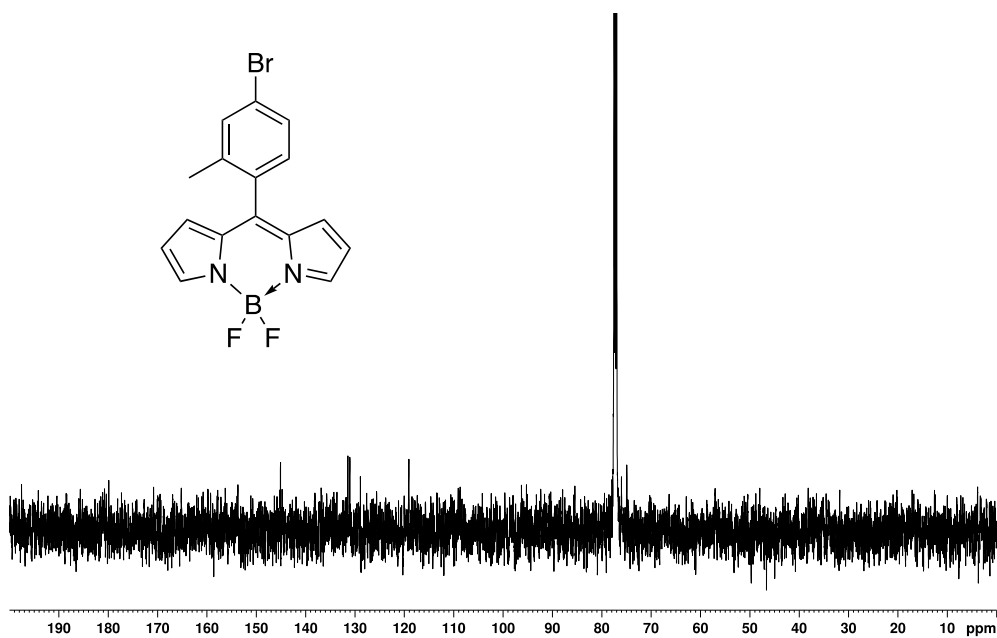


Figure 76. ^{11}B NMR (160 MHz) spectrum of compound **b6** in CDCl_3

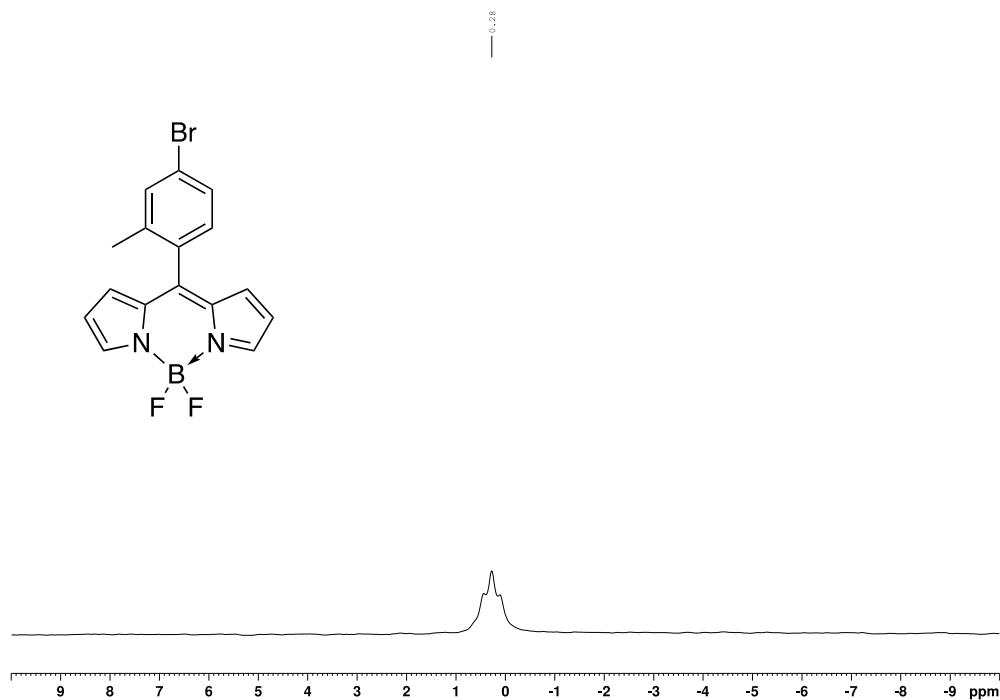


Figure 77. ^{19}F NMR (470 MHz) spectrum of compound **b6** in CDCl_3

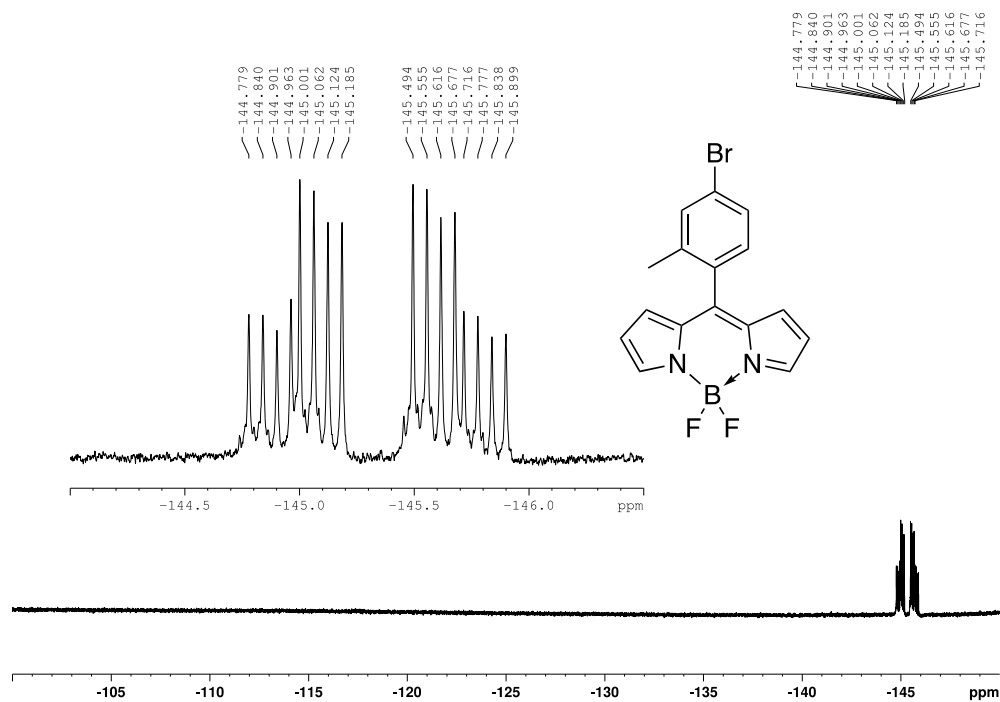


Figure 78. ^1H NMR (500 MHz) spectrum of compound **b10** in CDCl_3

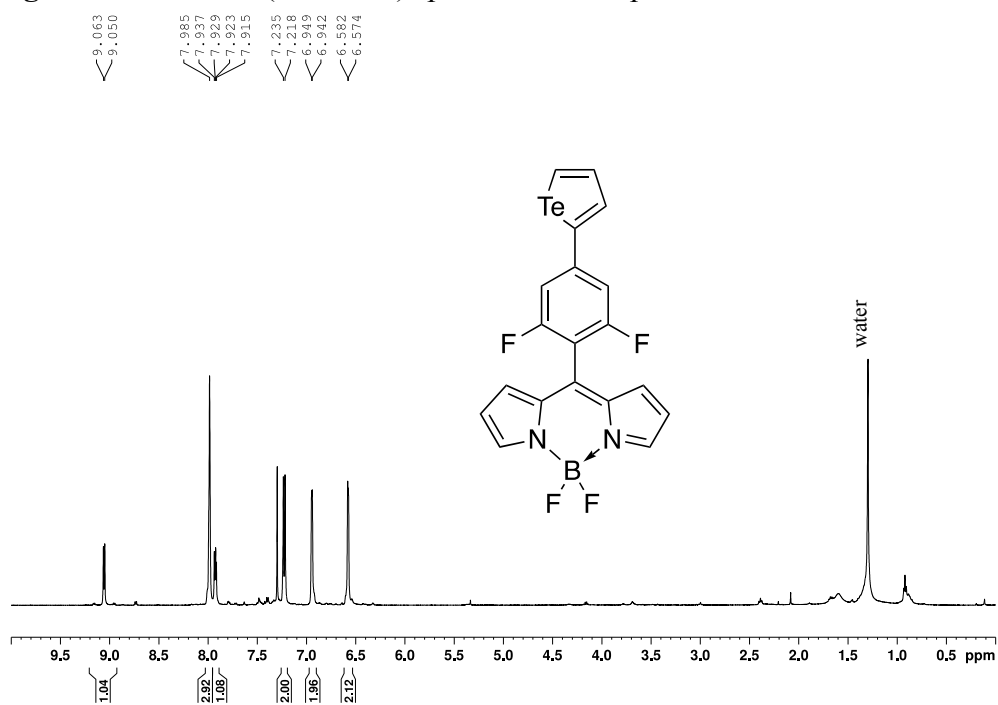


Figure 79. $^{13}\text{C}\{^1\text{H}\}$ NMR (126 MHz) spectrum of compound **b10** in CDCl_3

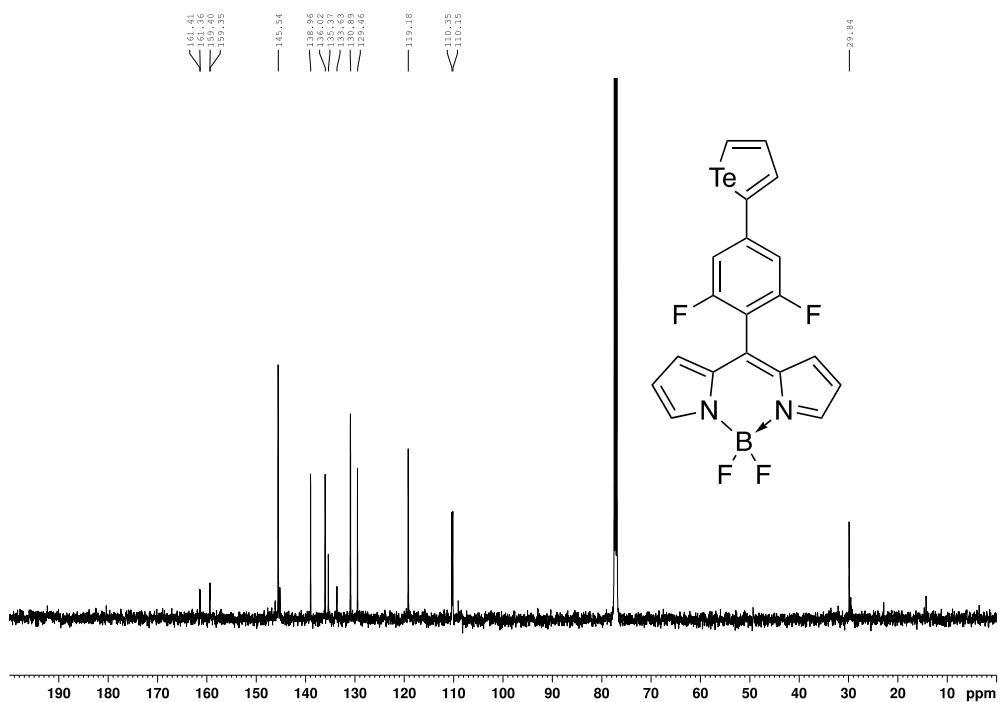


Figure 80. ^{11}B NMR (160 MHz) spectrum of compound **b10** in CDCl_3

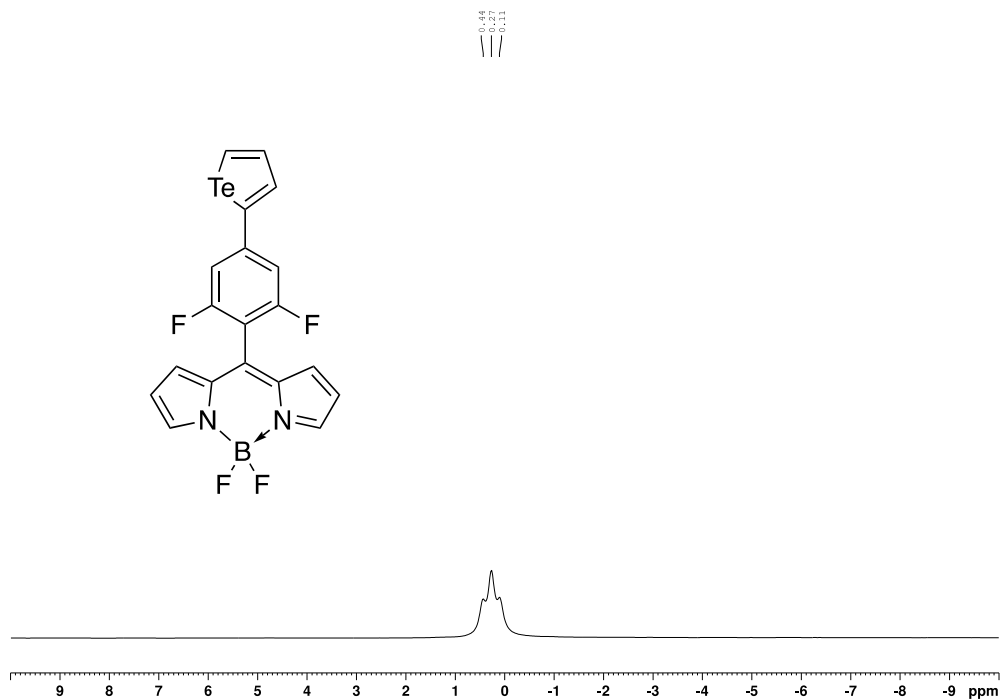


Figure 81. ^{19}F NMR (470 MHz) spectrum of compound **b10** in CDCl_3

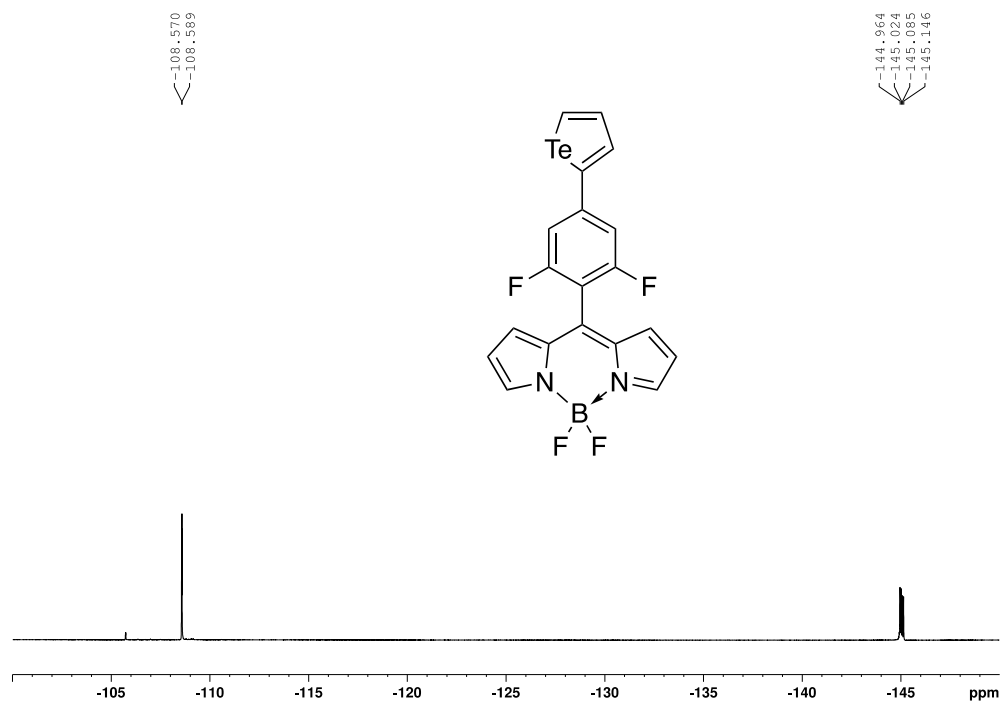
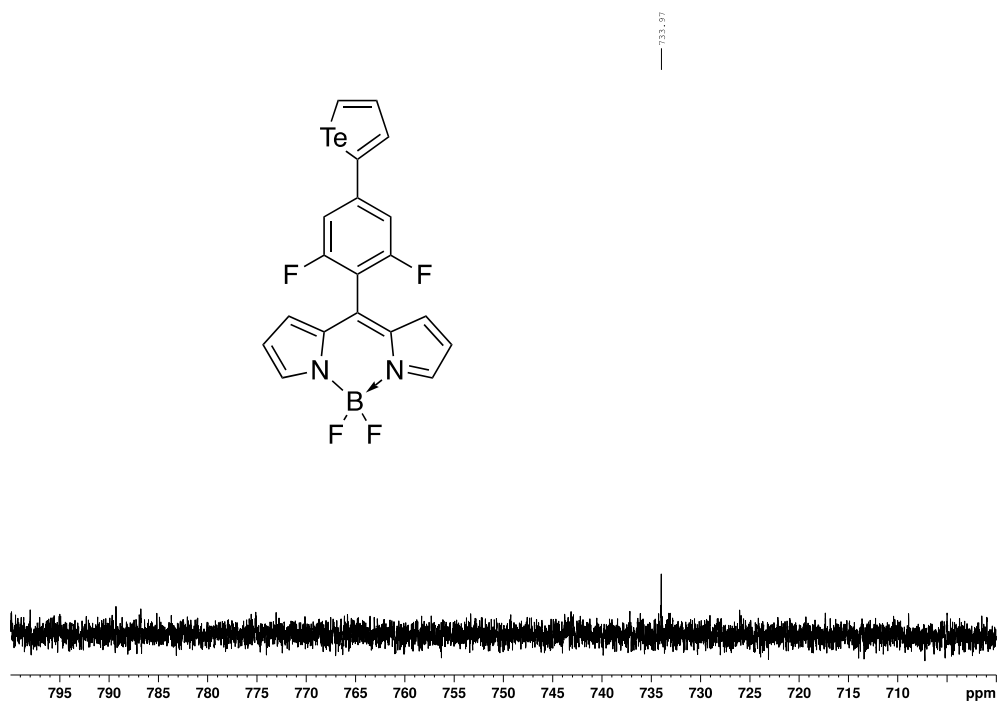


Figure 82. $^{125}\text{Te}\{^1\text{H}\}$ NMR (95 MHz) spectrum of compound **b10** in CDCl_3



Appendix C. Chapter 3 Supporting Information

C.1. Experimental Procedures

C.1.1. General Remarks

Absorption and fluorescent spectra were recorded using a quartz cuvette. Mass spectra were recorded using a time-of-flight mass spectrometer. Using a modified version of a literature procedure,²⁴⁷ photophysical properties of all compounds were determined in dichloromethane solution at room temperature. Molar absorptivity values were recorded at the peak maximum in dichloromethane for all cases. Fluorescence spectra were determined by exciting at 490 nm in all cases. Fluorescence quantum yield (Φ_f) was determined according to the equation: $\Phi_{\text{unk}} = (\Phi_{\text{std}})(n/n_{\text{std}})^2(I_{\text{unk}}/I_{\text{std}})(A_{\text{std}}/A_{\text{unk}})$,²⁴⁸ where Φ is the quantum yield, I is the area under the peaks in the fluorescence spectra, A is the absorbance at the excitation wavelength, and n is the refractive index (dichloromethane = 1.425, ethanol = 1.357). Rhodamine B ($\Phi_f = 0.70$ in ethanol)¹⁵⁸ was chosen as the standard. Quantum yield measurements were determined in dilute solutions ($\lambda_{\text{abs}}^{\text{max}} \leq 0.1$) to avoid inner filter effects and are the composites of ten scans in all cases.

The absorbance spectra used for determining singlet oxygen quantum yield (Φ_{Δ}) and photostability were obtained using a Shimadzu UV-1800 UV Spectrophotometer, with a 1.0 cm path length, 800 μL quartz cuvette from Starna Scientific Ltd. For both studies, measurements were conducted in MeOH containing 2% DMSO and absorbances of all compounds were within 10% of 0.085 AU at 530 nm. A 530 nm LED was purchased from

Thorlabs (M530L3) and the power of the LED was determined to be 2.15mW/cm² using a Newport Optical Power Meter Model 1916-R at a 1 cm distance from the LED. 1,3-diphenylisobenzofuran (DPBF) was chosen as the ¹O₂ sensor and 110 μM was spiked into the samples and Eosin Y (EosY, Φ_Δ = 0.42)¹⁸⁵ was chosen as the standard. Irradiation times varied depending on the compounds to generate a linear correlation between the degradation of DPBF and irradiation. The calculated Φ_Δ were obtained using the following equation:²⁵⁵

$$\Phi_{\Delta unk} = \Phi_{\Delta std} \left(\frac{1 - 10^{-A_{std}}}{1 - 10^{-A_{unk}}} \right) \left(\frac{m_{unk}}{m_{std}} \right)$$

Where: unk = unknown, std = standard, A = absorbance, m = slope of DPBF degradation

The equation does not consider differences in refractive indexes or irradiation powers as the experiments were all conducted in the same composition of solutions with the same LED. Finally, the photostability of the compounds were measured by monitoring the λ_{abs}^{max} over the irradiation period. All measurements were conducted in triplicate.

HeLa cells were used for fluorescent imaging and cell viability assays. HeLa cells were maintained in a 75 cm² culture flask (Nunc™ 75 cm² Nunclon™ Delta Surface) at 37 °C and 5% CO₂ atmosphere in a Thermo Scientific Forma Steri-Cycle CO₂ Incubator. The cells were grown in Dulbecco's Modified Eagle Medium (DMEM) with sodium pyruvate, 4.5 g/L glucose and L-glutamine (Winsent Inc.) supplemented with 10% fetal bovine serum

and 1% antibiotics/antimycotics (complete growth medium). Unless otherwise stated, all incubations were conducted in the incubator using DMEM. The 525 nm lamp, Philips LED 90 W equivalent PAR38 Green Lamp (Model #473736) was used, and the power was determined to be 15.60 mW/cm² using the Newport Optical Power Meter Model 1916-R at a 1 cm distance.

Reagents were commercially available and used without further purification unless otherwise discussed. Anhydrous solvents were purchased, and used without further drying. Manipulations requiring inert atmospheres were conducted under nitrogen and using Schlenk line procedures. Nuclear magnetic resonance (NMR) spectra were recorded using 500 MHz and 300 MHz spectrometers. ¹H chemical shifts are reported in ppm relative to tetramethylsilane using the solvent residual as an internal standard ($\delta = 7.26$ for chloroform, 5.32 for dichloromethane).²⁴² ¹³C chemical shifts are proton decoupled and reported in ppm relative to tetramethylsilane, referenced to the resonances of CDCl₃ ($\delta = 77.2$ ppm) or CD₂Cl₂ ($\delta = 53.84$ ppm).¹ Trace impurities and residual solvent peaks were determined using published tables.²⁴² Coupling constants are reported in Hertz (Hz) and spin multiplicities are reported using the following symbols: s (singlet), bs (broad singlet), d (doublet), dd (doublet of doublets), t (triplet), q (quartet), m (multiplet) and app (apparent). ¹¹B chemical shifts are reported in ppm, externally referenced to boron trifluoride diethyl etherate ($\delta = 0.00$). ¹⁹F chemical shifts are reported in ppm, externally referenced to CFC₃ ($\delta = 0.00$).¹²⁵Te chemical shifts are reported in ppm relative to Me₂Te₂, externally referenced to diphenyl ditelluride ($\delta = 422$ ppm).²⁴³ Thin layer chromatography was performed using commercially prepared silica gel plates and visualised using long- or

shortwave UV lamps. Column chromatography was performed using 230-400 mesh silica. The relative proportions of solvents mentioned in reference to TLC and column chromatography procedures correspond to volume-to-volume ratios. Mass spectral data were acquired using a QTOF mass spectrometer operating in positive electrospray ionisation mode.

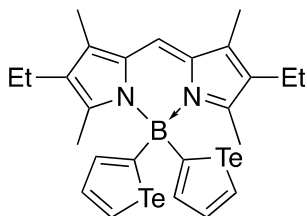
2,6-Diethyl-4,4-difluoro-1,3,5,7-tetramethyl-4-bora-3a,4a-diaza-s-indacene, **c1**, was synthesised according to a literature procedure.²⁵⁶

C.1.2. General Procedure for the Synthesis of /E/-BODIPYs, GP

Inside a nitrogen-filled glovebox, a solution of the corresponding heterocycle (2.2 equiv.) and dry tetrahydrofuran (2 mL) was stirred in a 15 mL vial at room temperature until complete dissolution was achieved (5 min). *n*-Butyllithium (2.0 M in hexanes, 2.4 equiv.) was added dropwise *via* syringe. The vial was then capped and the reaction mixture was stirred for 5 min. In a separate 15 mL vial **c1** (1 equiv.) was stirred in dry tetrahydrofuran (2 mL) until complete dissolution was achieved (5 min). The BODIPY solution was then added dropwise *via* syringe to the solution containing the lithiated heterocycle. The capped reaction mixture was stirred for 1 h. The crude reaction mixture was then taken out of the glovebox and dissolved in dichloromethane (20 mL), then washed with saturated ammonium chloride (1× 20 mL), water (1× 20 mL) and brine (1× 20 mL). The organic layer was dried over sodium sulfate and concentrated under reduced pressure. The resulting crude solid was purified *via* column chromatography over silica with wet-loading and elution with a gradient solution of dichloromethane/hexanes or ethyl acetate/hexanes. The

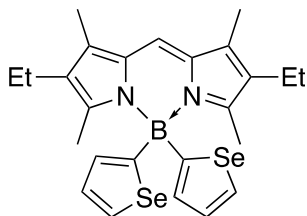
fractions containing the desired compounds were concentrated under reduced pressure to afford the desired *[E]*-BODIPYs.

C.1.3. Synthesis of 2,6-diethyl-1,3,5,7-tetramethyl-4,4-ditellurophenylBODIPY, **c2**



Following **GP**, a solution of tellurophene⁷⁵ (130 mg, 0.7 mmol) in tetrahydrofuran was lithiated using *n*-butyllithium (0.8 mmol) and then added to a solution of **c1** (100 mg, 0.33 mmol) in tetrahydrofuran. After work-up and column chromatography (0 ⇒ 20% dichloromethane/hexanes), the desired product was afforded as a scarlet red solid (51 mg, 25% yield). $R_f = 0.70$ (20% ethyl acetate/hexanes); $^1\text{H NMR}$ (500 MHz, CDCl_3) δ 8.92 (d with Te satellites, $J = 6.5$ Hz, 2H), 8.08 (d, $J = 3.5$ Hz, 2H), 7.81 (dd, $J = 6.5, 3.5$ Hz, 2H), 7.10 (s, 1H), 2.31 (q, $J = 7.6$ Hz, 4H), 2.22 (s, 6H), 2.11 (s, 6H), 0.98 (t, $J = 7.6$ Hz, 6H); $^{11}\text{B NMR}$ (160 MHz, CDCl_3) δ 0.50 (bs); $^{125}\text{Te}\{^1\text{H}\}$ NMR (95 MHz, CDCl_3) δ 835.5; $^{13}\text{C}\{^1\text{H}\}$ NMR (126 MHz, CDCl_3) δ 154.9, 140.3, 139.3, 134.6, 132.5, 131.3, 125.6, 119.0, 17.6, 14.9, 14.8, 9.5 (one signal missing); HRMS-ESI⁺ m/z [$\text{M}^+ + \text{Na}$] calc. for $\text{C}_{25}\text{H}_{29}\text{BN}_2^{130}\text{Te}_2\text{Na} = 651.0440$, found 651.0465; $\lambda_{\text{abs}}^{\text{max}} = 528$ nm (498 nm shoulder); $\epsilon = 66000$, $\lambda_{\text{em}}^{\text{max}} = 537$ nm; $\Phi_f = 0.01$; Stokes shift = 9 nm; $\Phi_{\Delta} = 0.68 \pm 0.08$.

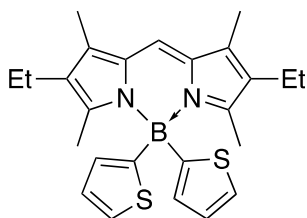
C.1.4. Synthesis of 2,6-diethyl-1,3,5,7-tetramethyl-4,4-diselenophenylBODIPY, **c3**



Following **GP**, a solution of selenophene (142 mg, 1.1 mmol) in tetrahydrofuran was lithiated using *n*-butyllithium (1.2 mmol) and then added to a solution of **c1** (150 mg, 0.49 mmol) in tetrahydrofuran. After work-up and column chromatography (0 ⇒ 20% dichloromethane in hexanes), the sample was concentrated under reduced pressure

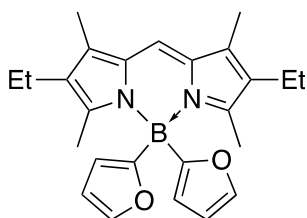
to afford the desired product as a scarlet red solid (77 mg, 30% yield). $R_f = 0.55$ (20% ethyl acetate/hexanes); ^1H NMR (500 MHz, CDCl_3) δ 8.02 (dd, $J = 5.3, 0.6$ Hz, 2H), 7.45 (dd, $J = 3.5, 0.6$ Hz, 2H), 7.27 (dd w/ CDCl_3 shoulder, $J = 5.3, 3.5$ Hz, 2H), 7.13 (s, 1H), 2.32 (q, $J = 7.6$ Hz, 4H), 2.22 (s, 6H), 2.00 (s, 6H), 0.99 (t, $J = 7.6$ Hz, 6H); ^{11}B NMR (160 MHz, CDCl_3) δ - 2.05 (bs); $^{13}\text{C}\{^1\text{H}\}$ NMR (126 MHz, CDCl_3) δ 154.9, 134.5, 133.2, 132.1, 131.7, 131.2, 129.9, 119.1, 17.6, 14.8, 14.2, 9.5 (one signal missing); HRMS-ESI $^+$ m/z [$\text{M}^+ + \text{Na}$] calc. for $\text{C}_{25}\text{H}_{29}\text{BN}_2^{80}\text{Se}_2\text{Na} = 551.0646$, found 551.0652; $\lambda_{\text{abs}}^{\text{max}} = 526$ nm (496 nm shoulder); $\epsilon = 77000$; $\lambda_{\text{em}}^{\text{max}} = 533$ nm; $\Phi_f = 0.38$; Stokes shift = 7 nm; $\Phi_{\Delta} = 0.63 \pm 0.05$.

C.1.5. Synthesis of 2,6-diethyl-1,3,5,7-tetramethyl-4,4-dithiophenylBODIPY, **c4**



Following **GP**, a solution of thiophene (91 mg, 1.1 mmol) in tetrahydrofuran was lithiated using *n*-butyllithium (1.2 mmol) and then added to a solution of **c1** (150 mg, 0.49 mmol) in tetrahydrofuran. After work-up and column chromatography (0 \Rightarrow 30% dichloromethane in hexanes), the sample was concentrated under reduced pressure to afford the desired product as a scarlet red solid (91 mg, 43% yield). $R_f = 0.70$ (20% ethyl acetate/hexanes); $^1\text{H NMR}$ (500 MHz, CDCl_3) δ 7.32 (dd, $J = 4.7, 0.8$ Hz, 2H), 7.15-7.10 (m, 3H), 7.02 (dd, $J = 4.7, 3.4$ Hz, 2H), 2.31 (q, $J = 7.6$ Hz, 4H), 2.22 (s, 6H), 1.91 (s, 6H), 0.99 (t, $J = 7.6$ Hz, 6H); $^{11}\text{B NMR}$ (160 MHz, CDCl_3) δ -3.30 (bs); $^{13}\text{C}\{^1\text{H}\}$ NMR (126 MHz, CDCl_3) δ 154.8, 134.4, 132.0, 131.8, 131.2, 127.0, 126.6, 119.1, 17.7, 14.8, 13.7, 9.5 (one signal missing); HRMS-ESI⁺ m/z [$\text{M}^+ + \text{H}$] calc. for $\text{C}_{25}\text{H}_{30}\text{BN}_2\text{S}_2 = 433.1938$, found 433.1948; $\lambda_{\text{abs}}^{\text{max}} = 524$ nm (494 nm shoulder); $\epsilon = 66000$; $\lambda_{\text{em}}^{\text{max}} = 532$ nm; $\Phi_f = 0.85$; Stokes shift = 8 nm; $\Phi_{\Delta} = 0.21 \pm 0.01$.

C.1.6. Synthesis of 2,6-diethyl-4,4-difuryl-1,3,5,7-tetramethylBODIPY, **c5**



Due to the low boiling point of furan (31 °C) and the relative instability of **c5**, the synthesis of this compound was unsuccessful following **GP**. Instead, this reaction was performed using Schlenk techniques at 0 °C using a 100 mL two-neck round-bottom flask equipped with a pressure-equalised addition funnel, a stir bar and rubber septa. The glassware was oven-dried and then evacuated and backfilled with inert gas and then allowed to cool to room temperature. Tetrahydrofuran (20 mL) was transferred *via* cannula into the reaction

flask and then cooled using a water/ice bath (~ 0 °C). Inside a nitrogen-filled glovebox, furan (168 mg, 2.5 mmol) and *n*-butyllithium (2.0 M in hexanes, 2.7 mmol) were weighed out *via* syringe. The syringes were plugged by pushing the needles into rubber stoppers, then transferred out of the glovebox. Furan was dispensed into the reaction flask and the mixture was stirred until complete dissolution was achieved (5 min). Then, *n*-butyllithium was dispensed dropwise into the reaction flask and the reaction mixture was stirred for 30 min. *F*-BODIPY **1** (250 mg, 0.82 mmol) was placed in a 25 mL single-neck round-bottom flask equipped with a rubber septum and stir bar. The flask was then evacuated and backfilled with inert gas. Tetrahydrofuran (10 mL) was transferred, *via* cannula, into this flask and the mixture was stirred until complete dissolution was achieved (5 min). Next, this solution was transferred *via* cannula to the pressure-equalising additional funnel. The additional funnel was then opened to achieve an addition rate to ~ 1 drop/s. Upon the completion of the addition the reaction mixture was then stirred for 1 h over which time it was allowed to warm to room temperature. The crude reaction mixture was then dissolved in dichloromethane (50 mL), and was washed with saturated ammonium chloride (1 \times 50 mL), water (1 \times 50 mL) and brine (1 \times 50 mL). The organic layer was dried over sodium sulfate and concentrated under reduced pressure. The resulting crude solid was purified *via* column chromatography on silica, with wet-loading and elution with 0 \Rightarrow 30% dichloromethane/hexanes. The sample was concentrated under reduced pressure to afford the desired product as a scarlet red solid (97 mg, 29% yield). $R_f = 0.75$ (20% ethyl acetate/hexanes); $^1\text{H NMR}$ (500 MHz, CDCl_3) δ 7.52 (d, $J = 1.4$ Hz, 2H), 7.16 (s, 1H), 6.36 (d, $J = 2.7$ Hz, 2H), 6.33 (dd, $J = 2.7, 1.4$ Hz, 2H), 2.37 (q, $J = 7.6$ Hz, 4H), 2.25 (s, 6H),

1.98 (s, 6H), 1.04 (t, $J = 7.6$ Hz, 6H); ^{11}B NMR (160 MHz, CDCl_3) δ -6.30 (bs); $^{13}\text{C}\{^1\text{H}\}$ NMR (126 MHz, CDCl_3) δ 154.7, 143.0, 134.3, 131.7, 131.5, 119.0, 114.9, 109.1, 17.7, 14.8, 12.6, 9.5 (one signal missing); HRMS-ESI $^+$ m/z [$\text{M}^+ + \text{Na}$] calc. for $\text{C}_{25}\text{H}_{29}\text{BN}_2\text{O}_2\text{Na}$ = 423.2214, found 423.2212; $\lambda_{\text{abs}}^{\text{max}} = 522$ nm; $\epsilon = 35000$; $\lambda_{\text{em}}^{\text{max}} = 529$ nm; $\Phi_{\text{f}} = 0.88$; Stokes shift = 7 nm; $\Phi_{\Delta} = 0.24 \pm 0.01$.

C.2. Photophysical Spectra

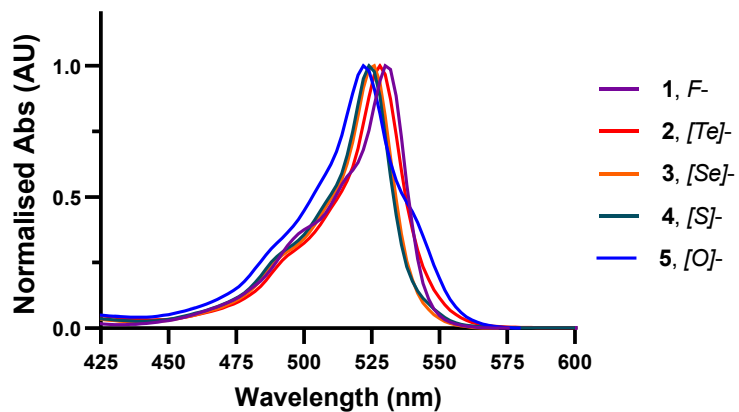


Figure 83. Normalised absorbance spectra for solutions of **c2-c5** in CH_2Cl_2 highlighting a slight bathochromic shift corresponding with the heavy-atom effect of the heteroatom.

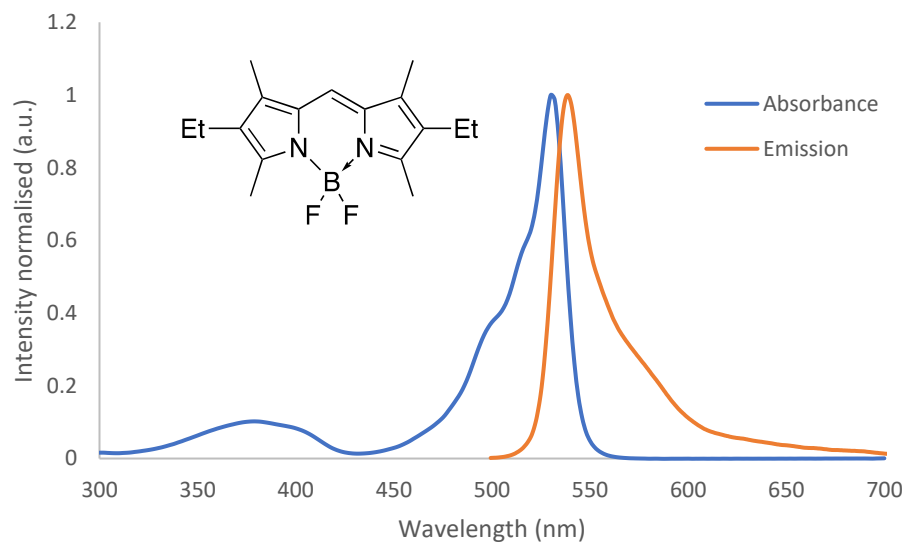


Figure 84. Normalised absorption and emission spectra of compound **c1** in dichloromethane.

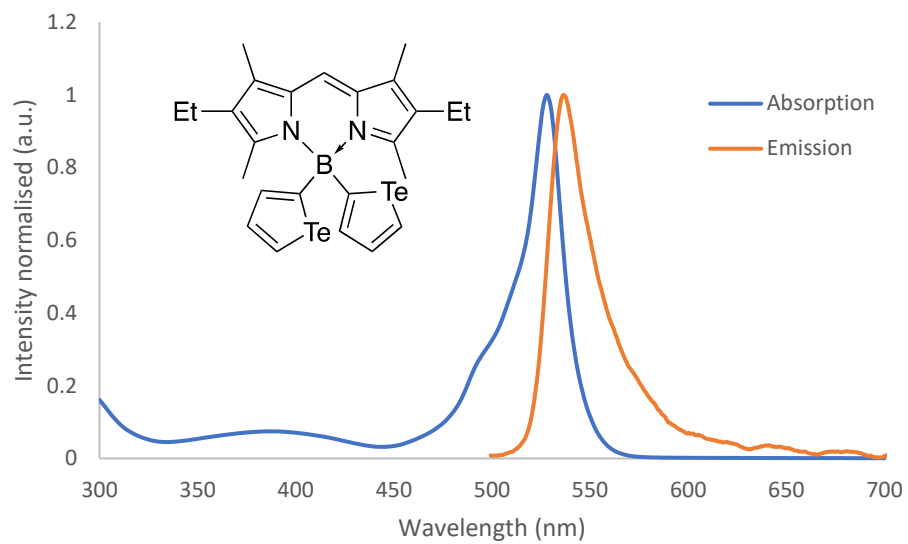


Figure 85. Normalised absorption and emission spectra of compound **c2** in dichloromethane.

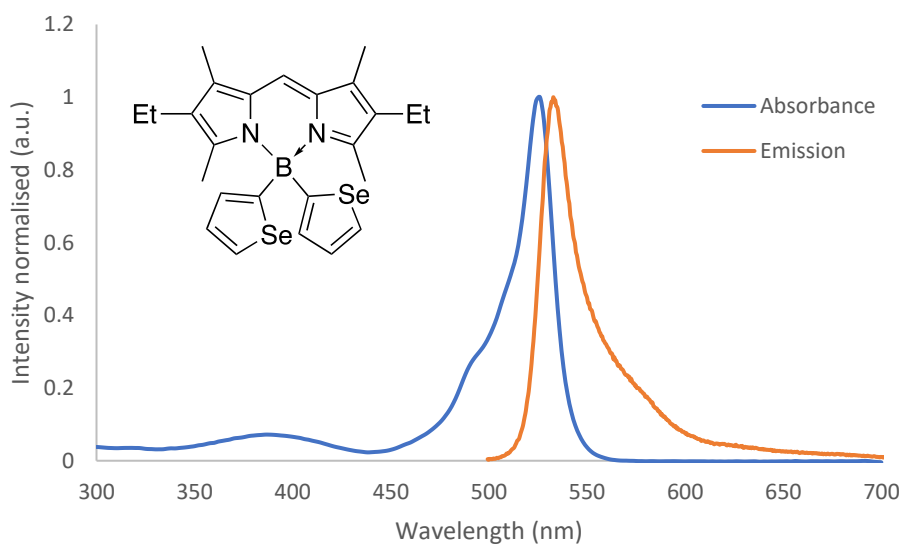


Figure 86. Normalised absorption and emission spectra of compound **c3** in dichloromethane.

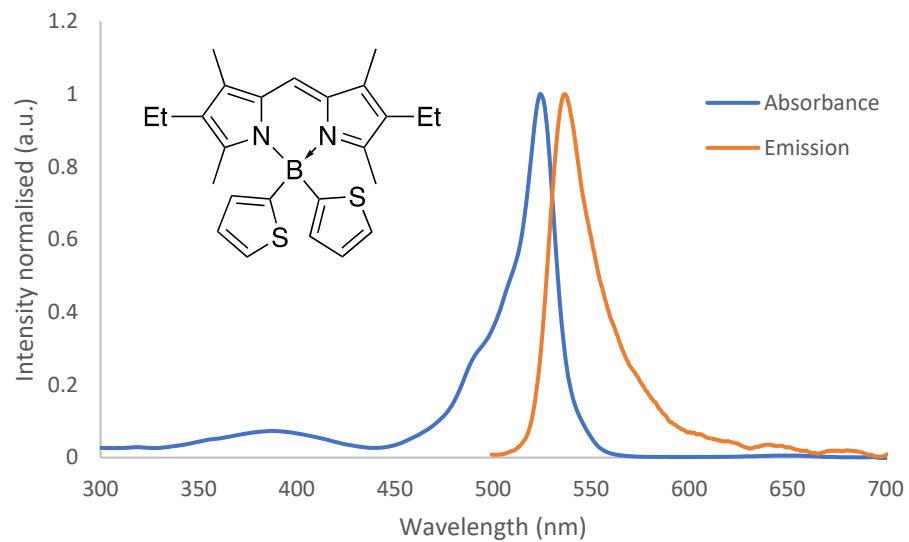


Figure 87. Normalised absorption and emission spectra of compound **c4** in dichloromethane.

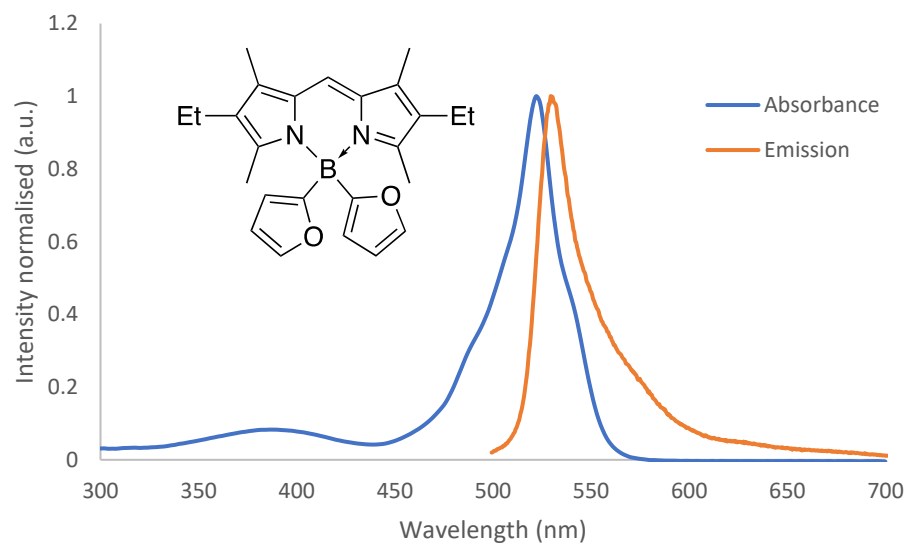


Figure 88. Normalised absorption and emission spectra of compound **c5** in dichloromethane.

C.3. Cell Assays and Viability

C.3.1. Fluorescent Images

HeLa cells were seeded at a density of 25,000 cells per well in an 8-well chamber (Thermo Scientific Lab-Tek™ Chambered #1.0 Borosilicate Coverglass System) and incubated with 250 μ L DMEM overnight. The cells were then washed with D-PBS once and replaced with 250 μ L Opti-MEM containing 1 μ M of the BODIPY compounds. Plates were incubated for 3 hours, washed once with D-PBS and imaged in D-PBS. All fluorescent microscopy images were taken on an Olympus 1X73 inverted microscope. Olympus CellSens Dimension V1.19 software was used to analyse and adjust the images. The EGFP filter cube used to image the BODIPY compounds had a 440 – 470 nm excitation bandpass filter, a 495 nm dichroic mirror and a 525 – 550 nm emission bandpass filter.

Figure 89 shows compounds **c2** and **c3** with longer exposure times and compared to controls with no compounds to show that they are fluorescent compared to the background (compound **c2** is only minimally fluorescent compared to the background).

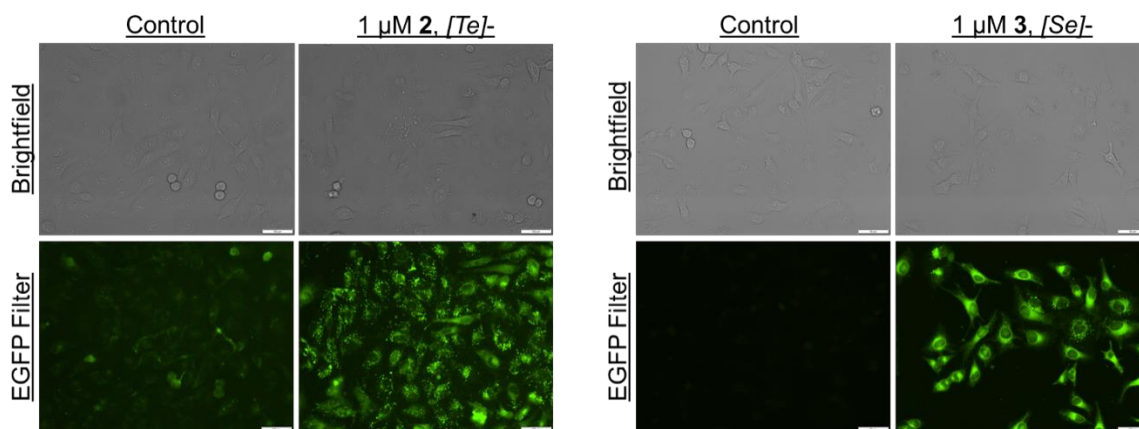


Figure 89. Fluorescent images of compounds **c2** and **c3** with longer exposure times compared to the background. 20x magnification, scale bar = 50 μm .

C.3.2. Cell viability assays

HeLa cells were seeded at a density of 10,000 cells per well in 96-well plates (Thermo Scientific Nunclon™ Delta Surface) and incubated in 200 μL DMEM overnight. The cells were then washed with D-PBS and replaced with 200 μL Opti-MEM. DMSO stocks of BODIPY compounds were added at a variety of concentrations to a final DMSO concentration of 1% and incubated for 3 hours. After incubation, cells were washed with D-PBS and the media was replaced with 200 μL DMEM. Plates were either kept in the dark or irradiated with a 525 nm lamp for 5 minutes (15.60 mW/cm^2 or 4.68 J/cm^2) and incubated overnight. On the following day, 20 μL of a 5 mg/mL solution of thiazolyl blue tetrazolium bromide (MTT) in D-PBS was added to each well and incubated for 3 hours. The media was then removed and 150 μL of DMSO was added to dissolve the formazan products. Plates were read at 565 nm and 800 nm using BioTek Synergy™ HTX Multi-Mode Microplate Reader to determine the concentration of formazan products and the

background respectively. Corrected absorbance values were then used to calculate the cell viability. Cell viability experiments were all conducted in triplicates.

C.4. Nuclear Magnetic Resonance Spectra

Figure 90. ^1H NMR (500 MHz) spectrum of compound **c2** in CDCl_3

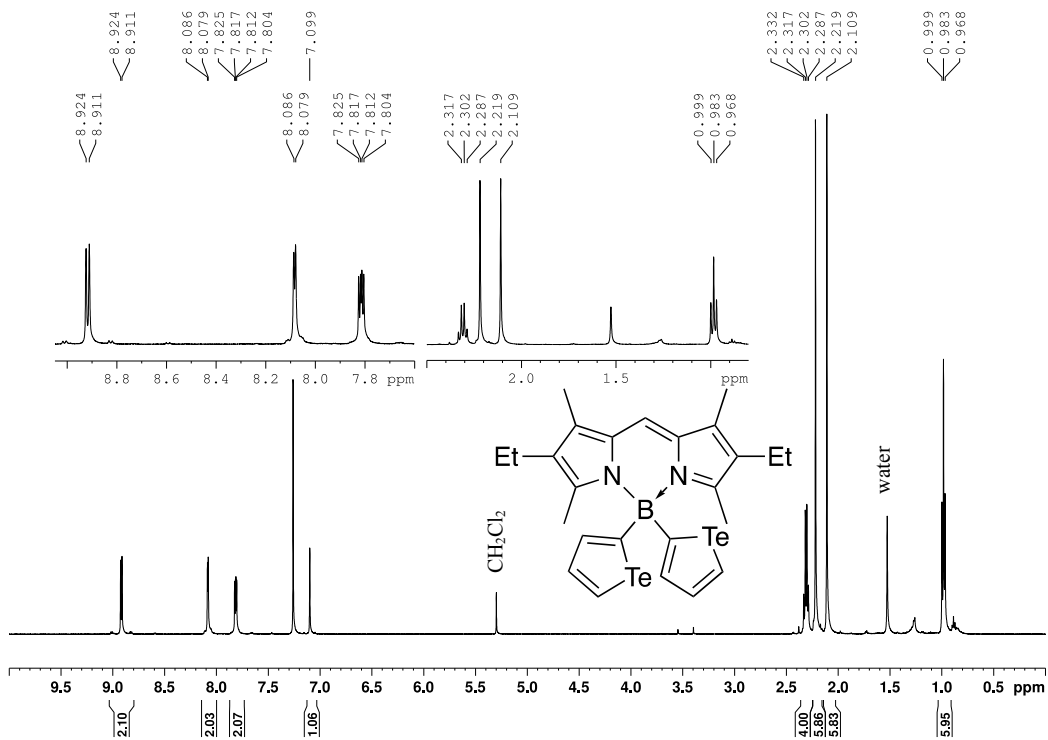


Figure 91. $^{13}\text{C}\{^1\text{H}\}$ NMR (126 MHz) spectrum of compound **c2** in CDCl_3

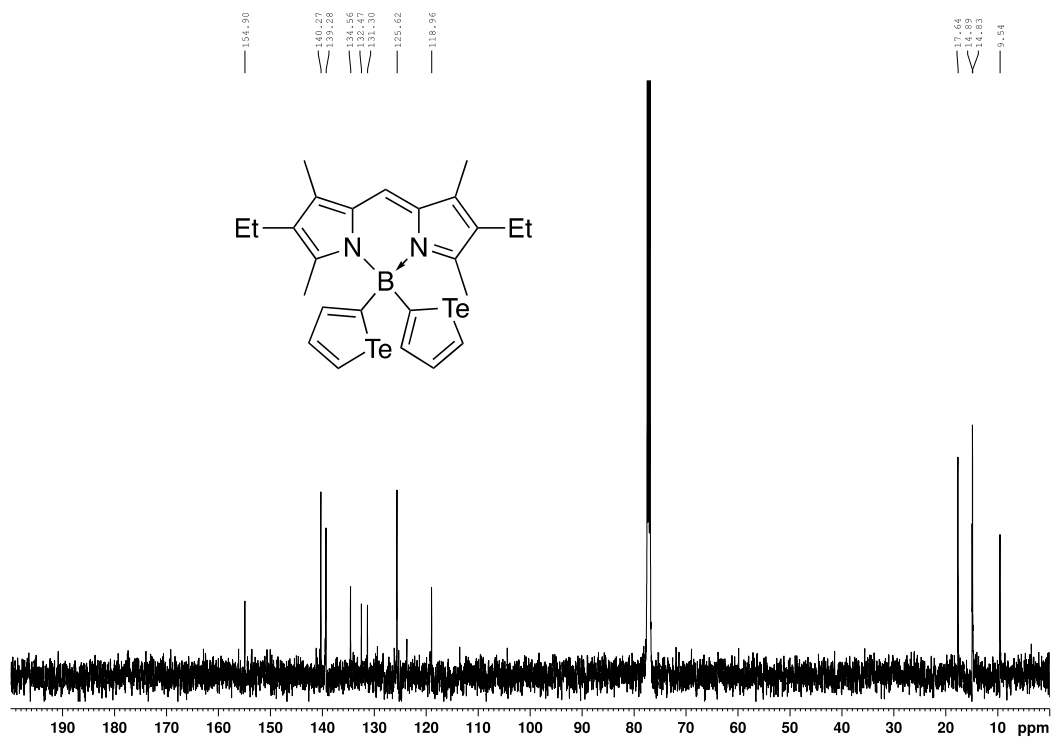


Figure 92. ^{11}B NMR (160 MHz) spectrum of compound **c2** in CDCl_3

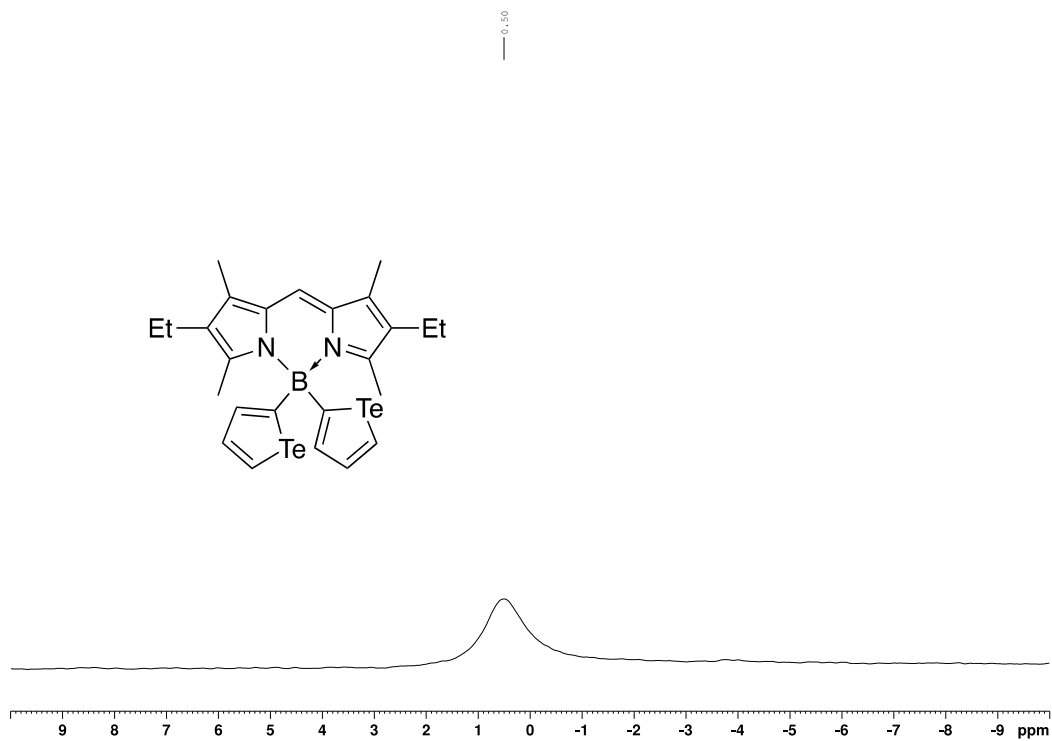


Figure 93. ^1H NMR (500 MHz) spectrum of compound **c3** in CDCl_3

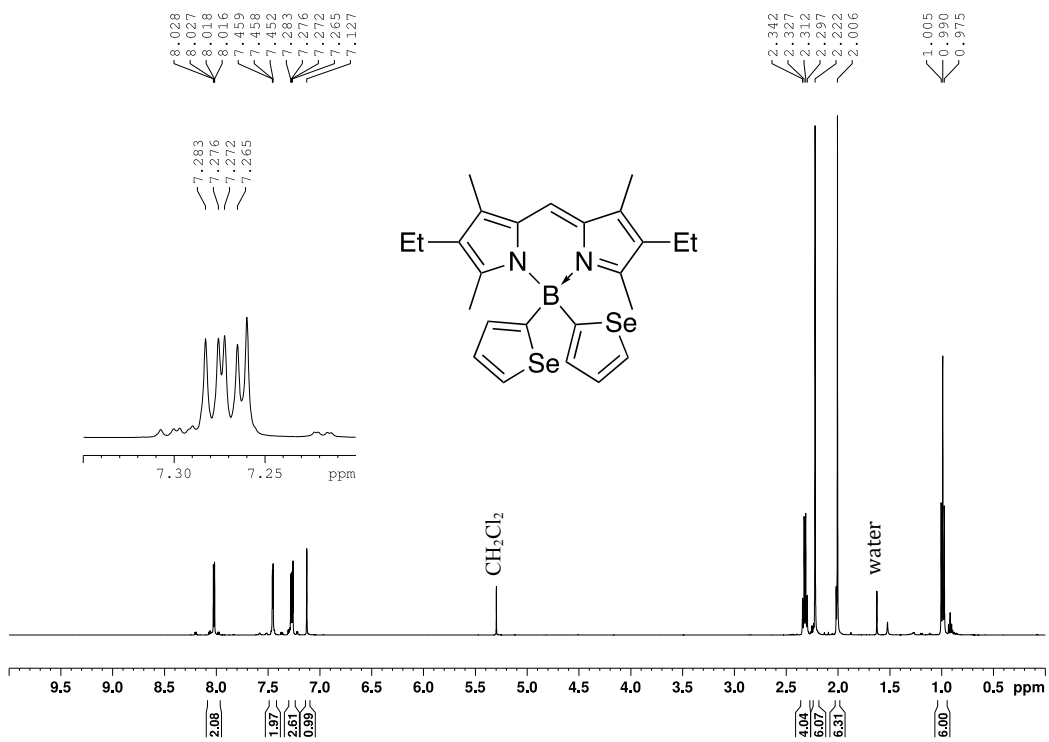


Figure 94. $^{13}\text{C}\{^1\text{H}\}$ NMR (126 MHz) spectrum of compound **c3** in CDCl_3

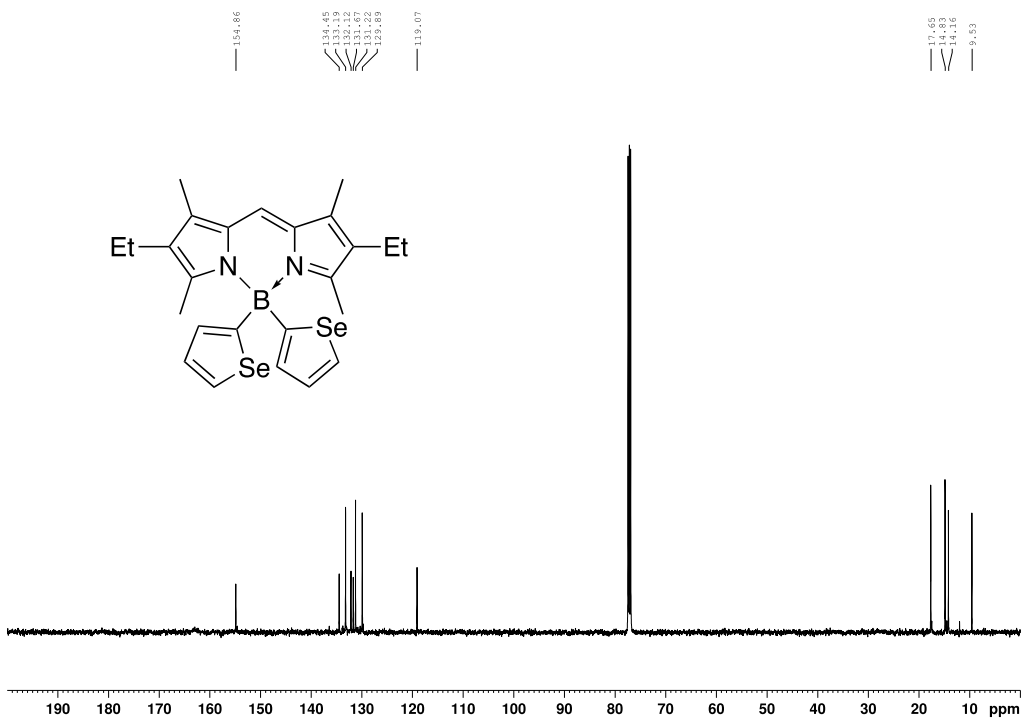


Figure 95. ^{11}B NMR (160 MHz) spectrum of compound **c3** in CDCl_3

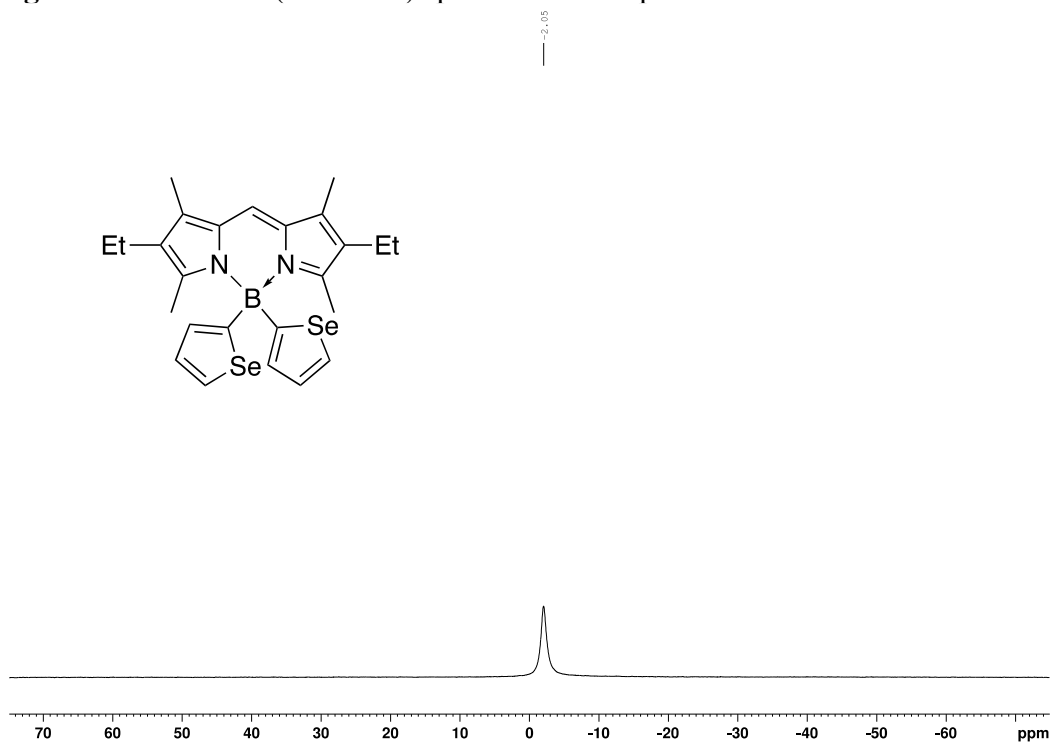


Figure 96. ^1H NMR (500 MHz) spectrum of compound **c4** in CDCl_3

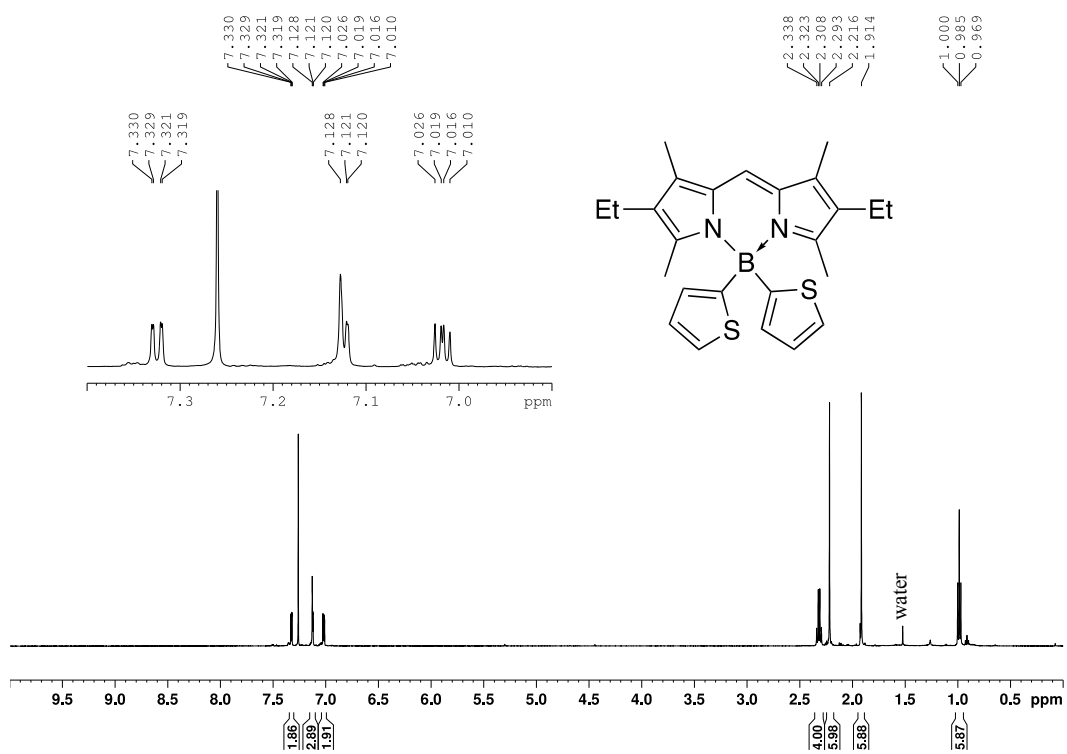


Figure 97. $^{13}\text{C}\{^1\text{H}\}$ NMR (126 MHz) spectrum of compound **c4** in CDCl_3

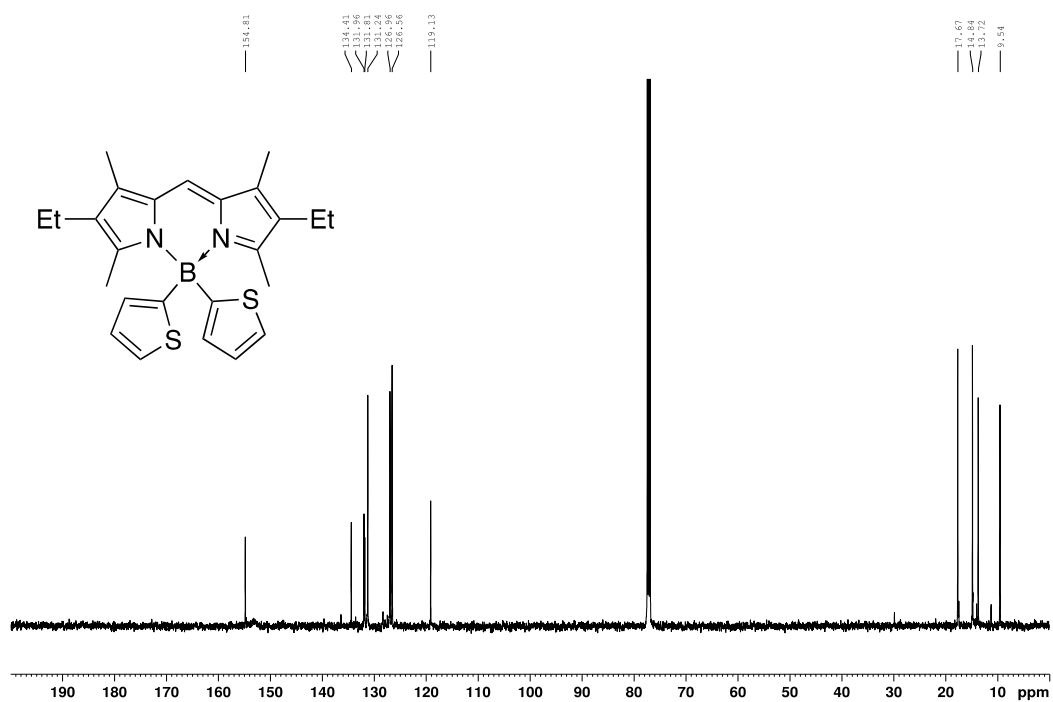


Figure 98. ^{11}B NMR (160 MHz) spectrum of compound **c4** in CDCl_3

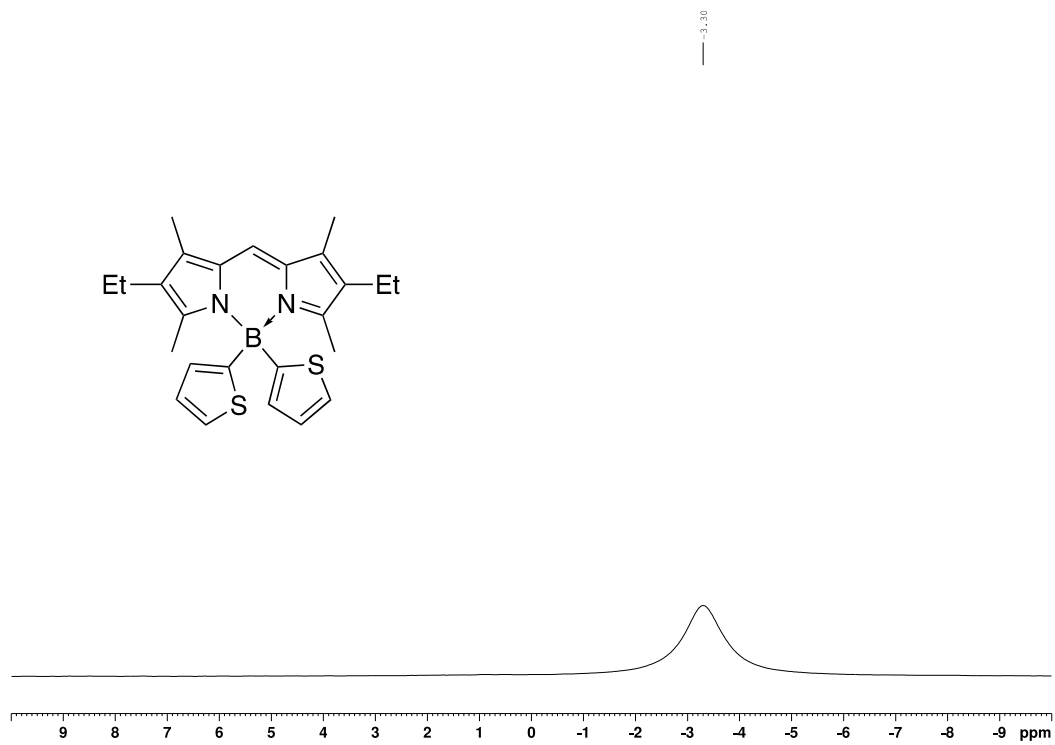


Figure 99. ^1H NMR (500 MHz) spectrum of compound **c5** in CDCl_3

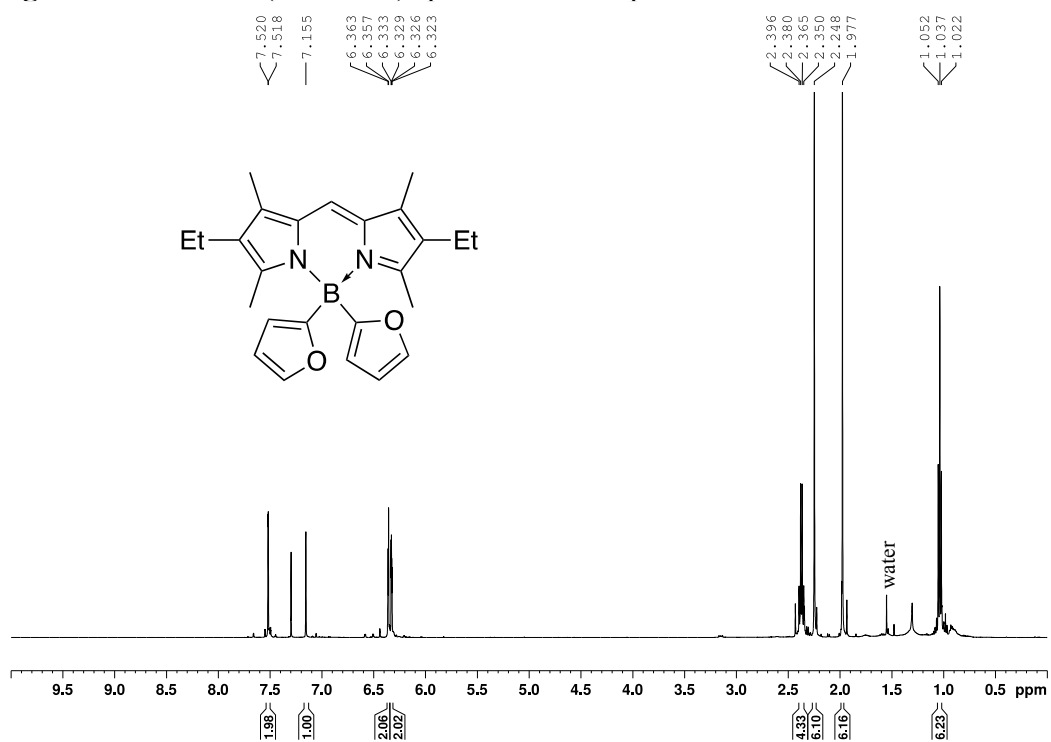


Figure 100. $^{13}\text{C}\{^1\text{H}\}$ NMR (126 MHz) spectrum of compound **c5** in CDCl_3

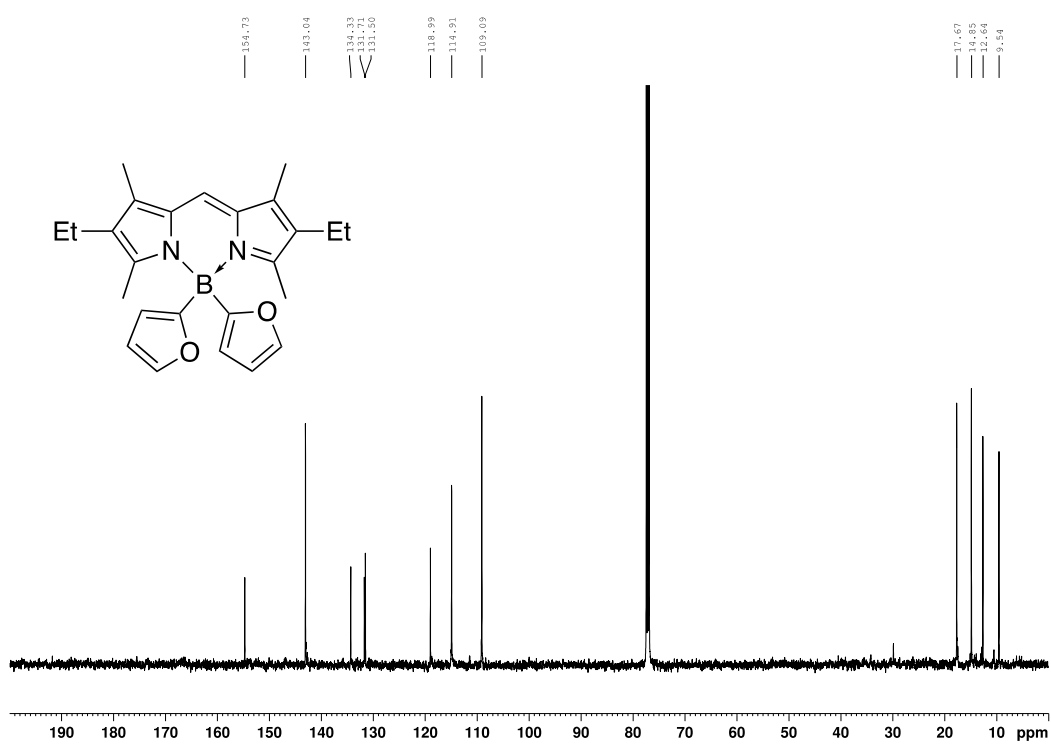


Figure 101. ^{11}B NMR (160 MHz) spectrum of compound **c5** in CDCl_3

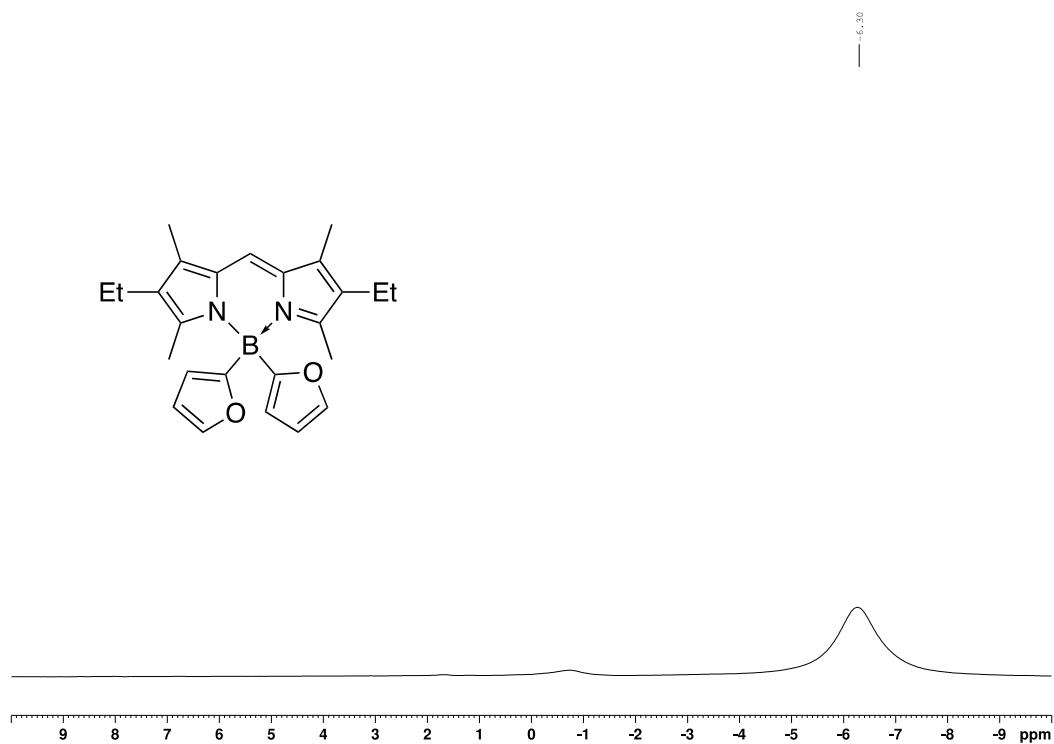
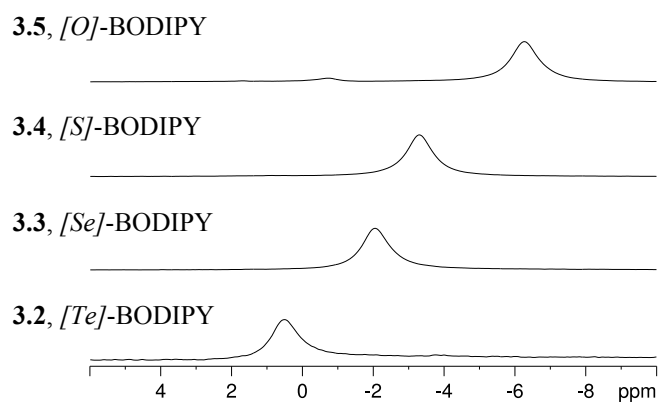


Figure 102. ^{11}B NMR spectra of the $[E]$ -BODIPYs series



C.5. Crystallographic Information

The crystal chosen was attached to the tip of a MicroLoop with Paratone-N oil. Measurements were made on a Bruker D8 VENTURE diffractometer equipped with a PHOTON III CMOS detector using monochromated radiation from Incoatec microfocus sealed tubes, Mo K α ($\lambda = 0.71073 \text{ \AA}$) for all structures except **c3**, where Cu K α ($\lambda = 1.54178 \text{ \AA}$) was used.²⁴⁹ The temperature of each data collection was 125 K except for the Cu collection which was carried out at 150 K. The initial orientations and unit cells were indexed using a least-squares analysis of the reflections collected from a complete 180° phi-scan, 3 to 10 seconds per frame and 1° per frame. For data collection, a strategy was calculated to maximise data completeness and multiplicity, in a reasonable amount of time, and then implemented using the Bruker Apex 4 software suite.²⁴⁹ The data were collected with 15 to 90 sec frame times for the Mo experiments, and using variable theta (θ) dependent frame times for the Cu experiment. The crystal to detector distance was set to 4 cm. Cell refinements and data reductions were performed with the Bruker SAINT software,²⁵⁰ which corrects for beam inhomogeneity, possible crystal decay, and Lorentz and polarisation effects. A multi-scan absorption correction was applied in every case (SADABS).²⁵⁷ The structures were solved using SHELXT-2014²⁵² and were refined using a full-matrix least-squares method on F^2 with SHELXL-2018.²⁵² The non-hydrogen atoms were refined anisotropically. The hydrogen atoms bonded to carbon were included at geometrically idealised positions and were allowed to ride on the atom to which they were bonded. The isotropic thermal parameters of these hydrogen atoms were fixed at $1.2U_{\text{eq}}$ of the parent carbon atom or $1.5U_{\text{eq}}$ for methyl hydrogens.

Structure c2, CSD 2217255

Data was collected and integrated to a maximum resolution of 0.55 Å. The initial structure refinement suggested the presence of a small twin component. The program Cell_Now²⁵⁸ was used to identify the main crystal domain and the frames were re-integrated at the same resolution using this domain only. Three reflections were removed from the final refinement because of poor agreement between F_{obs}^2 and F_{calc}^2 . At the last stages of the refinement, the data was cut to a resolution of 0.60 Å ($\theta_{max} = 36.32^\circ$) to remove some of the residual noise.

Structure c3, CSD 2217254

Data was collected and integrated to a maximum resolution of 0.82 Å ($\theta_{max} = 70.57^\circ$). Although the mean $I/\sigma(I)$ value was 7.14 at 0.82 Å resolution, data completeness was low, only 97.6 %. This did result in a low data to parameter ratio (with the disorder completely modelled) at the end of the refinement.

The compound crystallised in the centrosymmetric Monoclinic space group $P2/c$ with two molecules in the asymmetric unit but with only one half of each molecule being uniquely defined. The central boron and carbon atoms in each molecule lie on a C_2 axis and the other half of each molecule is generated by rotation about these axes. The unit cell, crystal system and space group for this compound proved to be identical (or nearly so for the unit cell parameters) to that of **c4**, which was collected first.

The routine TwinRotMat in Platon²⁵⁴ showed that the crystal chosen for analysis was a twin. The twin law [1 0 1 0 -1 0 0 0 -1] was added to the refinement and the original HKLF4

format reflection file used. BASF refined to a value of 48.8(3) %. Again, this is the same as found for **c4**.

The structure was found to be heavily disordered. In each molecule, the selenophene rings can be coordinated to the boron atom with either face up, resulting in the selenium atom being sometimes located on one side of the ring or the other. The same selenophene carbon atom is always bonded to the boron atom, so that the selenium atom is always adjacent to the carbon atom bonded to boron but partially occupied on each side of the ring.

These disorders were each defined using two-part models. The geometries of each part were restrained to be similar, and the atoms of the same type involved in each disordered group were restrained to have similar thermal parameters. The disordered carbon atoms of the selenophene ring directly bonded to boron, were assigned the same thermal parameters. Bonds from disordered parts to ordered parts of the molecules were restrained to be similar. Finally, a rigid bond restraint was placed over all of the atoms in both of the molecules and all of the rings were restrained to be planar.

At the end of the refinement of structure **c4** there was evidence of further whole molecule disorder in the structure beyond that included the final model. It appeared that there was a second minor orientation for each molecule in which they had flipped upside down and parallel to the orientation of the original molecules in such a way that they overlapped almost completely. Attempts were made to model this disorder, but they were not successful. In the selenium compound the same type of disorder was obviously present, and as a larger fraction of the unit cell contents. This allowed the positions of the atoms in the molecules to be split further and the disorder successfully modelled. (Please see the

included composite diagram, **Figure 111**, showing the breakdown of the disorder present in molecule one, so that this discussion is easier to follow).

The major component of each molecule had the selenophene ring in both a major and minor orientation, varying in the position of Se in the ring. The minor component of each molecule (inverted) was also found to have a major and orientation for the selenophene rings, again varying in the position of the Se atoms. The occupancies of all of these different parts were refined with free variables, which were combined to total one for the occupancy of each molecule in the asymmetric unit. Due to the considerable overlap of the major and minor contributors to the disorder, a number of the atoms in the two parts had to be restrained to have similar (or the same) anisotropic displacement parameters. Finally, all of the BC bond lengths were restrained to the same value, 1.60(2) Å.

At first a free variable refined was used to determine the occupancy of the atoms in the major component of the disorder of the backbone of both molecules 1 and 2. It refined to a value of 92.3(4) %, leaving an 8.6 % occupancy for the atoms of the minor component of the backbone of molecules 1 and 2. The occupancies of the selenophene rings were all calculated separately with different free variables. The selenophene ring on molecule 1, the major ring component of the major disordered form, was determined to have an occupancy of 48.9(4) %, while the minor component of the ring of the major disordered form was found to have an occupancy of 44.8(4) %. The total occupancy of these two parts of the ring disorder, $48.9 + 44.8 = 93.7$ %, matches reasonably well with the total occupancy of the backbone in the major disordered form. The same numbers for molecule 2 refined to 46.6(4) % and 41.3(4) % for a total of 87.9 %, a bit lower than those for molecule 1, but

still within the limit of agreement to the value refined for the occupancy of the backbone atoms in the major component of the disorder for molecule 2. To make the occupancies of the disordered atoms easier to constrain with SUMP instructions, the free variable describing the major and minor components of the backbone disorder of molecules 1 and 2 was removed. In its stead, the atoms of the major part of the disorder (A) were given fixed occupancies of 0.90 (reduced by symmetry where necessary) and the atoms of the minor part (B) were assigned occupancies of 0.10. These values (0.90 and 0.10) could then be used as the targets for the total occupancies of the further disordered selenophene rings in their major and minor orientations.

After fixing the occupancy of the atoms in the main part of the structure to 90%, the two orientations of the selenophene rings in that part were refined to give occupancies of 47.1(3) % and 42.8(3) % for a total of 89.9 %. For molecule 2, in the main parts of the disorder, the selenophene ring atoms had occupancies that refined to 47.8(3) % and 42.1(3) %, for a total of 89.9 %. The same comparisons can be made for the disordered selenophene rings in the minor component of the disordered molecules. When totaled, these values should sum to close to the value found for the occupancy of the atoms of the minor component of the backbone atoms (set to 10 %). For molecule 1, the occupancy of the first ring form refined to 6.1(3) % and the second ring form to 3.7(3) %. The total selenophene ring occupancy of the minor form of molecule one is thus 9.8 %. In molecule 2, the first selenophene ring atoms' have occupancies of 4.9(3) % and the second ring component 5.0(3) % for a total of 9.9 %. The differences observed, relative to the fixed 10 % for the backbone of the minor component, is accounted for by the uncertainties in the calculated

occupancies. These slight deviations from the fixed values, do result in minor disagreements between the calculated and reported formulae in the checkcif file.

After refining parameters for all of the disordered parts visible in the Fourier maps of this structure, the data over parameter ratio was low, raising a B level checkcif alert. The good agreement of the calculated occupancies for different parts of the molecules, particularly for the selenophene ring orientations in the main component of the disorder, supports the idea that the model chosen to describe the structure is reasonable, even if it has resulted in a low d/p ratio.

Structure c4, CSD 2217253

Data was collected and integrated to a maximum resolution of 0.75 Å. Four reflections, three of which were partially obscured by the beam stop, were removed from the final refinement because of poor agreement between F_{obs}^2 and F_{calc}^2 . At the last stages of the refinement, the data was cut to a resolution of 0.80 Å ($\theta_{max} = 26.35^\circ$) using a SHEL instruction to remove some of the residual noise and electron density.

The compound crystallised in the centrosymmetric Monoclinic space group $P2/c$ with two molecules in the asymmetric unit but with only one half of each molecule being uniquely defined. The central boron and carbon atoms in each molecule lie on a C_2 axis and the other half of each molecule is generated by rotation about these axes.

The routine TwinRotMat in Platon²⁵⁴ showed that the crystal chosen for analysis (and all others tried) was a twin. The twin law [1 0 1 0 -1 0 0 0 -1] was added to the refinement and the HKLF4 format reflection file used. BASF refined to a value of 49.6(2) %.

The structure was found to be heavily disordered. In each molecule, the thiophene rings can be coordinated to the boron atom with either face up, resulting in the sulfur atom being sometimes located on one side of the ring or the other. The same thiophene carbon atom is always bonded to the boron atom, so that the sulfur atom is always adjacent to the carbon atom bonded to boron but partially occupied on each side of the ring. In addition, the ethyl side group is also disordered in both molecules.

These disorders were each defined using two-part models, with the total occupancy always set to one. The geometries of each part were restrained to be similar, and the atoms of the same type involved in each disordered group were restrained to have similar thermal parameters. The disordered carbon atoms of the thiophene ring directly bonded to boron, were assigned the same thermal parameters. Bonds from disordered parts to ordered parts of the molecules were restrained to be similar. Finally, a rigid bond restraint was placed over all of the atoms in both of the molecules. For the thiophene rings, the occupancies of molecule 1 refined to 58.5(6) % and 41.5 % for parts one and two, respectively, while for molecule 2 the analogous values were found to be 52.2(6) % and 47.8 %. Refinement of the occupancies of the atoms of the ethyl group in molecule 1 gave 87(2) % and 13 % for parts 1 and 2, respectively, and for molecule 2 values of 59(3) % and 41 % were calculated. At the end of the refinement, the statistics were still a bit higher than expected. An unexpected C level alert remained in the checkcif file: Ratio of Maximum / Minimum Residual Density = 2.56. The pattern of the remaining peaks in the final Fourier difference map also suggested that there was some whole molecule disorder that had not yet been modelled. It appeared that perhaps there was a second minor orientation for each molecule

in which they had flipped upside down and parallel to the orientation of the original molecules. Attempts were made to model this disorder, but the peaks were too weak and there was not enough data for this to be successful. The contribution of the minor orientation remained visible in the final Fourier maps.

Once the refinement of **c3** was complete, the refinement of **c4**, where visible disorder had been left unaccounted for, was revisited. The two compounds crystallise in the same space group with nearly identical unit cells. It thus proved possible to transfer and then refine the same disordered model used for selenium to the sulfur structure. This entire process actually worked well. The model for **c3** is definitely the correct model to apply to the disorder present in **c4**.

Additional restraints had to be added to get things to refine nicely in the sulfur case. By the time it was complete, the results were still better for the disordered sulfur model than for the original refinement, but only slightly so (R1 had gone from just above **c7** to just below it). However, this is not much of an improvement considering all the extra parameters refined in the disordered model.

The overall disorder in the sulfur structure was found to be less (*i.e.*, the contribution of the minor component is less) when compared to that in its selenium analogue. The occupancy of the minor component of the disorder is about half in **c4** (5 %) what it is in **c3** (10 %). This is undoubtedly why the refinement was more difficult, with extra restraints having to be used in the former case.

In the end, the results did verify that this is the correct model to describe the disorder present in **c4**. However, ultimately the original results (where the disorder was visible but

not modelled) were retained, and are reported here, since the benefits of the more detailed model proved to be minor at best.

Structure c6, CSD 2217251

Data was collected to a maximum resolution of 0.80 Å but the final data set was integrated only to a resolution of 0.84 Å ($\theta = 25.11^\circ$ where the mean $I/\sigma(I)$ ratio was 3.09). One reflection (0 1 1), which was partially obscured by the beam stop, was removed from the final refinement because of poor agreement between F_{obs}^2 and F_{calc}^2 .

The compound crystallised in the centrosymmetric Triclinic space group $P-1$ with one unique molecule in the asymmetric unit. There was no solvent found in the lattice. The product was not that expected. The two furan rings thought to have been coordinated to the central boron atom had (for the most part) oxidised and opened, giving -OC(O)(CH)₂C(O)H chains coordinated in their stead.

The structure was also found to be disordered. In one position, the furan ring expected to have bonded to boron was totally absent. It had completely oxidised and opened, leaving only a -OC(O)(CH)₂C(O)H chain. In the other position, the ring had only partially oxidised. Thus, atoms for both the furan ring and the oxidised chain forms were partially present, occupying overlapping positions in the disordered part of the structure.

This occupational disorder was defined using a two-part model. The geometries of the two open chain groups were restrained to be similar. In the furan ring, the C-O bond lengths were also restrained to be similar. The two atoms bonded to boron in the disordered part (O4 and C26) were restrained to have similar anisotropic displacement parameters. Finally, a rigid bond restraint was placed over all of the atoms in the molecule. The occupancies of

the two parts of the disordered group (oxidised chain and furan ring) were refined to total one using a single free variable. The final occupancies obtained were 80.1(5) % and 19.9 % for the open chain form and the furan ring form, respectively.

Structure c7, CSD 2217252

Data was collected and integrated to a maximum resolution of 0.80 Å. One reflection (0 2 0), which was partially obscured by the beam stop, was removed from the final refinement because of poor agreement between F_{obs}^2 and F_{calc}^2 . At the last stages of the refinement, the data was cut to a resolution of 0.82 Å ($\theta_{max} = 25.68^\circ$) using a SHEL instruction to remove some of the residual noise and electron density, while still retaining enough reflections to maintain a reasonable d/p ratio.

The compound crystallised in the centrosymmetric Monoclinic space group $P2_1/c$ with one unique molecule in the asymmetric unit. There was no solvent found in the lattice. The product was found to have two furan rings coordinated to the central boron atom as expected. However, a third furan ring was also sometimes found to be bonded to the *meso* carbon of the BODIPY backbone. That furan ring was found to be only partially occupied, with a hydrogen atom being present at the C5 position the remainder of the time.

The structure was found to be disordered. In each case, the furan ring can be coordinated to the boron or carbon atom with either face up, resulting in the oxygen atom being sometimes located on one side of the ring or the other. The same furan carbon atom is always bonded to the boron or carbon atom, so that the oxygen atom is always adjacent to the carbon atom bonded to boron/carbon but partially occupied on each side of the ring. In

addition, the majority of the methyl side groups were found to be rotationally disordered, with a two-part model for the hydrogen atoms giving the best results.

The ring disorders were each also defined using two-part models. The geometries of each part of the same ring were restrained to be similar, and the atoms of the same type involved in each disordered group were restrained to have similar anisotropic displacement parameters. Bond lengths from disordered rings to the boron atom were restrained to be similar. The atoms in the minor part of the disordered rings were restrained to be flat. Finally, a rigid bond restraint was placed over all of the atoms in the molecule.

For the furan rings bonded to boron, the total occupancy was set to one using a different free variable for each ring. The occupancies of ring 1 refined to 78(1) % and 22 % for parts one and two, respectively, while for ring 2 the analogous values were found to be 72(1) % and 28 %. The occupancies of the furan ring atoms bonded to the *meso* carbon of the backbone had to be treated differently, as that ring was present only part of the time. The major component of the disorder, the minor component of the disorder and the occupancy of the hydrogen atom sometimes also present on C5 had to be refined using separate free variables. A SUMP instruction was used to make the total refine to one. The results obtained were 48(1) % for the major component and 29(1) % for the minor component of the disordered ring while 23(1) % of the time the furan ring was replaced by a hydrogen atom.

Discussion of the X-ray and Computational Results

The entire series of compounds (O, S, Se and Te) were investigated crystallographically and the tellurium structure was the only one in the series that was found not to be

substantially disordered. The presence of so much disorder made any distinct trends in the usual metrical parameters, bond lengths and angles (**Table 13**), impossible to assess. Instead, simple theoretical gas phase calculations were carried out on the isolated 5-membered heterocycles to identify trends that might be manifest in the X-ray crystallographic results. The energy minimised rings were optimised at the MP2 level with 6-31G* basis sets using the program Spartan'20.²⁵⁹ Electrostatic potential maps were then drawn on the same scale and mapped onto a 0.002 au isosurface so that they could be compared (**Figure 103**). The maps showed that in the furan ring the most negative region is located on the oxygen atom, but this migrates away from the hetero-atom and out onto the ring carbon atoms (or its π system) as one goes down the series. The negative potential centred on the oxygen atom in furan helps to explain its greater reactivity compared to the other compounds studied.

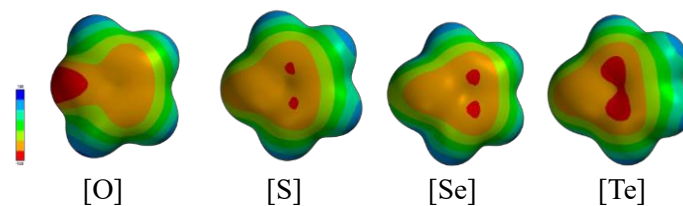


Figure 103. Calculated electrostatic potential maps of the gas phase heterocycles.

When the HOMO and LUMO of each ring were plotted (**Figure 104**), another obvious difference was observed between the Te compound and the others in the group. The HOMO is centred on the carbon atoms of the ring in the O, S and Se cases but in the Te ring it lies directly on the Te atom. The HOMO and LUMO of the heterocycle being centred on the tellurium atom (and not on the ring carbons as in the other compounds) suggested that it might be different from the others of the series in other respects. It also provided a possible reason that this is the one structure that is well ordered in the solid state.

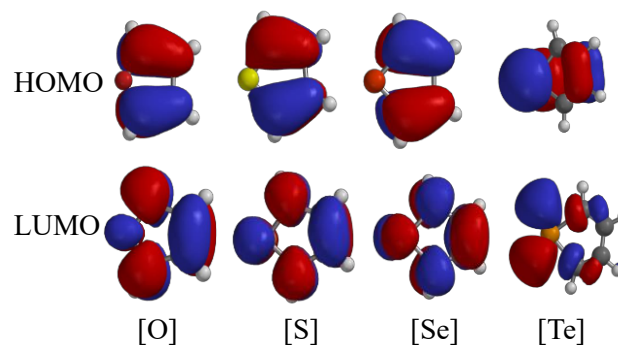


Figure 104. Calculated HOMO and LUMO diagrams of gas phase heterocycles.

The X-ray crystallographic results showed that in all of the structures studied the heterocycles are not coplanar with the BODIPY framework, suggesting that they are not conjugated. In all of the structures, the bond angles around the boron atoms are close to

tetrahedral for all of the components even when there is considerable disorder present. The structures **c3**, **c4** and **c7** are clearly all very similar, as shown in **Figure 105** of the main manuscript. In all three, the BODIPY plane is flat; by symmetry boron lies in the BODIPY plane of **c3** and **c4** compounds, while in the major component of **c7** boron lies 0.11 Å out of the plane defined by the framework of the BODIPY. For the tellurium compound the boron has been pulled much further out of the plane (0.44 Å). In addition, the entire BODIPY framework in **c2** is now noticeably bent. The tellurium structure is also markedly different from the others in the relative positions of the two heterocycles. In all of the other compounds, the planes defined by the heavy atoms of the two heterocycles intersect with angles that range from 15.3 ° to 31.2 ° (for the main part of the disordered molecules). In **c2** this angle is much closer to perpendicular, 67.3 °.

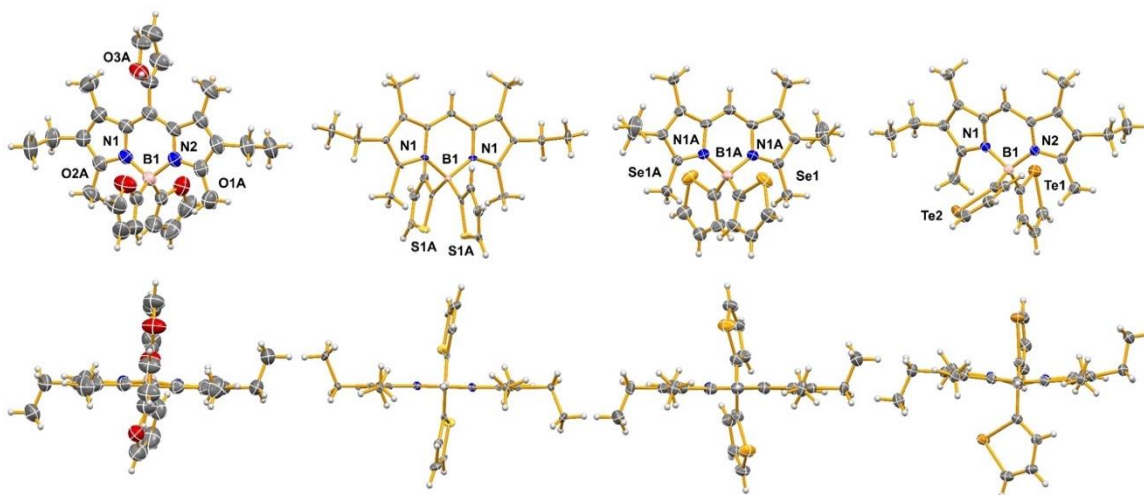


Figure 105. Structures of **c7** (one of the major components featuring three furan rings), **c4**, **c3** and **c2** (left to right), highlighting heterocyclic ring orientations at boron (top) and planarity (bottom). Disorder (where present) has been removed for clarity. Thermal ellipsoids are drawn at the 50% probability level and only selected atoms have been labelled.

The tellurium structure was the only one found to be well ordered. The oxygen containing structures, **c6** and **c7**, are both disordered but for compositional reasons, arising from the high chemical reactivity of the furan ring. The sulfur and selenium compounds proved to be different from these two extremes. In **c3**, **c4** and **c7**, the boron coordinated heterocycles always are disordered, but with the two orientations generally co-planar. The hetero-atom can be found in either position in the ring available to it, next to the carbon atom bonded to boron, equivalent to the ring being bonded to boron with either face up/down. This always results in the hetero-atoms of the two rings both facing either up (close to boron) or down (away from boron) in the major component of the disordered model. In the structure **c4**, the major component of the disorder has the sulfur atoms of the two rings both facing in the downward position away from boron, while in **c2**, **c6** and **c7**, the opposite is true and both hetero-atoms face up towards boron in the major component.

In addition to the ring disorder, **c3** and **c4** also pack with two molecules in the asymmetric unit and show alternative positions of the BODIPY backbone for both molecules. In each molecule the minor orientation has flipped upside down and parallel to the original orientation in such a way that they overlap almost completely, with the minor orientation also showing disordered positions for the hetero-atoms in the rings. In the **c3** the second orientation is more prevalent, which allowed the molecules to be split further and the disorder successfully modelled. These very complex crystal structures suggest that there are no strong intermolecular forces to guide the packing in these two compounds.

The presence of so much structural disorder made the analysis of intermolecular interactions more difficult. There do not appear to be any significant stacking interactions

in any of the structures studied. For the structures **c3**, **c4**, **c6** and **c7** most of the contacts appear to be C-H...E (E = O, S, Se) type, with C-H...ring (BODIPY) contacts also present. In these structures there are no E...E contacts and no E...ring contacts. The fact that the structures and interactions of **c3**, **c4** and **c7** are so similar, mirrors the fact that all three isolated heterocycles have electrostatic potential maps and HOMO/LUMO pairs that are also very similar.

The interactions in **c2** proved to be completely different. A significant Te...Te intermolecular contact and a related Te...ring interaction were located (**Figure 108**); nothing similar was observed in any of the other structures. The close approach between pairs of molecules of the tellurium compound result in a Te1...Te1 (1-x, -y, -z) intermolecular contact of 3.7512(3) Å, well below the sum of the van der Waals radii. In addition, there are short contacts between Te1 and C5, C6 and C7 of the second molecule. These interactions occur roughly perpendicular to the line joining Te1...Te1, at distances again well below the sum of the van der Waals radii. The interaction is best described as involving Te1 and the large ring comprising B1, N1, N2 and C4 to C9 of the BODIPY on the second molecule, as the distance to the centroid of this ring is 3.414 Å, shorter than the distance to any individual atom of the ring. The Te1...Te1(original)...centroid angle is 67°. Interestingly it is the ring containing Te1 that is involved in the intermolecular interactions. The ring with Te2 has twisted away from the arrangement observed in the other structures, however, Te2 is involved in only a single C-H...Te hydrogen bond, as the acceptor. The Te...Te contact distance is very similar to that reported by Braun et al.²⁶⁰ (3.78 Å) in the structure of a methoxy bearing tellura(benzo)bithiophene, where again two molecules

associate to form pairs in the solid state. In that structure the Te centres also make close contact with an aromatic ring on the second molecule in each pair, just as observed here. Clearly the structure and the intermolecular interactions in the structure of **c2** are different from those in the other compounds and arise from its unique electronic properties, as also found from the theoretical calculations. The heavy tellurium atom shows metalloid characteristics, with the HOMO centred on Te in the isolated ring and its propensity to form Te...Te contacts in the solid state. However, **c2** also shows an ability to form interactions with the organic portion of the molecule, a ring on the BODIPY framework, auguring well for its potential use in a variety of applications. The presence of tellurium makes the molecule more stable, in the sense that it is well behaved in the solid state, but also able to interact favorably with both inorganic (metalloid) and organic (BODIPY) materials.

Table 12. Crystal data and structural refinement details.

Identification code	c2	c3	c4	c6	c7
CCDC deposit number	2217255	2217254	2217253	2217251	2217252
Empirical formula	C ₂₅ H ₂₉ BN ₂ Te ₂	C ₂₅ H ₂₉ BN ₂ Se ₂	C ₂₅ H ₂₉ BN ₂ S ₂	C ₂₅ H ₂₉ BN ₂ O _{5.60}	C _{28.06} H _{30.53} BN ₂ O _{2.77}
Formula weight	623.51	526.23	432.43	457.83	450.84
Crystal system	Triclinic	Monoclinic	Monoclinic	Triclinic	Monoclinic
Space group	<i>P</i> -1	<i>P</i> 2/ <i>c</i>	<i>P</i> 2/ <i>c</i>	<i>P</i> -1	<i>P</i> 2 ₁ / <i>c</i>
Unit cell dimensions (Å and °)	<i>a</i> = 9.7534(3)	<i>a</i> = 17.7639(10)	<i>a</i> = 17.5426(13)	<i>a</i> = 10.0612(12)	<i>a</i> = 7.9699(4)
	<i>b</i> = 10.8894(3)	<i>b</i> = 9.0501(4)	<i>b</i> = 8.9372(7)	<i>b</i> = 11.1646(14)	<i>b</i> = 19.4642(10)

Identification code	c2	c3	c4	c6	c7
	$c = 11.5616(4)$	$c = 15.9539(7)$	$c = 15.8852(11)$	$c = 11.3960(14)$	$c = 16.1321(8)$
	$\alpha = 82.3449(10)$	$\alpha = 90$	$\alpha = 90$	$\alpha = 72.223(4)$	$\alpha = 90$
	$\beta = 82.0880(12)$	$\beta = 116.633(2)$	$\beta = 116.911(3)$	$\beta = 83.084(4)$	$\beta = 98.1542(17)$
	$\gamma = 87.4542(11)$	$\gamma = 90$	$\gamma = 90$	$\gamma = 88.701(5)$	$\gamma = 90$
Volume (\AA^3)	1204.99(7)	2292.7(2)	2220.8(3)	1210.0(3)	2477.2(2)
<i>Z</i>	2	4	4	2	4
Density (calculated, Mg/m^3)	1.718	1.525	1.293	1.257	1.209
Absorption coefficient (mm^{-1})	2.435	4.127	0.255	0.088	0.077

Identification code	c2	c3	c4	c6	c7
F(000)	604	1064	920	486	960
Crystal size (mm ³)	0.166x0.135x0.0	0.083x0.065x0.01	0.209x0.063x0.00	0.066x0.025x0.0	0.176x0.076x0.030
Theta range of data (°)	1.793 to 36.318	2.783 to 70.570	2.279 to 26.353	2.039 to 25.109	2.451 to 25.679
Index ranges (<i>h, k, l</i>)	-16/16, -18/18, - 19/19	-21/21, -10/11, - 19/16	-21/21, -11/11, - 19/17	-11/11, -13/13, - 13/13	-9/9, -23/23, -19/19
Reflections collected	150870	31748	44099	37508	70334
Independent reflections	11684	4298	4525	4269	4708

Identification code	c2	c3	c4	c6	c7
R(int)	0.0299	0.0684	0.0674	0.1072	0.1165
Completeness to 25.242° (%)	99.9	98.5	99.9	99.4	100.0
Max. and min. transmission	0.0619 and 0.0152	0.7360 and 0.5917	0.7457 and 0.6863	0.7452 and 0.5363	0.7454 and 0.6810
Data / restrains / parameters	11684 / 0 / 277	4298 / 1638 / 664	4525 / 615 / 386	4269 / 335 / 359	4708 / 770 / 462
Goodness-of-fit on F ²	1.145	1.109	1.133	1.060	1.038
Final R indices [I>2sigma(I)]	R1 = 0.0386 wR2 = 0.0714	R1 = 0.0701 wR2 = 0.1549	R1 = 0.0733 wR2 = 0.1674	R1 = 0.0735 wR2 = 0.1620	R1 = 0.0691 wR2 = 0.1689

Identification code	c2	c3	c4	c6	c7
R indices (all data)	R1 = 0.0473 wR2 = 0.0789	R1 = 0.0738 wR2 = 0.1575	R1 = 0.0782 wR2 = 0.1704	R1 = 0.1028 wR2 = 0.1776	R1 = 0.1201 wR2 = 0.2025
Largest diff. peak and hole (e.Å ⁻³)	1.768 and -1.025	0.527 and -0.378	0.917 and -0.358	0.262 and -0.250	0.268 and -0.197

Table 13. Selected structural properties of [*E*]-BODIPYs.

Parameter	[<i>O</i>]-	[<i>S</i>]-		[<i>Se</i>]-		[<i>Te</i>]-
	c7^a	c4		c3		c2
		Molecule	Molecule	Molecule	Molecule	
		1	2	1	2	
B-N bond lengths (Å)	1.570(4)	1.587(5)	1.588(5)	1.598(8)	1.586(8)	1.589(3)
B-C bond lengths (Å)	1.588(6)	1.640(9)	1.667(15)	1.547(12)	1.547(12)	1.606(3)
C-B-C bond angle (°)	112.6(7)	118.6(14)	123.1(13)	109.2(15)	108.0(14)	115.10(16)
N-B-N bond angle (°)	105.6(2)	106.2(4)	105.0(4)	106.1(7)	104.3(7)	105.26(14)
C-B-N bond angles (°)	109.1(5)	107.0(15)	104.2(9)	110.2(10)	110.2(10)	107.10(15)
Min /Max	110.1(5)	109(2)	109.5(14)	110.6(13)	112.1(8)	110.35(15)

^aData for compound **c7** in which the major component has a third furan ring. For the [*O*], [*S*] and [*Se*] structures data for Part A of the disorder is given.

Structure c2

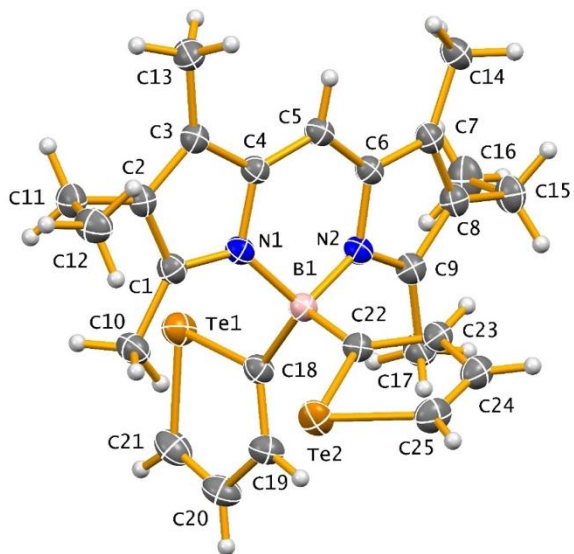


Figure 106. Structure of **c2**. Thermal ellipsoids have been drawn at the 50% probability level. Hydrogen atoms have not been labelled.

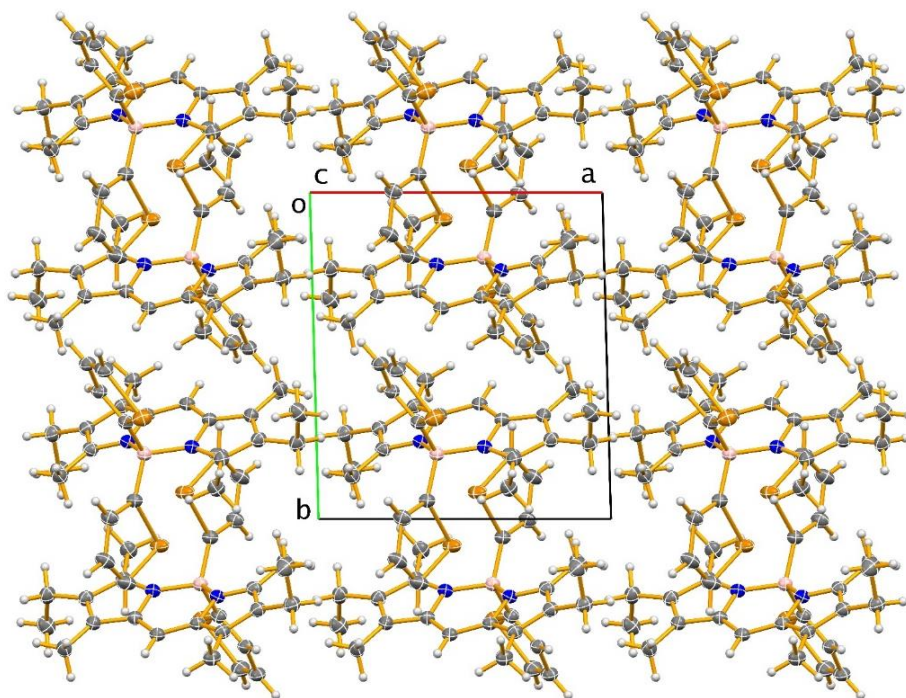


Figure 107. Packing diagram for **c2** viewed down the Z-axis.

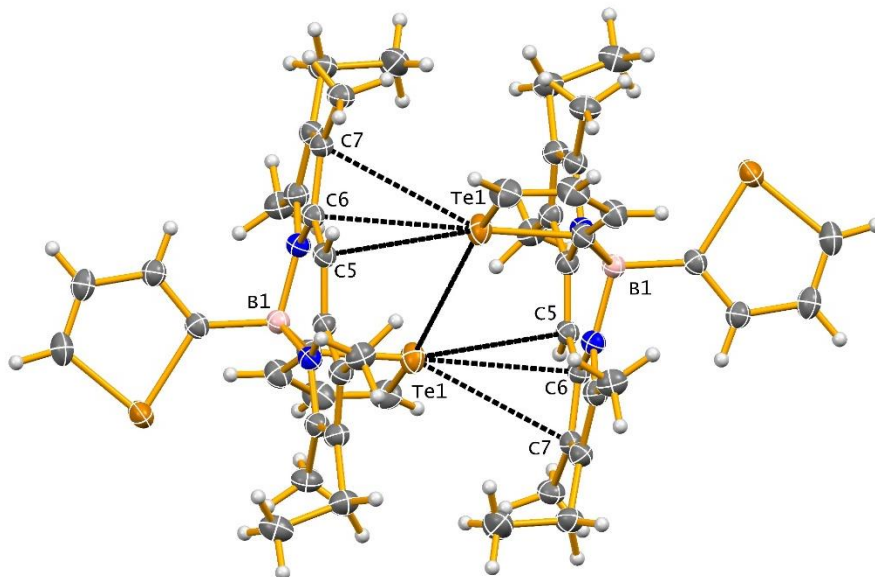


Figure 108. Intermolecular interactions involving Te (below the sum of the Van der Waals radii) in the solid-state structure of **c2**. Only those atoms directly involved in the contacts have been labelled.

Structure c3

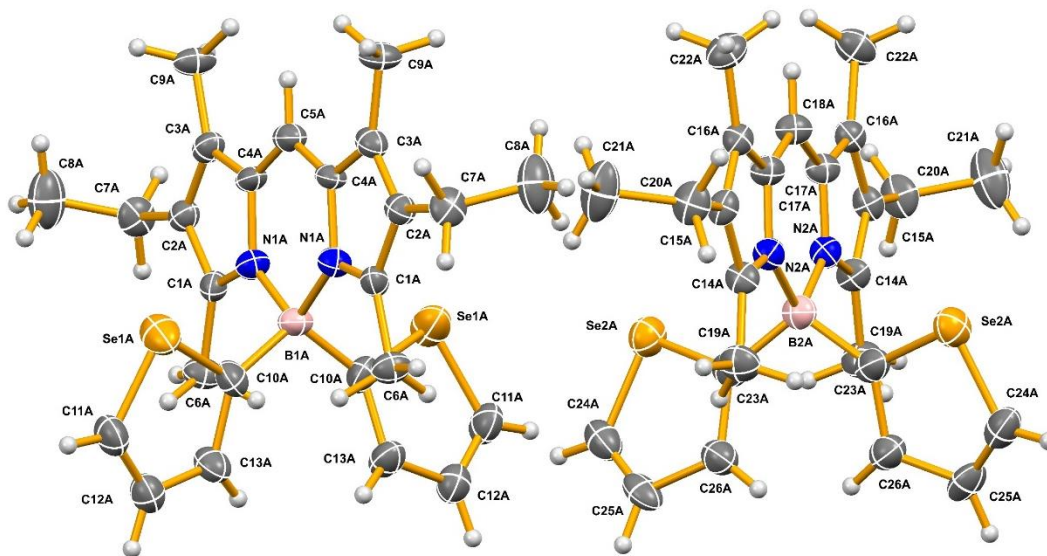


Figure 109. Structure of **c3** showing only the major component of the four total components refined for each of the independent molecules in the asymmetric unit. Thermal ellipsoids have been drawn at the 50% probability level. Hydrogen atoms have not been labelled.

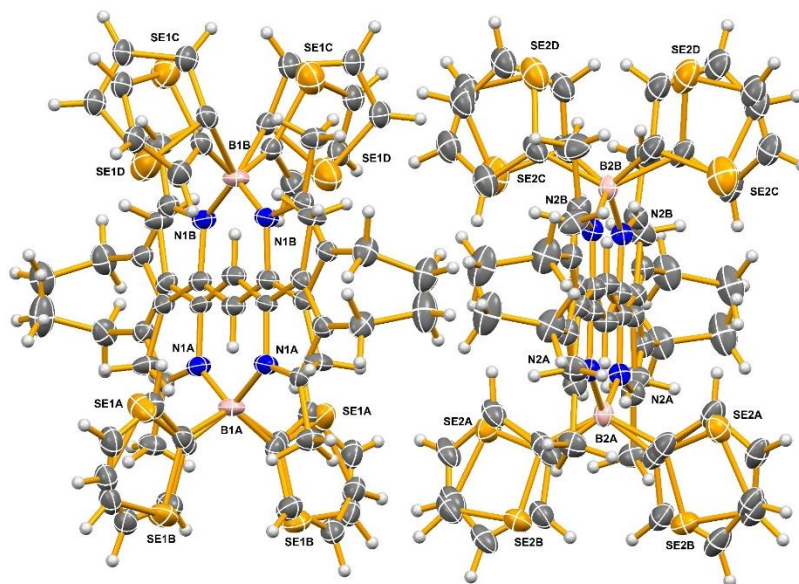


Figure 110. Structure of **c3** showing all four disordered components refined for each of the independent molecules in the asymmetric unit. Thermal ellipsoids have been drawn at the 50% probability level. Only selected atoms have been labelled for clarity.

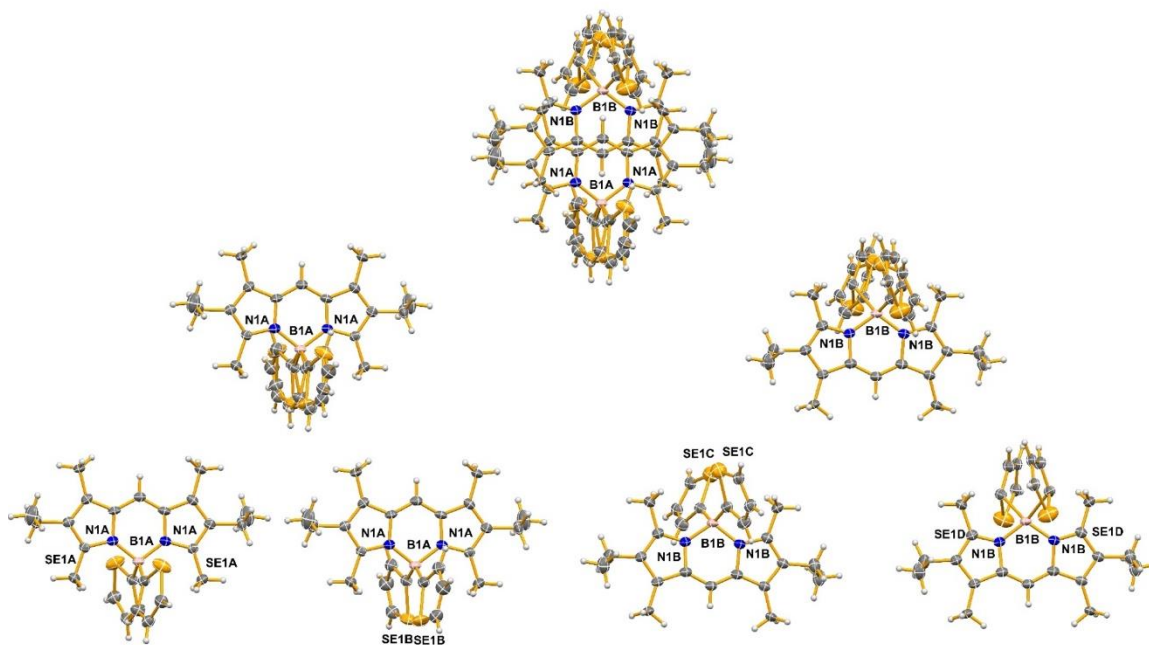


Figure 111. Composite diagram of molecule 1 in the structure of **c3** showing how the four disordered components are arranged relative to each other in the crystal. Top – all four components together. Middle – the two different orientations of the BODIPY framework separated. Bottom – the four different orientations of the selenophene ring separated. Thermal ellipsoids have been drawn at the 50% probability level. Only selected atoms have been labelled for clarity.

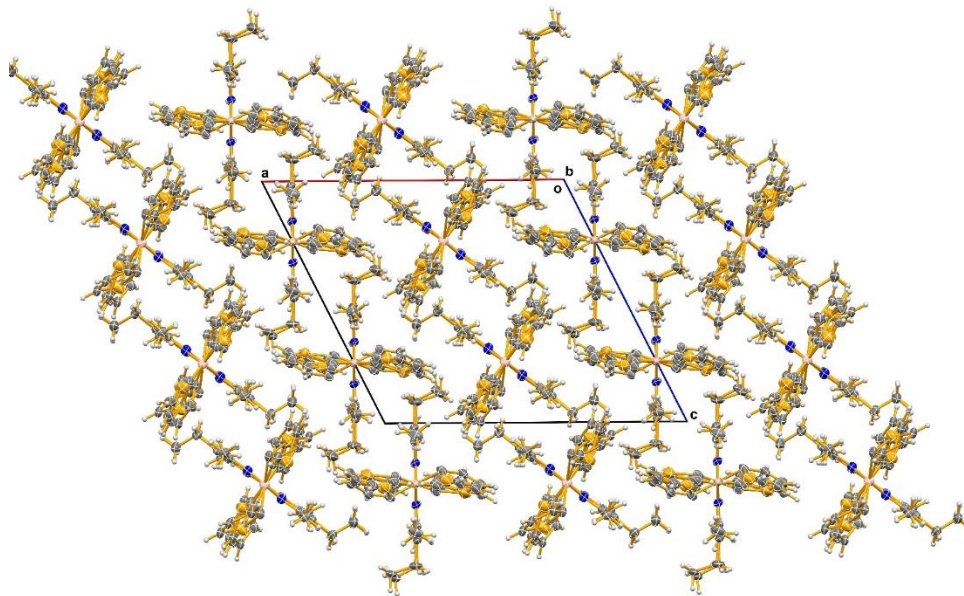


Figure 112. Packing diagram for **c3** viewed down the Y-axis. The disorder has not been removed.

Structure **c4**

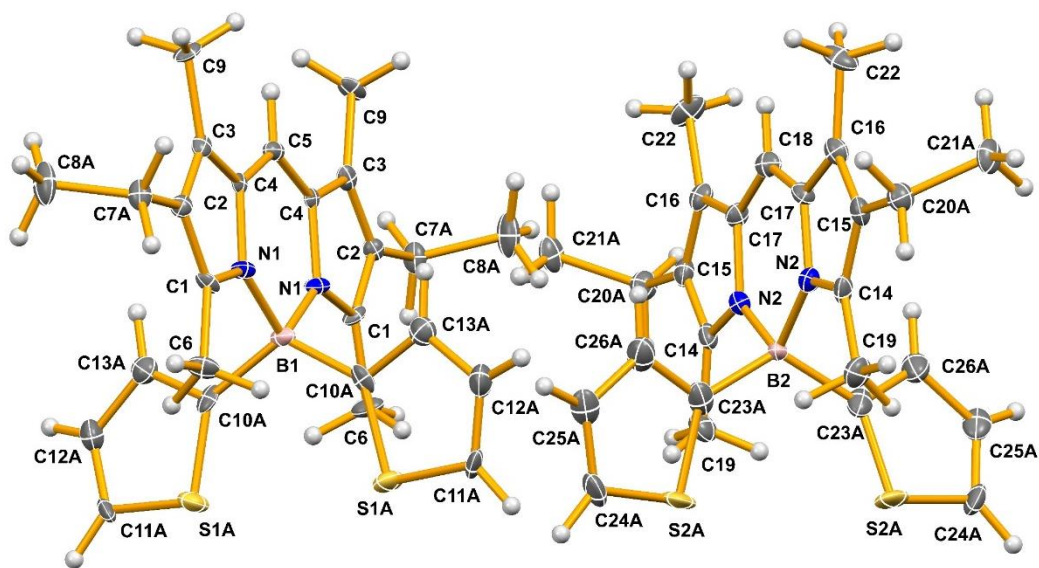


Figure 113. Structure of **c4** showing only the major component of the two total components refined for each of the independent molecules in the asymmetric unit. Thermal ellipsoids have been drawn at the 50% probability level. Hydrogen atoms have not been labelled.

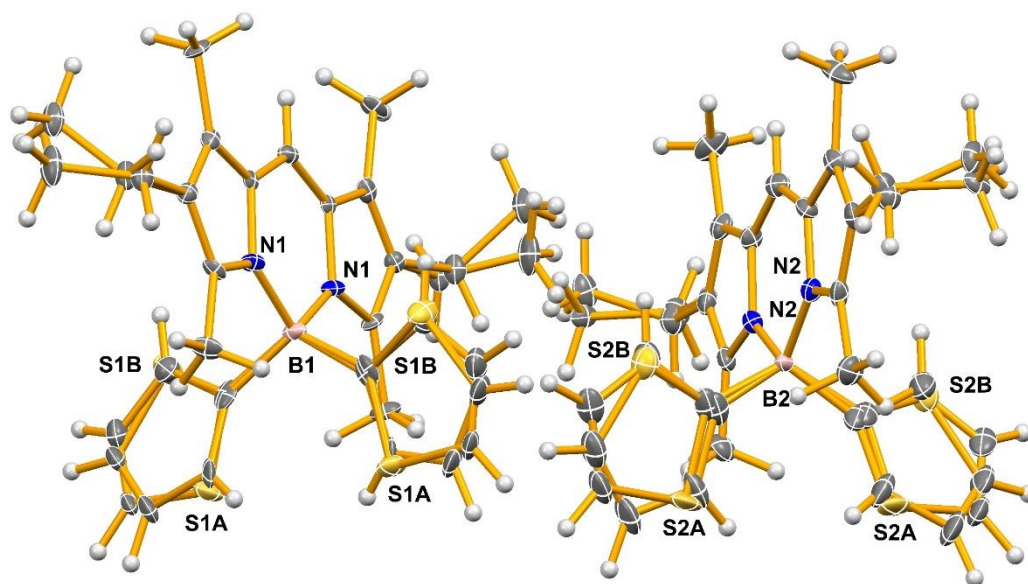


Figure 114. Structure of **c4** showing both disordered components refined for each of the independent molecules in the asymmetric unit. Thermal ellipsoids have been drawn at the 50% probability level. Only selected atoms have been labelled for clarity.

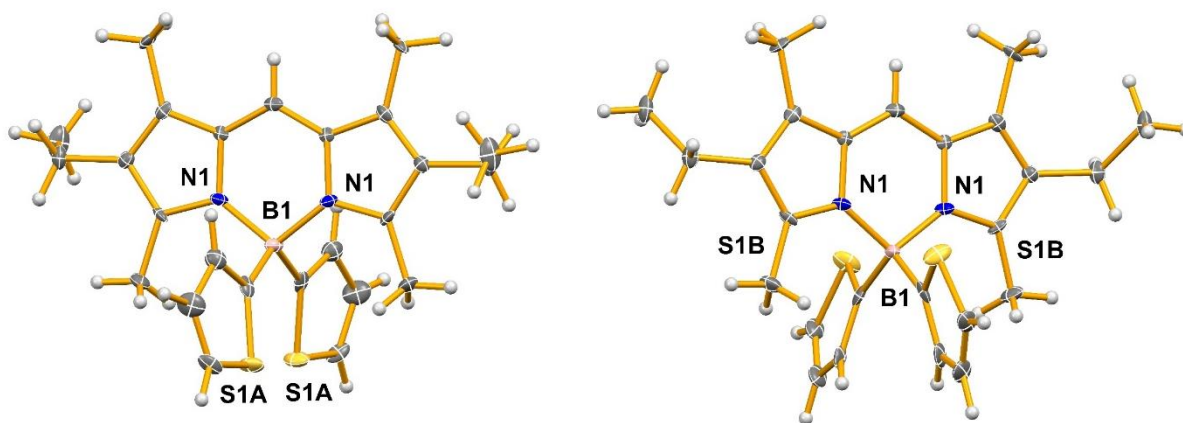


Figure 115. Molecule 1 in the structure of **c4** showing separately the two disordered components making up the refined model. Thermal ellipsoids have been drawn at the 50% probability level. Only selected atoms have been labelled for clarity.

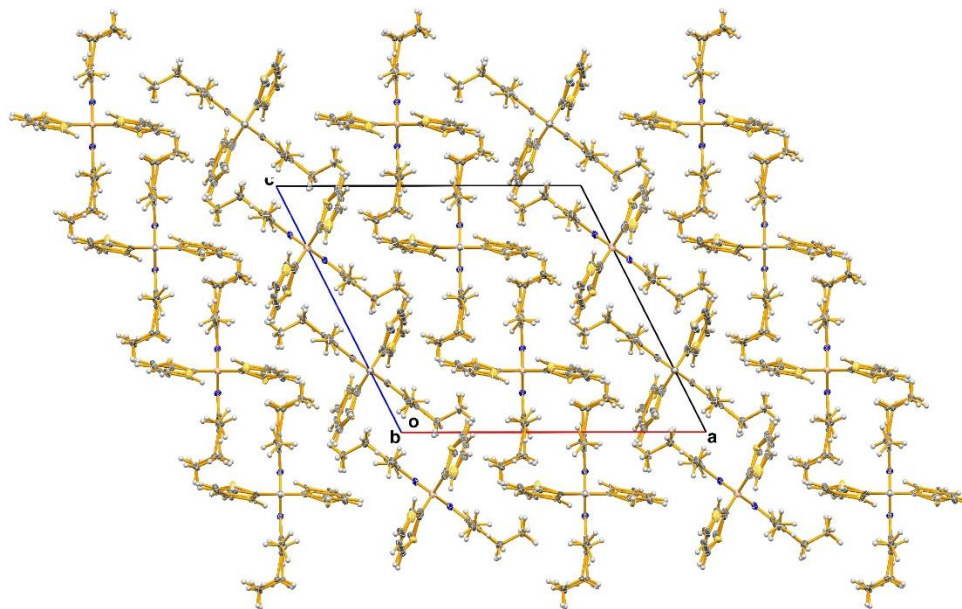


Figure 116. Packing diagram for *c4* viewed down the Y-axis. The disorder has not been removed.

Structure c6

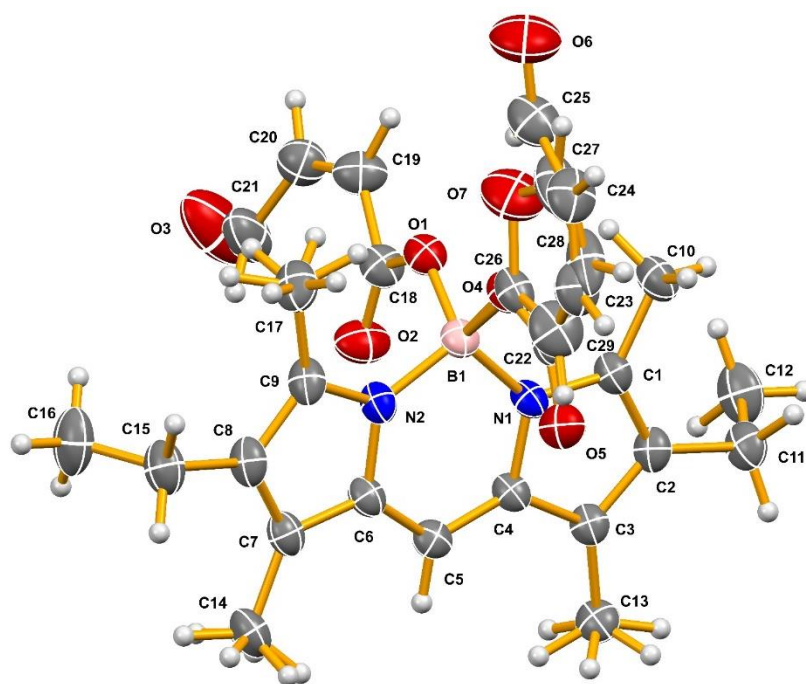


Figure 117. Structure of **c6** showing both disordered components refined. Thermal ellipsoids have been drawn at the 50% probability level. Hydrogen atoms have not been labelled.

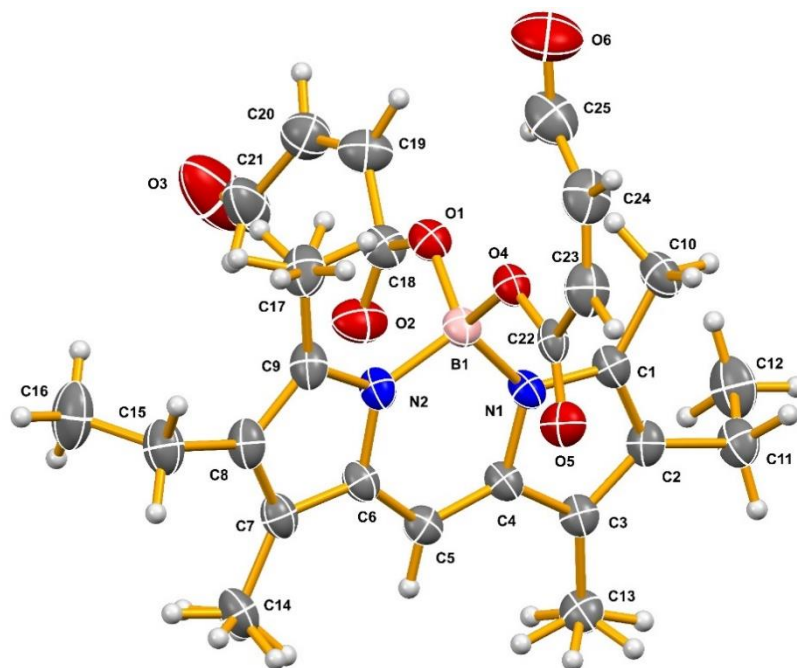


Figure 118. Structure of **c6** showing only the major component of the disordered model. Thermal ellipsoids have been drawn at the 50% probability level. Hydrogen atoms have not been labelled.

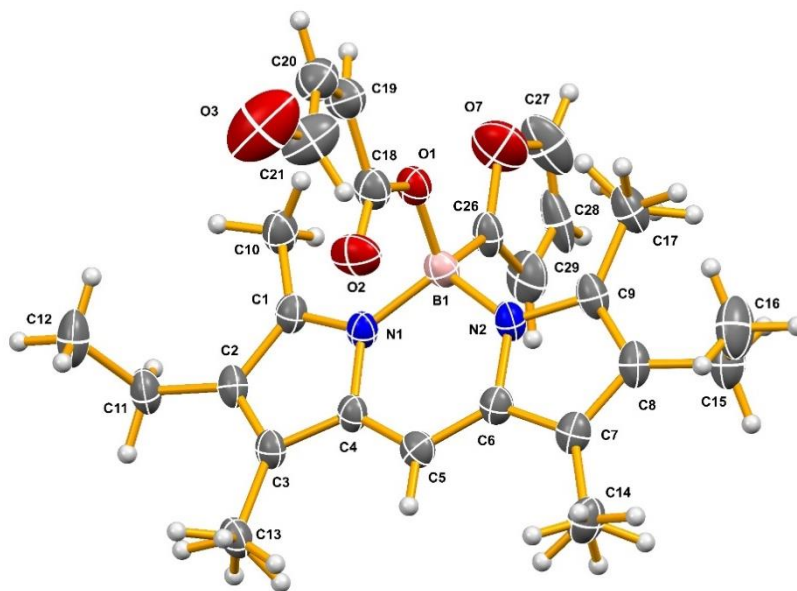


Figure 119. Structure of **c6** showing only the minor component of the disordered model (actually containing one intact furan ring). Thermal ellipsoids have been drawn at the 50% probability level. Hydrogen atoms have not been labelled.

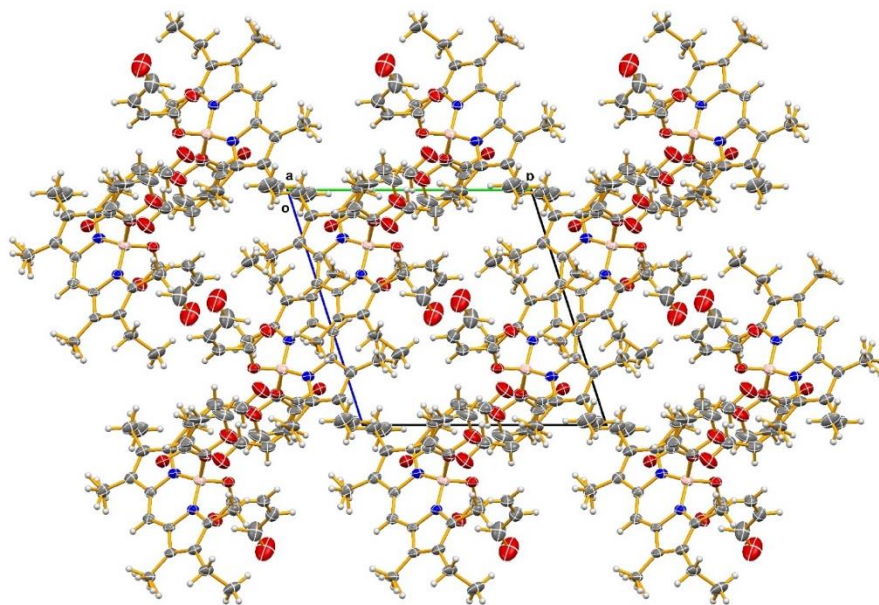


Figure 120. Packing diagram for **c6** viewed down the X-axis. The disorder has not been removed.

Structure c7

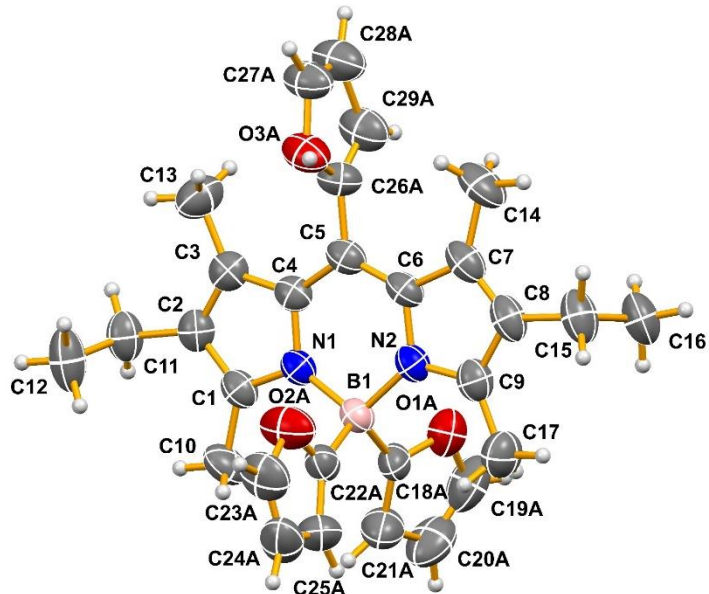


Figure 121. Structure of **c7** showing only the major component of the four total components refined in the disordered model. Thermal ellipsoids have been drawn at the 50% probability level. Hydrogen atoms have not been labelled.

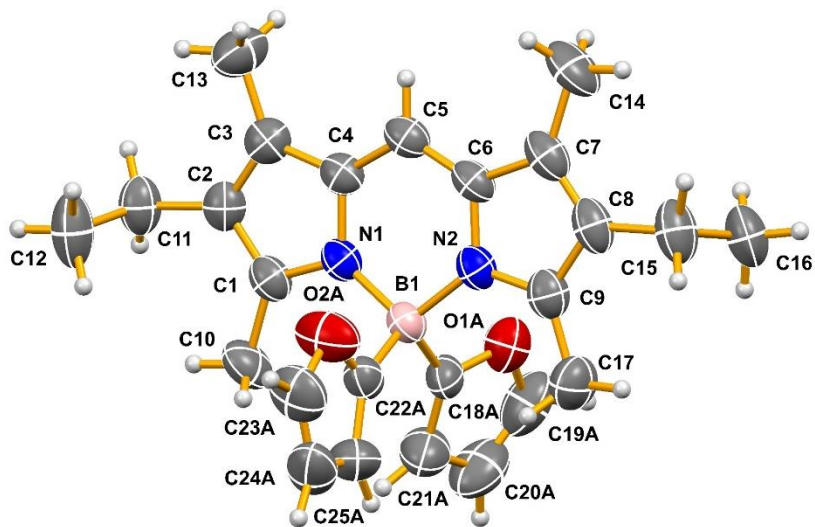


Figure 122. Structure of **c7** showing only the third component of the four total components refined in the disordered model. It is shown separately here as it is analogous to the other compounds being reported in this work. Thermal ellipsoids have been drawn at the 50% probability level. Hydrogen atoms have not been labelled.

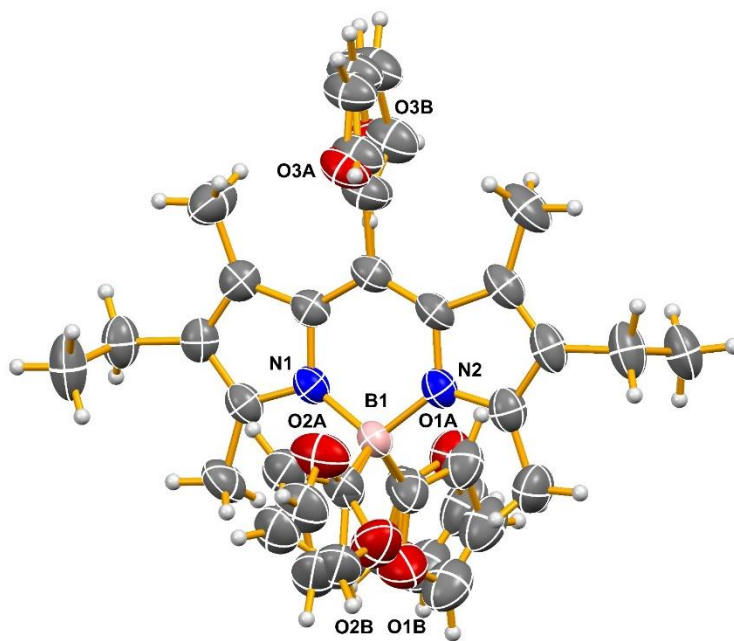


Figure 123. Structure of *c7* showing all four disordered components refined for the model chosen. Thermal ellipsoids have been drawn at the 50% probability level. Only selected atoms have been labelled for clarity.

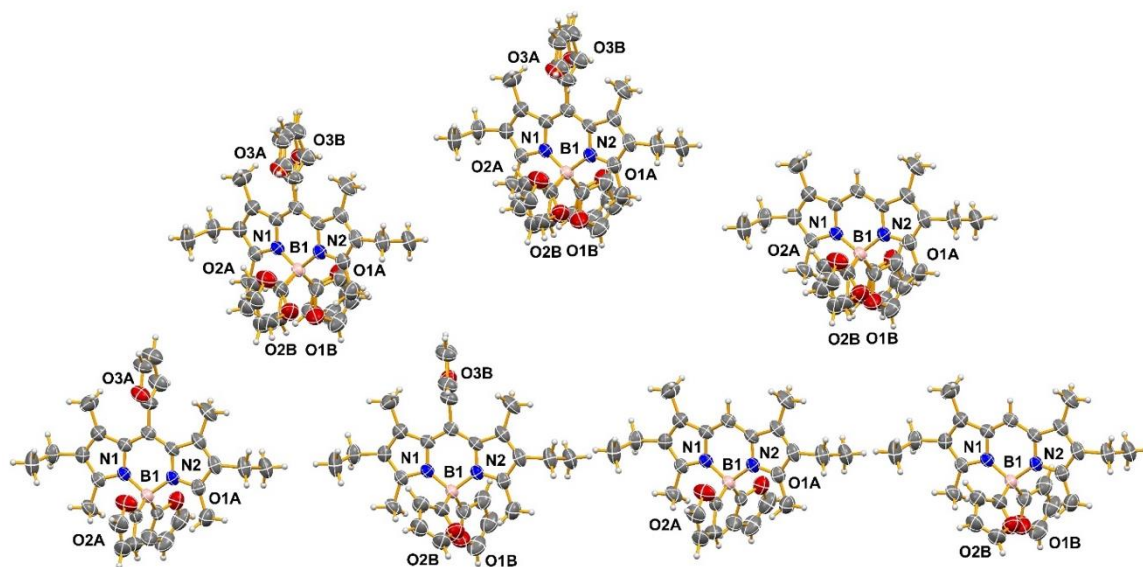


Figure 124. Composite diagram of *c*7 rings showing how the four disordered components are arranged relative to each other in the crystal. Top – all four components together. Middle – the two different substituents on the BODIPY framework (furan ring or hydrogen atom) separated. Bottom – the different orientations of the furan ring separated. Thermal ellipsoids have been drawn at the 50% probability level. Only selected atoms have been labelled for clarity.

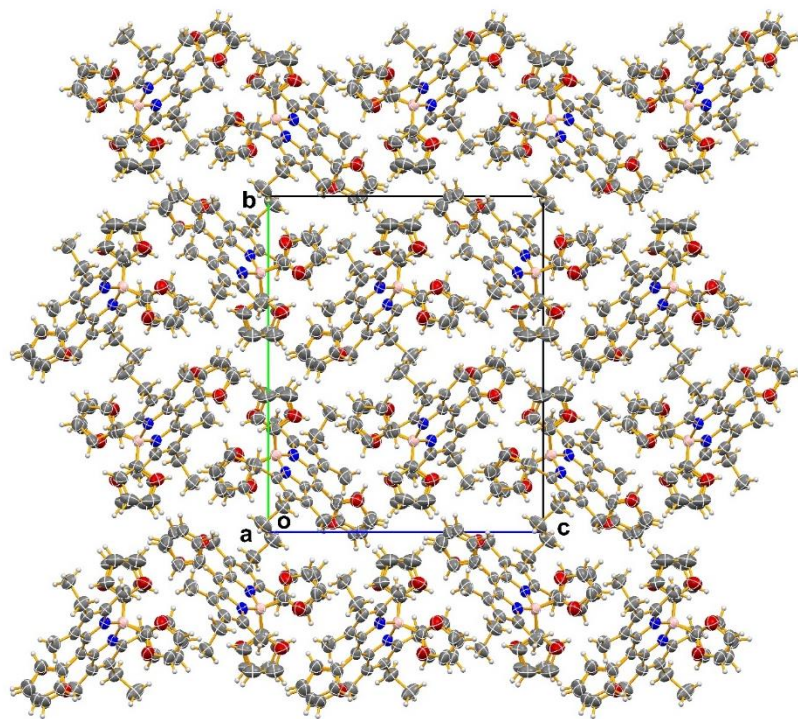


Figure 125. Packing diagram for compound **c7** viewed down the X-axis. The disorder has not been removed.

Appendix D. Chapter 4 Supporting Information

D.1. Experimental Procedures

D.1.1. General Remarks

Reagents were commercially available and used without further purification unless otherwise discussed. Anhydrous solvents were purchased, and used without further drying. The following compounds were synthesised according to literature procedures: tellurophene,⁷⁵ 4-(3-azidopropyl)-3,5-dimethyl-1H-pyrrole-2-carboxaldehyde,²²¹ 2,4-dimethyl-3-ethylpyrrole,²⁶¹ **d2**,¹⁷¹ **d3a**,¹⁸¹ **d3b**,²⁶² **d3c**,²⁶³ **d3e**,²⁶⁴ **d3g**,²⁴ **d3h**,²⁵⁶ **d3j**,¹⁸¹ **d3k**,²⁶⁵ **d3m**,²⁶⁶ **d3n**,²⁶⁷ and **d3o**.²⁶⁸ Manipulations requiring inert atmospheres were conducted under nitrogen and using Schlenk line procedures. Nuclear magnetic resonance (NMR) spectra were recorded using 500 MHz and 300 MHz spectrometers. ¹H chemical shifts are reported in ppm relative to tetramethylsilane using the solvent residual as an internal standard ($\delta = 7.26$ for chloroform, 5.32 for dichloromethane).²⁴² ¹³C chemical shifts are proton decoupled and reported in ppm relative to tetramethylsilane, referenced to the resonances of CDCl₃ ($\delta = 77.20$ ppm) or CD₂Cl₂ ($\delta = 53.84$ ppm).¹ Trace impurities and residual solvent peaks were determined using published tables.²⁴² Coupling constants are reported in hertz (Hz) and spin multiplicities are reported using the following symbols: s (singlet), bs (broad singlet), d (doublet), dd (doublet of doublets), t (triplet), q (quartet), m (multiplet), p (pentet), sept (septet) and app (apparent). ¹¹B chemical shifts are reported in ppm, externally referenced to boron trifluoride diethyl etherate ($\delta = 0.00$). ¹⁹F Chemical

shifts are reported in ppm, externally referenced to CFCl_3 ($\delta = 0.00$). Thin layer chromatography was performed using commercially prepared silica gel plates and visualised using long- or short-wave UV lamps. Column chromatography was performed using 230-400 mesh silica. The relative proportions of solvents mentioned in reference to TLC and column chromatography procedures correspond to volume-to-volume ratios. Mass spectral data were acquired using a QTOF mass spectrometer operating in positive electrospray ionisation mode.

Absorption and fluorescence spectra were recorded using a quartz cuvette. Using a modified version of a literature procedure,²⁴⁷ photophysical properties of all compounds were determined in dichloromethane solution at room temperature. Molar absorptivity values were recorded at the peak maximum in dichloromethane for all cases. Fluorescence spectra were determined by exciting at 490 nm in all cases. Fluorescence quantum yield (Φ_f) was determined according to the equation: $\Phi_{\text{unk}} = (\Phi_{\text{std}})(n/n_{\text{std}})^2(I_{\text{unk}}/I_{\text{std}})(A_{\text{std}}/A_{\text{unk}})$,²⁴⁸ where Φ is the quantum yield, I is the area under the peaks in the fluorescence spectra, A is the absorbance at the excitation wavelength, and n is the refractive index (dichloromethane = 1.425,²⁶⁹ ethanol = 1.357).²⁷⁰ Rhodamine B ($\Phi_f = 0.70$ in ethanol)¹⁵⁸ was chosen as the standard. Quantum yield measurements were determined in dilute solutions ($\lambda_{\text{abs}}^{\text{max}} \leq 0.1$) to avoid inner filter effects and are the composites of ten scans in all cases.

The absorbance spectra used for determining singlet oxygen quantum yield (Φ_{Δ}) and photostability were obtained using a Shimadzu UV-1800 UV Spectrophotometer, with a

1.0 cm path length, and an 800 μL quartz cuvette from Starna Scientific Ltd. For both experiments, measurements were conducted in MeOH containing 1% DMSO and the absorbances of compounds **d4a-d4f** were matched within 10% of 0.09 AU at 530 nm, while compounds **d4g-d4i** were matched within 10% of 0.09 AU at 490 nm. Two LEDs, a 490nm (M490L4) and a 530 nm (M530L3), were used for irradiation and were purchased from Thorlabs. The power of each LED was determined to be 17 mW/cm² and 2.15 mW/cm² for the 490 nm LED and 530 nm LED respectively by using a Newport Optical Power Meter Model 1916-R at a 1 cm distance from the LED. 1,3-Diphenylisobenzofuran (DPBF) was chosen as the ¹O₂ sensor and 110 μM was spiked into the samples and Eosin Y (EY, $\Phi_{\Delta} = 0.42$)¹⁸⁵ was chosen as the standard. Irradiation times varied depending on the compounds to generate a linear correlation between the degradation of DPBF and irradiation. The calculated Φ_{Δ} were obtained using the following equation:²⁵⁵

$$\Phi_{\Delta\text{unk}} = \Phi_{\Delta\text{std}} \left(\frac{1 - 10^{-A_{\text{std}}}}{1 - 10^{-A_{\text{unk}}}} \right) \left(\frac{m_{\text{unk}}}{m_{\text{std}}} \right)$$

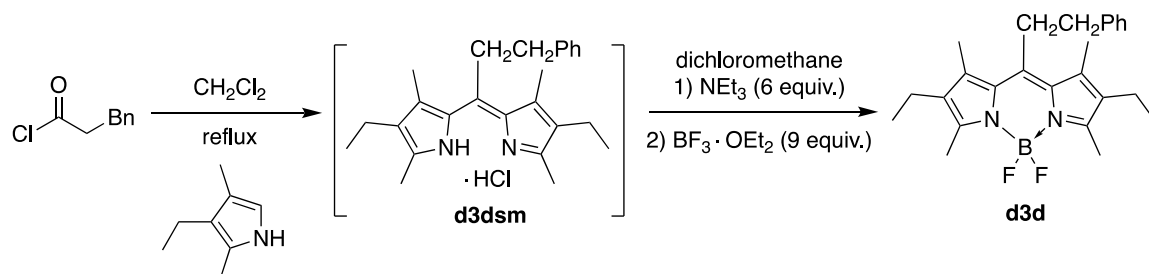
Where: unk = unknown, std = standard, A = absorbance, m = slope of DPBF degradation

The equation does not consider differences in refractive indexes or irradiation powers as the experiments were all conducted in the same composition of solutions with the same LED. Finally, the photostabilities of the compounds were measured by monitoring the $\lambda_{\text{abs}}^{\text{max}}$ over the irradiation period. All measurements were conducted in triplicate.

HeLa cells were used for fluorescent imaging and cell viability assays. HeLa cells were maintained in a 75 cm² culture flask (Nunc™ 75 cm² Nunclon™ Delta Surface) at 37 °C and 5% CO₂ atmosphere in a Thermo Scientific Forma Steri-Cycle CO₂ Incubator. The cells were grown in Dulbecco's Modified Eagle Medium (DMEM) with sodium pyruvate, 4.5 g/L glucose and L-glutamine (Winsent Inc.) supplemented with 10% fetal bovine serum and 1% antibiotics/antimycotics (complete growth medium). Unless otherwise stated, all incubations were conducted in the incubator using DMEM. The 525 nm lamp, Philips LED 90 W equivalent PAR38 Green Lamp (Model #473736) was used, and the power was determined to be 15.60 mW/cm² using the Newport Optical Power Meter Model 1916-R at a 1 cm distance.

D.2. Procedures

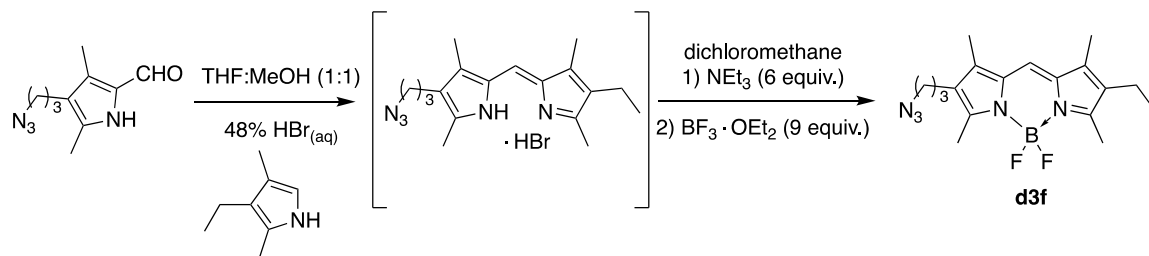
D.2.1. Synthesis of d3d



Following a literature procedure for a similar substrate,²⁶³ the requisite HCl dipyrin salt **d3dsm** was synthesised by first dissolving 2,4-dimethyl-3-ethylpyrrole²⁶¹ (1.00 g, 8.12 mmol) in dry dichloromethane (8 mL) in a two-necked round-bottom flask equipped with a water condenser and a septum under a nitrogen atmosphere. 3-Phenylpropionyl chloride (1.81 mL, 12.2 mmol) was then added and the resulting mixture was heated at reflux temperature for one hour. The reaction mixture was then allowed to cool before dilution with water (30 mL), and the organic fraction was separated and then dried over sodium sulfate and concentrated under reduced pressure. The resulting solid hydrochloride dipyrin salt was then triturated with ether and then used without further purification. Next, the dipyrin salt **d3dsm** was dissolved in dichloromethane (30 mL). Following a literature procedure,²⁴⁴ triethylamine (3.4 mL, 24.4 mmol) was then added to the reaction mixture, *via* syringe, followed by boron trifluoride diethyl etherate (4.5 mL, 36.5 mmol). After stirring the reaction mixture for 1.5 h, second aliquots of triethylamine (3.4 mL, 24.4 mmol) and trifluoride diethyl etherate (4.5 mL, 36.5 mmol) were added, followed by stirring for a further 1.5 h. The crude reaction mixture was filtered through a silica gel plug, eluting with dichloromethane, and the resulting solution was evaporated under reduced pressure. The

residue was taken up in ether (50 mL) and washed with 1 M HCl (5× 50 mL), and then 6 M HCl (1× 50 mL). The organic layer was dried over sodium sulfate and concentrated under reduced pressure. The resulting crude solid was purified *via* column chromatography over silica with dry loading and then eluting with 0 ⇒ 5% ethyl acetate in hexanes to afford the desired compound as a dark red crystalline material (0.24 g, 15% yield). ¹H NMR (400 MHz, CDCl₃) δ 7.27-7.39 (m, 5H), 3.30-3.41 (m, 2H), 2.91-3.01 (m, 2H), 2.52 (s, 6H), 2.38-2.46 (m, 10H), 1.06 (t, *J* = 7.6 Hz, 6H). ¹¹B NMR (128 MHz, CDCl₃) δ 0.66 (t, *J* = 31 Hz); ¹⁹F NMR (377 MHz, CDCl₃) δ -146.2-(-145.7) (m); ¹³C{¹H} NMR (101 MHz, CDCl₃) δ 152.6, 143.6, 140.5, 135.8, 132.9, 131.1, 128.9, 128.0, 126.7, 37.4, 29.6, 17.3, 15.0, 13.8, 12.6; HRMS-ESI⁺ *m/z* [*M*⁺ + Na] calc. for C₂₅H₃₁BF₂N₂Na = 431.2441, found 431.2459.

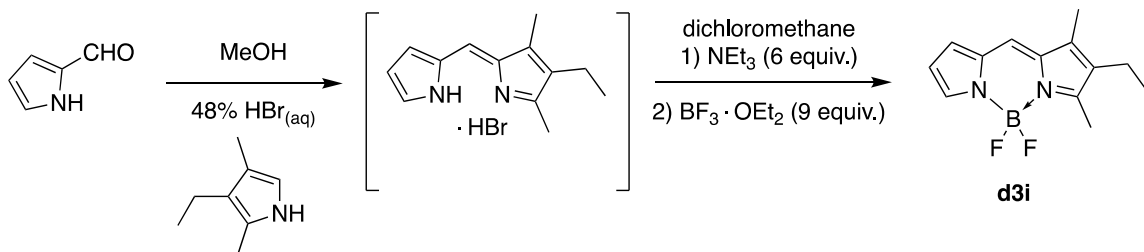
D.2.2. Synthesis of d3f



4-(3-Azidopropyl)-3,5-dimethyl-1H-pyrrole-2-carboxaldehyde²²¹ (800 mg, 3.88 mmol) and 2,4-dimethyl-3-ethylpyrrole²⁶¹ (478 mg, 3.88 mmol) were dissolved in tetrahydrofuran (5 mL) and methanol (5 mL). The resulting solution was stirred for 10 minutes. Aqueous hydrobromic acid (48%, 0.68 mL, 7.77 mmol) was added and the reaction mixture was stirred for an additional 16 h. After concentration to half volume under reduced pressure, the mixture was diluted with a diethyl ether:hexanes (1:1, 10 mL) solution. The resulting

orange precipitate was isolated *via* filtration and then washed with diethyl ether:hexanes (1:1, 10 mL). The hydrogen bromide dipyrin salt was allowed to dry in air and then used without further purification. Next, the dipyrin salt (1.08 g, 2.75 mmol) was dissolved in dichloromethane (30 mL). Following a literature procedure,²⁴⁴ triethylamine (2.3 mL, 16.5 mmol) was then added to the reaction mixture, *via* syringe, followed by boron trifluoride diethyl etherate (3.0 mL, 24.8 mmol). After stirring for 1.5 h, second aliquots of triethylamine (2.3 mL, 16.5 mmol) and boron trifluoride diethyl etherate (3.0 mL, 24.8 mmol) were added, followed by stirring for a further 1.5 h. The crude reaction mixture was filtered through a silica gel plug, eluting with dichloromethane, and the resulting solution was evaporated under reduced pressure. The residue was taken up in ether (50 mL) and washed with 1 M HCl (5× 50 mL), and then 6 M HCl (1× 50 mL). The organic layer was dried over sodium sulfate and concentrated under reduced pressure. The resulting crude solid was purified *via* column chromatography over silica, loading as a solution and then eluting with 0 ⇒ 70% dichloromethane in hexanes to afford the desired compound as a dark purple crystalline material (0.80 g, 58% yield). ¹H NMR (500 MHz, CDCl₃) δ 6.96 (s, 1H), 3.29 (t, *J* = 6.6 Hz, 2H), 2.43-2.54 (m, 8H), 2.39 (q, *J* = 7.6 Hz, 2H), 2.14-2.20 (m, 6H), 1.73 (p, *J* = 6.6 Hz, 2H), 1.07 (t, *J* = 7.6 Hz, 3H); ¹¹B NMR (160 MHz, CDCl₃) δ 0.88 (t, *J* = 32 Hz); ¹⁹F NMR (471 MHz, CDCl₃) δ -146.3 (q, *J* = 32 Hz); ¹³C {1H} NMR (126 MHz, CDCl₃) δ 156.1, 154.0, 137.4, 137.0, 133.0, 132.3, 128.1, 118.9, 50.8, 29.2, 21.2, 17.4, 14.6, 12.8, 12.7, 9.7, 9.5 (one signal missing); HRMS-ESI⁺ *m/z* [M⁺ + Na] calc. for C₁₈H₂₄BF₂N₅Na = 382.1985, found 382.1987.

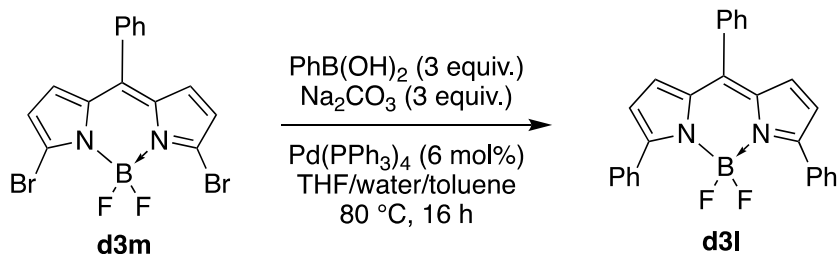
D.2.3. Synthesis of **d3i**



The title compound **d3i** was synthesised by first condensing formyl pyrrole (0.77 g, 8.10 mmol) and 2,4-dimethyl-3-ethylpyrrole²⁶¹ (1.00 g, 8.10 mmol) were dissolved in (20 mL), the resulting solution was stirred for 10 minutes. Concentrated aqueous hydrobromic acid (2 mL, excess) was added and reaction mixture was stirred for an additional 2 h. The stirring was stopped and the reaction mixture was left to crystallise overnight. The resulting orange precipitate was isolated *via* filtration and was washed with methanol (4 mL) and then diethyl ether (20 mL). The hydrogen bromide dipyrryn salt was allowed to dry in air and then used without further purification. Next, the dipyrryn salt (1.46 g, 5.19 mmol) was dissolved in dichloromethane (30 mL). Following a literature procedure,²⁴⁴ triethylamine (4.3 mL, 31.1 mmol) was then added to the reaction mixture, *via* syringe, followed by boron trifluoride diethyl etherate (5.8 mL, 46.7 mmol). After stirring the reaction mixture for 1.5 h, second aliquots of triethylamine (4.3 mL, 31.1 mmol) and boron trifluoride diethyl etherate (5.8 mL, 46.7 mmol) were added, followed by stirring for a further 1.5 h. The crude reaction mixture was filtered through a silica gel plug, eluting with dichloromethane, and the resulting solution was evaporated under reduced pressure. The residue was taken up in ether (50 mL) and washed with 1 M HCl (5 × 50 mL), and 6 M HCl (1 × 50 mL). The organic layer was dried over sodium sulfate and concentrated under

reduced pressure to afford the desired compound as a dark purple crystalline material (0.87 g, 43% yield). ^1H NMR (500 MHz, CDCl_3) δ 7.58 (s, 1H), 7.12 (s, 1H), 6.86 (s, 1H), 6.39 (s, 1H), 2.57 (s, 3H), 2.41 (q, $J = 7.7$ Hz, 2H), 2.19 (s, 3H), 1.08 (t, $J = 7.7$ Hz, 3H). This data is in accordance with reported data.²⁷¹

D.2.4. Synthesis of d3l



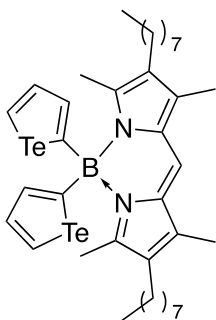
The title compound was synthesised by first dissolving **d3m**²⁶⁶ (700 mg, 1.64 mmol) in tetrahydrofuran/water/toluene (1:1:1, 50 mL) in a two-necked round-bottomed flask equipped with a water condenser and a stopper. Then, phenylboronic acid (600 mg, 5.01 mmol), sodium carbonate (531 mg, 5.01 mmol) and tetrakis(triphenylphosphine)palladium(0) (113 mg, 0.098 mmol) were added as solids. The reaction mixture was heated to 80 °C for 16 hours. The completion of the reaction was confirmed by analysis using TLC. The resulting mixture was allowed to cool before being extracted with dichloromethane (2× 75 mL). The combined organic fractions were then washed with brine (150 mL) and then dried over sodium sulfate. After concentrating under reduced pressure, the resulting crude solid was purified *via* column chromatography over silica with dry loading and then eluting with 0 \Rightarrow 30% dichloromethane in hexanes to afford the desired compound as an orange solid (0.38 g, 55% yield). ^1H NMR (500 MHz,

CDCl₃) δ 7.85-7.90 (m, 4H), 7.51-7.63 (m, 5H), 7.38-7.46 (m, 6H), 6.90 (d, $J = 4.4$ Hz, 2H), 6.63 (d, $J = 4.4$ Hz, 2H). This data is in accordance with reported data.²⁷²

D.2.5. General procedure for the synthesis of [Te]-BODIPYs (GP)

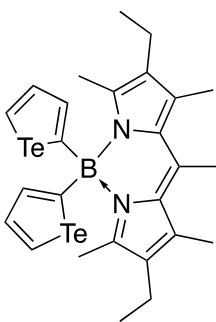
Inside a nitrogen-filled glovebox, a solution of tellurophene⁷⁵ (2.2 equiv.) and dry tetrahydrofuran (2 mL) was stirred in a 15 mL vial at room temperature until complete dissolution was achieved (5 min). *n*-Butyllithium (2.0 M in hexanes, 2.4 equiv.) was added dropwise *via* syringe. The vial was then capped and the reaction mixture was stirred for 5 min. In a separate 15 mL vial the corresponding BODIPY (1 equiv.) was stirred in dry tetrahydrofuran (2 mL) until complete dissolution was achieved (5 min). The cap on the reaction vial was removed and the BODIPY solution was then added dropwise *via* syringe to the solution containing the lithiated heterocycle. The capped reaction mixture was stirred for 1 h, and was then removed from the glovebox. The crude reaction mixture dissolved in dichloromethane (20 mL), and the resulting solution was washed with saturated ammonium chloride (1 \times 20 mL), water (1 \times 20 mL) and brine (1 \times 20 mL). The organic layer was dried over sodium sulfate and concentrated under reduced pressure. The resulting crude solid was purified *via* column chromatography over silica with wet-loading and then elution with a gradient solution of dichloromethane/hexanes, ethyl acetate/hexanes or dichloromethane/ethyl acetate. The fractions containing the desired compounds were concentrated under reduced pressure to afford the desired [Te]-BODIPYs.

D.2.6. Synthesis of d4a



Following **GP**, a solution of tellurophene (84 mg, 0.47 mmol) in tetrahydrofuran was lithiated using *n*-butyllithium (0.51 mmol) and then added to a solution of **d3a**¹⁸¹ (100 mg, 0.21 mmol) in tetrahydrofuran. After workup and column chromatography (0 \Rightarrow 15% dichloromethane/hexanes), the desired product was afforded as a scarlet red solid (45 mg, 27% yield). ¹H NMR (500 MHz, CDCl₃) δ 8.92 (dd, J = 6.5, 0.5 Hz, 2H), 8.08 (dd, J = 3.5, 0.5 Hz, 2H), 7.81 (dd, J = 6.5, 3.5 Hz, 2H), 7.10 (s, 1H), 2.28 (t, J = 7.6, 4H), 2.21 (s, 6H), 2.10 (s, 6H), 1.15-1.31 (m, 24H), 0.87 (t, J = 6.9, 6H); ¹¹B NMR (160 MHz, CDCl₃) δ 0.53 (bs); ¹³C {¹H} NMR (126 MHz, CDCl₃) δ 155.1, 140.2, 139.2, 134.9, 131.3, 131.0, 125.6, 118.9, 32.0, 30.3, 29.6, 29.5, 29.4, 24.4, 22.8, 15.1, 14.2, 9.7 (one signal missing); HRMS-ESI⁺ m/z [M^+ + Na] calc. for C₃₇H₅₃BN₂¹³⁰Te₂Na = 819.2318, found 819.2335; $\lambda_{\text{abs}}^{\text{max}}$ = 528 nm (498 nm shoulder); ϵ = 70000; $\lambda_{\text{em}}^{\text{max}}$ = 559 nm; Φ_f = 0.02; Stokes shift = 31 nm; Φ_{Δ} = 0.48 \pm 0.05.

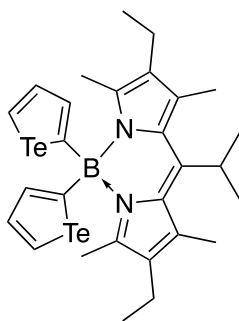
D.2.7. Synthesis of d4b



Following **GP**, a solution of tellurophene (124 mg, 0.69 mmol) in tetrahydrofuran was lithiated using *n*-butyllithium (0.75 mmol) and then added to a solution of **d3b**²⁶² (100 mg, 0.31 mmol) in tetrahydrofuran. After workup and column chromatography (0 \Rightarrow 30% dichloromethane/hexanes), the desired product was afforded as a scarlet red solid (98 mg, 49% yield). ¹H NMR (500 MHz, CDCl₃) δ 8.90 (dd, J = 6.6, 0.9 Hz, 2H), 8.08 (dd, J = 3.8, 0.9 Hz, 2H), 7.80 (dd, J = 6.6, 3.8 Hz, 2H), 2.70 (s, 3H), 2.39

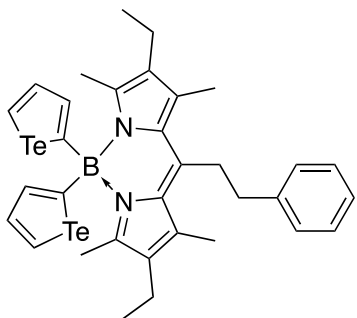
(s, 6H), 2.31 (q, $J = 7.5$ Hz, 4H), 2.10 (s, 6H), 0.96 (t, $J = 7.5$ Hz, 6H); ^{11}B NMR (160 MHz, CDCl_3) δ -0.10 (bs); ^{13}C {1H} NMR (126 MHz, CDCl_3) δ 152.2, 140.1, 139.6, 139.1, 134.3, 133.3, 131.1, 125.4, 17.9, 17.5, 15.1, 15.0, 14.9 (one signal missing); HRMS-ESI⁺ m/z [$\text{M}^+ + \text{Na}$] calc. for $\text{C}_{26}\text{H}_{31}\text{BN}_2^{130}\text{Te}_2\text{Na} = 665.0597$, found 665.0613; $\lambda_{\text{abs}}^{\text{max}} = 518$ nm (488 nm shoulder); $\epsilon = 75600$; $\lambda_{\text{em}}^{\text{max}} = 554$ nm; $\Phi_{\text{f}} = 0.03$; Stokes shift = 36 nm; $\Phi_{\Delta} = 0.54 \pm 0.03$.

D.2.8. Synthesis of d4c



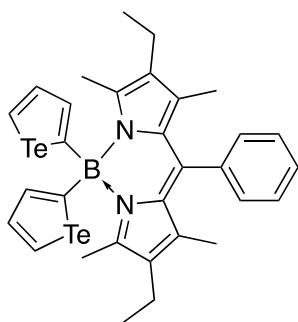
Following **GP**, a solution of tellurophene (81 mg, 0.45 mmol) in tetrahydrofuran was lithiated using *n*-butyllithium (0.49 mmol) and then added to a solution of **d3c**²⁶³ (71 mg, 0.20 mmol) in tetrahydrofuran. After workup and column chromatography (0 \Rightarrow 30% dichloromethane/hexanes), the desired product was afforded as a scarlet red solid (42 mg, 27% yield). ^1H NMR (500 MHz, CDCl_3) δ 8.90 (dd, $J = 6.6, 0.8$ Hz, 2H), 8.15 (dd, $J = 3.8, 0.8$ Hz, 2H), 7.80 (dd, $J = 6.6, 3.8$ Hz, 2H), 4.04 (sept, $J = 7.5$ Hz, 1H), 2.44 (s, 6H), 2.31 (q, $J = 7.6$ Hz, 4H), 2.08 (s, 6H), 1.58 (d, $J = 7.5$ Hz, 6H), 0.96 (t, $J = 7.6$ Hz, 6H); ^{11}B NMR (160 MHz, CDCl_3) δ -0.56 (bs); ^{13}C {1H} NMR (126 MHz, CDCl_3) δ 152.6, 151.8, 140.3, 140.0, 139.1, 134.2, 133.1, 131.4, 125.2, 28.2, 22.1, 17.8, 15.4, 15.3, 14.7; HRMS-ESI⁺ m/z [$\text{M}^+ + \text{H}$] calc. for $\text{C}_{28}\text{H}_{36}\text{BN}_2^{130}\text{Te}_2 = 671.1091$, found 671.1097; $\lambda_{\text{abs}}^{\text{max}} = 530$ nm (496 nm shoulder); $\epsilon = 56000$, trace emission; $\Phi_{\Delta} = 0.17 \pm 0.01$.

D.2.9. Synthesis of d4d



Following **GP**, a solution of tellurophene (97 mg, 0.54 mmol) in tetrahydrofuran was lithiated using *n*-butyllithium (0.59 mmol) and then added to a solution of **d3d** (100 mg, 0.24 mmol) in tetrahydrofuran. After workup and column chromatography (0 \Rightarrow 30% dichloromethane/hexanes), the desired product was afforded as a scarlet red solid (62 mg, 34% yield). ^1H NMR (500 MHz, CDCl_3) δ 8.93 (bs, 2H), 8.21 (app d, 2H), 7.84 (bs, 2H), 7.31-7.41 (m, 4H), 7.26-7.31 (m, 1H), 3.47-3.57 (m, 2H), 3.01-3.12 (m, 2H), 2.48 (s, 6H), 2.34 (q, $J = 7.7$ Hz, 4H), 2.14 (s, 6H), 0.98 (t, $J = 7.7$ Hz, 6H); ^{11}B NMR (160 MHz, CDCl_3) δ -0.13 (bs); $^{13}\text{C}\{^1\text{H}\}$ NMR (126 MHz, CDCl_3) δ 152.9, 143.5, 140.8, 139.3, 139.0, 133.8, 133.5, 130.0, 128.8, 128.2, 126.6, 125.6, 125.1, 37.9, 29.7, 17.5, 15.1, 15.0, 14.3; HRMS-ESI $^+$ m/z [$\text{M}^+ + \text{H}$] calc. for $\text{C}_{33}\text{H}_{38}\text{BN}_2^{130}\text{Te}_2 = 733.1247$, found 733.1259; $\lambda_{\text{abs}}^{\text{max}} = 522$ nm (498 nm shoulder); $\epsilon = 75900$; $\lambda_{\text{em}}^{\text{max}} = 546$ nm; $\Phi_{\text{f}} = 0.03$; Stokes shift = 24 nm; $\Phi_{\Delta} = 0.85 \pm 0.11$.

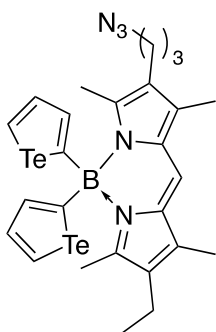
D.2.10. Synthesis of d4e



Following **GP**, a solution of tellurophene (104 mg, 0.58 mmol) in tetrahydrofuran was lithiated using *n*-butyllithium (0.63 mmol) and then added to a solution of **d3e**²⁶⁴ (100 mg, 0.26 mmol) in tetrahydrofuran. After workup and column chromatography (0 \Rightarrow 30% dichloromethane/ethyl acetate), the desired product was afforded as a scarlet red solid (42 mg, 23% yield). ^1H NMR (500 MHz, CDCl_3) δ 8.95 (dd, $J = 6.6, 0.8$ Hz, 2H), 8.24 (dd, $J = 3.7, 0.8$ Hz, 2H), 7.85 (dd, $J = 6.6,$

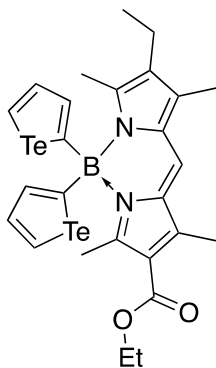
3.7 Hz, 2H), 7.45-7.54 (m, 3H), 7.36-7.42 (m, 2H), 2.21 (q, $J = 7.4$ Hz, 4H), 2.13 (s, 6H), 1.32 (s, 6H), 0.89 (t, $J = 7.4$ Hz, 6H); ^{11}B NMR (160 MHz, CDCl_3) δ 0.05 (bs); $^{13}\text{C}\{^1\text{H}\}$ NMR (126 MHz, CDCl_3) δ 154.2, 140.2, 139.3, 138.0, 136.9, 136.4, 133.8, 129.8, 129.0, 128.9, 128.7, 126.4, 125.5, 17.5, 15.1, 14.9, 12.1; HRMS-ESI $^+$ m/z [$\text{M}^+ + \text{H}$] calc. for $\text{C}_{31}\text{H}_{34}\text{BN}_2^{130}\text{Te}_2 = 705.0934$, found 705.0950; $\lambda_{\text{abs}}^{\text{max}} = 524$ nm (492 nm shoulder); $\epsilon = 50100$; $\lambda_{\text{em}}^{\text{max}} = 541$ nm; $\Phi_{\text{f}} = 0.005$; Stokes shift = 17 nm; $\Phi_{\Delta} = 0.82 \pm 0.09$.

D.2.11. Synthesis of **d4f**



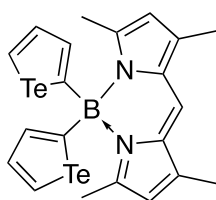
Following **GP**, a solution of tellurophene (110 mg, 0.61 mmol) in tetrahydrofuran was lithiated using *n*-butyllithium (0.69 mmol) and then added to a solution of **d3f** (100 mg, 0.28 mmol) in tetrahydrofuran. After workup and column chromatography (0 \Rightarrow 45% dichloromethane/hexanes), the desired product was afforded as a scarlet red solid (86 mg, 45% yield). ^1H NMR (400 MHz, CDCl_3) δ 8.92 (d, $J = 6.6$ Hz, 2H), 8.11 (d, $J = 3.7$ Hz, 2H), 7.82 (dd, $J = 6.6, 3.7$ Hz, 2H), 7.12 (s, 1H), 3.24 (t, $J = 6.7$ Hz, 2H), 2.40 (t, $J = 7.5$ Hz, 2H), 2.31 (q, $J = 7.5$ Hz, 2H), 2.18-2.26 (m, 6H), 2.05-2.17 (m, 6H), 1.66 (dt, $J = 7.5, 6.7$ Hz, 2H), 0.98 (t, $J = 7.5$ Hz, 3H); ^{11}B NMR (160 MHz, CDCl_3) δ 0.79 (bs); $^{13}\text{C}\{^1\text{H}\}$ NMR (126 MHz, CDCl_3) δ 156.2, 154.1, 140.4, 139.3, 135.3, 134.9, 134.0, 133.0, 131.7, 131.0, 128.6, 125.8, 119.2, 50.8, 29.3, 21.3, 17.7, 15.0, 14.9, 14.8, 9.8, 9.6; HRMS-ESI $^+$ m/z [$\text{M}^+ + \text{Na}$] calc. for $\text{C}_{26}\text{H}_{30}\text{BN}_5^{130}\text{Te}_2\text{Na} = 706.0611$, found 706.0640; $\lambda_{\text{abs}}^{\text{max}} = 526$ nm (496 nm shoulder); $\epsilon = 60200$; $\lambda_{\text{em}}^{\text{max}} = 543$ nm; $\Phi_{\text{f}} = 0.01$; Stokes shift = 17 nm; $\Phi_{\Delta} = 0.45 \pm 0.02$.

D.2.12. Synthesis of d4g



Following **GP**, a solution of tellurophene (170 mg, 0.95 mmol) in tetrahydrofuran was lithiated using *n*-butyllithium (1.03 mmol) and then added to a solution of **d3g**²⁴ (150 mg, 0.43 mmol) in tetrahydrofuran. After workup and column chromatography (0 \Rightarrow 75% dichloromethane/hexanes), the desired product was afforded as a scarlet red solid (54 mg, 19% yield). ¹H NMR (500 MHz, CDCl₃) δ 8.94 (dd, *J* = 6.6, 0.9 Hz, 2H), 8.13 (dd, *J* = 3.8, 0.9 Hz, 2H), 7.82 (dd, *J* = 6.6, 3.8 Hz, 2H), 7.30 (s, 1H), 4.23 (q, *J* = 7.2 Hz, 2H), 2.52 (s, 3H), 2.44 (s, 3H), 2.32 (q, *J* = 7.6 Hz, 2H), 2.26 (s, 3H), 2.17 (s, 3H), 1.31 (t, *J* = 7.2 Hz, 3H), 0.99 (t, *J* = 7.6 Hz, 3H); ¹¹B NMR (160 MHz, CDCl₃) δ 0.97 (bs); ¹³C {¹H} NMR (126 MHz, CDCl₃) δ 165.2, 161.5, 156.5, 140.6, 139.3, 137.8, 135.4, 133.9, 129.6, 126.2, 120.5, 119.0, 59.8, 17.6, 16.9, 15.4, 14.5, 14.4, 12.0, 9.6 (two signals missing); HRMS-ESI⁺ *m/z* [*M*⁺ + Na] calc. for C₂₆H₂₉BN₂O₂¹³⁰Te₂Na = 695.0339, found 695.0357; $\lambda_{\text{abs}}^{\text{max}}$ = 508 nm (482 nm shoulder); ϵ = 70600; trace emission; Φ_{Δ} = 0.55 \pm 0.07.

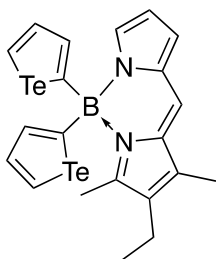
D.2.13. Synthesis of d4h



Following **GP**, a solution of tellurophene (159 mg, 0.89 mmol) in tetrahydrofuran was lithiated using *n*-butyllithium (0.97 mmol) and then added to a solution of **d3h**²⁵⁶ (100 mg, 0.40 mmol) in tetrahydrofuran. After workup and column chromatography (0 \Rightarrow 20% ethyl acetate/hexanes), the desired product was afforded as a scarlet red solid (22 mg, 10% yield). ¹H NMR (500 MHz, CDCl₃) δ 8.93 (d, *J* = 6.5 Hz, 2H), 8.09 (d, *J* = 3.5 Hz, 2H), 7.82 (dd,

$J = 6.5, 3.5$ Hz, 2H), 7.19 (s, 1H), 6.00 (s, 2H), 2.30 (s, 6H), 2.15 (s, 6H); ^{11}B NMR (160 MHz, CDCl_3) δ 0.73 (bs); $^{13}\text{C}\{1\text{H}\}$ NMR (126 MHz, CDCl_3) δ 156.7, 140.3, 139.1, 139.0, 132.1, 125.7, 120.5, 120.1, 17.1, 11.3 (one signal missing); HRMS-ESI⁺ m/z [$\text{M}^+ + \text{Na}$] calc. for $\text{C}_{21}\text{H}_{21}\text{BN}_2^{130}\text{Te}_2\text{Na} = 594.9820$, found 594.9815; $\lambda_{\text{abs}}^{\text{max}} = 506$ nm (480 nm shoulder); $\epsilon = 72000$; $\lambda_{\text{em}}^{\text{max}} = 524$ nm; $\Phi_{\text{f}} = 0.006$; Stokes shift = 18 nm; $\Phi_{\Delta} = 0.57 \pm 0.08$.

D.2.14. Synthesis of d4i



Following **GP**, a solution of tellurophene (159 mg, 0.89 mmol) in tetrahydrofuran was lithiated using *n*-butyllithium (0.97 mmol) and then added to a solution of **d3i** (100 mg, 0.40 mmol) in tetrahydrofuran.

After workup and column chromatography (0 \Rightarrow 20% dichloromethane/hexanes), the desired product was afforded as a scarlet red solid (40 mg, 17% yield). ^1H NMR (500 MHz, CDCl_3) δ 8.92 (dd, $J = 6.5, 1.0$ Hz, 2H), 7.80 (dd, $J = 6.5, 3.8$ Hz, 2H), 7.72 (dd, $J = 3.8, 1.0$ Hz, 2H), 7.33 (bs, 1H), 7.27 (s, 1H), 6.92 (dd, $J = 3.9, 1.2$ Hz, 1H), 6.38 (dd, $J = 3.9, 2.0$ Hz, 1H), 2.41 (q, $J = 7.7$ Hz, 2H), 2.26 (s, 3H), 2.23 (s, 3H), 1.07 (t, $J = 7.7$ Hz, 3H); ^{11}B NMR (160 MHz, CDCl_3) δ 0.82 (bs); $^{13}\text{C}\{1\text{H}\}$ NMR (126 MHz, CDCl_3) δ 161.9, 140.0, 139.9, 139.6, 139.5, 139.0, 135.8, 135.1, 131.4, 126.5, 124.3, 123.9, 115.7, 17.7, 15.8, 14.5, 9.7; HRMS-ESI⁺ m/z [$\text{M}^+ + \text{Na}$] calc. for $\text{C}_{21}\text{H}_{21}\text{BN}_2^{130}\text{Te}_2\text{Na} = 594.9814$, found 594.9816; $\lambda_{\text{abs}}^{\text{max}} = 506$ nm (476 nm shoulder); $\epsilon = 38700$; trace emission; $\Phi_{\Delta} = 0.47 \pm 0.04$.

D.3. Photophysical Spectra

Table 14. Photophysical characteristics of *[Te]*-BODIPYs in CH₂Cl₂ and PBS

	λ_{maxabs} (CH ₂ Cl ₂ , nm)	Φ_f (CH ₂ Cl ₂)	ϵ (CH ₂ Cl ₂ , M ⁻¹ cm ⁻¹)	λ_{max} (PBS, nm)
d2	528	0.01	65700	543
d4a	528	0.02	70000	538
d4b	518	0.03	75600	526
d4c	530	N/A	56000	541
d4d	522	0.03	75900	533
d4e	524	0.005	50100	532
4f	526	0.01	60200	530
d4g	508	N/A	70600	515
d4h	506	0.006	72000	524
d4i	506	N/A	38700	518

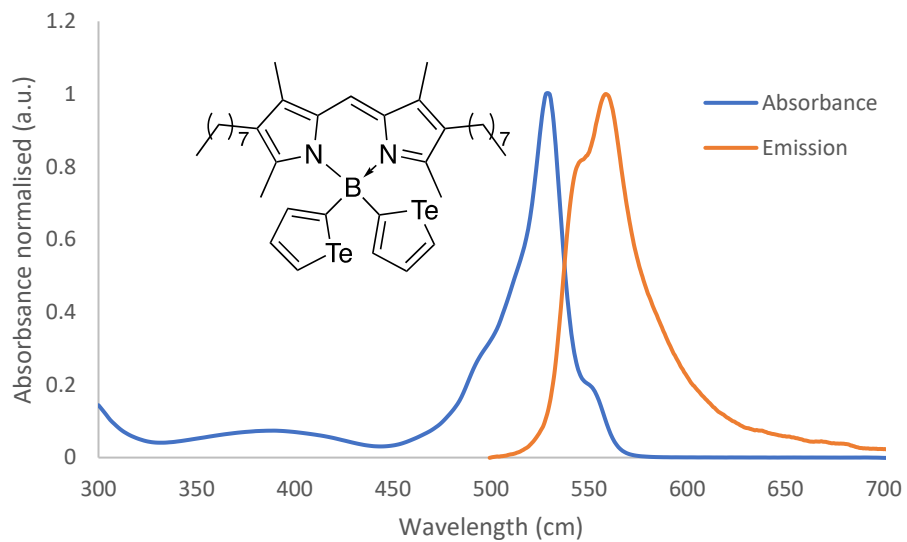


Figure 126. Normalised absorption and emission spectra of compound **d4a** in CH_2Cl_2 .

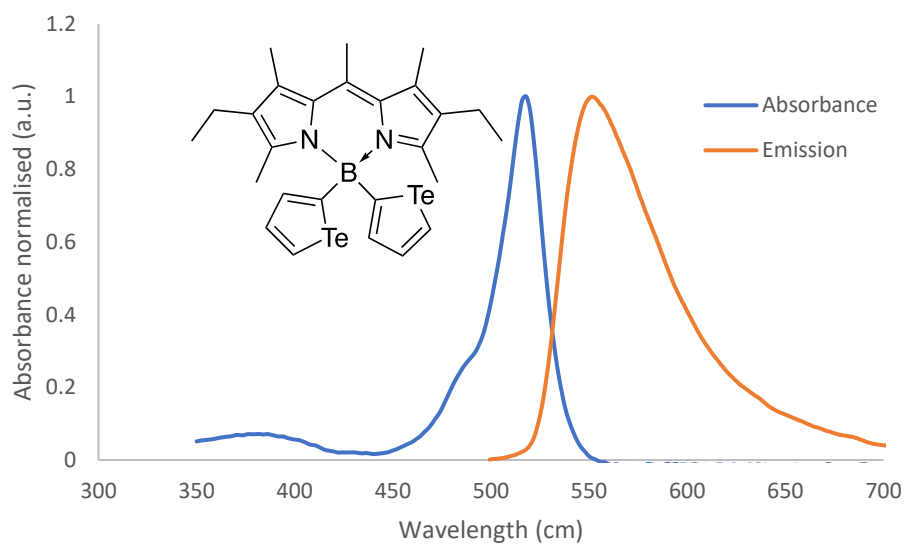


Figure 127. Normalised absorption and emission spectra of compound **d4b** in CH_2Cl_2 .

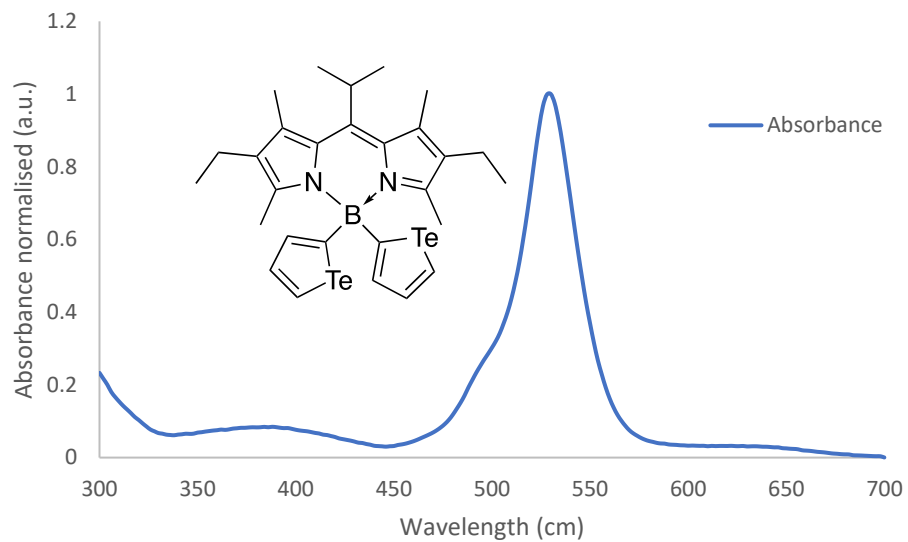


Figure 128. Normalised absorption spectrum of compound **d4c** in CH_2Cl_2 .

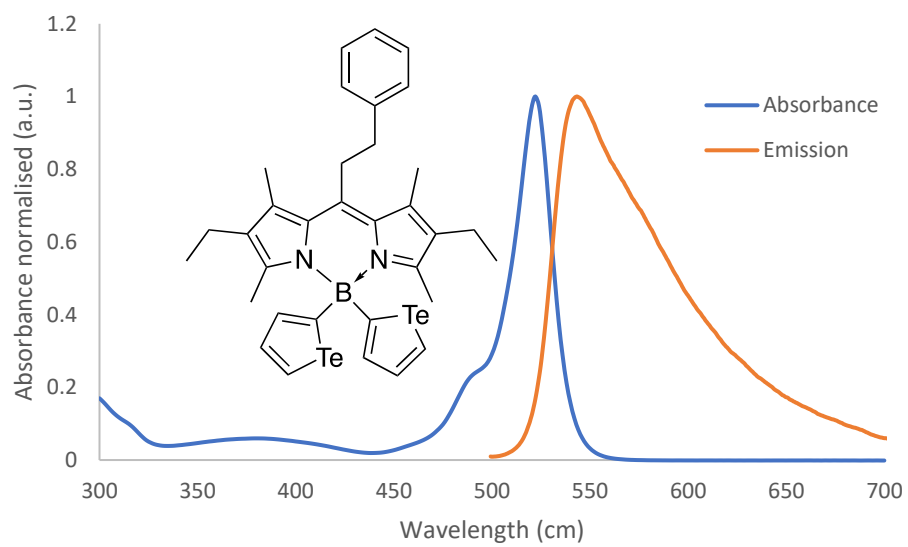


Figure 129. Normalised absorption and emission spectra of compound **d4d** in CH_2Cl_2 .

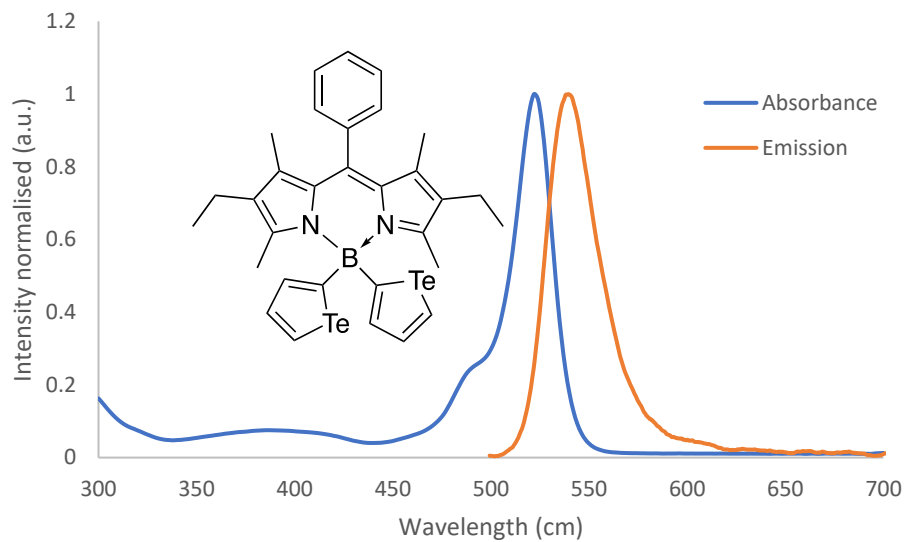


Figure 130. Normalised absorption and emission spectra of compound **d4e** in CH_2Cl_2 .

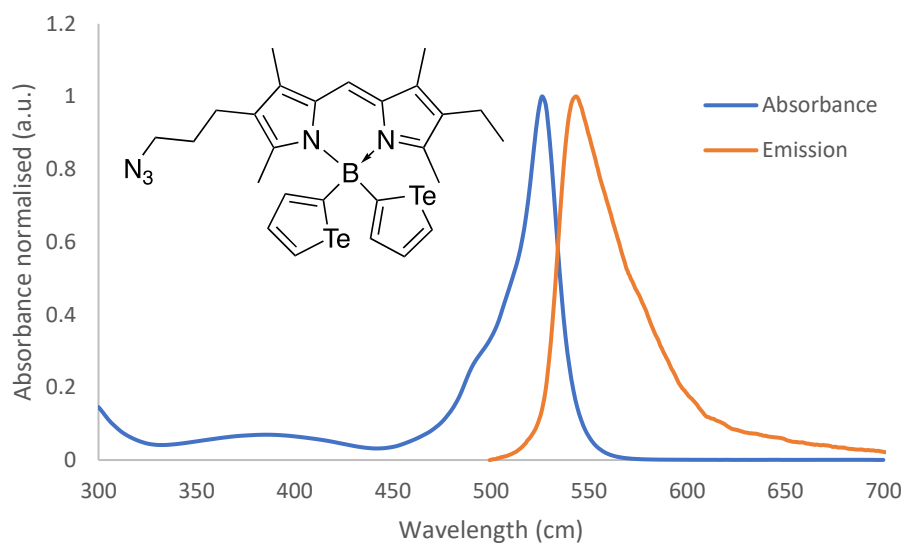


Figure 131. Normalised absorption and emission spectra of compound **d4f** in CH_2Cl_2 .

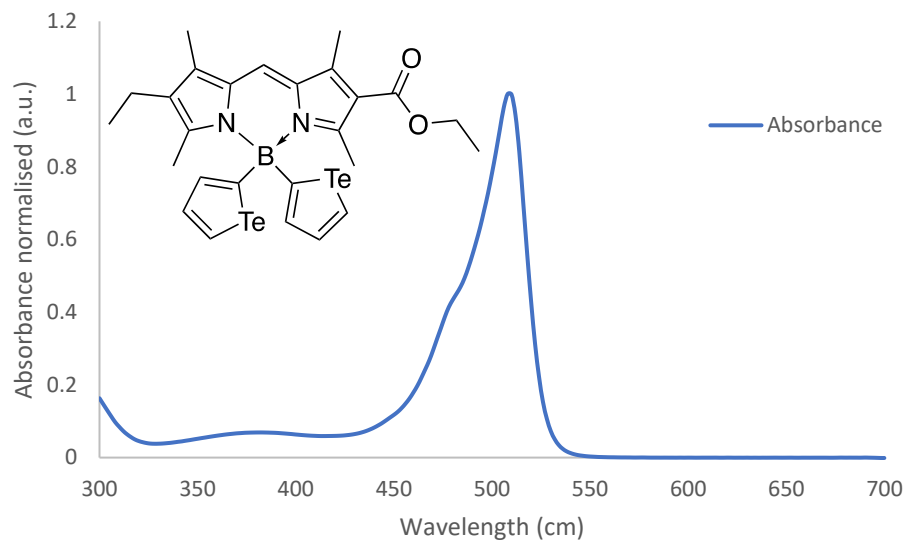


Figure 132. Normalised absorption spectrum of compound **d4g** in CH_2Cl_2 .

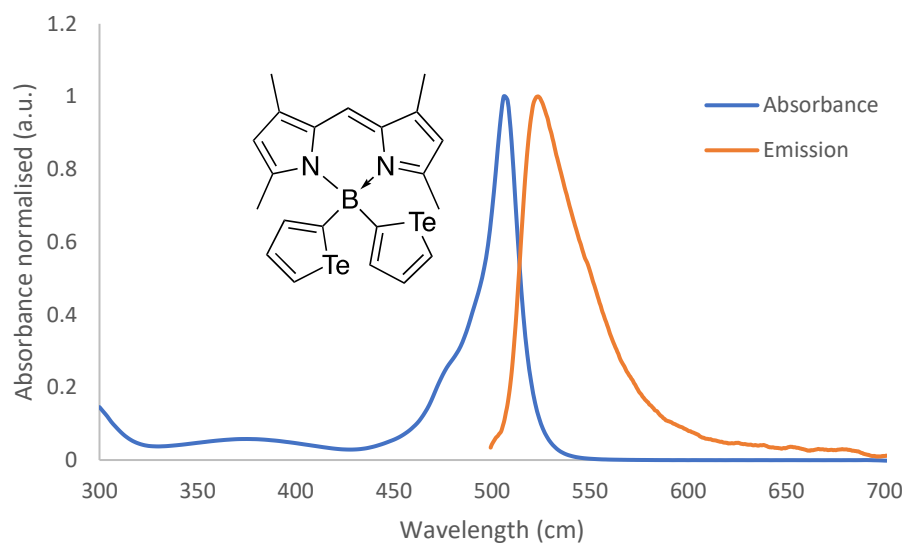


Figure 133. Normalised absorption and emission spectra of compound **d4h** in CH_2Cl_2 .

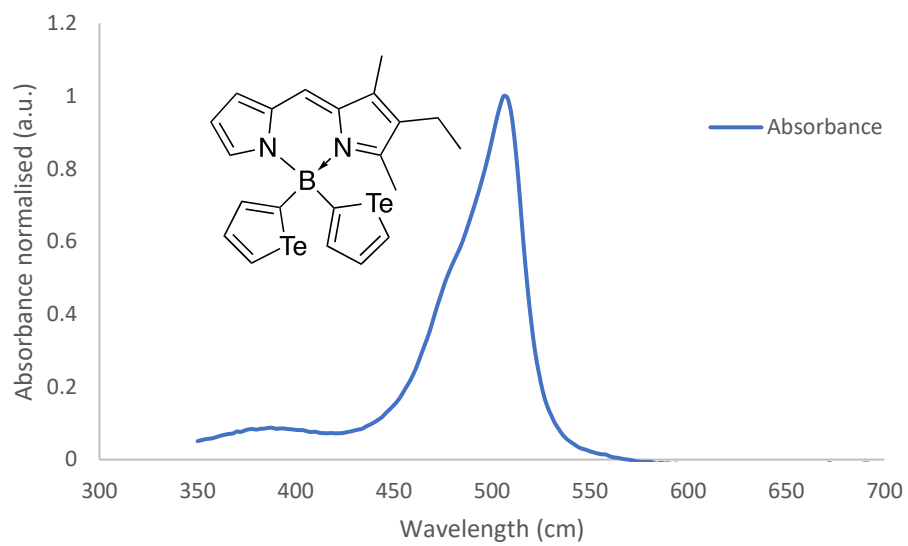


Figure 134. Normalised absorption spectrum of compound **d4i** in CH_2Cl_2 .

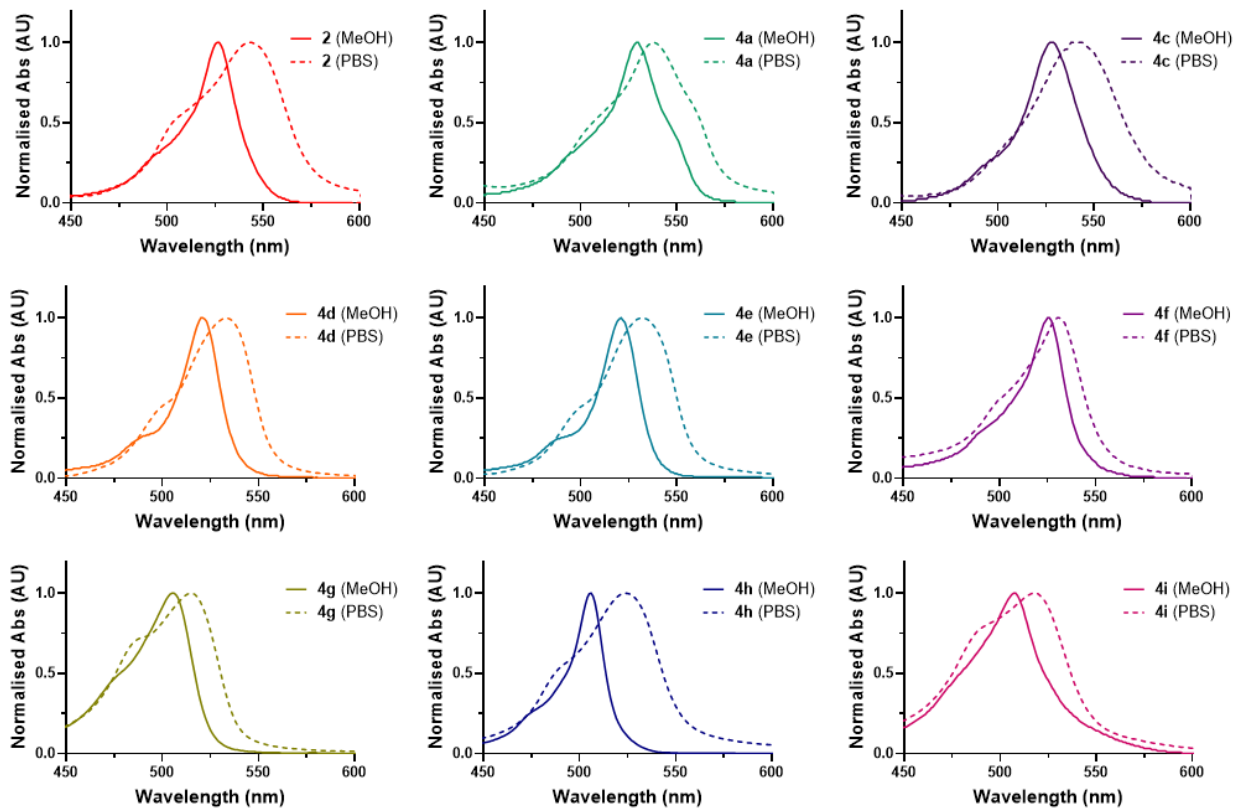


Figure 135. Normalised absorbance spectra of $[Te]$ -BODIPYs in MeOH and PBS (containing 1% DMSO).

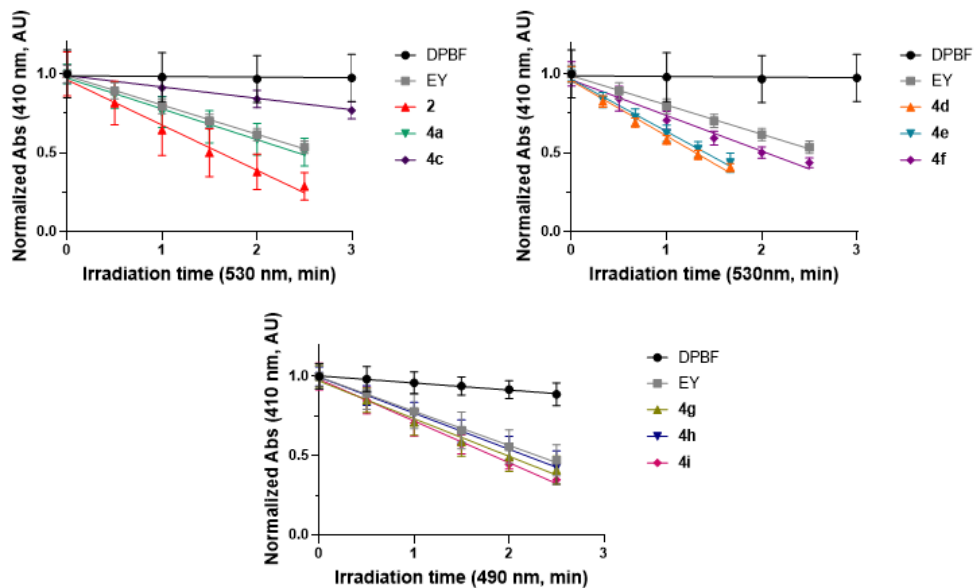


Figure 136. Singlet oxygen generation of [Te]-BODIPYs detected by DPBF in 1% DMSO in MeOH.

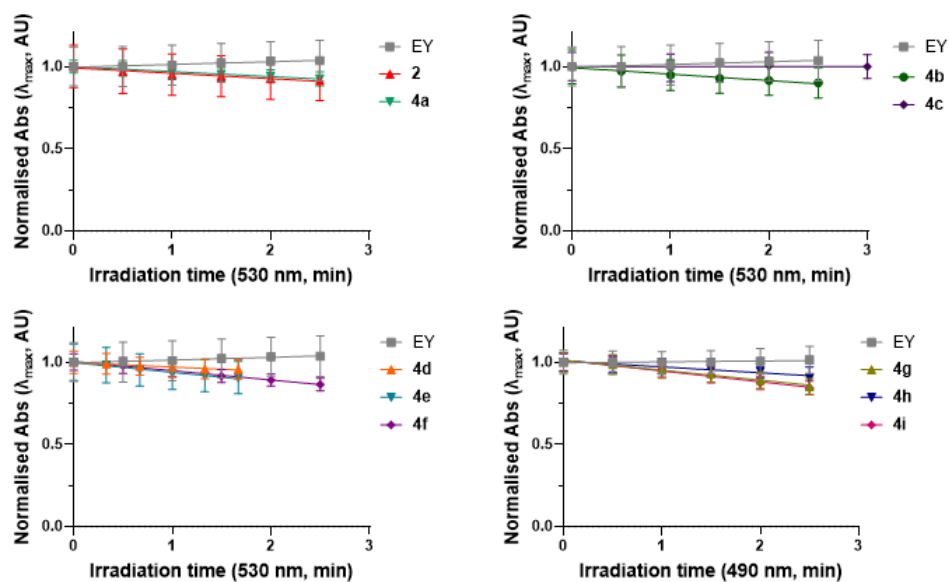


Figure 137. Photostability of [Te]-BODIPYs under irradiation.

D.4. Cell Assays and Viability

HeLa cells were seeded at a density of 10,000 cells per well in 96-well plates (Thermo Scientific Nunclon™ Delta Surface) and incubated in 200 μ L DMEM overnight. The cells were then washed with D-PBS and replaced with 200 μ L minimal essential media (Opti-MEM). DMSO stocks of the [Te]-BODIPY compounds were added at a variety of concentrations to a final DMSO concentration of 1% and incubated for 3 hours. After incubation, cells were washed with D-PBS and the media was replaced with 200 μ L DMEM. Plates were either kept in the dark or irradiated with a 525 nm lamp for 5 minutes (15.60 mW/cm² or 4.68 J/cm²) and incubated overnight. On the following day, 20 μ L of a 5 mg/mL solution of thiazolyl blue tetrazolium bromide (MTT) in D-PBS was added to each well and incubated for 3 hours. The media was then removed and 150 μ L of DMSO was added to dissolve the formazan products. Plates were read at 560 nm and 800 nm using BioTek Synergy™ HTX Multi-Mode Microplate Reader to determine the concentration of formazan products and the background respectively. Corrected absorbance values were then used to calculate the cell viability. Cell viability experiments were all conducted with n = 9.

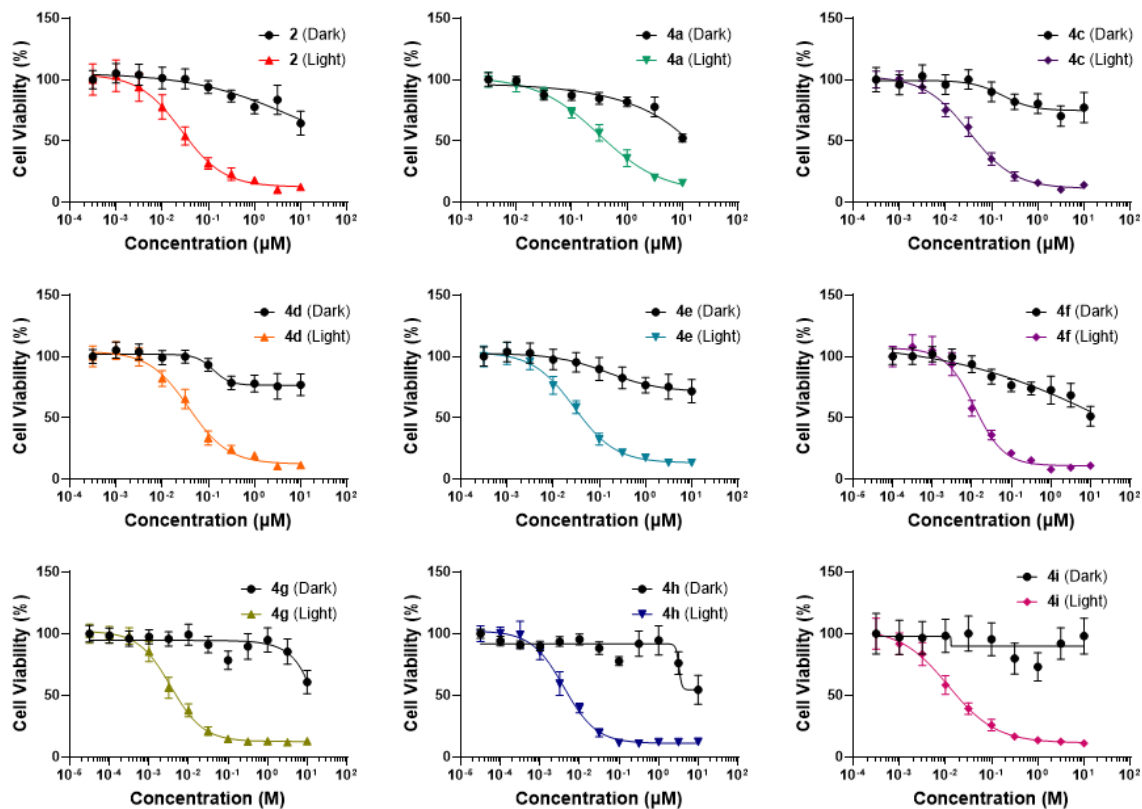


Figure 138. Cell viability of HeLa cells incubated with varying concentrations of [Te]-BODIPYs in dark or light conditions.

D.5. NMR Spectra

Figure 139. ^1H NMR (400 MHz) spectrum of compound **d3d** in CDCl_3

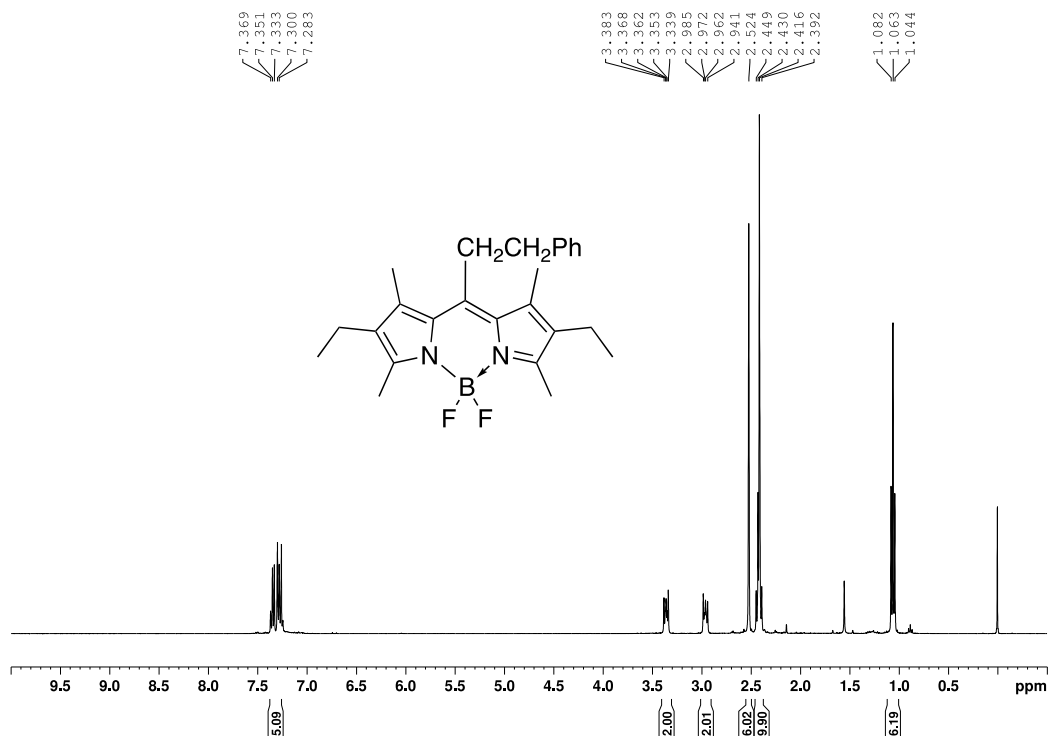


Figure 140. $^{13}\text{C}\{^1\text{H}\}$ NMR (101 MHz) spectrum of compound **d3d** in CDCl_3

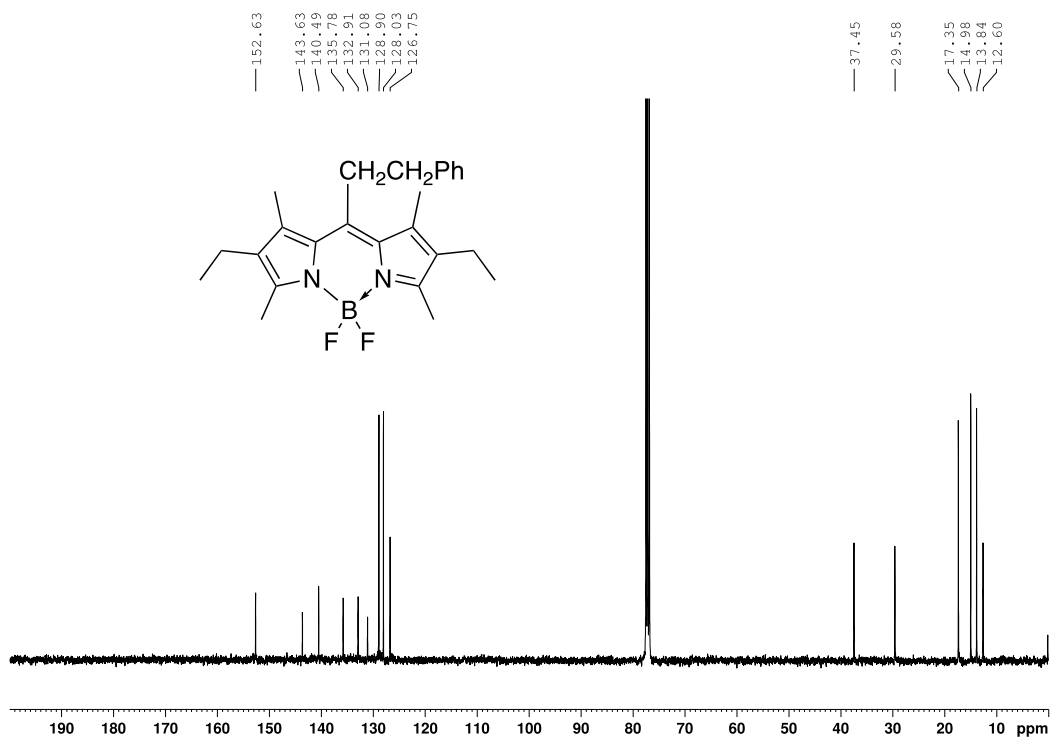


Figure 141. ^{11}B NMR (128 MHz) spectrum of compound **d3d** in CDCl_3

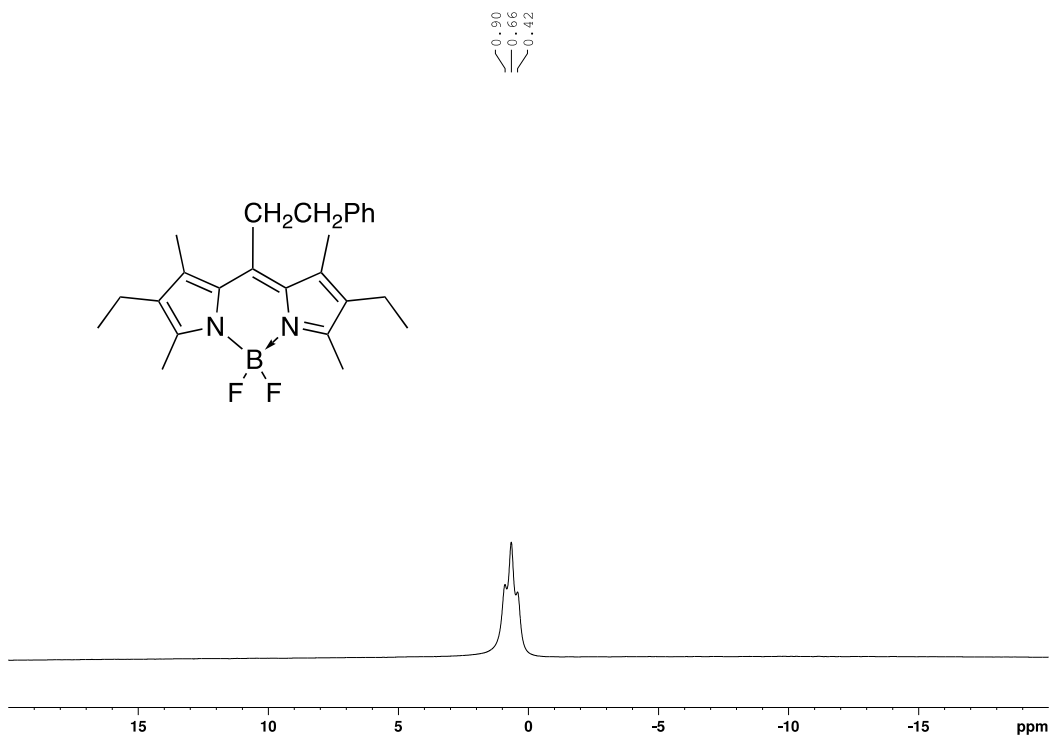


Figure 142. ^{19}F NMR (377 MHz) spectrum of compound **d3d** in CDCl_3

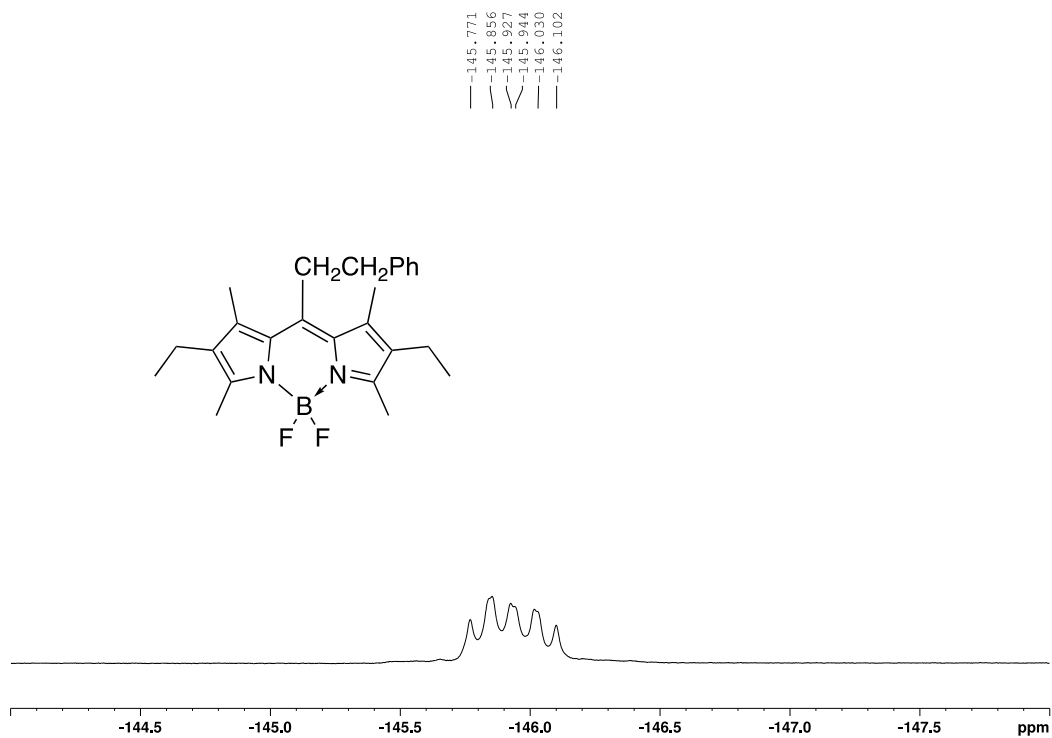


Figure 143. ^1H NMR (500 MHz) spectrum of compound **d3f** in CDCl_3

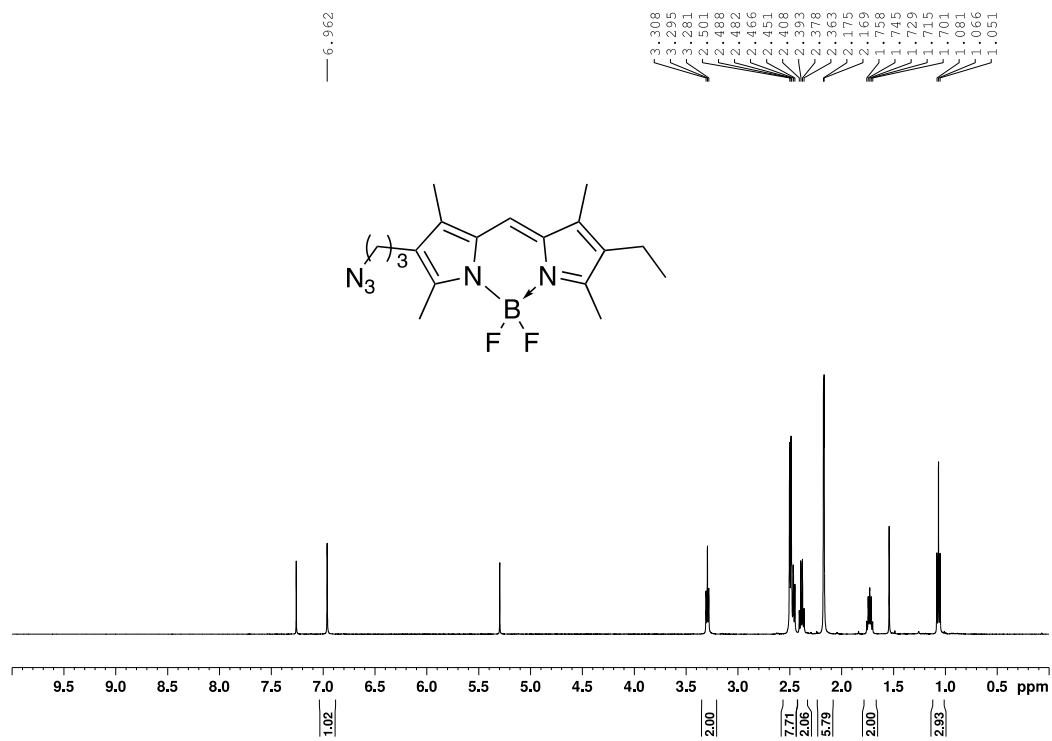


Figure 144. $^{13}\text{C}\{^1\text{H}\}$ NMR (126 MHz) spectrum of compound **d3f** in CDCl_3

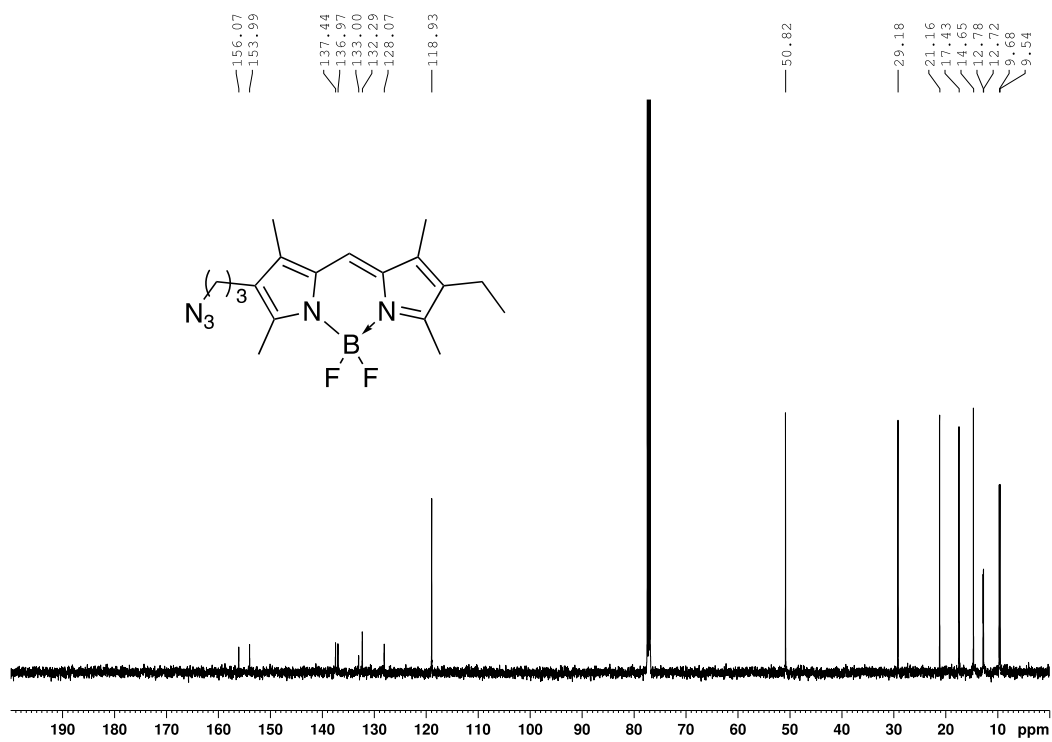


Figure 145. ^{11}B NMR (160 MHz) spectrum of compound **d3f** in CDCl_3

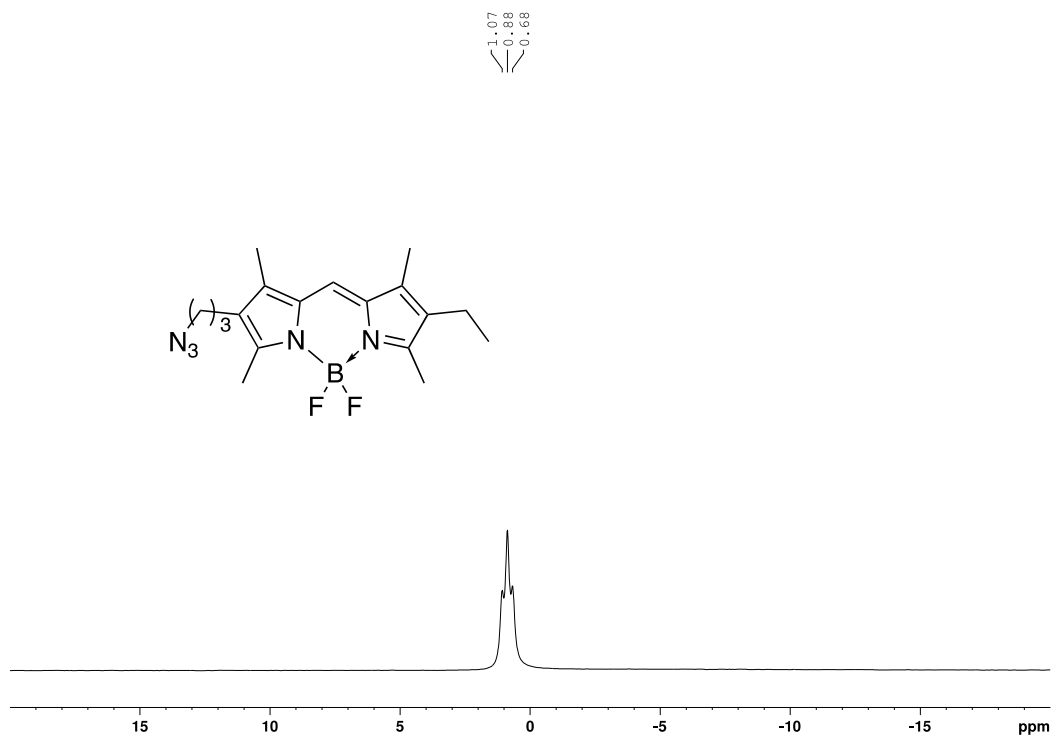


Figure 146. ^{19}F NMR (470 MHz) spectrum of compound **d3f** in CDCl_3

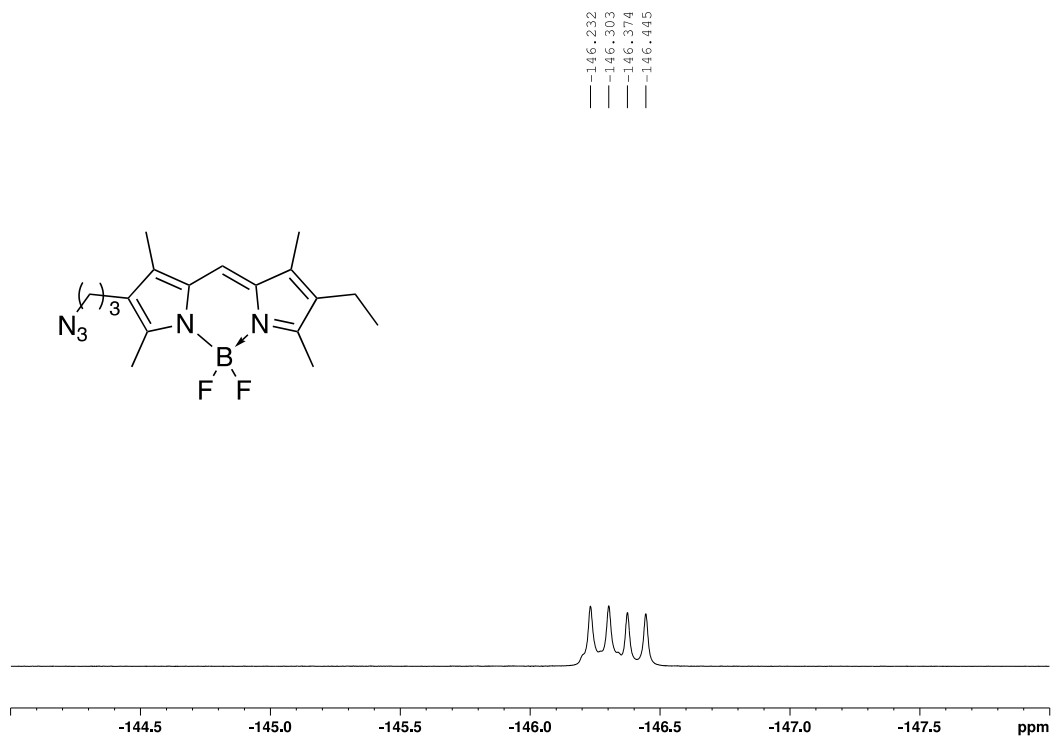


Figure 147. ^1H NMR (500 MHz) spectrum of compound **d3i** in CDCl_3

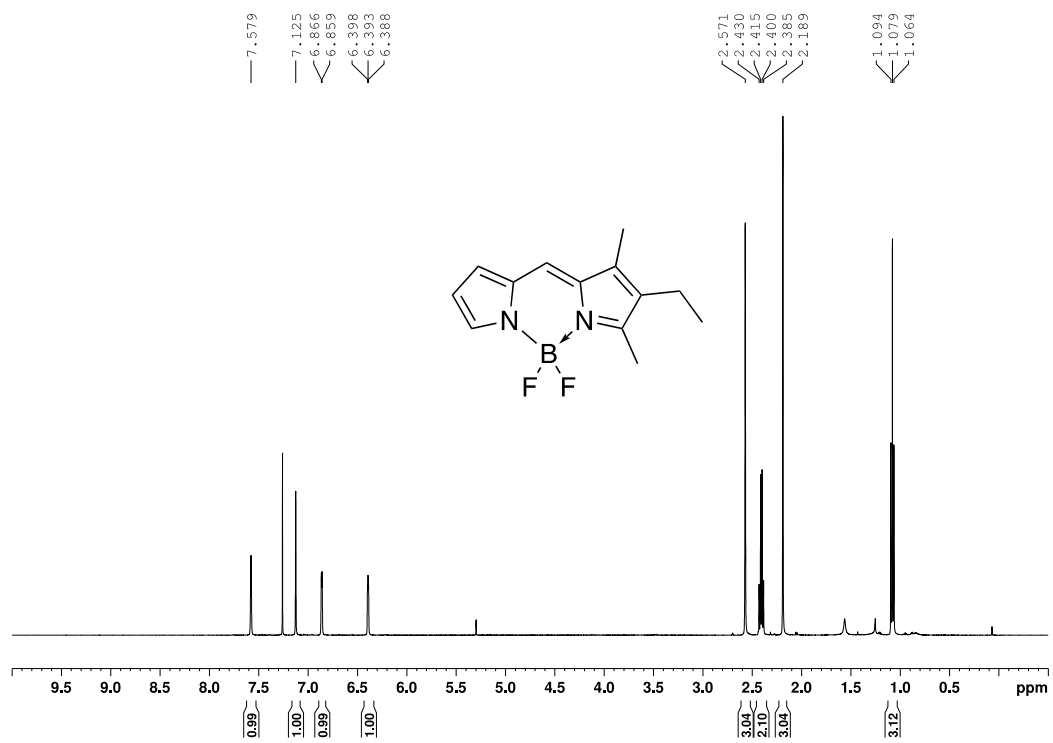


Figure 148. ^1H NMR (500 MHz) spectrum of compound **d31** in CDCl_3

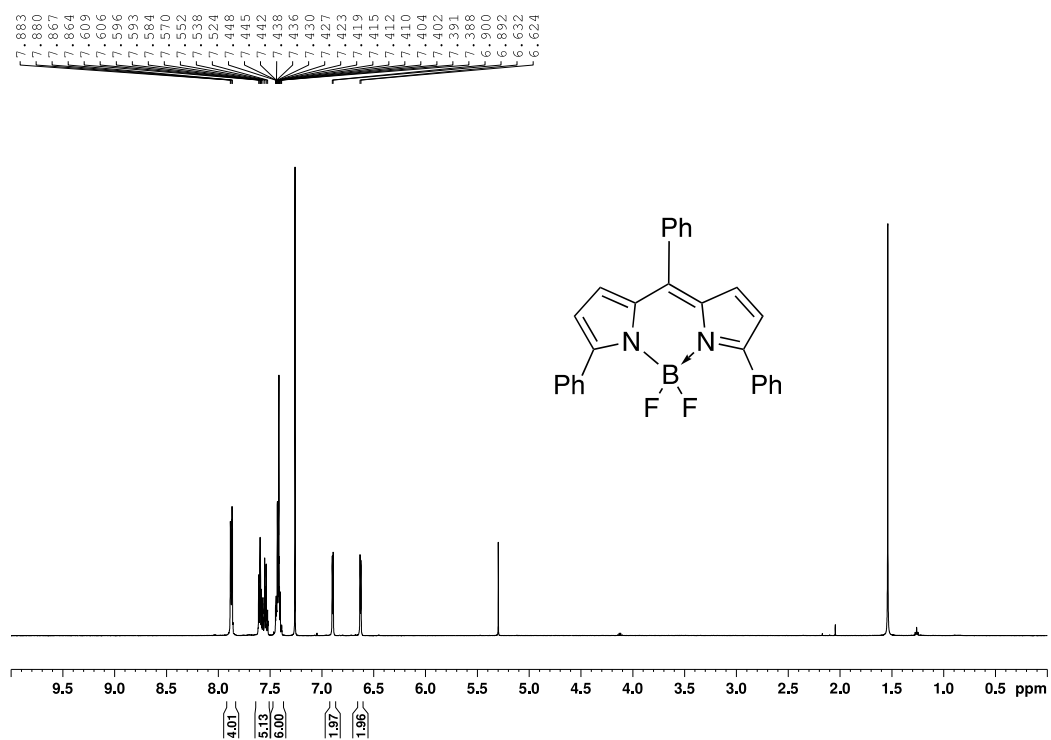


Figure 149. ^1H NMR (500 MHz) spectrum of compound **d4a** in CDCl_3

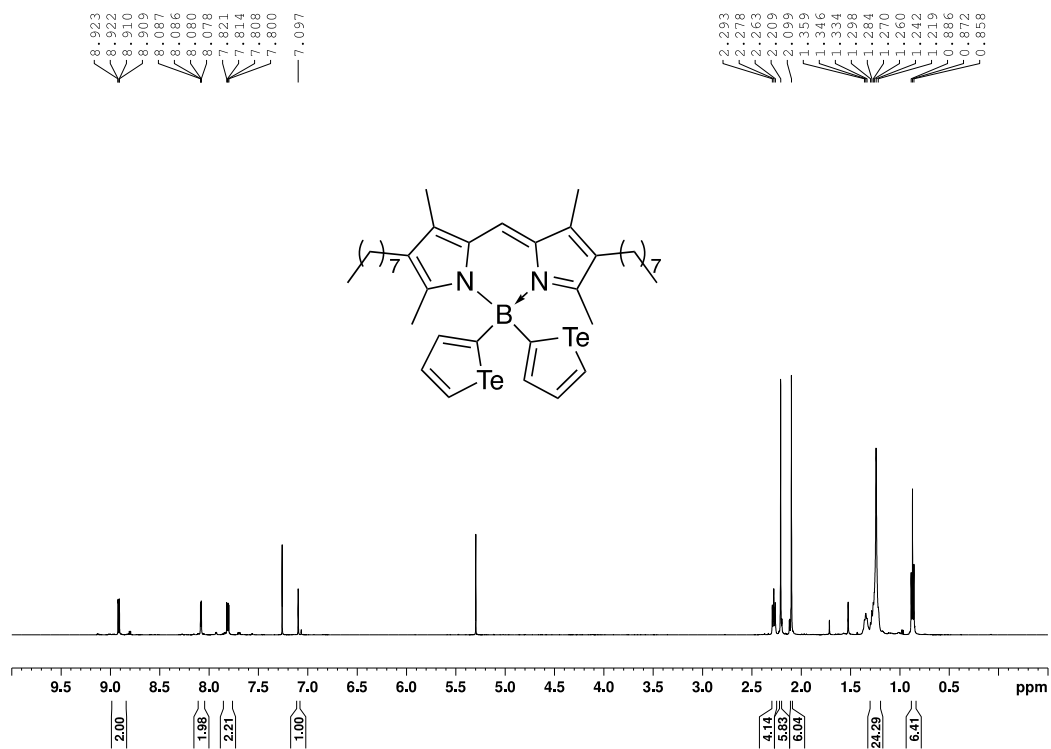


Figure 150. $^{13}\text{C}\{^1\text{H}\}$ NMR (126 MHz) spectrum of compound **d4a** in CDCl_3

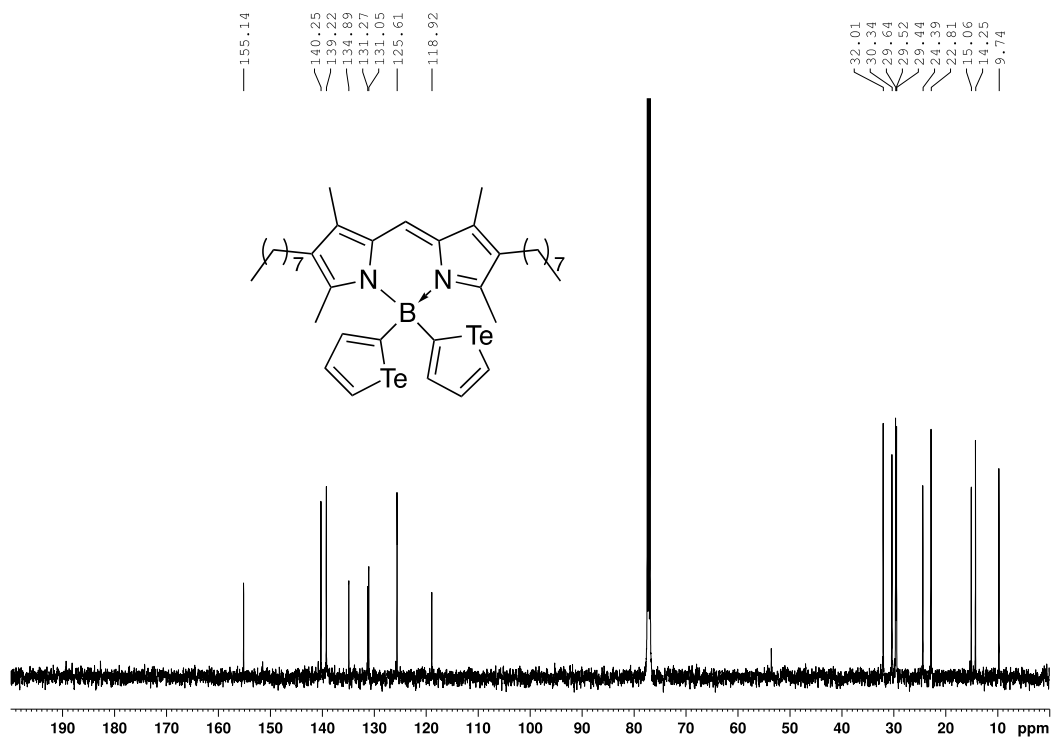


Figure 151. ^{11}B NMR (160 MHz) spectrum of compound **d4a** in CDCl_3

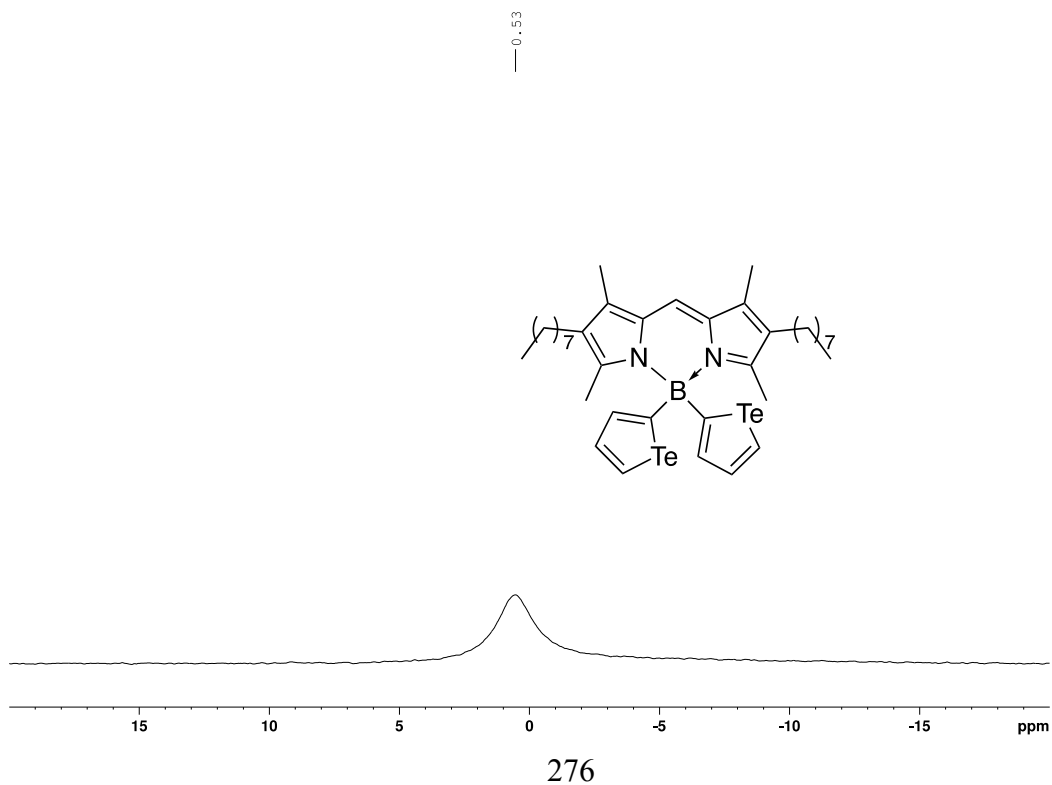


Figure 152. ^1H NMR (500 MHz) spectrum of compound **d4b** in CDCl_3

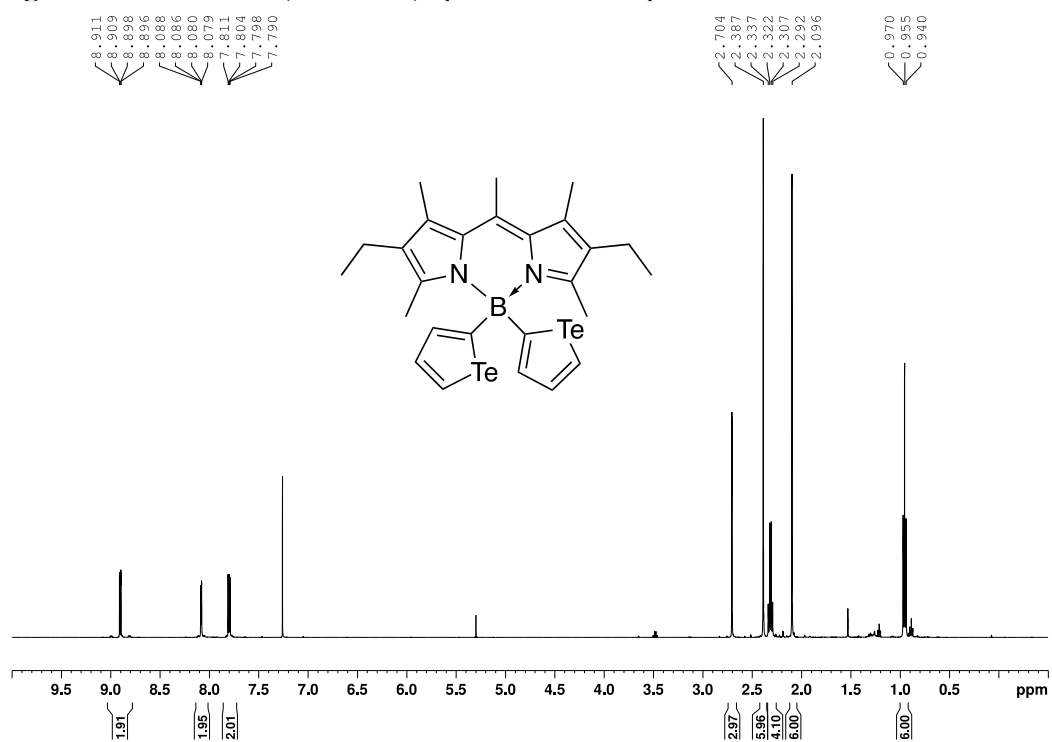


Figure 153. $^{13}\text{C}\{^1\text{H}\}$ NMR (126 MHz) spectrum of compound **d4b** in CDCl_3

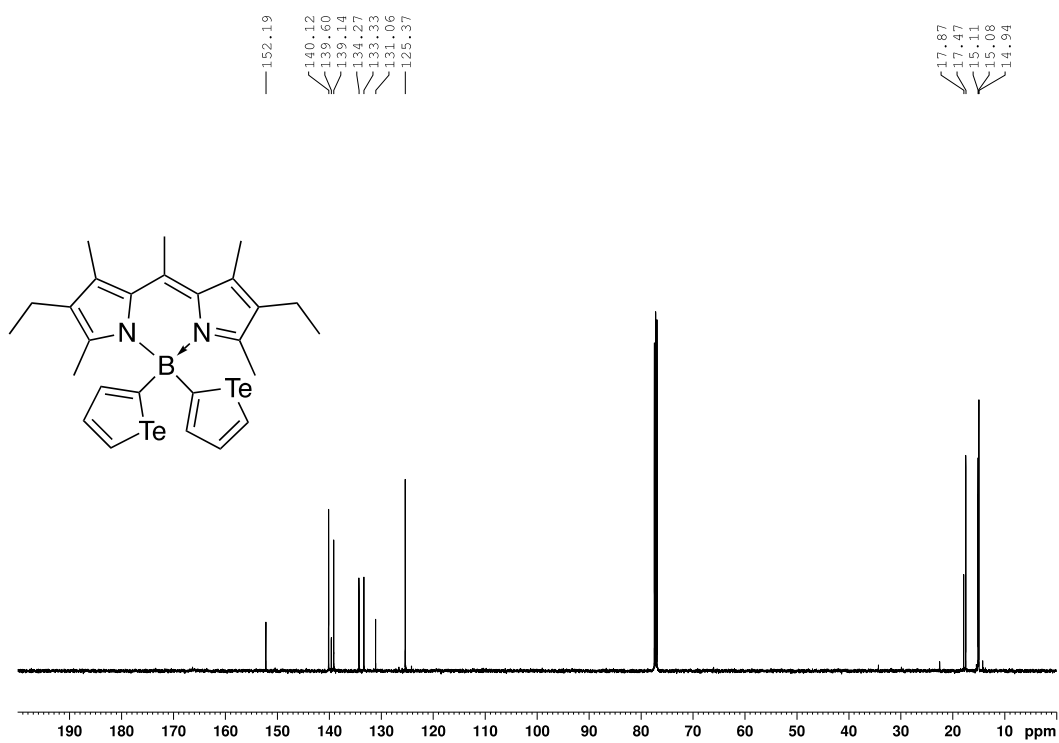


Figure 154. ^{11}B NMR (160 MHz) spectrum of compound **d4b** in CDCl_3

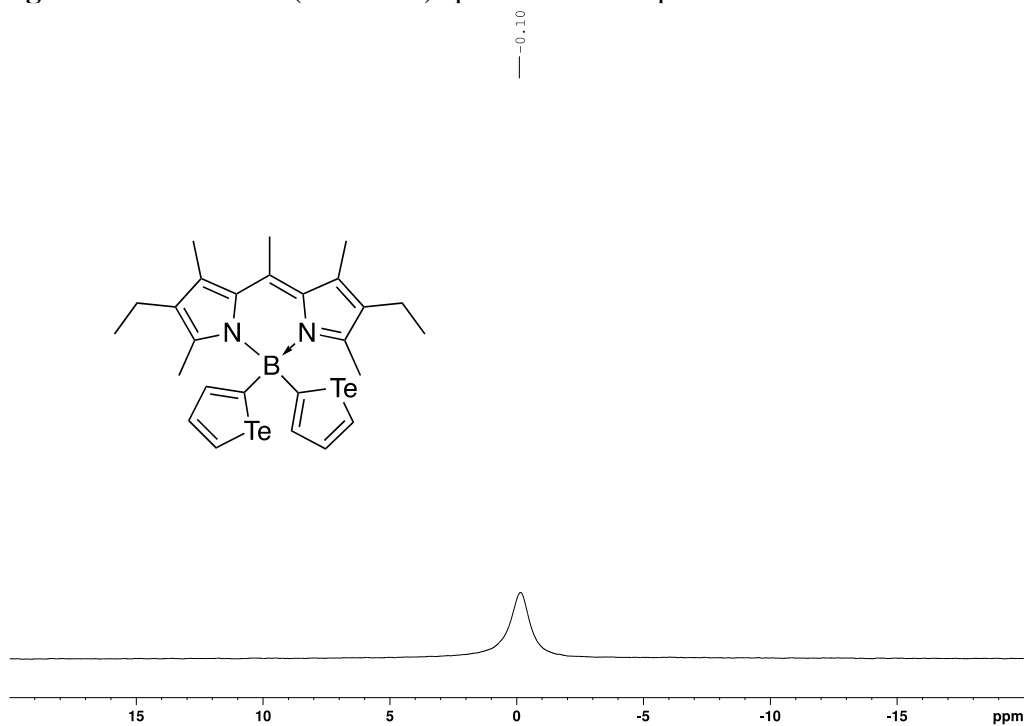


Figure 155. ^1H NMR (500 MHz) spectrum of compound **d4c** in CDCl_3

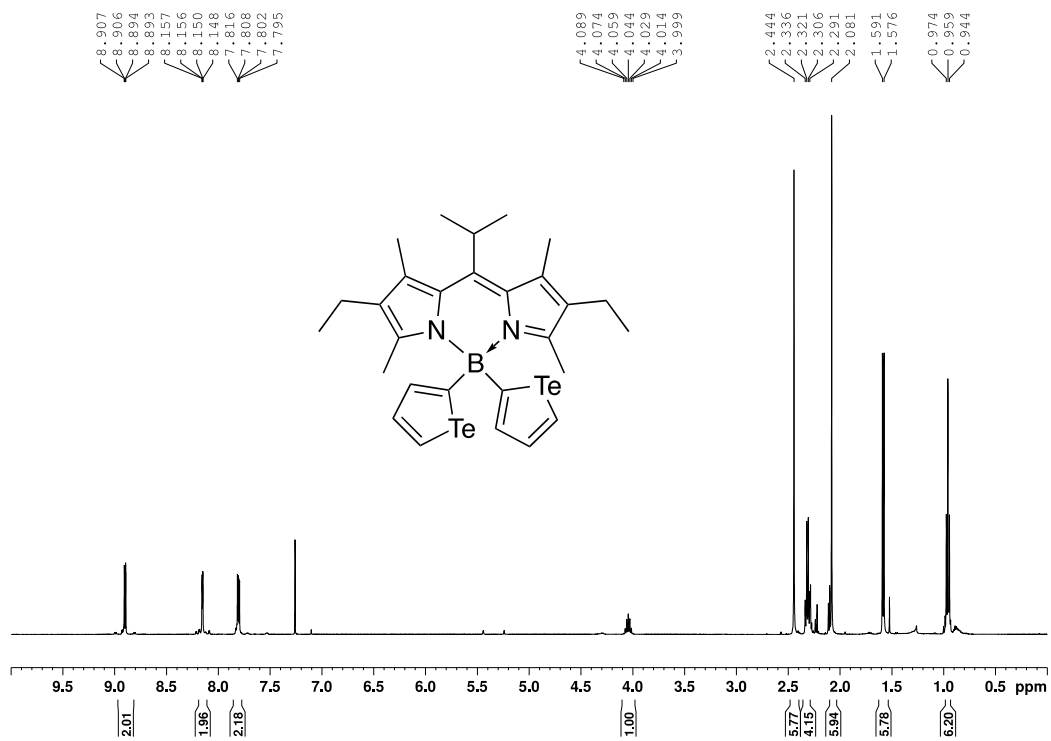


Figure 156. $^{13}\text{C}\{^1\text{H}\}$ NMR (126 MHz) spectrum of compound **d4c** in CDCl_3

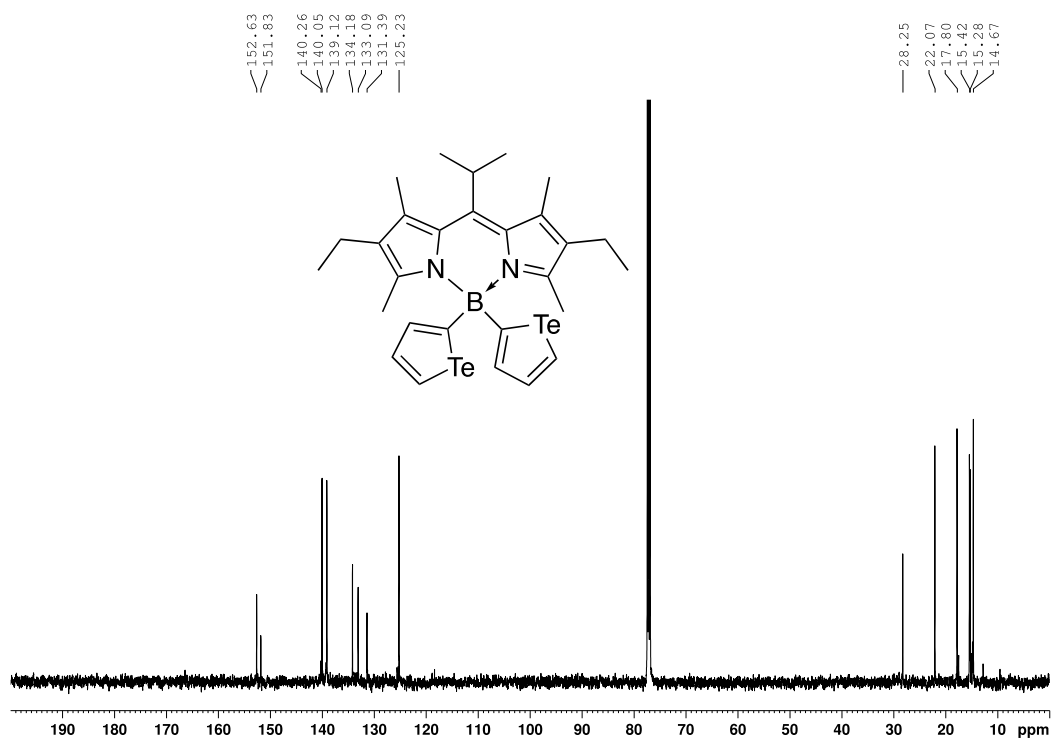


Figure 157. ^{11}B NMR (160 MHz) spectrum of compound **d4c** in CDCl_3

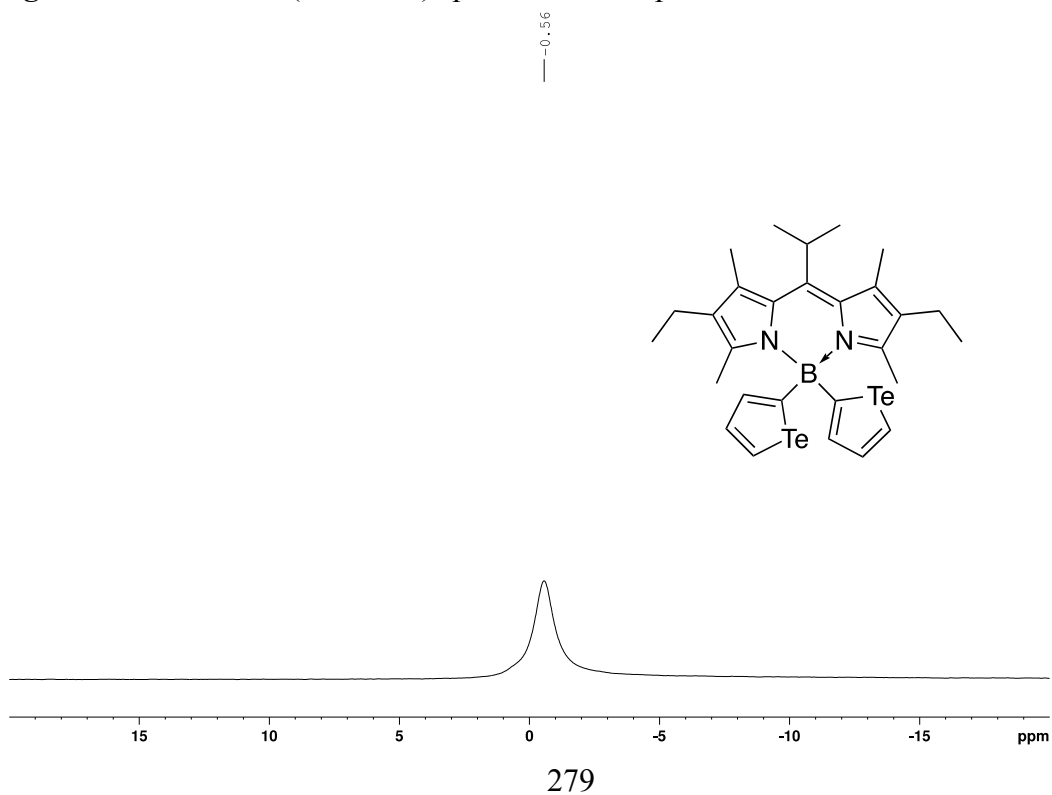


Figure 158. ^1H NMR (500 MHz) spectrum of compound **d4d** in CDCl_3

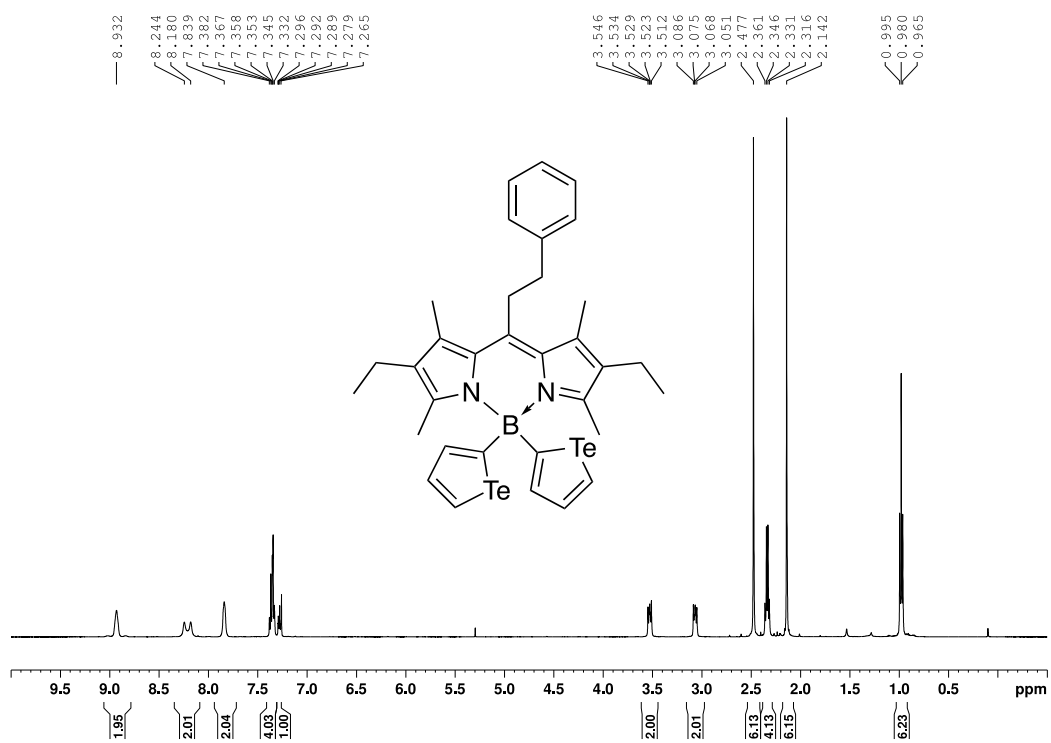


Figure 159. $^{13}\text{C}\{^1\text{H}\}$ NMR (126 MHz) spectrum of compound **d4d** in CDCl_3

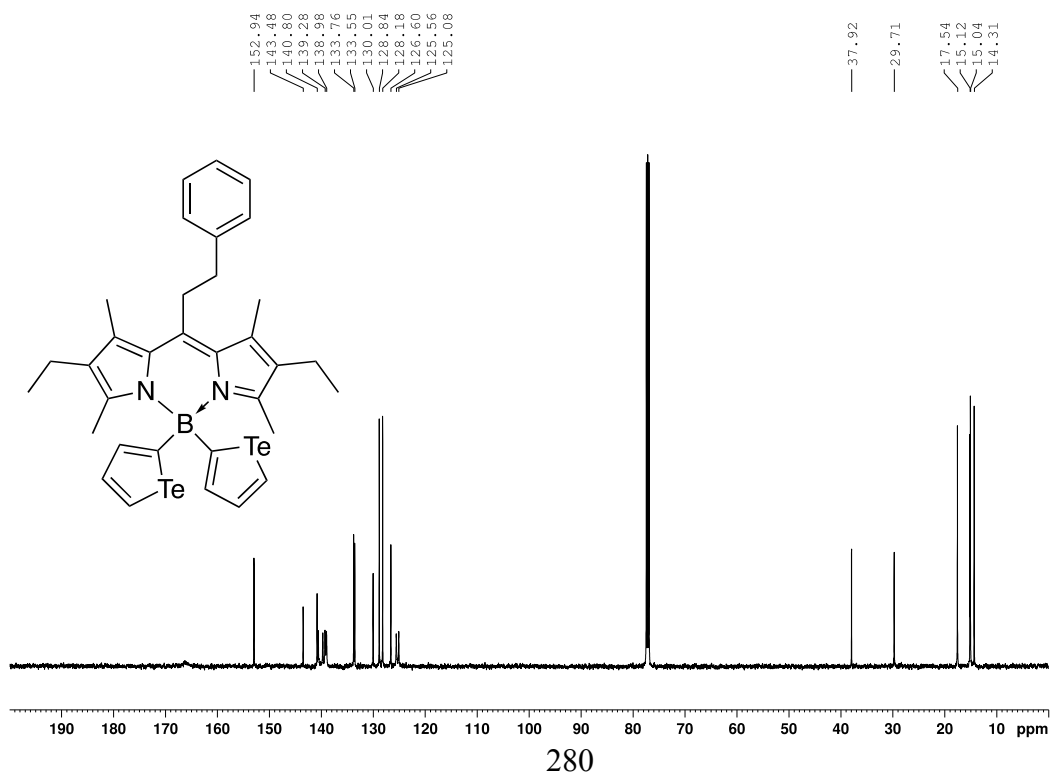


Figure 160. ^{11}B NMR (160 MHz) spectrum of compound **d4d** in CDCl_3

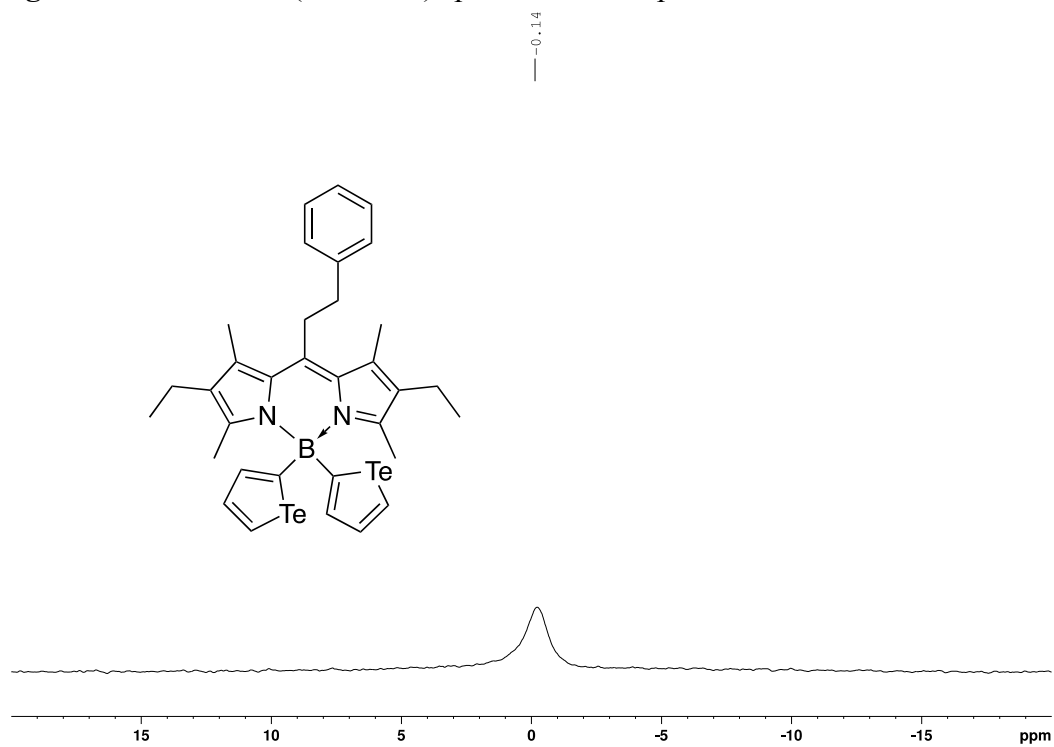


Figure 161. ^1H NMR (500 MHz) spectrum of compound **d4e** in CDCl_3

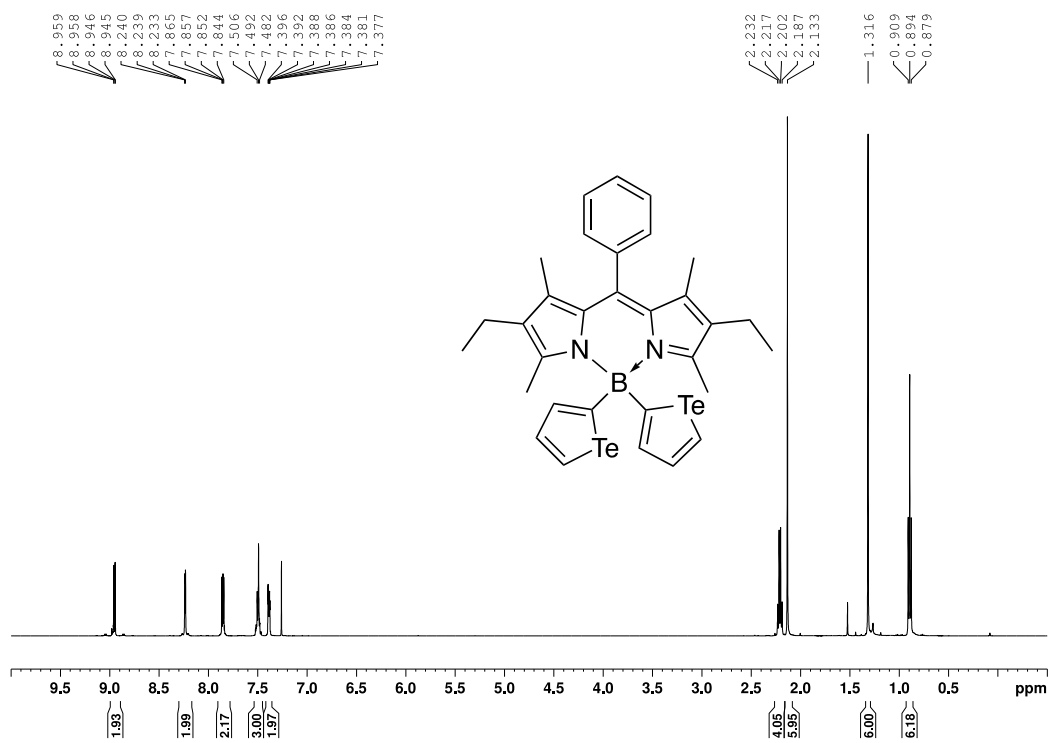


Figure 162. $^{13}\text{C}\{^1\text{H}\}$ NMR (126 MHz) spectrum of compound **d4e** in CDCl_3

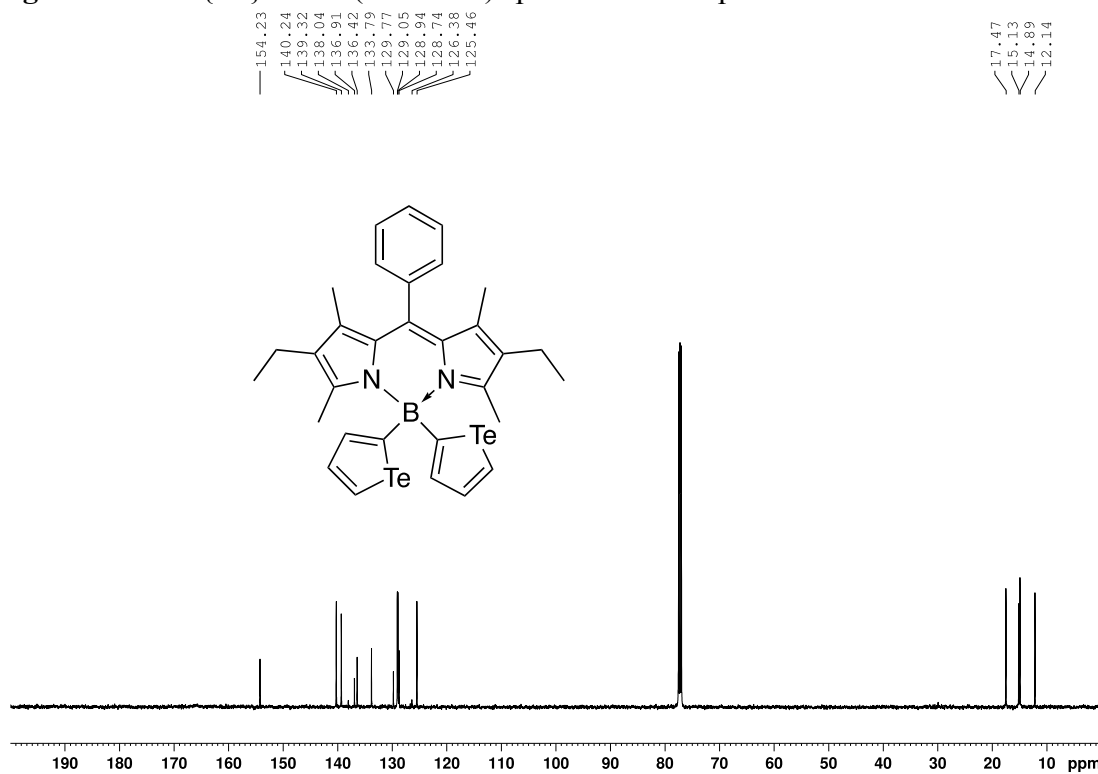


Figure 163. ^{11}B NMR (160 MHz) spectrum of compound **d4e** in CDCl_3

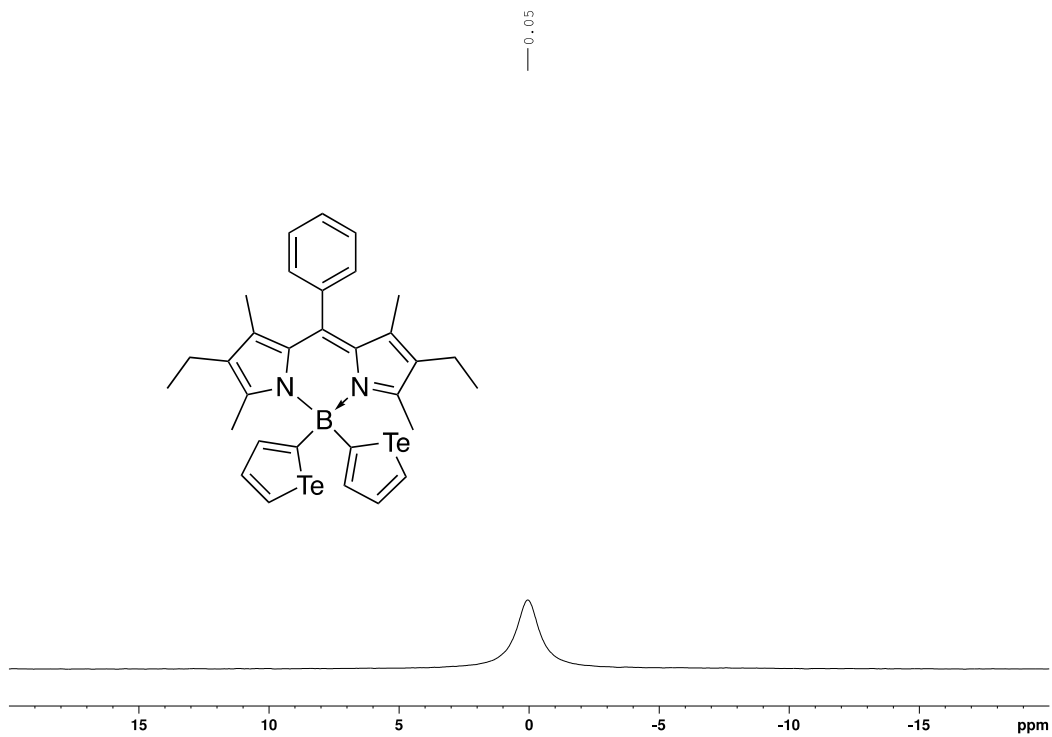


Figure 164. ^1H NMR (400 MHz) spectrum of compound **d4f** in CDCl_3

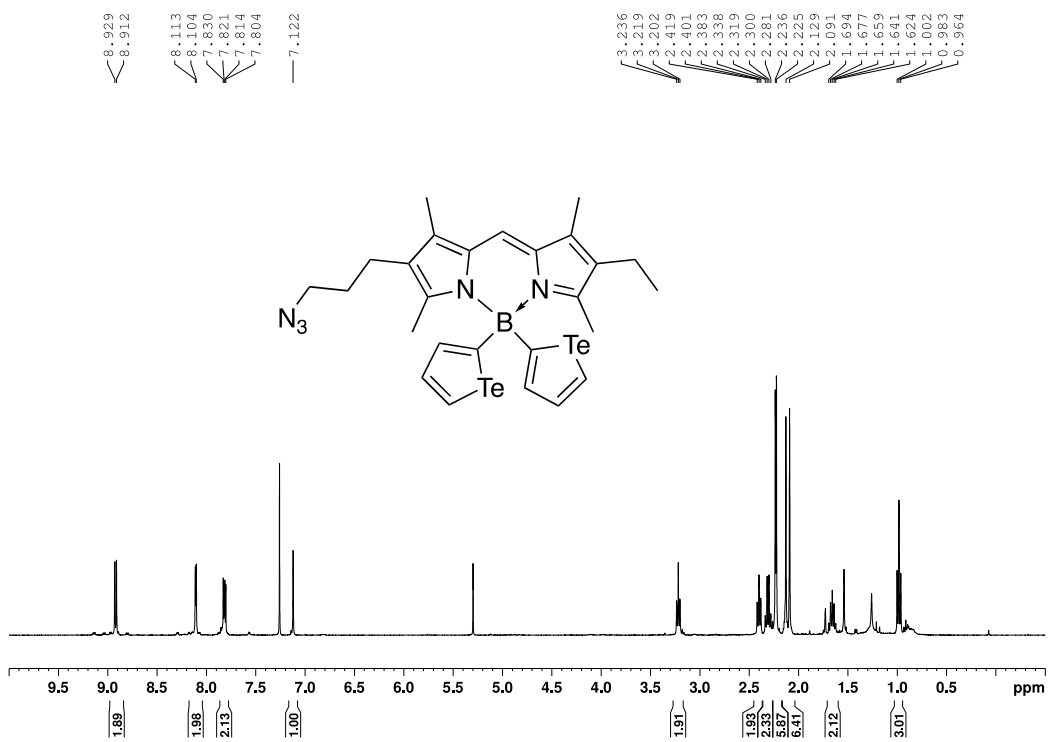


Figure 165. $^{13}\text{C}\{^1\text{H}\}$ NMR (126 MHz) spectrum of compound **d4f** in CDCl_3

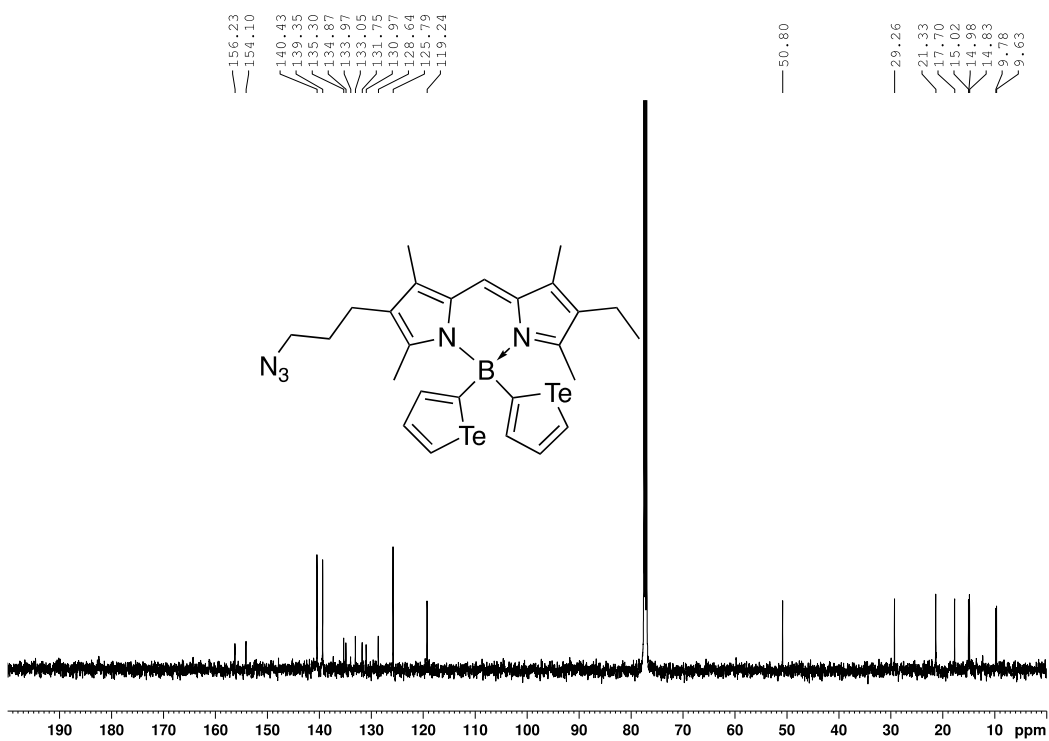


Figure 166. ^{11}B NMR (160 MHz) spectrum of compound **d4f** in CDCl_3

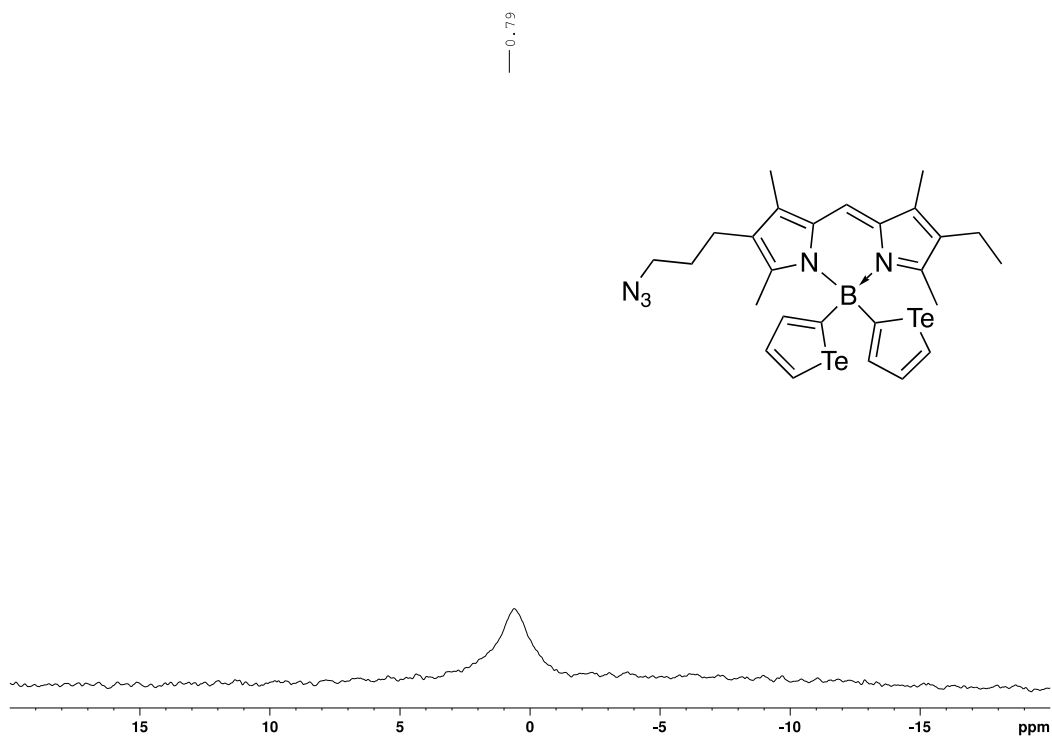


Figure 167. ^1H NMR (500 MHz) spectrum of compound **d4g** in CDCl_3

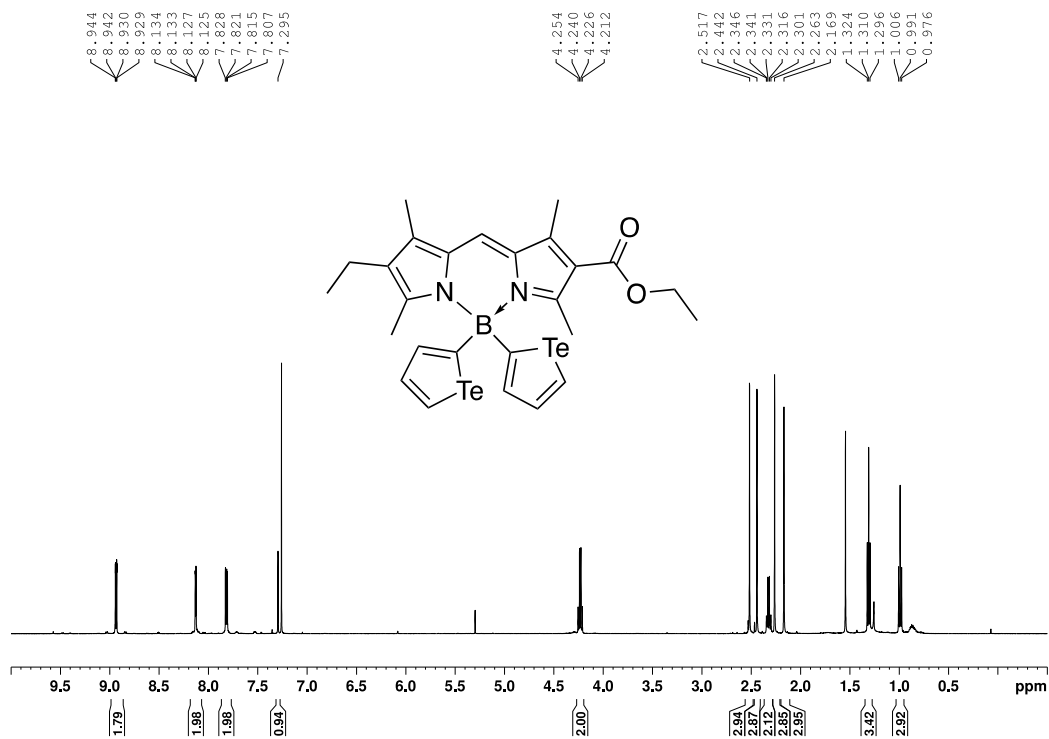


Figure 168. $^{13}\text{C}\{^1\text{H}\}$ NMR (126 MHz) spectrum of compound **d4g** in CDCl_3

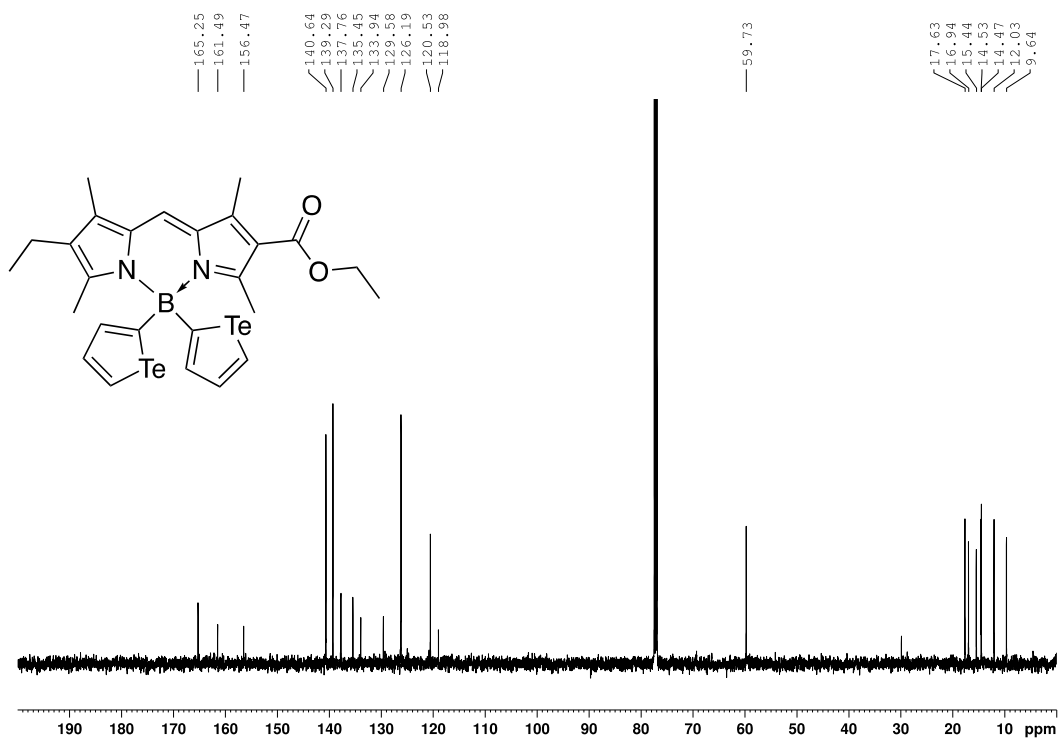


Figure 169. ^{11}B NMR (160 MHz) spectrum of compound **d4g** in CDCl_3

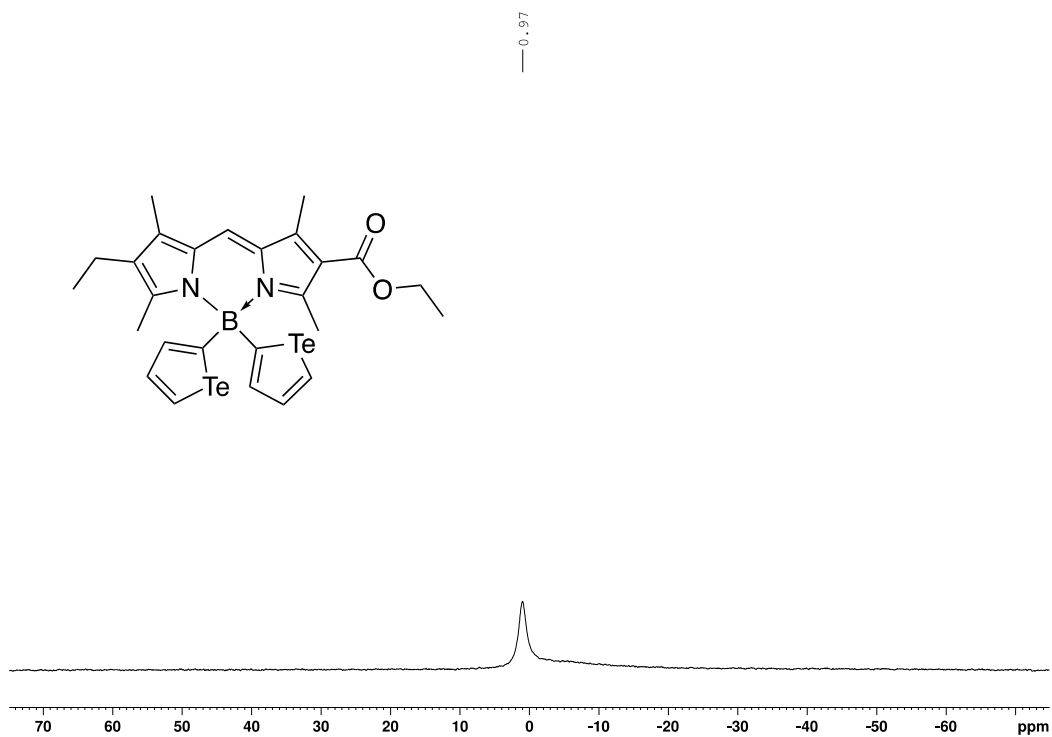


Figure 170. ^1H NMR (500 MHz) spectrum of compound **d4h** in CDCl_3

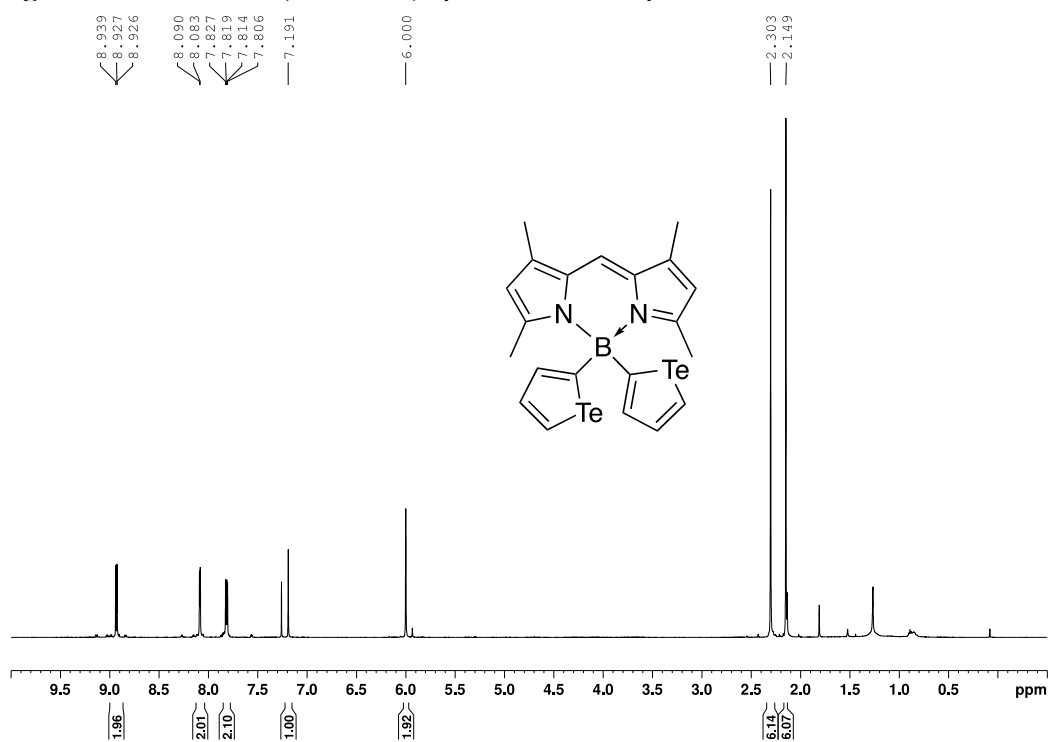


Figure 171. $^{13}\text{C}\{^1\text{H}\}$ NMR (126 MHz) spectrum of compound **d4h** in CDCl_3

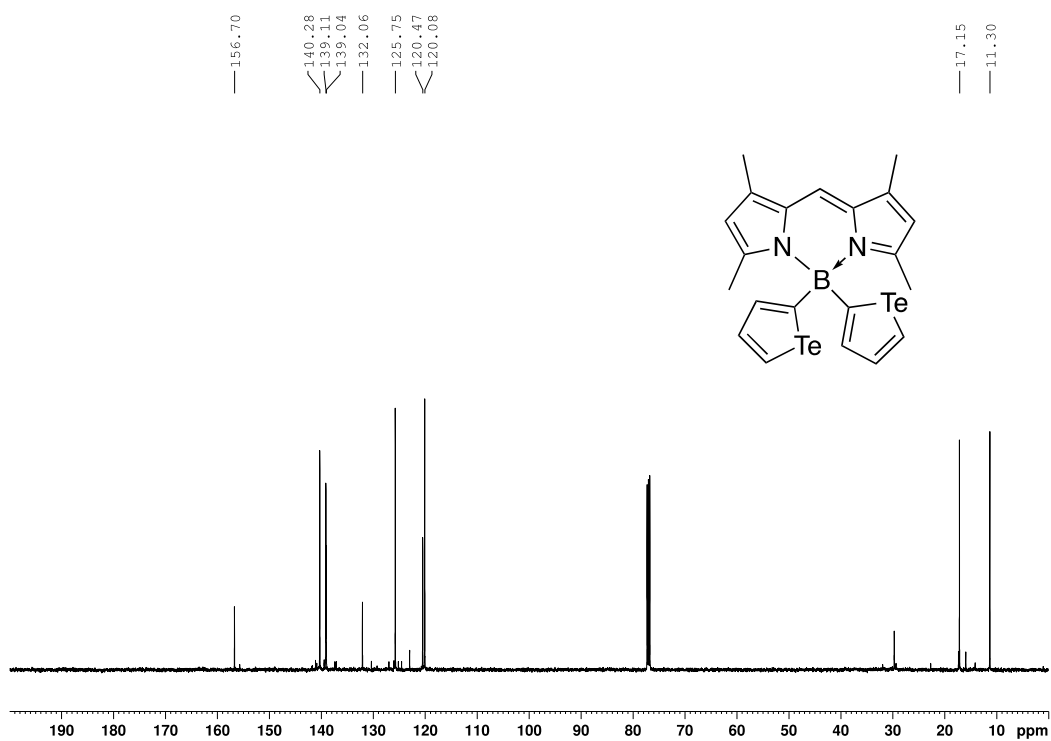


Figure 172. ^{11}B NMR (160 MHz) spectrum of compound **d4h** in CDCl_3

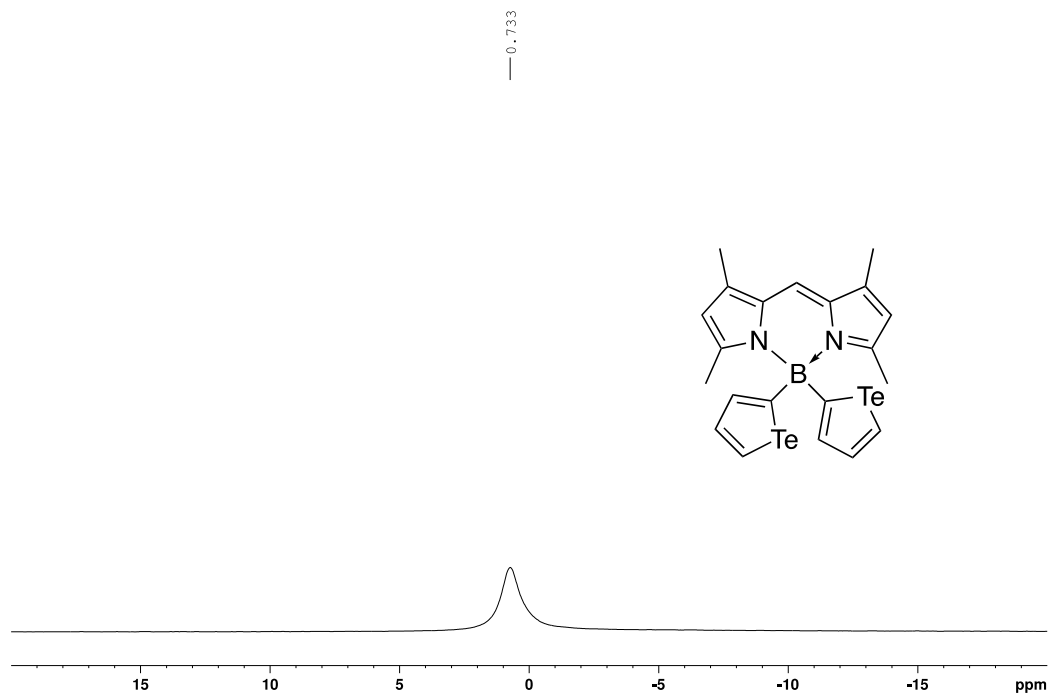


Figure 173. ^1H NMR (500 MHz) spectrum of compound **d4i** in CDCl_3

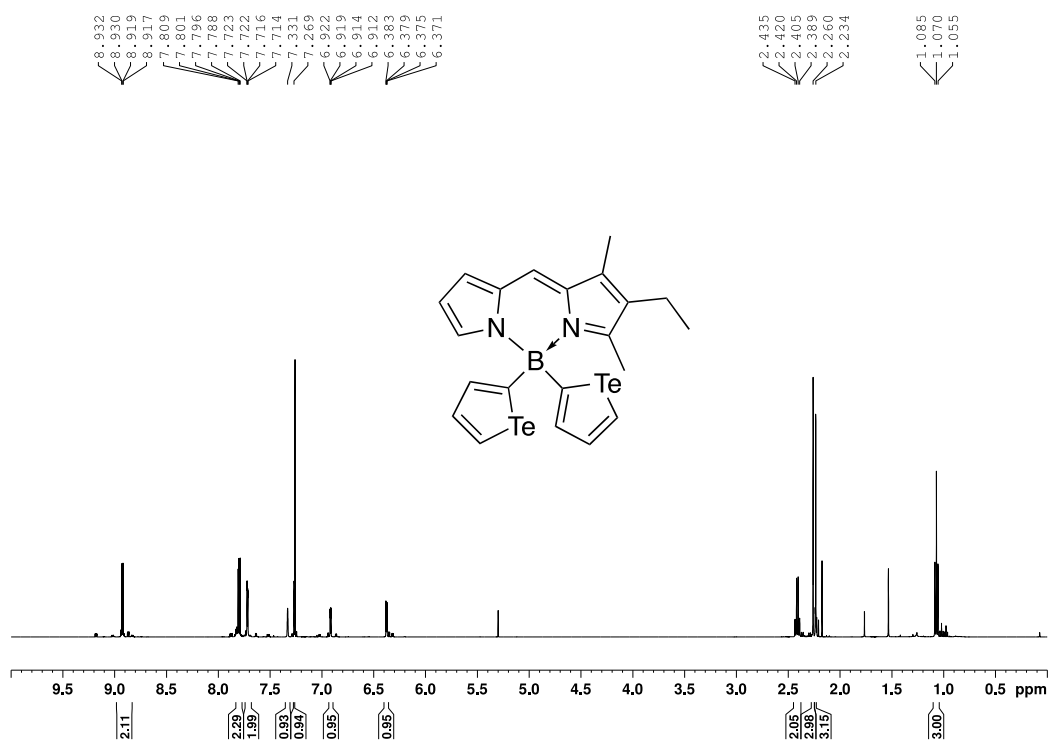


Figure 174. $^{13}\text{C}\{^1\text{H}\}$ NMR (126 MHz) spectrum of compound **d4i** in CDCl_3

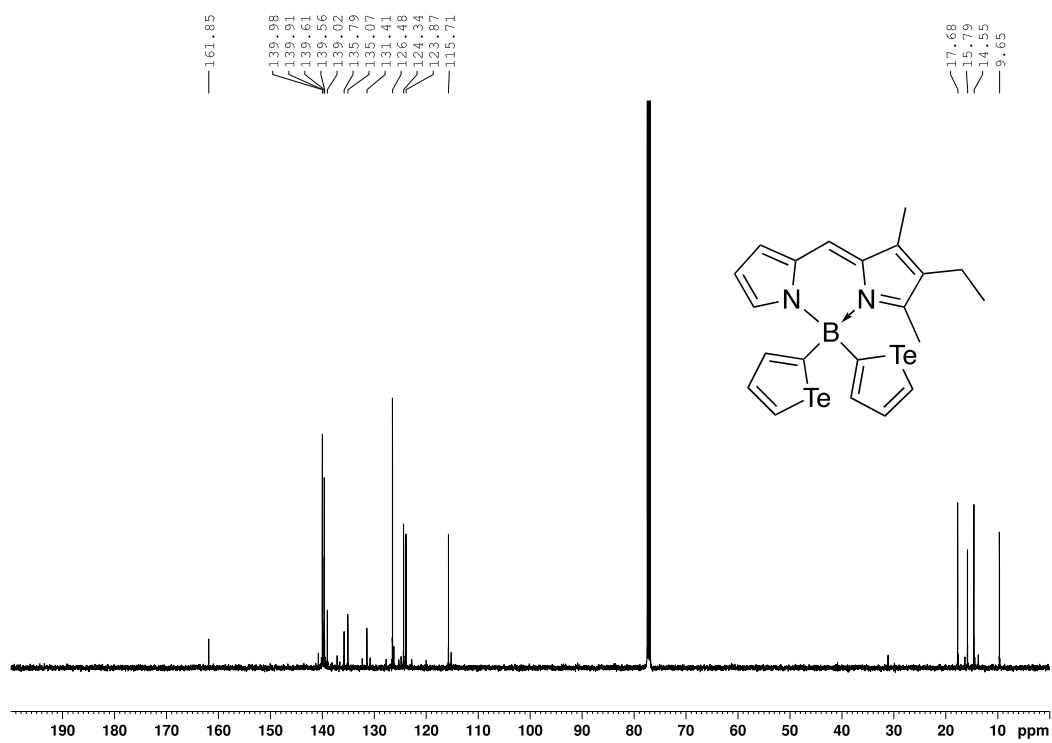
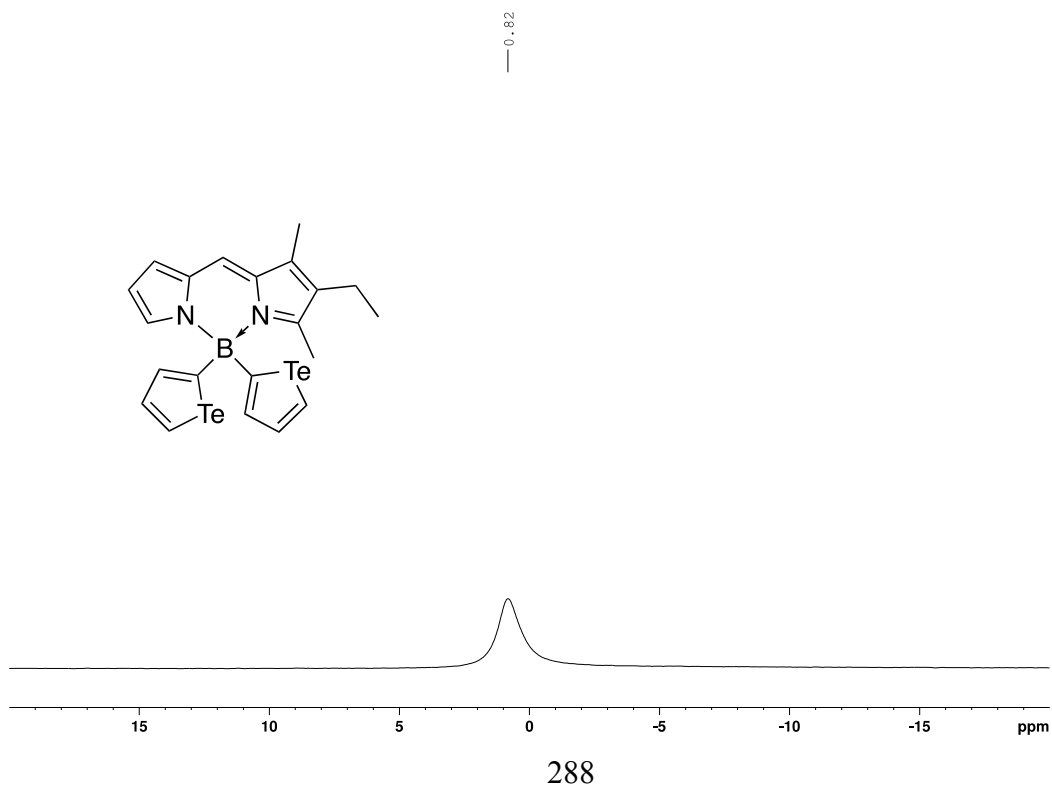


Figure 175. ^{11}B NMR (160 MHz) spectrum of compound **d4i** in CDCl_3



Appendix E. Chapter 5 Supporting Information

E.1. Experimental Procedures

E.1.1. General Remarks

Reagents were commercially available and used without further purification unless otherwise discussed. Anhydrous solvents were purchased and used without further drying. The following compounds were synthesised according to literature procedures: **e5**,²³² **e6a**²²¹ and **e6b**.²²¹ Manipulations requiring inert atmospheres were conducted under nitrogen and using Schlenk line procedures. Nuclear magnetic resonance (NMR) spectra were recorded using a 500 MHz spectrometer. ¹H chemical shifts are reported in ppm relative to tetramethylsilane using the solvent residual as an internal standard ($\delta = 7.26$ for chloroform, 5.32 for dichloromethane).²⁴² ¹³C chemical shifts are proton decoupled and reported in ppm relative to tetramethylsilane, referenced to the resonances of CDCl₃ ($\delta = 77.20$ ppm) or CD₂Cl₂ ($\delta = 53.84$ ppm).¹ Trace impurities and residual solvent peaks were determined using published tables.²⁴² Coupling constants are reported in hertz (Hz) and spin multiplicities are reported using the following symbols: s (singlet), bs (broad singlet), d (doublet), dd (doublet of doublets), t (triplet), q (quartet) and m (multiplet). ¹¹B chemical shifts are reported in ppm, externally referenced to boron trifluoride diethyl etherate ($\delta = 0.00$). ¹⁹F Chemical shifts are reported in ppm, externally referenced to CFC₃ ($\delta = 0.00$). Thin layer chromatography was performed using commercially prepared silica gel plates and visualised using long- or short-wave UV lamps. Column chromatography was

performed using 230-400 mesh silica. The relative proportions of solvents mentioned in reference to TLC and column chromatography procedures correspond to volume-to-volume ratios. Mass spectral data were acquired using a QTOF mass spectrometer operating in positive electrospray ionisation mode.

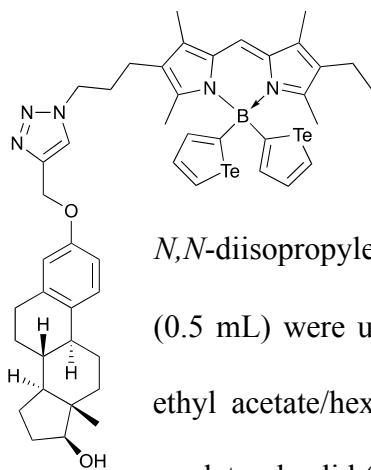
Absorption and fluorescence spectra were recorded using a quartz cuvette. Using a modified version of a literature procedure,²⁴⁷ photophysical properties of all compounds were determined in dichloromethane solution at room temperature. Molar absorptivity values were recorded at the peak maximum in dichloromethane for all cases. Fluorescence spectra were determined by exciting at 490 nm in all cases. Fluorescence quantum yield (Φ_f) was determined according to the equation: $\Phi_{\text{unk}} = (\Phi_{\text{std}})(n/n_{\text{std}})^2(I_{\text{unk}}/I_{\text{std}})(A_{\text{std}}/A_{\text{unk}})$,²⁴⁸ where Φ is the quantum yield, I is the area under the peaks in the fluorescence spectra, A is the absorbance at the excitation wavelength, and n is the refractive index (dichloromethane = 1.425,²⁶⁹ ethanol = 1.357).²⁷⁰ Rhodamine B ($\Phi_f = 0.70$ in ethanol)¹⁵⁸ was chosen as the standard. Quantum yield measurements were determined in dilute solutions ($\lambda_{\text{abs}}^{\text{max}} \leq 0.1$) to avoid inner filter effects and are the composites of ten scans in all cases.

E.2. Procedures

E.2.1. General procedure for the synthesis of estradiol-appended *[Te]*-BODIPYs, GP

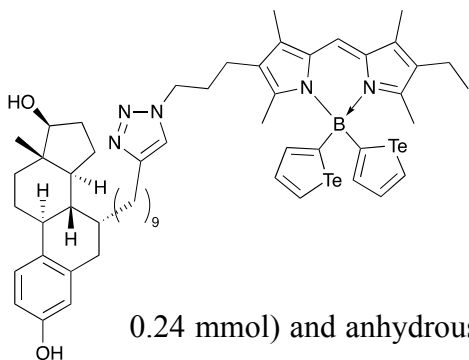
Following a literature procedure for similar substrates,²²¹ **d4f**,¹⁹⁰ alkyne-functionalised estradiol (0.08 or 0.16 mmol, 2.0 equiv.), copper iodide (10 mol%) and tris(benzyltriazolylmethyl)amine (10 mol%) were added to a 5 mL round-bottom flask equipped with a septa and stir bar. The flask was then evacuated and refilled 3× with argon. Next, anhydrous tetrahydrofuran (0.5 mL) and *N,N*-diisopropylethylamine (6.0 equiv.) were added *via* syringe and the reaction mixture was stirred at room temperature for 5 h. After confirmation of full consumption of **d4f** by TLC analysis, the reaction mixture was diluted in dichloromethane (20 mL), and the resulting solution was washed with a saturated sodium bicarbonate solution (1× 20 mL), water (1× 20 mL) and then brine (1× 20 mL). The organic layer was dried over sodium sulfate and concentrated under reduced pressure. The resulting crude solid was purified *via* column chromatography. After purification, the fractions containing the desired compounds were concentrated under reduced pressure to afford the desired estradiol-appended *[Te]*-BODIPYs. In some cases, subsequent crystallisation(s) was/were required using dichloromethane/hexanes or dichloromethane/pentane.

E.2.2. Synthesis of e1



Following **GP**, **d4f**¹⁹⁰ (54 mg, 0.08 mmol), **e5**²³² (50 mg, 0.16 mmol), copper iodide (3 mg, 0.016 mmol), tris(benzyltriazolylmethyl)amine (8.5 mg, 0.016 mmol), *N,N*-diisopropylethylamine (84 μ L, 0.48 mmol) and anhydrous tetrahydrofuran (0.5 mL) were used. After workup and column chromatography (0 \Rightarrow 60% ethyl acetate/hexanes, dry-loading), the desired product was afforded as a scarlet red solid (27 mg, 34% yield). ¹H NMR (500 MHz, CDCl₃) δ 8.91 (d, *J* = 6.4 Hz, 2H), 8.12 (d, *J* = 3.6 Hz, 2H), 7.82 (dd, *J* = 6.4, 3.6 Hz, 2H), 7.50 (s, 1H), 7.20 (d, *J* = 9 Hz, 1H), 7.12 (s, 1H), 6.77 (dd, *J* = 9 Hz, 2.5 Hz, 1H), 6.70 (d, *J* = 2.5 Hz, 1H), 5.16 (s, 2H), 4.26 (t, *J* = 7 Hz, 2H), 3.73 (dd, *J* = 15, 8.5 Hz, 1H), 2.78-2.89 (m, 2H), 2.38 (t, *J* = 7.5 Hz, 2H), 2.30 (q, *J* = 7.7 Hz, 3H), 2.22 (s, 3H), 2.18 (s, 3H), 2.13 (s, 3H), 1.98-2.08 (m, 5H), 1.91-1.97 (m, 1H), 1.84-1.90 (m, 1H), 1.65-1.75 (m, 2H), 1.15-1.52 (m, 9H), 0.99 (t, *J* = 7.7 Hz, 3H), 0.78 (s, 3H); ¹¹B NMR (160 MHz, CDCl₃) δ 0.99 (bs); ¹³C {¹H} NMR (126 MHz, CDCl₃) δ 161.2, 153.2, 144.5, 140.2, 139.1, 138.1, 136.1, 136.0, 134.4, 133.2, 133.1, 131.7, 130.9, 127.5, 126.4, 125.6, 122.5, 119.1, 114.7, 112.2, 81.9, 62.1, 50.0, 49.6, 44.0, 43.2, 38.8, 36.7, 30.6, 30.4, 29.8, 29.7, 27.2, 26.3, 23.1, 21.1, 17.4, 14.8, 14.7, 14.6, 11.0, 9.6, 9.4 (signals missing); HRMS-ESI⁺ *m/z* [*M*⁺ + Na] calc. for C₄₇H₅₆BN₅O₂¹³⁰Te₂Na = 1016.2540, found 1016.2544.

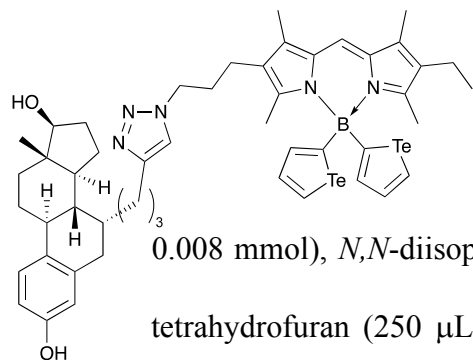
E.2.3. Synthesis of e2a



Following **GP**, **d4f**¹⁹⁰ (27 mg, 0.04 mmol), **e6a**²²¹ (34 mg, 0.08 mmol), copper iodide (1.5 mg, 0.008 mmol), tris(benzyltriazolylmethyl)amine (4 mg, 0.008 mmol), *N,N*-diisopropylethylamine (42 μ L,

0.24 mmol) and anhydrous tetrahydrofuran (250 μ L) were used. After workup, column chromatography (0 \Rightarrow 70% ethyl acetate/hexanes, dry-loading), and two recrystallisations (dichloromethane/pentane) and the desired product was afforded as a scarlet red solid (8 mg, 18% yield). ¹H NMR (500 MHz, CDCl₃) δ 8.75 (d, *J* = 6.6 Hz, 2H), 8.08 (d, *J* = 3.7 Hz, 2H), 7.79 (dd, *J* = 6.6, 3.7 Hz, 2H), 7.24 (s, 1H), 7.21 (s, 1H), 7.12 (d, *J* = 8.5 Hz, 1H), 6.59 (dd, *J* = 8.5, 2.6 Hz, 1H), 6.51 (d, *J* = 2.6 Hz, 1H), 4.26 (t, *J* = 7.3 Hz, 2H), 3.69 (t, *J* = 8.6 Hz, 1H), 2.80 (dd, *J* = 17.1, 5.1 Hz, 1H), 2.58-2.73 (m, 3H), 2.26-2.40 (m, 7H), 2.24 (s, 3H), 2.21 (s, 3H), 2.12 (s, 3H), 2.03 (s, 3H), 1.83-1.90 (m, 2H), 1.14-1.68 (m, 26H), 0.99 (t, *J* = 7.7 Hz, 3H), 0.76 (s, 3H); ¹¹B NMR (160 MHz, CDCl₃) δ 0.74 (bs); ¹³C {1H} NMR (126 MHz, CDCl₃) δ 148.2, 140.2, 139.0, 137.0, 135.6, 133.1, 131.2, 128.1, 126.9, 125.6, 124.8, 120.9, 120.8, 119.3, 115.9, 112.9, 81.8, 49.6, 46.5, 43.4, 42.1, 38.4, 37.0, 34.8, 33.4, 31.9, 30.5, 30.4, 29.7, 29.3, 29.1, 29.1, 29.0, 28.6, 28.5, 27.3, 27.1, 25.4, 24.8, 22.6, 21.0, 17.4, 15.0, 14.6, 14.4, 10.9, 9.3, 9.1 (missing signals); HRMS-ESI⁺ *m/z* [M⁺ + Na] calc. for C₅₅H₇₁BN₅O₂¹³⁰Te₂Na = 1104.3839, found 1104.3820.

E.2.4. Synthesis of e2b



Following **GP**, **d4f**¹⁹⁰ (27 mg, 0.04 mmol), **e6b**²²¹ (27 mg, 0.08 mmol), copper iodide (1.5 mg, 0.008 mmol), tris(benzyltriazolylmethyl)amine (4 mg, 0.008 mmol), *N,N*-diisopropylethylamine (42 μ L, 0.24 mmol) and anhydrous tetrahydrofuran (250 μ L) were used. After workup, the crude material was filtered through a silica plug (eluted with ethyl acetate) and then the filtrate was subjected to two recrystallisations (dichloromethane/hexanes) and the desired product was afforded as a scarlet red solid (9 mg, 22% yield). ¹H NMR (500 MHz, CDCl₃) δ 8.90 (dd, *J* = 6.6, 0.9 Hz, 2H), 8.09 (dd, *J* = 3.8, 0.9 Hz, 2H), 7.80 (dd, *J* = 6.6, 3.8 Hz, 2H), 7.21 (s, 1H), 7.16 (s, 1H), 7.10 (d, *J* = 8.5 Hz, 1H), 6.56 (dd, *J* = 8.5, 2.6 Hz, 1H), 6.50 (d, *J* = 2.6 Hz, 1H), 4.21 (t, *J* = 7.3 Hz, 2H), 3.68 (t, *J* = 8.5 Hz, 1H), 2.86 (dd, *J* = 16.8, 5.2 Hz, 1H), 2.63-2.75 (m, 2H), 2.51-2.61 (m, 1H), 2.22-2.38 (m, 12H), 2.17-2.22 (m, 4H), 2.08-2.14 (m, 4H), 1.99-2.07 (m, 5H), 1.90-1.98 (m, 2H), 1.82-1.89 (m, 2H), 1.72-1.82 (m, 3H), 1.19-1.67 (m, 1H), 0.99 (t, *J* = 7.6 Hz, 3H), 0.88 (t, *J* = 7.3 Hz, 3H), 0.75 (s, 3H); ¹¹B NMR (160 MHz, CDCl₃) δ 0.93 (bs); ¹³C {¹H} NMR (126 MHz, CDCl₃) δ 161.2, 153.2, 144.5, 140.2, 139.1, 138.1, 136.1, 136.0, 134.4, 133.2, 133.1, 131.7, 130.9, 130.5, 127.5, 126.4, 125.6, 122.5, 119.1, 114.8, 112.2, 81.9, 62.1, 50.0, 49.6, 44.0, 43.2, 38.8, 36.7, 30.6, 30.4, 29.8, 29.7, 27.2, 26.3, 23.1, 21.1, 17.5, 14.8, 14.60, 14.57, 11.0, 9.6, 9.4; HRMS-ESI⁺ *m/z* [*M*⁺ + H] calc. for C₄₉H₆₀BN₅O₂¹³⁰Te₂ = 1021.2979, found 1021.2959.

E.3. Photophysical Spectra

Figure 176. Normalised absorption and emission spectra of compound **e1** in CH₂Cl₂

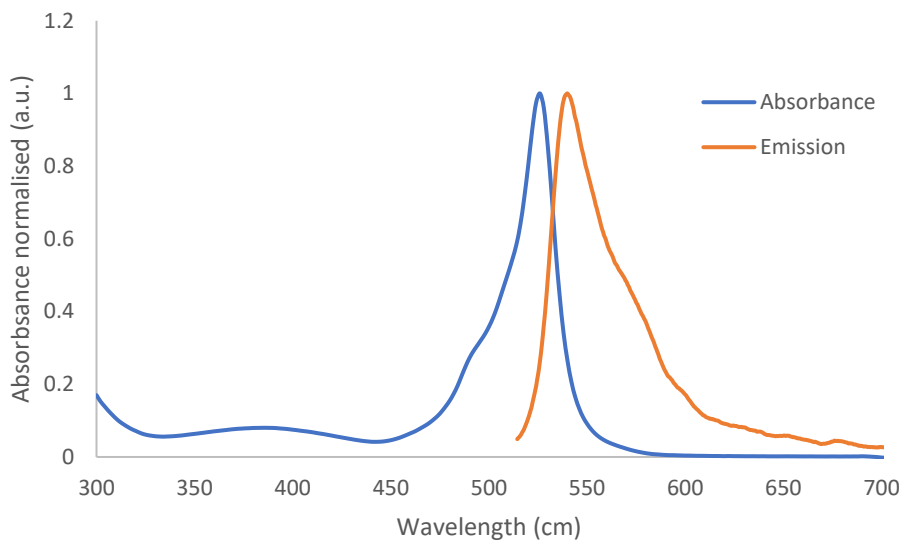


Figure 177. Normalised absorption and emission spectra of compound **e2a** in CH₂Cl₂

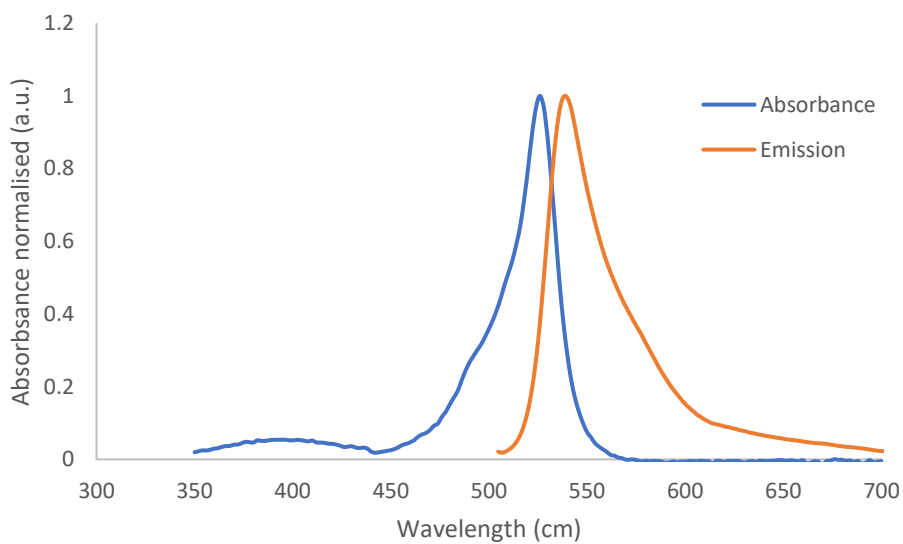
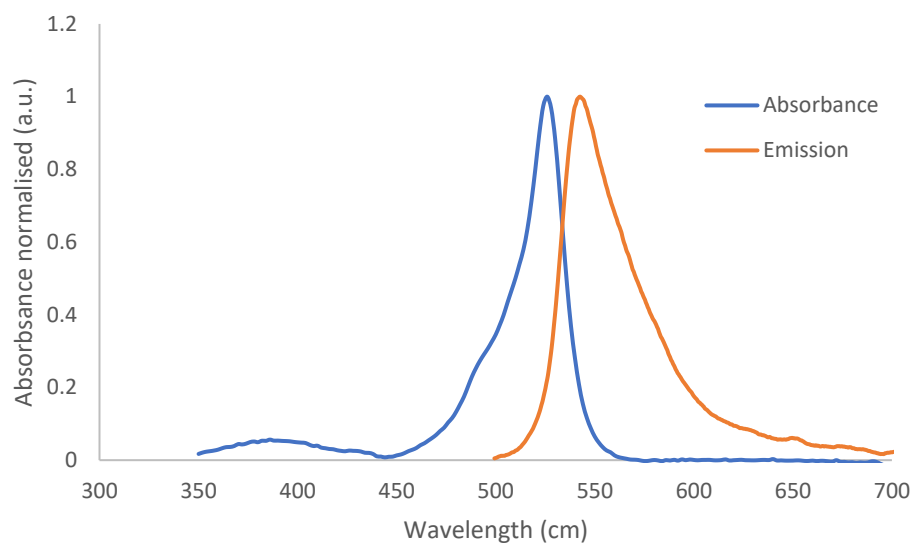


Figure 178. Normalised absorption and emission spectra of compound **e2b** in CH₂Cl₂



E.4. Nuclear Magnetic Resonance Spectra

Figure 179. ^1H NMR (500 MHz) spectrum of compound **e1** in CDCl_3

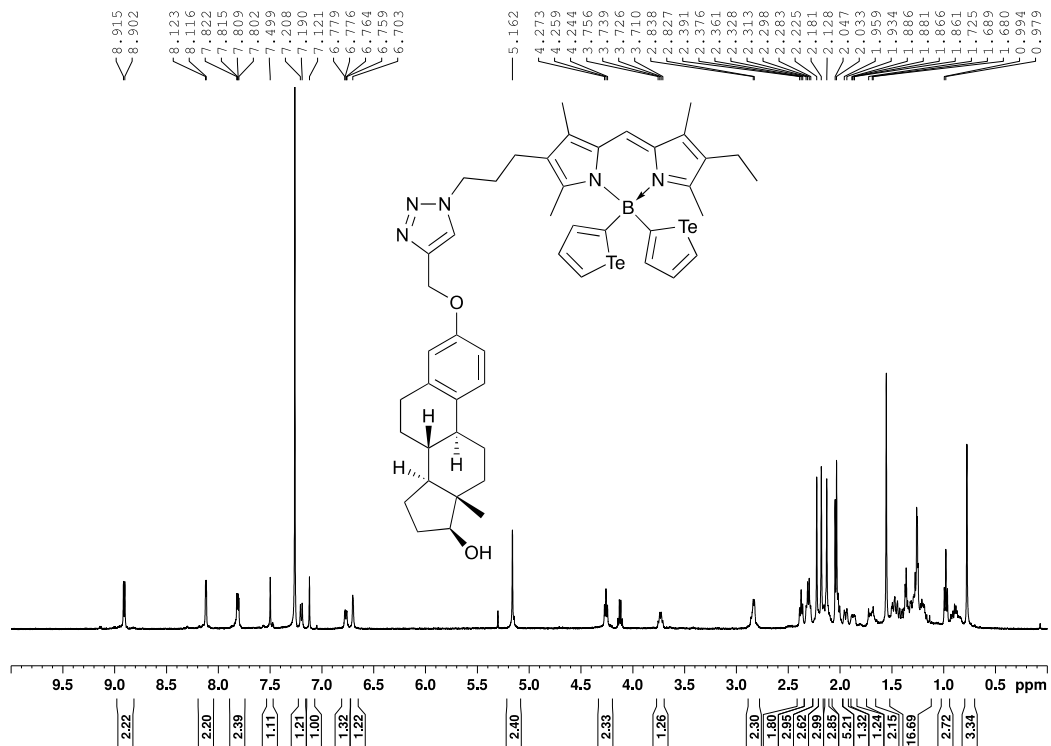


Figure 180. $^{13}\text{C}\{^1\text{H}\}$ NMR (126 MHz) spectrum of compound **e1** in CDCl_3

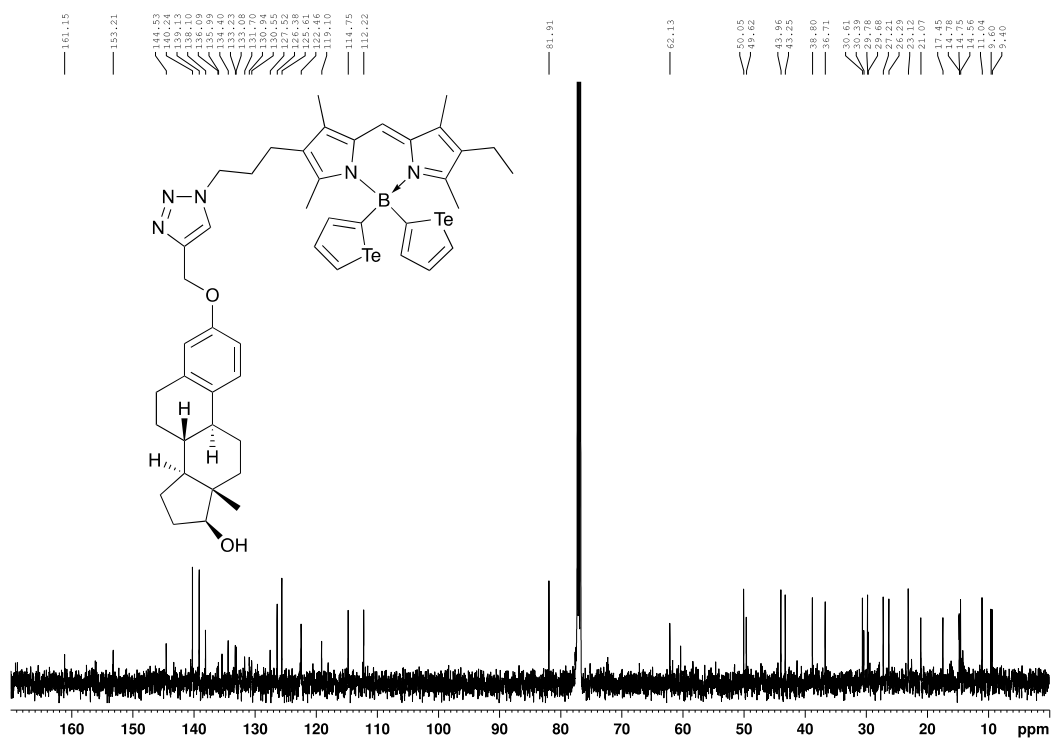


Figure 181. ^{11}B NMR (160 MHz) spectrum of compound **e1** in CDCl_3

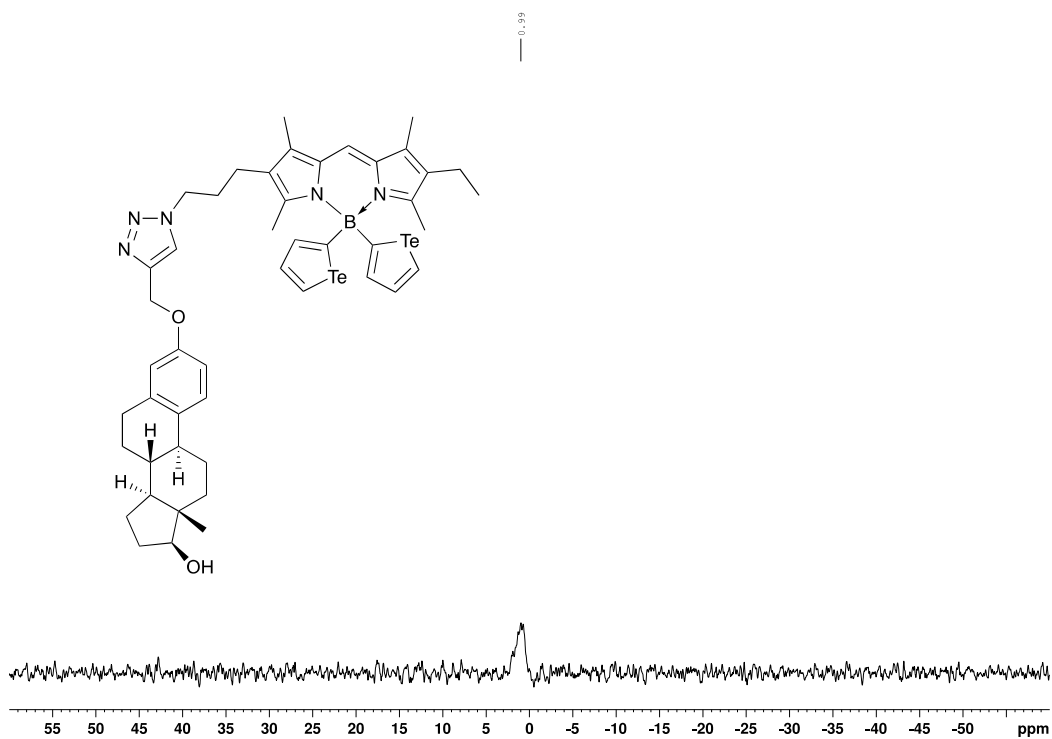


Figure 182. ^1H NMR (500 MHz) spectrum of compound **e2a** in CD_2Cl_2

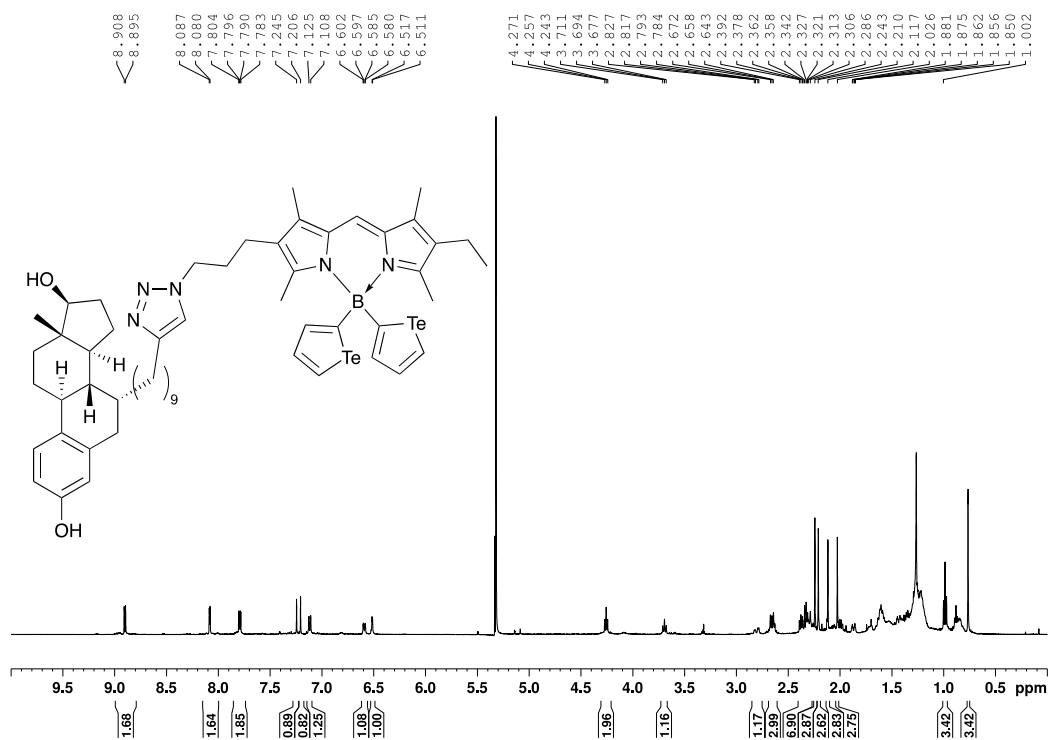


Figure 183. $^{13}\text{C}\{^1\text{H}\}$ NMR (126 MHz) spectrum of compound **e2a** in CD_2Cl_2

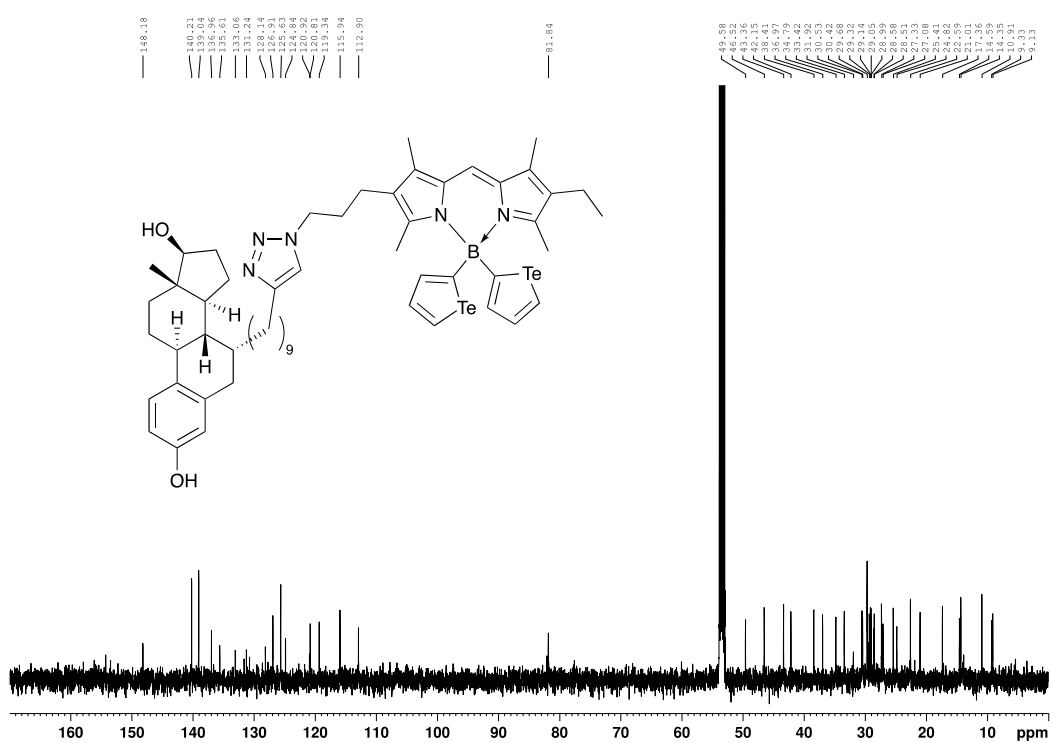


Figure 184. ^{11}B NMR (160 MHz) spectrum of compound **e2a** in CD_2Cl_2

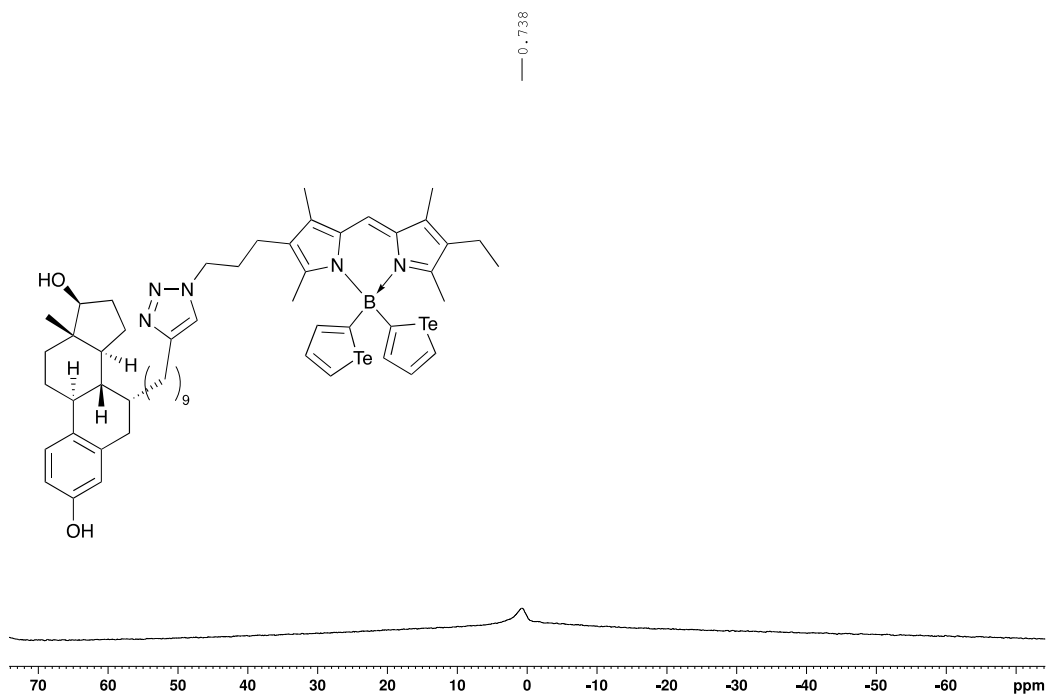
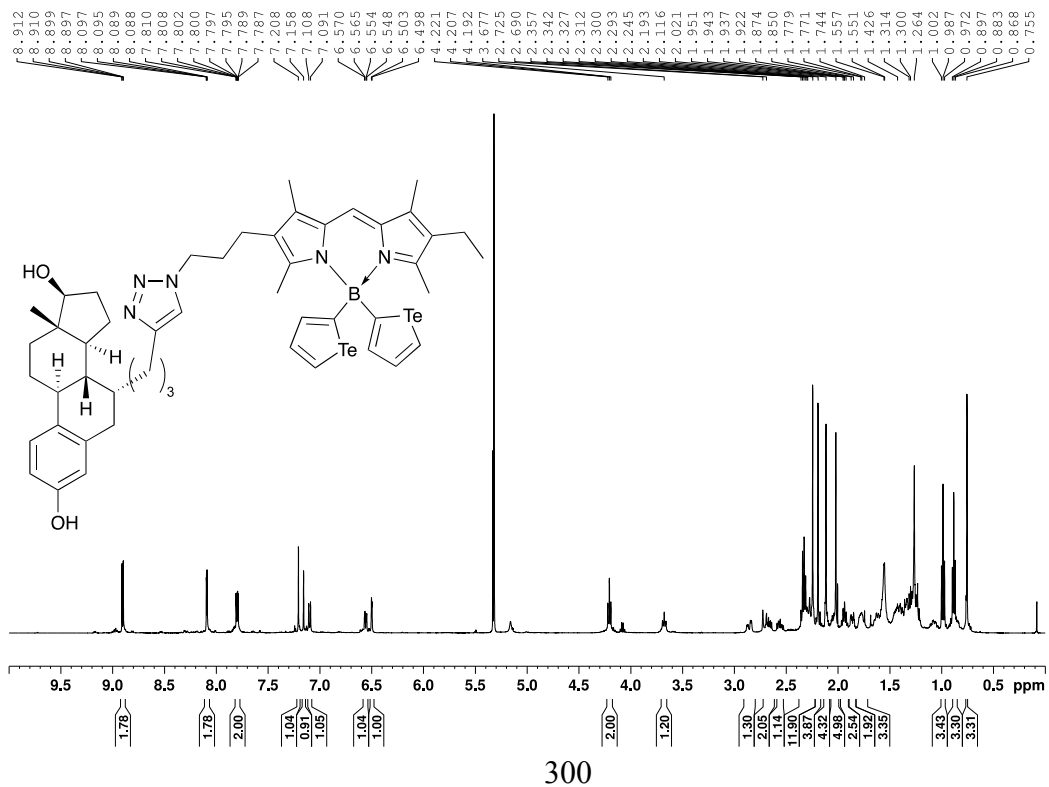


Figure 185. ^1H NMR (500 MHz) spectrum of compound **e2b** in CD_2Cl_2



Appendix F. Copywrite Permission Letters



Introducing the Tellurophene-Appended BODIPY: PDT Agent with Mass Cytometry Tracking Capabilities

Author: Jacob W. Campbell, Matthew T. Tung, Roberto M. Diaz-Rodriguez, et al

Publication: ACS Medicinal Chemistry Letters

Publisher: American Chemical Society

Date: Dec 1, 2021

Copyright © 2021, American Chemical Society

PERMISSION/LICENSE IS GRANTED FOR YOUR ORDER AT NO CHARGE

This type of permission/license, instead of the standard Terms and Conditions, is sent to you because no fee is being charged for your order. Please note the following:

- Permission is granted for your request in both print and electronic formats, and translations.
- If figures and/or tables were requested, they may be adapted or used in part.
- Please print this page for your records and send a copy of it to your publisher/graduate school.
- Appropriate credit for the requested material should be given as follows: "Reprinted (adapted) with permission from {COMPLETE REFERENCE CITATION}. Copyright {YEAR} American Chemical Society." Insert appropriate information in place of the capitalized words.
- One-time permission is granted only for the use specified in your RightsLink request. No additional uses are granted (such as derivative works or other editions). For any uses, please submit a new request.

If credit is given to another source for the material you requested from RightsLink, permission must be obtained from that source.

[BACK](#)

[CLOSE WINDOW](#)



BODIPYs with Chalcogenophenes at Boron: Synthesis and Properties

Author: Jacob W. Campbell, Matthew T. Tung, Katherine N. Robertson, et al

Publication: The Journal of Organic Chemistry

Publisher: American Chemical Society

Date: Aug 1, 2023

Copyright © 2023, American Chemical Society

PERMISSION/LICENSE IS GRANTED FOR YOUR ORDER AT NO CHARGE

This type of permission/license, instead of the standard Terms and Conditions, is sent to you because no fee is being charged for your order. Please note the following:

- Permission is granted for your request in both print and electronic formats, and translations.
- If figures and/or tables were requested, they may be adapted or used in part.
- Please print this page for your records and send a copy of it to your publisher/graduate school.
- Appropriate credit for the requested material should be given as follows: "Reprinted (adapted) with permission from {COMPLETE REFERENCE CITATION}. Copyright {YEAR} American Chemical Society." Insert appropriate information in place of the capitalized words.
- One-time permission is granted only for the use specified in your RightsLink request. No additional uses are granted (such as derivative works or other editions). For any uses, please submit a new request.

If credit is given to another source for the material you requested from RightsLink, permission must be obtained from that source.

[BACK](#)

[CLOSE WINDOW](#)



Sales Operations
 Thomas Graham House
 Science Park, Milton Road
 Cambridge CB4 0WF, UK

Tel +44 (0) 1223 420066

Email contracts-copyright@rsc.org

www.rsc.org

Permission Request Form for RSC Material

To request permission to use material from material published by The Royal Society of Chemistry (RSC), please complete and return this form.

From: Name: Jacob W. Campbell E-mail: Jacob.campbell@dal.ca
 Address: Department of Chemistry Room 212, Chemistry Building
Dalhousie University, 6243 Alumni Crescent Halifax, NS B3H 4R2

I am preparing the following work for publication:

Article/Chapter Title PhD thesis
 Journal/Book Title _____
 Editor/Author(s) Jacob W. Campbell
 Publisher Dalhousie University

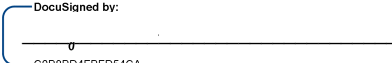
I would very much appreciate your permission to use the following material:

Journal/Book Title Organic & Biomolecular Chemistry
A series of potent BODIPY photosensitisers featuring tellurophene motifs at boron
 Article/Chapter Title _____
 RSC Editor/Author(s) Jacob W. Campbell, Matthew T. Tung, Breanna B. Taylor, Andrew A. Beharry and Alison Thompson
 DOI DOI: 10.1039/d4ob00546e
 Year of Publication 2024
 Description of Material Material will be reproduced for inclusion in PhD thesis
 Page(s) _____

I will acknowledge the original source as specified at the <https://rsc.li/permissions>.

Signed: _____ Date: May 8, 2024

The Royal Society of Chemistry hereby grants permission for the use of the material specified above in the work described and in all subsequent editions of the work for distribution throughout the world, in all media including electronic and microfilm. You may use the material in conjunction with computer-based electronic and information retrieval systems, grant permissions for photocopying, reproductions and reprints, translate the material and to publish the translation, and authorise document delivery and abstracting and indexing services. Please note that if the material specified above or any part of it appears with credit or acknowledgement to a third party then you must also secure permission from that third party before reproducing that material. The Royal Society of Chemistry is a signatory to the STM Guidelines on Permissions (available on request).

Signed:  Date: 9/5/2024 | 12:01 AM BST

Appendix G. Contribution to Manuscript Form



DALHOUSIE
UNIVERSITY

FACULTY OF
GRADUATE STUDIES

STUDENT CONTRIBUTION TO MANUSCRIPTS IN THESIS

MUST BE WORD-PROCESSED OR TYPEWRITTEN.

NAME: Jacob W. Campbell	STUDENT ID #: B00712276
DEPARTMENT: Chemistry	PROGRAMME: Doctoral
PHONE: 1(902)-718-9001	E-MAIL: Jacob.campbell@dal.ca

MANUSCRIPT AUTHORS:	Campbell, J. W., Tung, M. T., Diaz-Rodriguez, R. M., Robertson, K. N., Beharry, A. A., Thompson, A.
MANUSCRIPT TITLE:	Introducing the Tellurophene Appended BODIPY: PDT Agent with Mass Cytometry Tracking Capabilities
JOURNAL:	ACS Medicinal Chemistry Letters
STUDENT CONTRIBUTION:	<ul style="list-style-type: none">- Design, synthesis and characterisation of all molecules- Writing original draft- Coordinating and participating in reviewing and editing process
SUPERVISOR SIGNATURE:	

MANUSCRIPT AUTHORS:	Campbell, J. W., Tung, M. T., Robertson, K. N., Beharry, A. A., Thompson, A.
MANUSCRIPT TITLE:	BODIPYs with Chalcogenophenes at Boron: Synthesis and Properties
JOURNAL:	ACS Journal of Organic Chemistry
STUDENT CONTRIBUTION:	<ul style="list-style-type: none">- Project discussion and conceptualisation- Design, synthesis and characterisation of all molecules- Writing original draft- Coordinating and participating in reviewing and editing process
SUPERVISOR SIGNATURE:	

MANUSCRIPT AUTHORS:	Campbell, J. W., Tung, M. T., Taylor, B. B., Beharry, A. A., Thompson, A.
MANUSCRIPT TITLE:	A Series of Potent BODIPY Photosensitisers Featuring Tellurophene at Boron
JOURNAL:	RSC Organic and Biomolecular Chemistry
STUDENT CONTRIBUTION:	<ul style="list-style-type: none">- Project discussion and conceptualisation- Design, synthesis and characterisation of all molecules bar some works by Taylor B. B.- Writing original draft- Coordinating and participating in reviewing and editing process
SUPERVISOR SIGNATURE:	